Self-assembled, nanostructured organic materials for applications in electronics and optoelectronic devices.

Myles Rooney

Università degli Studi di Milano Bicocca

Supervisor: Dr. Luca Beverina

Abstract

This thesis incorporates the investigation of two methods for molecular control of the nano-morphology of opto-electronic devices. Firstly, a photocrosslinking method for creating insoluble semiconductor layers suitable for organic photovoltaic devices. A large series of squaraine based semiconductors are investigated in a bulk heterojunction device. This approach is extended to diketopyrrolopyrrole and naphthalene diimide semiconducting cores. Detailed study of the materials film structure is carried out.

The second approach is an investigation of the applicability of latent pigments for organic opto-electronics. A series of organic photovoltaics are produced in planar bilayer and bulk heterojunction architectures. The thin film devices are tested with a variety of interlayers and processing parameters. The control of the nanostructure of these thin film devices is examined with X-ray studies. Incorporating X-ray reflectivity, Specular x-ray, Gradient temperature X-ray and grazing wide angle x-ray studies. In this manner the bulk and interfaces of thin film devices can be examined and characterised. The latent pigment approach is also applied to the field of organic field effect transistors as the active semiconducting layer. The solvent resistant nature of a parent semiconducting pigment shows a substantial benefit to the fabrication of such devices. The unique crystalline rearrangement which occurs upon deprotection of a latent pigment results in an improvement in charge carrier mobility of up to three orders of magnitude while extending the processing possibilities of the subsequent deposition steps required to complete an organic field effect transistor

These two techniques are developed with the thoughts of industrial compatibility in mind. As such, a novel synthetic method for facile, cheap, and environmentally friendly production of organic semiconductors is explored. A micellar reaction environment is created through the use of the common surfactant and drug excipient Kolliphor EL. The unique oxygen free core of this surfactant offers a new environment for carrying out common cross coupling reactions such as Suzuki-Miyaura, Stille and Heck reactions in air and water at ambient temperature. High Yields of over 90% are recovered for complex organic semiconducting cores. The versatility of this approach is extended by the use of toluene as a co-solvent. This co-solvent system results in the development of an emulsion which can be used to perform complex chemistries. Emulsion chemistry offers a unique way to synthesis complex organic semiconductors with low metallic catalyst loading at high yield.

Acknowledgements

First and foremost, I would sincerely like to thank Prof. Luca Beverina. The constant support, advice, and encouragement (through science and bureaucracy). Your continued genuine passion for chemistry and its materials has served as a great inspiration for me these passed years.

For all the training and tips for organic synthesis and patience you have shared to me I would also like to thank Dr. Mauro Sassi. One day we will be successful business partners.

Further thanks must be given to Prof. Morten Madsen and his group for hosting me at the university of southern Denmark for getting me up to date on the fabrication of OPV. Thanks to Prof. Roland Resel at the technical university of Graz, Austria for training and help obtaining and understand X-ray data.

I would like to thank and acknowledge Dr. Matteo Salamone and Dr. Riccardo Ruffo for the electrochemical characterisations of materials within this thesis. Dr. Giorgio Patriarca for NMR spectra of my compounds. Isis Maqueira, Giorgio Bonacchini and Mario Caironi from the IIT Milan for Transistor measurements. Francesco Carulli and Silvia Luzzati for help with OPV measurements.

Special thanks must be extended to the LASMO group at Bicocca for welcoming me to the group, the many Italian language lessons and most of all for the continuing friendships.

Last but not least I would like to thank my family for the support and encouragement required to complete this work.

Table of Contents

Organic devices

Chapter 1- Background and introduction to solar applications

1.1 Solar as an alternative energy source

The state of the environment is a matter of worldwide concern. The challenge of developing energy is intrinsically linked to the environment. Roughly 80% of all current energy sources are derived from fossil fuels.[1] Fossil fuels have proven to be very useful energy providers. Unfortunately, they have some issues. The sourcing, refining, and burning of fossil fuels results in the production of carbon dioxide and other greenhouse gases which contribute to the greenhouse effect. The limited supply and difficult access to fuels such as oil and gas often require offshore drilling and environmentally expensive transportation systems to be developed. Not to mention the unique geopolitical situation that often surrounds oil deposits.

These negative aspects of fossil fuels have driven research into investigating green renewable energy sources such as wind, hydropower, biomass, geothermal and solar sources. Solar energy has arguably one of the largest potentials of renewable energy sources to date. In 2000 the United Nations Development Programme estimated that between 1,575 and 49,837 exajoules (EJ) of potentially useable energy irradiates the earth annually. This is many times the annual global energy consumption. The use of this massive source of free, clean energy could have a large impact on the environmental footprint of global energy industry.

Solar energy, in a very general manner, can be harvested in two ways.

1) Concentrated solar power
2) Use of the photoelectric effect.

Concentrated solar power (seen in Fig. 1.1) is a relatively simple concept where solar energy is concentrated into a focal point, often by large lenses or mirrors. The concentrated solar energy irradiates a source of water or air, heating it. This powers steam engines or turbines which can produce electrical energy.

Fig. 1.1. Example of solar concentrator in Spain. The mirrors direct the solar energy onto the water tower. The water powers a steam turbine to produce electrical energy.[2]

The second method involves the use of organic and inorganic materials to carry out photoelectric conversions by using the photoelectric effect. This method uses photovoltaic devices to capture light and convert it to electrical current. This technology is described in detail below.

1.2 Photovoltaics a quick history

In 1839, Edmund Becquerel was attributed with the experimental discovery of the photovoltaic effect. He discovered that useful electrical energy can be generated from sunlight. Becquerel recorded small amounts of current being generated when certain materials were placed in an electrolytic cell[3]. This work was later explained theoretically by Einstein in 1905.[4] Photons incident on the metal contacts of Becquerel's electrolytic cell caused an excitation of electrons which instead of relaxing back to their initial state could be separated into a hole and an electron. These free charges could then be collected at their respective contacts resulting in a charge.

Photons have varying energies depending on the frequency of the light. With sunlight, we encompass ultraviolet (UV) to infrared (IR) wavelengths. Roughly 30% of energy from sunlight is in the visible region of the solar spectrum whereas over 50% is in the IR region. This 50% is usually too weak to generate electricity with today's technology (some exceptions are being introduced with near infrared polymers for transparent photovoltaics)[5], however the visible and UV regions of the solar spectrum are energetic enough to be used for charge generation.

In 1873, Willoughby Smith observed the photoconductivity of selenium while testing underwater telegraph poles[6]. Three years later William Adams and Richard Day made the first

solid photovoltaic cell from selenium with platinum contacts and a bottle neck opening for light[7].

The first large-area photovoltaic device was developed by Charles Fritts. It was made from selenium on metal contacts in 1883, 44 years after Becquerel's first experiments showing the photoelectric effect. This cell reached power conversion efficiencies of 1%.[8]

It wasn't until 1954 before the world took real notice of photovoltaics when Bell Labs released to the world the first "high powered" (for the time) silicon solar cells, stirring The New York Times to forecast that solar cells would lead to a way to harness the "limitless energy of the sun".

Western Electric sold licences for silicon PVs in 1955 for small devices such as dollar bill changers. This marked the start of commercial solar cell technologies, but it wasn't until 1958 when the US Vanguard I space satellite used solar powered radios that interest in solar power began to peak.[9] In the 1970s, photovoltaic research was further encouraged by an oil crisis that highlighted the need for renewable energy sources. The race for higher efficiency silicon solar cells began.

The first evidence of photoconductivity in an organic compound was reported by Italian scientist A. Pochettino in 1906 and German physical chemist Max Volmer in 1913 with work on the polycyclic material, anthracene[10,11]. In the 1950s and 1960s the first work on organic materials as photoreceptors was carried out which led to further study into photoconductivity of organic materials, with notable input from Edwin Alan J. Heeger et al who in 1977 showed a series of simple polymers that could have their semiconducting properties controlled by doping with halides.[12]

Awareness of global warming and the ever-rising price of oil has led governments to offer subsidies for PV research and installations allowing solar cell companies to get a foothold in the energy production market. The high cost of fabricating inorganic solar cells has led to the development of a new field of photovoltaics, organic photovoltaics, which have the potential to be significantly more cost effective than their inorganic counterparts.

The benefits of organic photovoltaics (OPV) are numerous. The main attractive feature of organics is their potential for low cost in comparison to silicon photovoltaics. This is driven mainly by the benefits of thin film fabrication techniques from solution. Silicon requires expensive refinement before high temperature deposition and careful crystal growth. Dyes and pigments offer extremely high absorption coefficients allowing organic devices to be processed

as very thin films resulting in low material consumption. Solution processability opens the door for high speed printing techniques allowing for the development of organic materials in a high throughput, low cost manner.

Organic materials also benefit from their inherent tuneability through structural tailoring. This leads to tailor made organic electronics. Variations in colours and intensities lead to ample selection for design applications in the building industry such as smart solar windows and flexible integrated devices. The free form nature of organic materials allows architects and designers to enjoy limitless creativity in integrating positive energy balance devices to a building or structure. The lightweight and highly flexible nature of organic devices is also a major bonus over the rigid, heavy inorganic counterparts. The opportunities for low temperature produced plastic cells offer countless opportunities for retrofitting of organic cells to everyday technologies. The market for indoor light reclamation and low incident light devices are quite well suited for organic PV.

Organic materials have already seen successful integration into electronics at a commercial level. The development of efficient organic light emitting diodes (OLED) for screen technologies is a prime example of successful organic devices. The first OLED screens were brought to market by Samsung in 2012. Further commercialisation is in progress for other organic devices such as hand held organic photovoltaic devices. These devices are commercialised for charging personal electronic devices such as mobile phones (Fig. 1.2).

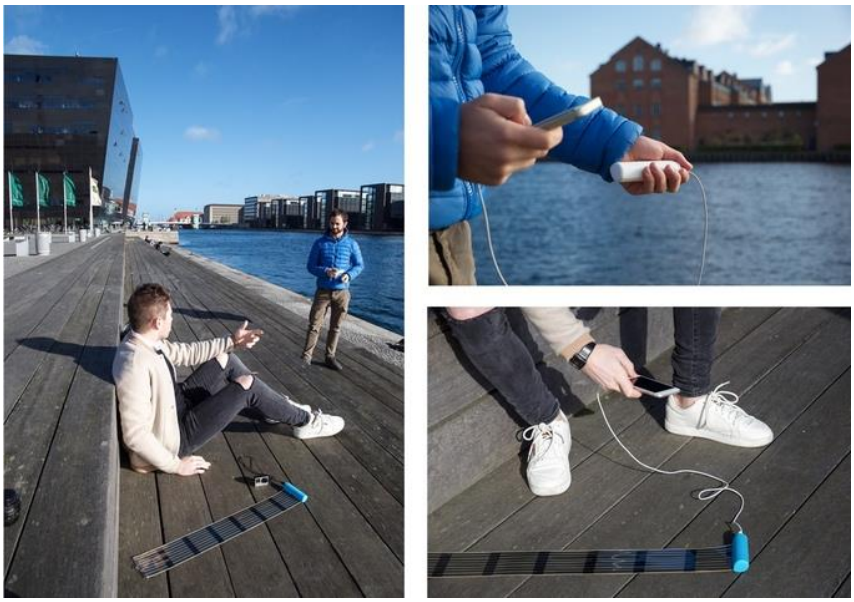

Fig. 1.2. Advertisement for Heli-on infinity PV " the world's most compact solar charger using polymer materials"[13]

The lightweight and flexible nature of organic devices and the ability of organic materials to operate efficiently in areas of low light irradiance (where standard PV underperform) opens up niche markets for indoor applications as showcased by companies such as Ribestech in Milan, Italy. The availability of such organic based devices is expected to increase as research groups are constantly reporting higher efficiency devices.

Basic principles of operation

1.3 Inorganic photovoltaics.

In crystalline inorganic semiconductors a 3D crystal lattice allows for the formation of a conduction band (CB) and a valence band (VB) through which charge transport occurs. For a typical silicon solar cell, the energy gap (bandgap) between CB and VB is roughly 1.1eV.[14] A single material cell absorbs light which results in the generation of free charge carriers, electrons which move through a material's conduction band, and holes which travel through the valence band. These free charges can then diffuse to separate electrodes for collection. The open circuit voltage (voltage when the current is zero) of this type of cell is limited to the difference in work function of the positive and negative contacts. The single material inorganic cell has some draw backs in that the charge recombination of hole and electron results in photocurrent loss. [15]

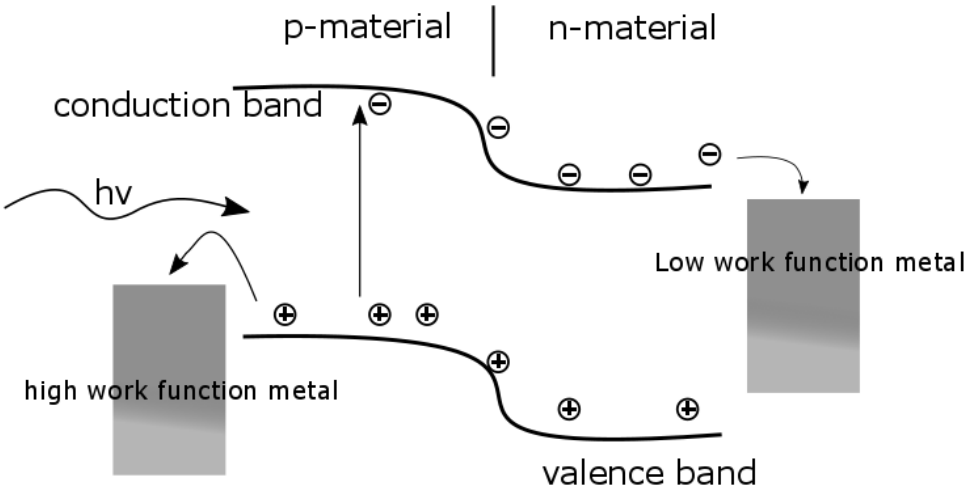

Fig. 1.3. A working schematic for a p/n junction inorganic device similar to the ones first made at Bell labs

To reduce this effect a p/n junction can be developed (Fig. 1.3) . This is a junction between two semiconductors, one which has high electron density (negatively doped n-material) and one that has high hole density (positively doped p-material). The excess electrons diffuse from the n-material to the p-material and the excess holes move from p to n-material. This results in negative ions being formed in the p-material and positive ions forming in the n-material. This area at the p-n junction is now known as the depletion region. This area now has an electric field due to the separated charges at the junction. This reduces the chance for electrons and holes to recombine as they do in the single material devices. The electric field at the depletion region quickly sweeps out any free charge carriers driving them towards their respective electrodes.[16]

1.4 Organic photovoltaics.

There is a striking difference between the operating principles of an organic device to one formed with inorganic semiconductors. Organic semiconductors lack the strong intermolecular electronic overlap required for the formation of the conduction and valence bands. Organic semiconductors instead rely on localised frontier orbitals: highest occupied molecular orbital (HOMO) and the lowest unoccupied molecular orbital (LUMO). Upon absorption, a strongly bound (binding energy ~0.3eV) electron and hole pair called an exciton is formed. The low dielectric constant of organic materials hinders photovoltaic performance due to difficulties with charge separation. The exciton requires a driving force to separate it into a free electron and hole which can be then transported by a hopping process. This is a slow process compared to transport in inorganic systems resulting in higher incidences of charge recombination. Organic materials have intrinsically lower charge mobilities than in inorganic systems. This accounts, in part, for the lower power conversion efficiencies in OPV.[17,18,]

The low level of charge delocalisation and small dielectric constants of organic materials results in the requirement of two organic materials to be used in a photovoltaic cell: a donor (electron rich) and an acceptor (electron poor) material. A bi-layer system was first proposed by Ching W. Tang in 1986 with a breakthrough paper called “two-layer organic photovoltaic cell”. [19] This cell differed from all single layer systems in that the interface between donor and acceptor is the key element responsible for photovoltaic performance. Until C. W. Tang’s paper the interface between semiconducting material and metal electrode had been the determining factor in performance. C. W. Tang’s cells had a power conversion efficiency of 1% which was a huge improvement on single layer devices. The offset of the HOMO and LUMO levels

between the two materials generates sufficient driving force to overcome the coulombic forces holding an electron and hole together in an exciton.

The photovoltaic process is made up of four steps:

1) Light is absorbed

2) Charge generation and separation

3) Charge transportation

4) Charge collection

1) Absorption is controlled by the bandgap of the material. Organic semiconductors tend to have relatively high absorption coefficients (>50,000$M^{-1}cm^{-1}$) when compared to their inorganic counterparts. The absorption is strong, but a lot of the solar spectrum is lost due to the narrow bandwidth of these absorptions. Generally, when fabricating an OPV, the absorption features of the donor and acceptor materials are chosen to be as complimentary as possible. Optimising the complementary absorption characteristics of the two materials ensures as much of the light, incident on the cell, as possible is harvested. [20]

2) Absorption of the photon results in the formation of an exciton. The binding energy of the exciton is high, but it can be overcome by the frontier orbital energy offset of a donor and acceptor material (the energy offset between the HOMO's and LUMO's of the two materials). When the energy gap between donor and acceptor is larger than the exciton binding energy the exciton can be split into a free electron and hole. The difference between bound exciton free energy and that of the resulting dissociated electron-hole pair is the driving force for this electron transfer process. If the energy gap between HOMOs and LUMOs of the donor and acceptor is too large then the electron transfer process will be slow as shown by Marcus theory.[21] If the driving force is larger than required, the excess is lost through thermalization. This results in a reduction of the open circuit voltage (Voc) of a cell. This tells us the HOMO and LUMO energy offset of the donor and acceptor is critical for optimising the charge transfer process.[2122]

3) The holes and electrons are then transported through the material by a hopping process. The electrons move from the LUMO of the photoexcited donor material to the LUMO of the acceptor material. This process is driven by the internal electric field across the electrodes. This photo induced electron transfer occurs at the interface between donor and acceptor materials.[23] At this stage, a series of charge recombination processes can occur due to charge traps and material defects.[24] The diffusion length of free charges in each material is a key factor in the efficiency of this step.

4) If the charges do not recombine they can arrive at the electrode interface where they are collected. The work function of the electrodes must be optimised with the energy levels of the semiconducting materials. Blocking layers can be added at the contacts to ensure this process is optimized. Cathodes are usually made from a low work function metal such as aluminium while typically the anode is made from a transparent tin doped indium oxide (ITO).

Each stage of the photovoltaic process can limit the power produced by a solar cell. It is necessary to optimise all 4 of these processes to achieve a high-power conversion efficiency (PCE) solar cell.

In organic photovoltaics, the absorption of light results in the formation of an exciton. Excitons are neutral species so their movement through a cell is not influenced by the electric field created by the electrodes. These excitons move through random diffusion in a cell until one of two things happens.[25] Ideally, the exciton will find the interface between donor and acceptor material and be split into charged species. The second possibility is that the exciton will run its diffusion length and simply decay back to the ground state. Short exciton diffusion lengths significantly inhibit cell performance as they are typically much smaller than device thickness. Limiting the cell thickness results in much lower light absorption which also results in fewer photo generated charges. A balance between layer thickness and light absorption must be established to enhance cell performance.

Once an exciton reaches an interface a coulombic charge-transfer state forms. In this situation, the hole is in the HOMO of the donor and the electron is in the LUMO of the acceptor material, but they still require an external electric field to act as a driving force for charge dissociation.[26] From this state, where the charges are now free to travel to their respective electrodes, charge

transport properties become the important factor in dictating the cell performance. The charge transport competes directly with charge recombination.

The hole mobility generally limits the charge transport properties as they are usually lower than electron mobilities in organic semiconductors.[27] Once the charge carriers have been transported to the electrodes the energy levels of the semiconductor must be well tuned to the electrodes work function. If they are not aligned carrier loss will occur.

The design of organic semiconductors has restrictions as a result. The organic materials must be optimised in terms of absorption and extinction coefficient. Secondly, the energy levels must be well aligned with both cathode and the semiconductors organic counterpart and thirdly, the transport properties which are often related to a materials crystallinity or morphology must also be optimised. Practical elements must also be taken into consideration. Semiconductor processability, stability and often miscibility with other semiconductors must be considered within chemical design. OPVs are relatively complex devices and their optimisation, on both a molecular and architectural level, is an area of massive research interest.

1.5 Basic cell structures

Single layer cells (Schottky type)

Schottky type cells are made from an organic material sandwiched between two metal contacts with different work functions. The area near the semiconductor/low work function metal interface forms what's known as a Schottky barrier. The electrons moving from the active metal into the organic p type material results in a depletion zone. This causes a small field which raises the HOMO and LUMO levels in this barrier region. This depleted area can then be used to dissociate excitons. If a p-type organic material (electron donor material) is used in this sandwich style cell a Schottky barrier (a potential energy barrier for electrons) is seen between the organic layer and the cathode. This is a depletion area at the cathode that causes the material to act as an electrical rectifier (converting alternating current into direct current). If an n-type material (acceptor material) is used the Schottky barrier forms at the anode. The low photoelectric efficiency of this type of cell is attributed to the small diffusion lengths of the exciton. Only excitons generated in the close vicinity of the Schottky barrier will result in charge generation. As a result, this type of cell is rarely studied.

In 1993, S. Karg proposed that poly(*p*-phenylene-vinylene (PPV)) may be used in photovoltaic applications while he was studying optical properties of the material for light emitting diodes.[28] The following year R. N. Marks et al. designed a single layer organic solar cell with a standard photodiode structure. 100nm thin films of PPV were sandwiched between two electrodes of Indium/tin oxide (ITO) and Al/Mg/Ca. Device efficiencies were in the order of 0.1% due to low exciton diffusion lengths in the organic material. The energy required for excitons to split into free charges reduces the open circuit voltage of a device, resulting in OPV efficiencies lower than the estimated Shockley-Quessier limit (a measurement for defining the upper limits of efficiency for a p-n junction for inorganic cells). It was also seen that PPV has a chemical reaction with aluminium contacts with the formation of an insulating layer which results in the increased electron injection barrier. Today, it is common to evaporate a thin layer of hole blocking material in between the aluminium and the semiconductor to reduce this effect.[29,30,31]

Heterojunction cells (bilayer system)

It was found that excitons dissociate more efficiently at donor acceptor interfaces. First realised by Chien W. Tang, the bi layer or heterojunction solar cell consists of two electrodes and two organic materials (a donor and an acceptor). This is the second generation of organic PV cells. Essentially, a p-n junction forms between two organic materials with a band edge offset. The frontier orbital offsets at the organic-organic interface is the key driving force for electron-hole separation. The donor is a material with low lying HOMO levels and relatively high ionisation potential while the acceptor is a material with a comparatively high affinity for electrons and ideally a low lying LUMO level. Separated holes hop to the HOMO of the donor material. Electrons hop from the LUMO level of the donor to the acceptor. The internal field across the electrodes then drives the separate charges away from the interface towards their respective electrode. The electron and hole are kept in separate materials, so the chances of carrier recombination are greatly reduced as a result.

Although this structure has many advantages over the single layer device, they are still limited by the exciton diffusion length, typically in the order of 5-20nm for organic semiconductors. As such, very thin films of donor and acceptor material must be made. This restricts the light harvesting capabilities of the device and restricts the efficiency of this type of device. It is also quite a difficult task to layer two materials on top of each other in very thin films without the use of relatively expensive low throughput processes such as vacuum deposition.

Bulk heterojunction

The bulk heterojunction (BHJ) was proposed in 1995 as a method to circumnavigate the necessity for very thin films resulting from low exciton diffusion lengths.[32] A bulk heterojunction consists of an intimately mixed donor and acceptor layer. The BHJ is a continuous interpenetrating network of donor and acceptor. It results in a massive increase in donor acceptor interface area which significantly reduces the distance for an exciton to travel for splitting. The increased likelihood of a generated exciton dissociating at the interface results in a substantial improvement to power conversion efficiencies. The layer thickness can also be increased so more light is harvested.

This is the most common type of organic photovoltaic seen in literature. This architecture has seen many rigorous studies for adopting ideal morphologies within the bulk heterojunction.[32,33,34,35.]

Issues with the BHJ arise from the lack of control of morphology and the thermodynamic instability of the nanoscale morphologies in the intricately mixed bulk layer. Carrier loss is common due to poor phase continuity. The bi-continuous donor and acceptor blend often results in isolated domains of donor or acceptor materials which cannot connect to their respective electrode. If the conduction pathways in each material are not of desirable morphology the poor charge carrier mobilities of organic materials will dictate a restriction to the thickness of the active layer (usually between 100-200nm, this is still an improvement on bilayer heterojunctions which usually have a maximum thickness of 70-100nm). In contrast to this charge trapping issue, if a material is simultaneously in contact with both electrodes carrier recombination at the organic-electrode interface will become an issue.[24] So, for a BHJ to be successful it is evident that the control over the blend morphology must be very strict. Stability and reproducibility of these blends are a significant issue. The morphology is strongly dependant on conditions of processing. Lab to lab discrepancies are a serious issue within the field of OPV. Low levels of reproducibility often stem from the many variables associated with non-standardised fabrication methods.

Tandem cell

The first example of an organic tandem solar cell was shown in 1990 by M. Hiramoto. In this study, a cell made with two sets of identical materials separated by a thin layer of gold (2-3nm) resulted in almost doubling of the open current voltage when compared to the material in a single bilayer. [36]

The absorption spectra of organic semiconductors are typically of a narrow bandwidth with a mismatch in absorption between donor and acceptor. Organic semiconductors absorb light of an energy close to the optical energy gap. Thick devices are desirable for optimal light absorption. Unfortunately, transport properties of organic materials limit the thickness of OPVs but by using the tandem cell architecture we can combine various materials with complementing absorption spectra. This method uses a number of semiconducting materials stacked upon each other connected in series. Connecting these sub cells in series covers more of the solar spectrum while overcoming the transport issues of thick BHJ devices.

In a tandem cell, the top cell will absorb the section of the solar spectrum not covered by the bottom cell. The broader spectrum of light absorption (in some cases from the UV as far as the IR regions) increases the Voc of a tandem cell (as the subcells are connected in series the photo voltage of each subcell adds up). This architecture offers a method to obtain high efficiency organic devices with the highest performing devices being produced in the order of 13.2% by Heliatek in 2016. Obviously, the downside to these devices is the high level of control over processing parameters which is required to successfully deposit multiple layers within a device

1.6 The IV curve

To characterise the performance of an OPV device one must measure the current generated in the cell over a sweeping range of voltages, in the dark and under illumination (standard AM1.5 G illumination). The resulting output from such a measurement is called a current voltage curve (IV curve) (Fig. 1.4). This is the main characterisation for examining a photovoltaic device's performance.

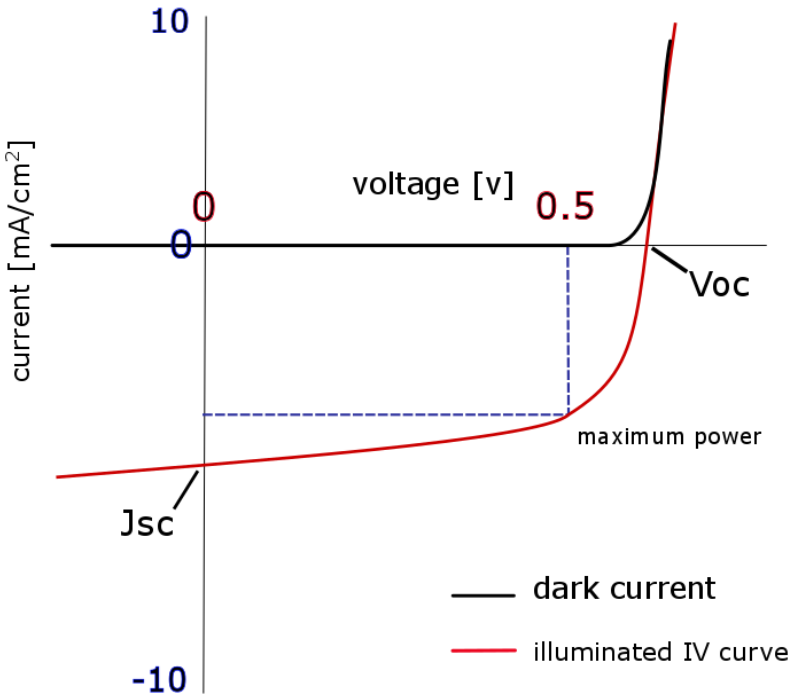

Fig. 1.4. Schematic diagram of a typical current density vs voltage output curve under illumination in red and under dark conditions in black

The resulting information is obtained from an IV curve:

1. Open circuit voltage, (Voc).

This is the maximum voltage of the cell: occurring at zero current the Voc correlates the forward bias on the cell to the bias of the cell with light generated current. The maximum Voc of a cell is generally limited by the energy difference between the HOMO of the donor and the LUMO of the acceptor material. For inorganic devices, the work function of the electrodes plays an important role in dictating the Voc of a cell.

A loss of energy is expected when the exciton splits into its individual free charges. It costs roughly 0.3 eV to drive the electron and hole apart. If the difference between the HOMO and LUMO of the materials is less than this exciton splitting energy the exciton is unlikely to split into charges. Thus, the donor and acceptor materials must be chosen carefully.

A donor should ideally have low lying HOMO (~-5eV/-5.5eV) with good offset from the acceptor to increase the Voc. Although, lowering the HOMO can also result in a band broadening which will reduce the short circuit current (Jsc). Finding a balance is key for the design of efficient donor acceptor systems. One approach for lowering the HOMO levels of a material is to extend the conjugation with groups with strong donating character, such as

thiophene. It must be noted that while lowering the HOMO level can result in an increased Voc, the energy alignment of the accepting material and the work function of the metal electrode holds a great importance to the Voc of the device.

2. Short circuit current, (Jsc).

When measuring an OPV in the dark it is expected that almost no current will flow until the forward bias surpasses the Voc. When the system is illuminated with zero bias the photogenerated charges are collected at their respective electrodes and a current is recorded. This value is the Jsc. The applied forward bias supresses this current until the applied voltage reaches a value where the current is reduced to zero (Voc).

Jsc is a value for the current passing through a solar cell when the voltage is zero. The Jsc is related to the efficiency of transport of free carriers in the device and the extraction at the electrodes. Therefore, Jsc is a combination of the quality of materials within the device; the area of the cell, the power of the light source and the optical properties of the organics (only photons with an energy matching the optical energy gap of the absorbing material will be absorbed). Increasing the band gap of the organic semiconductors generally decreases the Jsc.[37] Some methods for ensuring a low band gap involve alternating electron rich and electron deficient groups along a conjugated chain. Also, increasing conjugation should reduce the band gap of a material accompanying a red shift in absorption. Materials with low lying HOMO levels coupled with a low bandgap should generally be a good material for OPV.[38]

A method for controlling the bandgap has been outlined by J. Roncali in 1997. This acts as a useful tool for designing materials for OPV[37]

$$\mathrm{Eg} = \mathrm{Eres} + \mathrm{Edr} + \mathrm{Esub} + \mathrm{E}\theta + \mathrm{Eint}$$

Eg=Optical bandgap, Eres+Edr=Conjugated backbone and conjugation length, Esub=Electronic effects of substituents, Eθ = Steric effects of substituents, Eint = Interchain interactions

3. Fill Factor, (FF).

The fill factor is a comparative value for the overall performance of a cell's real operation in comparison with the ideal. It is a general reflection of the recombination processes within the cell. Recombination rates in a BHJ are typically an order of magnitude lower than charge

generation rates, allowing for the ionized stated to be long lived. FF is a measure of squareness fit of a cell's performance and can be used in conjunction with Jsc and Voc to determine the maximum power of a solar cell. Additionally, electron and hole mobilities in donor and acceptor materials should be relatively balanced as a slower mobility of either electron or hole will result in a build-up of space-charge in the active material. This results in a distortion to the electric field resulting in a slower charge extraction.[39] High mobilities results in efficient charge extraction from the interface which in turn reduces steady state build up. The consequent low density of charge carriers at the interface reduces rates of recombination in a device, improving the FF.[40]

Materials with excessively high mobilities can be detrimental to device performance as it can result in a device with reduced charge accumulation. This effectively reduces the Voc of a device by shifting the energy levels of the donor and acceptor. This has negative effects on both FF and power conversion efficiency. The fill factor and general shape of the IV curve tells a lot about the quality of the material layers. Low shunt resistance, for example, will present itself as a S-shaped IV curve. This may be indicative of poor film quality and pinholes in the device.

Using these above parameters, we can calculate the power conversion efficiency of the cell (being the efficiency of conversion of light to energy) with the following formula.

$$\eta = FF\,\frac{JscVoc}{A(Pmax)}$$

FF=Fill factor, Jsc = short circuit current, A= area of device, Pmax= maximum incident power, Voc=open circuit Voltage.

1.7 Materials and state of the art

At this point in time, polymer based bulk heterojunctions are the most likely system to be upscaled. This is not only because polymer based cells tend to have higher PCE, but rather because they are highly solution processable and tend to provide higher quality films than highly crystalline small molecules. Solution processability is a key to significantly reducing fabrication cost when compared to vacuum deposition processing.[41]

Organic photovoltaics are complex multi-material devices. Rigorous optimisation of each individual layer and material is required to produce high performance devices. The interlayers between active semiconductor and electrode are hugely important for the transport properties

of a cell. However this thesis is concentrating on the morphology of the active semiconducting layers of organic electronics and these are the materials which will be discussed.

Working with small molecules with post-deposition processes, we look to make a level playing field with polymer based cells in terms of processability. The possibility of lowering costs with small molecule solar cells is large. Small molecules also carry the added benefit of having well defined structure, higher purity, wide variety of synthetic procedures and a generally more ordered nanostructure.

The structure of organic semiconductors is based on a series of alternating σ and π bonds which results in conjugated π-electrons. These π-electrons have much higher mobility than the σ-electrons. Mutual overlap of π-orbitals throughout a conjugated species allows for the delocalisation of the wave function through the conjugated portion of the material. This system has the perfect electronic features for light absorption and charge generation.[42]

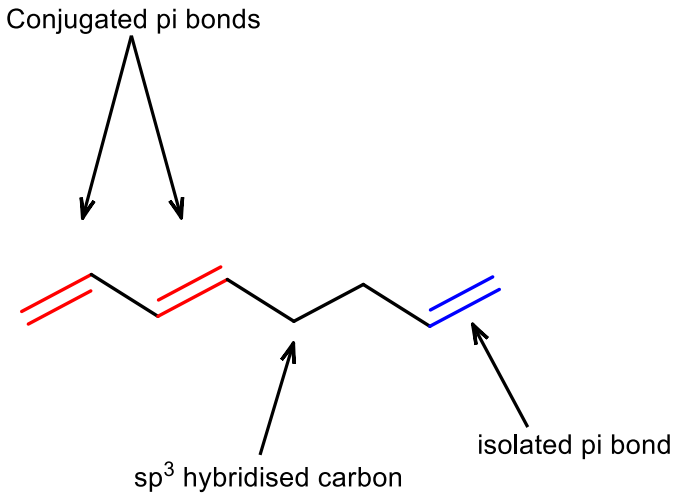

Fig. 1.5. conjugation allows for the delocalisation of electrons across a molecular backbone. Isolated π bonds cannot contribute to this conjugation.

Organic semiconductors, whether they be used for transistors, solar cells, or light emitting diodes all rely on π-conjugated structures (Fig.1.5). The delocalised π-electrons act in a similar way to the free delocalised electrons in a metal. The solid-state structure of organic materials relies on weak van der Waals forces between neighbouring molecules. This gives organic materials both semiconductor and insulator like properties. The metal like conductivity of organic materials stems from the π-conjugation. As a result, novel semiconductors are generally based on a series of conjugated aromatic ring structures.

Below is a table showing examples of a few common organic semiconductors (Fig. 1.6). Most of these materials have a high level of aromaticity. Crystallinity and molecular alignment of materials in a device plays an important part in the performance of an organic semiconductor. High mobilities often come from very planar, 2D materials such as pentacene or polythiophene. Although great advancements have been made with high performance organic materials, poor environmental stability, processability and low performance in comparison to inorganic counterparts remains an issue. The systematic study of novel semiconductors is key to furthering the understanding of charge transport efficiencies in relation to film morphologies, molecular structure and organisation.

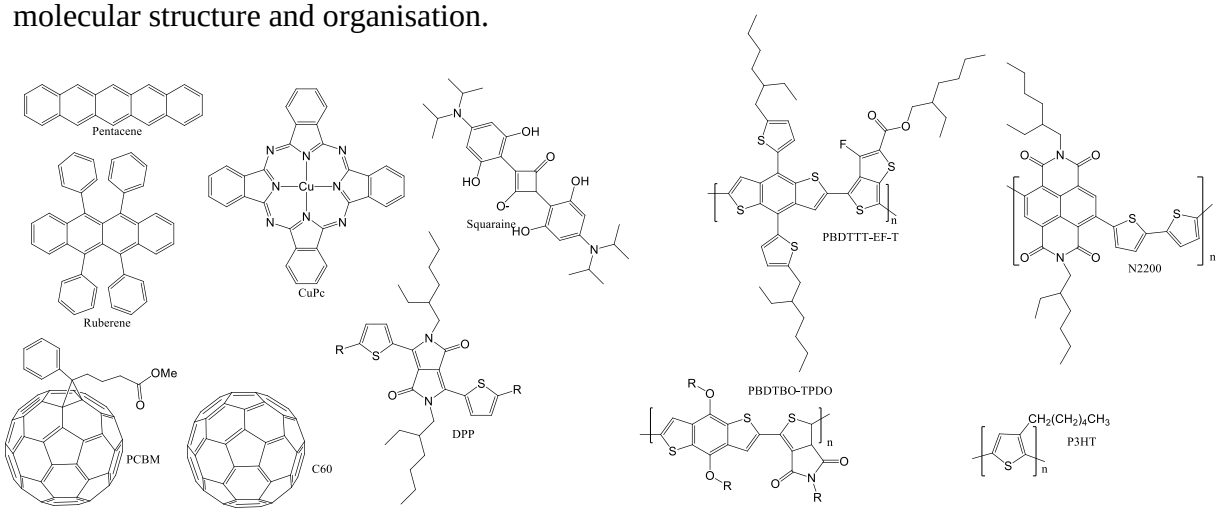

Fig. 1.6. A series of common organic semiconductors used in photovoltaic, transistor and light emitting diode technologies.

The current state of the art for organic photovoltaics can be split into two categories: those which have achieved scale up and those which remain at a laboratory scale device.

Perhaps the two most well-known and studied materials in the OPV industry are Poly(hexylthiophene) (P3HT), a versatile donor polymer, and an acceptor material called Phenyl-C61-butyric acid methyl ester (PCBM) which is a soluble Buckminster fullerene derivative. (Fig. 1.7)

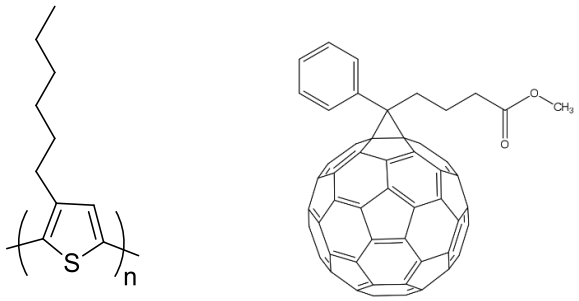

Fig, 1.7. chemical structure of P3HT (left) and PCBM (right)

When used in tandem with each other, P3HT acting as a donor material and PCBM acting as the acceptor, these materials have reported power conversion efficiencies around 4-5%.[35,43,]The variations in PCE are due here to the processing conditions. These two materials are most often used in a BHJ architecture. The initial mixture of these materials is dynamic and complex. The ratio of donor to acceptor, the thickness of the resulting films, and the interlayers and substrate types all effect the nano-morphology and resulting PCE of these devices. Furthermore, thermal annealing processes can be used to control and enhance the morphologies within this system. Thermal annealing has been proven to be a useful post deposition method for controlling the phase distribution within the active layer of intricately mixed donor and acceptor.[44,45] Organic materials have low exciton diffusion lengths so the improvements in PCE after thermal annealing have been attributed to an improved phase distribution[46,35]. As a result, a large portion of research has been allocated to optimizing the thermal annealing of P3HT: PCBM BHJ films. This has led to a strong understanding of charge carrier injection and recombination processes as well as the interface nature of this complex system.

These materials have also undergone the upscaling process to roll to roll printing systems. The upscaling of OPV is a complex process (Fig. 1.8). Many articles claim that the high-performance systems produced in a laboratory on small glass slides are roll-to-roll compatible and industry applicable. These statements are often untrue as the larger devices have unique challenges not seen in small scale laboratory devices.

In the words of Frederik Krebs et al. "*The view held here is that claiming to be roll-to-roll and industrially compatible without such instruments is similar to claiming that one can learn how to swim on a floor."* [47]

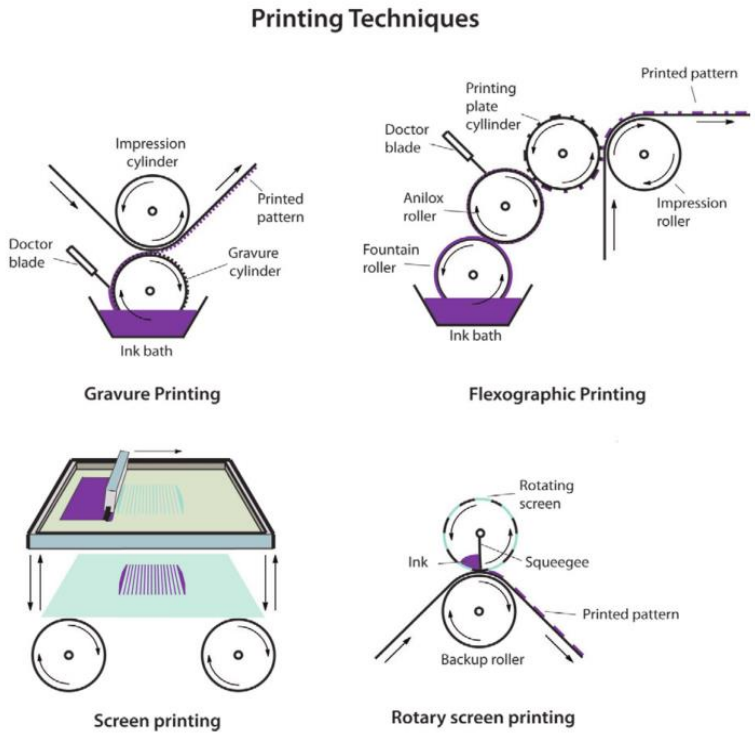

Fig. 1.8. A variety of different solution based fabrication techniques are available for large scale Roll-to-Roll process

The general observation when moving to the large scale is that the PCE of well optimised small-scale systems, such as in the case of PCBM and P3HT, is substantially reduced as cell size increases. This is partly due to the parasitic series resistance of large contacts but is also due to the methods used for fabricating small-scale devices, spincoating in inert conditions in a glovebox with a thermally evaporated interlayer and contacts is not made compatible with roll to roll technologies easily.

The requirement for processing parameters such as deposition method, solvents used and the drying/annealing techniques to be changed devalues the highly optimised performances achieved from small scale devices. Difficulties arising from lower levels of film homogeneity in larger area devices account for lower FF and PCE in these large devices.

The thickness of industrial scale OPV is generally in the order of 200-250nm. This thickness causes some issues for the standard P3HT: PCBM system. Typically, a decrease in photocurrent is observed as device thickness is increased, away from the small scale optimised thickness. This has led to the development of non-fullerene based systems where low band-gap polymers such as indacenodithiophenoindacenodithiophene (IDTIDT-IC) replace the fullerene acceptors. This appears to create a set of devices with performances which are insensitive to

device thickness. This more robust and forgiving combination is more suitable to industrial applications.[48]

Recently new methods for coating large scale devices such as the partially overlapped spray coating method has been refined to produce higher levels of homogeneity in films. A high efficiency of 5.27% on a 38.5cm^2 cell was achieved using this technique with the conjugated donor polymer poly[N-(2-hexyldodecyl)-2,2′ -bithiophene-3,3′ -dicarboximide-alt-5,5-(2,5-bis(3-decylthiophen-2-yl)- thiophene) (PBTI3T) and a C_{70} fullerene derivative $PC_{70}BM$.[49] Although these materials showcase an impressive PCE of 8.42% when optimised in a small-scale laboratory device with FF approaching 80% [50] this novel large-scale fabrication technique illuminates the progress being made for roll to roll upscaling.

Moving away from large roll-to-roll devices we can note a strong importance has been placed on the high-power conversion efficiency throughout relevant OPV literature. Small molecules are an attractive possibility for organic solar cells. High purity, solution processability, batch to batch homogeneity and versatile, tuneable molecular structures are some of the most enticing properties of small molecules. Characteristics such as absorption properties, charge carrier mobilities and energy levels are all controlled by the carefully designed electronic structure of a material. This tailorable character results in the possibility to use a wide variety of different core structures for optoelectronic applications. A number of different techniques can be combined to design materials for OPV applications.

Donor-acceptor architecture

Recently, it has been revealed that high performance small molecule donor materials can be developed using a donor-acceptor-donor type structure. This type of material (see schematic below Fig. 1.9.) consists of a weakly accepting core connected by a conjugated linker to cores with strong donating character. Generally, a series of solubilising chains are added to these structures to increase the processability of the material.

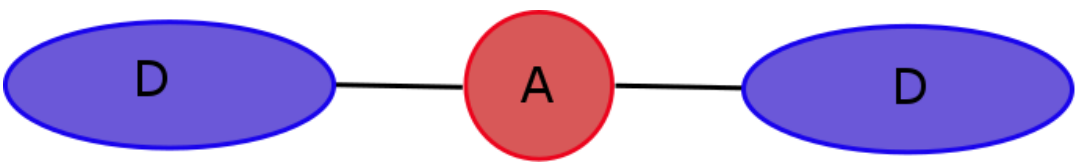

Fig. 1.9. General structure of donor-acceptor small molecule. Donor moiety (blue) is connected by a conjugated bridge to core with acceptor like character (red).

A number of these donor-acceptor materials have become promising candidates for BHJ style devices. For example, a dialkylthiol-substituted benzo[1,2-b:4,5-b′]dithiophene material called DR3TSBDT was incorporated into a BHJ with $PC_{71}BM$ with a short annealing resulted in a impressive PCE of 9.95%. The device exhibited good light absorption and a balanced charge mobility with a FF of 75%.[51]

Planar materials

Highly planar materials have also shown good potential for small molecule OPVs. Recent studies show high PCE of 7.23% for a porphyrin material (Fig. 1.10), symmetrically functionalised with two diketopyrrolopyrrole (DPP) units, used in BHJ format with $PC_{61}BM$.[52] Porphyrins are a class of heterocyclic macromolecules which exhibit planar character over an extensive conjugated core.

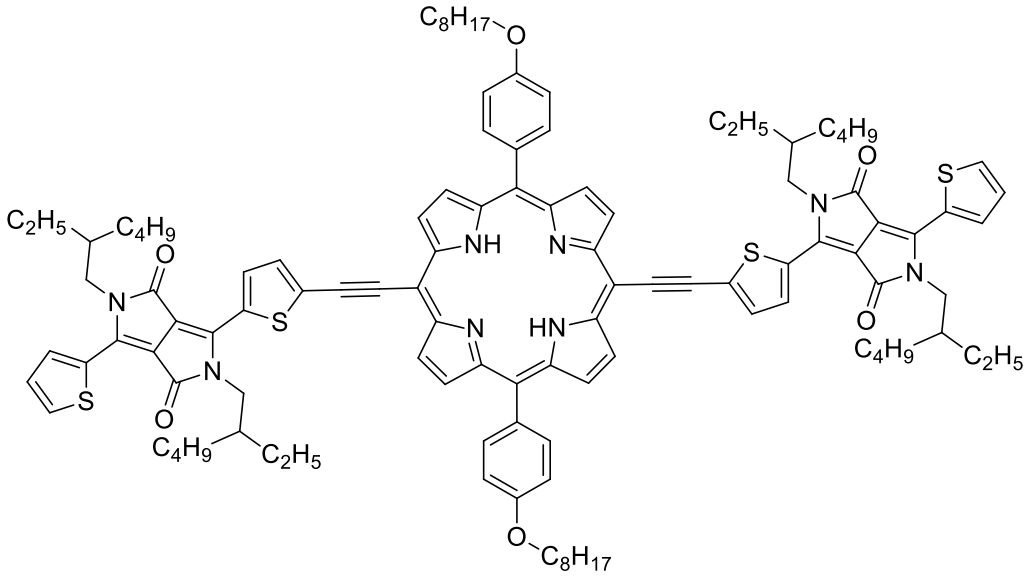

Fig. 1.10. Structure of high performance porphyrin functionalised with DPP units.

Having a material of high planarity can help in forming strong and tightly packed π-π stacked structures within a film. High levels of order throughout a film can lead to optimal charge carrier transport. Generated charges travel efficiently through the π stack. This leads to low levels of exciton recombination or charge trapping.

Side chain engineering

Choosing a suitable side chain can be a difficult decision. The side chain is usually the portion of a semiconductor which donates a solubilising ability to the material. The length and degree of branching must be carefully optimised so that a material is soluble enough to be processed into a film. The issue being that these long alky chains have an insulating character and can

disrupt the packing modes of a material. The steric contribution of side chains can have a drastic effect on a semiconductor. Increasing carbon chain lengths has been known to lower HOMO levels and raise LUMO levels. This is due to steric changes straining localised conjugation which restricts the delocalisation of electrons throughout the π-network.[53]

In BHJ cells it is often the scale of side chain engineering which will control a materials tendency to aggregate and has a profound effect on the phase segregation within the bulk mixture[54,55]

Diketopyrrolopyrrole dyes

The DPP dye is a popular semiconducting core for both OFET and OPV applications. This accepting core consists of 2,5-Dihydropyrrolo[3,4-c] pyrrol-1,4-dione unit which has a high thermal stability. The most famous of these dyes is perhaps pigment 254, also known as Ferrari red. This material is of interest for photovoltaic and OFET applications due to its good stability, rigid planar backbone, and facile functionalisation which can be adapted to tune the absorption and emission characteristics of the material.

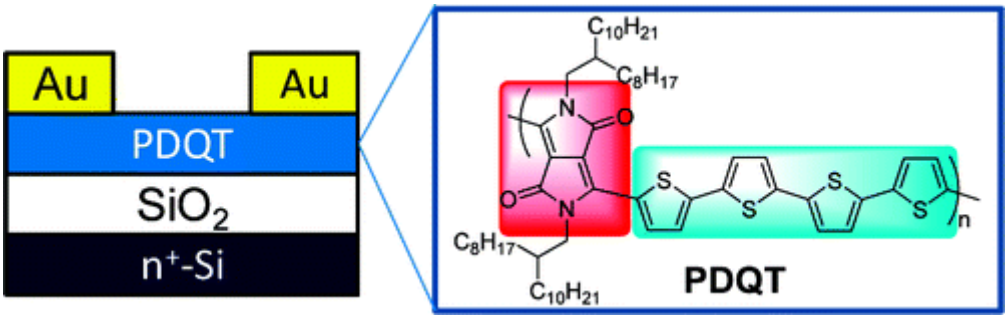

Fig. 1.11. Jozel Tan et. al developed high-performance transistors with a thiophene-DPP polymer without the need for thermal annealing[56]

Many examples are available where functionalisation of this core with thiophene-based donating groups has resulted in high performance devices and good charge transfer properties. This material has been successfully incorporated into OPV, OFET and OLED devices. The DPP core is regularly seen in use as a copolymer semiconductor within these fields. [57,58,59]

Squaraine dyes

For a time squaraine based semiconductors (Fig. 1.12) received a lot of attention due to the short synthetic procedures required to synthesis theses donor cores. Extremely high extinction coefficient near the visible-IR region, deep lying HOMO levels and easily tuneable bandgap make this highly stable and crystalline material a very attractive option for incorporation into organic electronics.[60,61]

Although devices involving heterojunctions of squaraine dyes acting as a donor material in conjunction with C60 have surpassed 5% PCE [62], low charge carrier mobility and relatively thin absorption bandwidth coupled with low solubility (unless extensively functionalised with alkyl chains) restricts the potential of this material for OPV use.

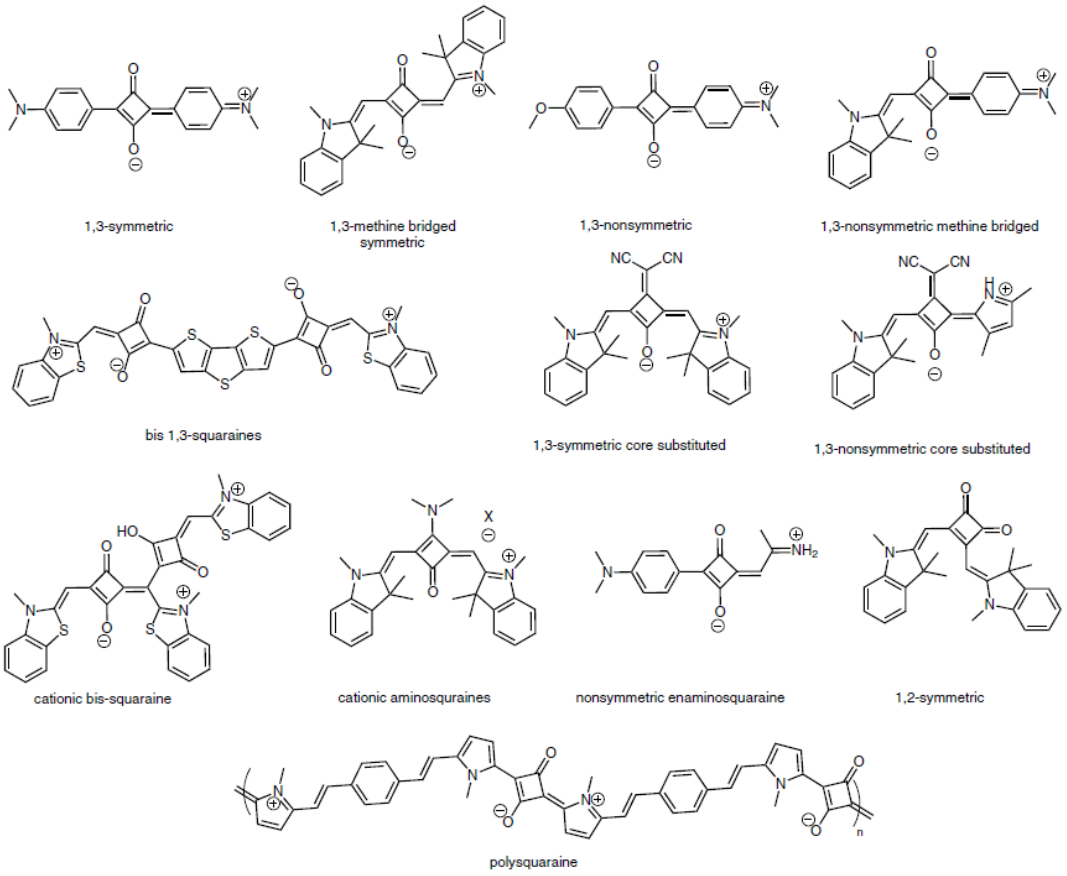

Fig. 1.12. The diverse library of squaraine materials [63]

Evolution of OPV

From a device architecture point of view huge steps have been taken in the field of OPV. Record performance has been achieved by the German fabricator Heliatek. The 13.2% PCE device was fabricated with a tandem architecture in 2016. This is an important marker of the success of OPV. 10 years previously Heliatek was boasting performances of only 3%. This improvement over the short timescale indicates the potential of this technology in the future.

The two main production techniques used in the fabrication of OPV are wet processing and thermal evaporation. The latter of which offers the benefits of precise control of thickness and facile access to multilayer depositions which are difficult with solution methods.

Unfortunately, thermal evaporation is not suitable for low-cost, large-scale production as high temperatures and strong vacuum are required for this process. This leaves solution processing as the most viable method for roll to roll fabrications.

To truly be more cost effective than silicon PV, organic materials must be processed with a high throughput in a low temperature roll to roll manner. The nature of organic materials opens the possibility of integrating standard high-speed printing processes in the fabrication of large scale devices.

The solution processability of organic materials also offers the possibility of a reduction in the energetic pay-back time of solar cells but at this point the scale up of devices has been difficult as often the efficiencies of devices see a dramatic drop upon upscaling.

References

1. Consumption, C. *et al.* BP Statistical Review of World Energy June 2017. (2017).
2. http://www.energyresourcefulness.org/Power/solar.html.
3. E, B. A. Recherches sur les effets de la radiation chimique de la lumiere solaire au moyen des courants electriques. *Comptes Rendus L´Academie des Sci.* **9,** 145–149 (1839).
4. Einstein, A. Concerning an Heuristic Point of View Toward the Emission and Transformation of Light. *Ann. Phys.* **17,** (1905).
5. Chen, C. *et al.* Visibly Transparent Polymer Solar Cells Produced by Solution Processing. *ACS Nano* **6,** 7185–7190 (2012).
6. Smith, W. Effect of Light on Selenium During the Passage of An Electric Current*. *Nature* **7,** 303–303 (1873).
7. Adams, W. G. & Day, R. E. The Action of Light on Selenium. [Abstract]. *Proc. R. Soc. London* **25,** 113–117 (1876).
8. Fritts, C. E. On the fritts selenium cells and batteries. *J. Franklin Inst.* **119,** 221–232 (1885).
9. https://en.wikipedia.org/wiki/Vanguard_1#cite_note-NRL-3.
10. Pochettino, A. sul comportamento foto-electtrico dell'anthracene. *Accad. Naz. dei Lincei* **15,** 355 (1906).

11. Volmer, M. Die verschiedenen lichtelektrischen Erscheinungen am Anthracen, ihre Beziehungen zueinander, zur Fluoreszenz und Dianthracenbildung. *Ann. Phys.* **345,** 775–796 (1913).

12. Shirakawa, H., Louis, J. & Macdiarmid, A. G. Synthesis of Electrically Conducting Organic Polymers : Halogene Derivatives of Polyacetylene, (CH)x. *J. C. S. Chem. Comm* 578–580 (1977).

13. HeLi-on-White @ infinitypv.com.

14. Ben Streetman, S. B. *Solid state Electronic devices*. (1999).

15. Hussein, R., Borchert, D., Grabosch, G. & Fahrner, W. R. Dark I-V-T measurements and characteristics of (n) a-Si /(p) c-Si heterojunction solar cells. *Sol. Energy Mater. Sol. Cells* **69,** 1–7 (2001).

16. http://www.pveducation.org/pvcdrom/welcome-to-pvcdrom/pn-junctions.

17. Hoppe, H. & Sariciftci, N. S. Organic solar cells: An overview. *J. Mater. Res.* **19,** 1924–1945 (2004).

18. Christoph Brabec, Ullrich Scherf, V. D. *Organic Photovoltaics: Materials, Device physics and Manufacturing technologies*.

19. Tang, C. W. Two-layer organic photovoltaic cell. *Appl. Phys. Lett.* **48,** 183–185 (1986).

20. Berkley, S. The Fabrication and Characterization of Organic Solar Cells. (2009).

21. Ward, A. J. *et al.* The Impact of Driving Force on Electron Transfer Rates in Photovoltaic Donor – Acceptor Blends. *Adv. Mater.* **27,** 2496–2500 (2015).

22. Beaujuge, P. M., Fréchet, J. M. J. & Fr, J. M. J. Molecular design and ordering effects in π-functional materials for transistor and solar cell applications. *J. Am. Chem. Soc.* **133,** 20009–29 (2011).

23. Song, P., Li, Y. & Ma, F. Photoinduced Electron Transfer in Organic Solar Cells. *Chem. Rec.* **16,** 734–753 (2016).

24. Proctor, C. M., Kuik, M. & Nguyen, T.-Q. Charge carrier recombination in organic solar cells. *Prog. Polym. Sci.* **38,** 1941–1960 (2013).

25. Szarko, J. M., Guo, J., Rolczynski, B. S. & Chen, L. X. Nanoscale structure, dynamics

and power conversion efficiency correlations in small molecule and oligomer-based photovoltaic devices. *Nano Rev.* **2,** 1–17 (2011).

26. Bakulin, A. A. *et al.* Charge-Transfer State Dynamics Following Hole and Electron Transfer in Organic Photovoltaic Devices. *J. Phys. Chem. Lett.* **4,** 209–215 (2013).

27. Abbas, M. & Tekin, N. Balanced charge carrier mobilities in bulk heterojunction organic solar cells. **73302,** 1–4 (2012).

28. Karg, S., Dyakonov, V., Meier, M., Rieβ, W. & Paasch, G. Transient electroluminescence in poly(p-phenylenevinylene) light-emitting diodes. *Synth. Met.* **67,** 165–168 (1994).

29. Brabec, B. C. J. *et al.* Origin of the Open Circuit Voltage of Plastic Solar Cells. 374–380 (2001).

30. Trukhanov, V. A., Bruevich, V. V & Paraschuk, D. Y. Fill factor in organic solar cells can exceed the Shockley-Queisser limit. *Nat. Publ. Gr.* 1–10 (2015).

31. Shockley, W. & Queisser, H. J. Detailed Balance Limit of Efficiency of pn Junction Solar Cells. *Journal of applied Physics* **510,** (1961).

32. Yu, G., Gao, J., Hummelen, J. C., Wudl, F. & Heeger, A. J. Polymer Photovoltaic Cells - Enhanced Efficiencies Via a Network of Internal Donor-Acceptor Heterojunctions. *Science (80-.).* **270,** 1789–1791 (1995).

33. Rogers, J. T., Schmidt, K., Toney, M. F., Kramer, E. J. & Bazan, G. C. Structural Order in Bulk Heterojunction Films Prepared with Solvent Additives. *Adv. Materials* 2284–2288 (2011).

34. Loiudice, A., Rizzo, A., Biasiucci, M. & Gigli, G. Bulk heterojunction versus diffused bilayer: The role of device geometry in solution p-doped polymer-based solar cells. *J. Phys. Chem. Lett.* **3,** 1908–1915 (2012).

35. Kadem, B., Hassan, A. & Cranton, W. Efficient P3HT : PCBM bulk heterojunction organic solar cells ; effect of post deposition thermal treatment. *J. Mater. Sci. Mater. Electron.* **27,** 7038–7048 (2016).

36. Hiramoto, M., Suezaki, M. & Yokoyama, M. Effect of thin gold interstitial-layer on the photovoltaic properties of tandem organic solar cell. *Chemistry Letters* 327–330 (1990).

37. Roncali, J. Synthetic Principles for Bandgap Control in Linear π -Conjugated Systems. *Chem. Rev.* **97,** 173–205 (1997).

38. Wang, L., Yin, L., Ji, C. & Li, Y. Tuning the photovoltaic performance of BT-TPA chromophore based solution-processed solar cells through molecular design incorporating of bithiophene unit and flouorine-substitution. *Dye. Pigment.* **118,** 37–44 (2015).

39. Guo, X. *et al.* Polymer solar cells with enhanced fill factors. *nature photonics* 1–9 (2013).

40. Janssen, R. A. J. & Nelson, J. Factors Limiting Device Efficiency in Organic Photovoltaics. *Adv. Materials* (2012).

41. Chiechi, R. C., Havenith, R. W. A., Hummelen, J. C., Koster, L. J. A. & Loi, M. A. Modern plastic solar cells: Materials, mechanisms and modeling. *Mater. Today* **16,** 281–289 (2013).

42. Bagher, A. M. Introduction to Organic Solar Cells. *Sustain. Energy* **2,** 85–90 (2014).

43. Thoeming, A. L. An investigation into the paintbrush deposition technique for P3HT : PCBM based organic heterojunction solar cells. (2011).

44. Sun, M., Jin, H. & Jang, J. Effects of thermal annealing of polymer : fullerene photovoltaic solar cells for high efficiency. *Curr. Appl. Phys.* **10,** S206–S209 (2010).

45. Moulé, B. A. J. & Meerholz, K. Controlling Morphology in Polymer – Fullerene Mixtures **. *Adv. Mater.* **20,** 240–245 (2008).

46. Kim, K., Liu, J., Namboothiry, M. A., Carroll, D. L. & Kim, K. Roles of donor and acceptor nanodomains in 6 % efficient thermally annealed polymer photovoltaics. *Appl. Phys. Lett.* **90,** 1–4 (2007).

47. Søndergaard, R., Hösel, M., Angmo, D., Larsen-olsen, T. T. & Krebs, F. C. Roll-to-roll fabrication of polymer solar cells. *Mater. Today* **15,** 36–49 (2012).

48. Liu, X. *et al.* Highly efficient and thickness-tolerable bulk heterojunction polymer solar cells based on P3HT donor and a low-bandgap non-fullerene acceptor. *J. Power Sources* **364,** 426–431 (2017).

49. Zhang, T., Chen, Z., Yang, D., Wu, F. & Zhao, X. Fabricating high performance polymer

photovoltaic modules by creating large-scale uniform fi lms. *Org. Electron.* **32,** 126–133 (2016).

50. Guo, X. *et al.* Polymer solar cells with enhanced fill factors. *Nat. Photonics* **7,** 825–833 (2013).

51. Kan, B. *et al.* Solution-Processed Organic Solar Cells Based on Dialkylthiol- Substituted Benzodithiophene Unit with E ffi ciency near 10%. 1–4 (2014).

52. Hongmei Qin, Lisheng Li, Fangqing Guo, Shijian Su, Junbiao Peng, Yong Cao, X. P. Solution-processed bulk heterojunction solar cells based on a porphyrin small molecule with 7% power conversion efficiency. *Energy Environ. Sci.* **7,** 1397–1401 (2014).

53. Yan, C. *et al.* Enhancing performance of non-fullerene organic solar cells via side chain engineering of fused-ring electron acceptors. *Dye. Pigment.* **139,** 627–634 (2017).

54. Lei, T. *et al.* Roles of Flexible Chains in Organic Semiconducting Materials. *Chem. Mater.* **26,** 594–603 (2014).

55. Liu, Y. *et al.* Aggregation and morphology control enables multiple cases of high-efficiency polymer solar cells. *Nat. Commun.* **5,** 1–8 (2014).

56. Li, Y. *et al.* Annealing-Free High-Mobility Diketopyrrolopyrrole - Quaterthiophene Copolymer for Solution-Processed Organic Thin Film Transistors. *J. Am. Chem. Soc.* **133,** 2198–2204 (2011).

57. Zhang, C. & Zhu, X. Thieno[3,4-b]thiophene-Based Novel Small-Molecule Optoelectronic Materials. *Acc. Chem. Res.* **50,** 1342–1350 (2017).

58. Li, B. Y., Singh, S. P. & Sonar, P. A High Mobility P-Type DPP-Thieno [3,2-b] thiophene Copolymer for Organic Thin-Film Transistors. *Adv. Mater.* **22,** 4862–4866 (2010).

59. munazza shahid, Raja Shahid Ashraf, Zhenggang Huang, Auke J. Kronemeijer. Thomas McCarthy-Ward, Iain McCulloch, James R. Durrant, Henning Sirringhaus, M. H. Photovoltaic and field effect transistor performance of selenophene and thiophene diketopyrrolopyrrole co-polymers with dithienothiophene. *J. Mater. Chem.* **22,** 12817–12823 (2012).

60. Chem, J. M. Squaraine dyes for organic photovoltaic cells. *J. Mater. Chem. A Mater.*

energy Sustain. **3,** 14517–14534 (2015).

61. Wang, S. *et al.* N,N-Di arylanilinosquaraines and their Application to Organic Photovoltaics. *Chem. Mater.* **23,** 4789–4798 (2011).

62. Wei, G. *et al.* Functionalized Squaraine Donors for Nanocrystalline Organic Photovoltaics. *ACS Nano* **6,** 972–978 (2012).

63. Beverina, L. & Sassi, M. Twists and Turns Around a Square : The Many Faces of Squaraine Chemistry. *synlett* **25,** 477–490 (2014).

64. Rumer, J. W. & McCulloch, I. Organic photovoltaics: Crosslinking for optimal morphology and stability. *Mater. Today* **18,** 425–435 (2015).

Aims

A key issue with organic photovoltaics, and indeed the majority of optoelectronics, is that there is a misconception that organic materials offer cheaper, (when compared to inorganic counterparts) easily processable devices from a very abundant material, carbon. This misconception enforces the idea that organic materials are directly comparable to inorganic counterparts. This is, at this current date, a false claim. The reality is that organic materials do have the potential to provide cheap, processable devices from an abundant material but the current methods of synthesis, design and fabrication of organic based devices limits this potential.

The somewhat combinatorial approach to semiconductor design has resulted in the creation of evermore complex molecules. Although this approach has resulted in high performance organic photovoltaics, the synthetic techniques are often complex with multi step synthesis require high financial and environmental costs. High performance devices are typically reported on small scale devices incorporating extended solvent annealing or expensive evaporation depositions. Organic materials have limited performance in comparison to inorganic materials, this is an intrinsic characteristic of the materials. It could be suggested that instead of aiming for increasingly complicated materials to achieve small gains in performance we instead should look to develop methods to separate organic photovoltaics from the inorganic devices.

Niche market applications concentrating on indoor light reclaiming and the powering of small electronics is an area in which flexible organic devices could excel. These types of applications rely less on high performance but rather on ease of fabrication with the use of cheap accessible materials and processes. Roll to roll printing through liquid media is key to establish this field. The issue with processing devices from a liquid solution is that it is very difficult to control the film quality and the morphology of the material in the resulting thin film.

The aims and objectives of this work are to establish, at a proof of concept level, new methods for controlling the morphologies of active layers within optoelectronics on the nano-scale.

These methods have been developed with the thought of technology transfer to larger scale industrial processes in mind. So far in literature there has been a strong emphasis on improving the power conversion efficiencies of organic solar cells. Generally, this has been achieved by two approaches. Firstly, by providing conditions to create optimum material morphology to tailor electron and hole mobilities for a specific device, often achieved by adapting the crystallinity of common semiconducting cores. Secondly, by providing conditions to create

good interaction between donor and acceptor materials at the interface, often resulting in the extension of conjugation which creates a unique orbital level alignment between the two semiconductors. Through these approaches, at a laboratory level, the main benefit of organic materials (the low cost) is completely lost.

To this end we have developed two novel methods for controlling film morphologies in a post deposition manner.

1. Photocrosslinking of active layers
2. Latent pigment activation

Both processes are aimed at ensuring a practical modification to morphology post deposition. The principle idea behind these new methods is to allow for facile, low cost device fabrication with the potential for scalability. An aim was to ensure solution processability coupled with techniques that could be easily incorporated into an industrial set up. The nature of the chemistries involved also has potential to instil a level of stability to these organic devices which has been an issue of rising importance.

Photocrosslinking has been seen to stabilise OPV devices by reducing the phase segregation that is seen over time in bulk devices. The chemical process stabilises the film's morphology even with low levels of crosslinking[64]. Pigments, themselves, are also known to be intrinsically stable molecules in comparison to their dye-like analogues.

In this work a series of novel organic semiconductors have been synthesised, characterised, and fabricated into devices. A comparison of how these methods can be applied in both linear and bulk heterojunction devices has been made. Detailed surface and X-ray studies have been carried out, morphological changes are compared while examining notable features in the IV curves such as series and shunt resistance.

Furthermore, the use of organic semiconductors is not limited to photovoltaics. Organic field effect transistors have also been fabricated from a series of latent pigments. The latent pigment approach takes advantage of latent hydrogen bonding sites that can be activated thermally.

Fabrication of transistors allows us to examine more closely the effects of this approach on the mobilities of the material throughout the different crystalline phases seen with this approach.

As cost and environmental issues are of serious concern to the general field of organic optoelectronics, an interesting new approach to semiconductor preparation was also

investigated in this work. A novel reaction media was created with the surfactant Kolliphor EL and was investigated for carrying out cross coupling reactions in water. This surfactant forms oxygen free micelles which are ideal for carrying out palladium catalysed coupling reactions such as Suzuki Miyaura and Stille couplings.

Chapter 2 Photocrosslinking

Introduction

Photocrosslinking is the process of forming a covalent bond between two molecules through a photoinduced reaction.[1] By functionalising a material with photocrosslinkable functionalities we can generate a negative photoresist. A negative photoresist is a material which reduces its solubility after exposure to light.

Photoresists are usually implemented in different photo patterning processes such as lithography or photoengraving.[2]

Crosslinkable organic electronics have the potential to address the issues of low stability and reproducibility in photovoltaic devices. The following section explains the background and main principles of this approach followed by an explanation of the reasoning for developing materials to bring this approach to small molecule OPV.

Fully functional photo patterned organic semiconductors have been previously reported with a post deposition photo induced polymerisation. This method provides access to processable and patternable electronic devices.

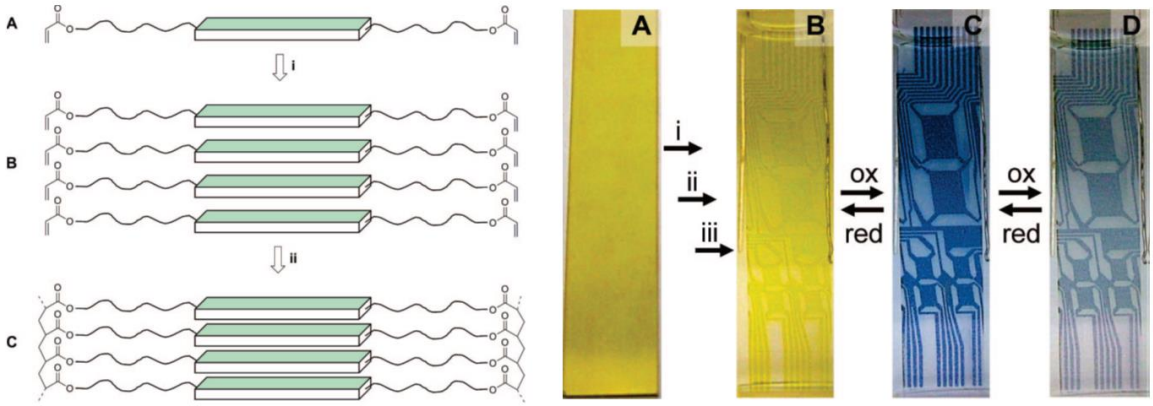

Fig. 2.1. Electrochromic materials photo patterned with acrylic crosslinking in various oxidation states.

In 2008 Reynolds et al successfully fabricated a series of photo patternable electrochromic devices seen in Fig. 2.1. above. UV curable conjugated oligomers resulted in insoluble thin films. The relevant portion of this work shows that acrylic functionalities on a conjugated core can "lock" a film into an insoluble state. [3] It was observed that the photocrosslinked materials

had a high stability in both oxidised and reduced states. Furthermore, the crosslinked oligomers retained the high contrast rate and cycle stability which are important features for electrochromic devices.

The thermodynamically instable nano-morphologies found in a BHJ are vulnerable to large scale phase separation over time. This is typically observed as a crystallisation of PCBM acceptors.

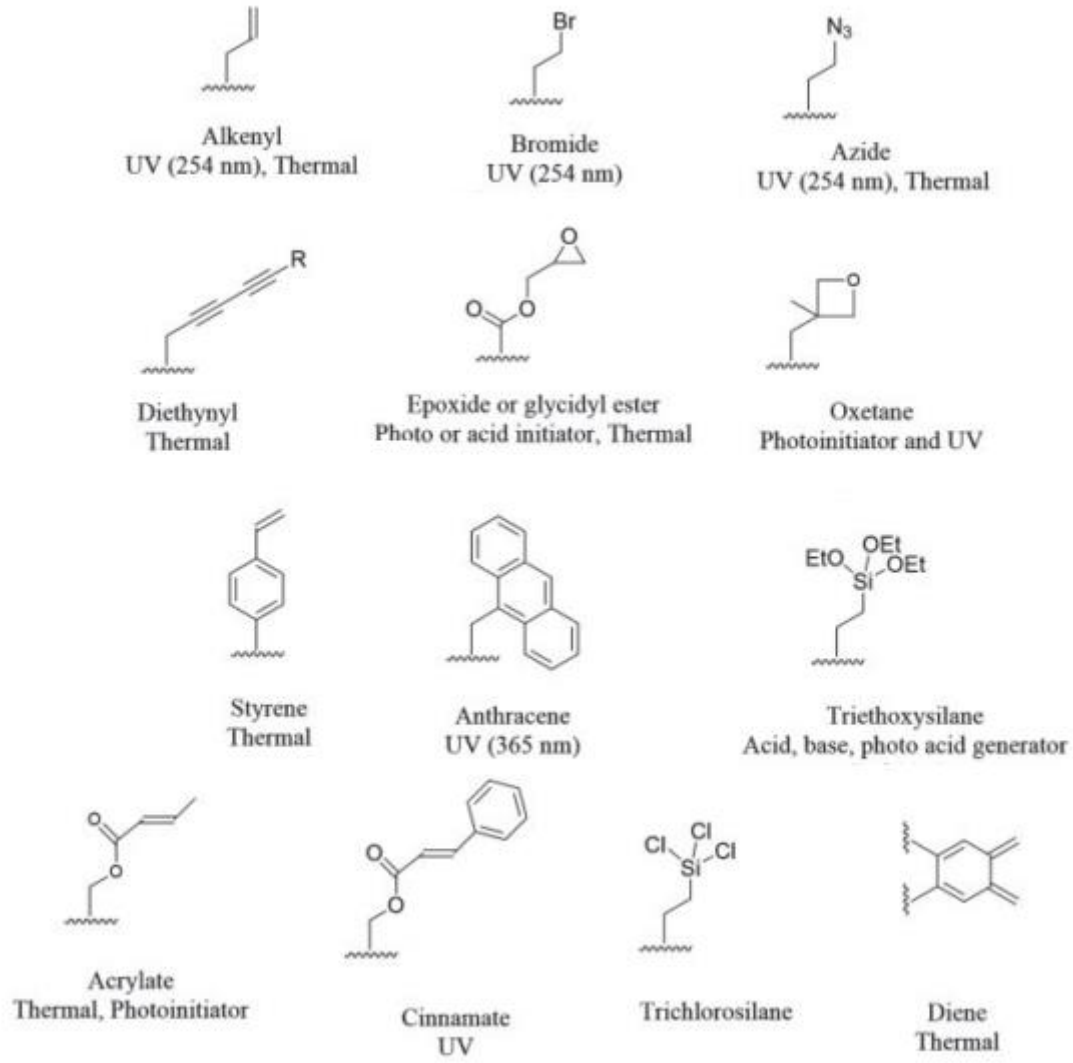

Fig. 2.2. A plethora of crosslinkable chemistries are applicable for this technique. The divers array above is a small selection of possible fictionisations for crosslinkable semiconductors.[4]

The thermal cycle experienced by a solar cell during daily operation can drive this phase separation causing an OPVs carefully controlled nano-morphology to change.[5] This, coupled with general photodegradation of the active materials results in a loss in performance over time.

The stabilisation effect of crosslinking has been previously observed in polymeric photovoltaic and OLED devices[5,6].

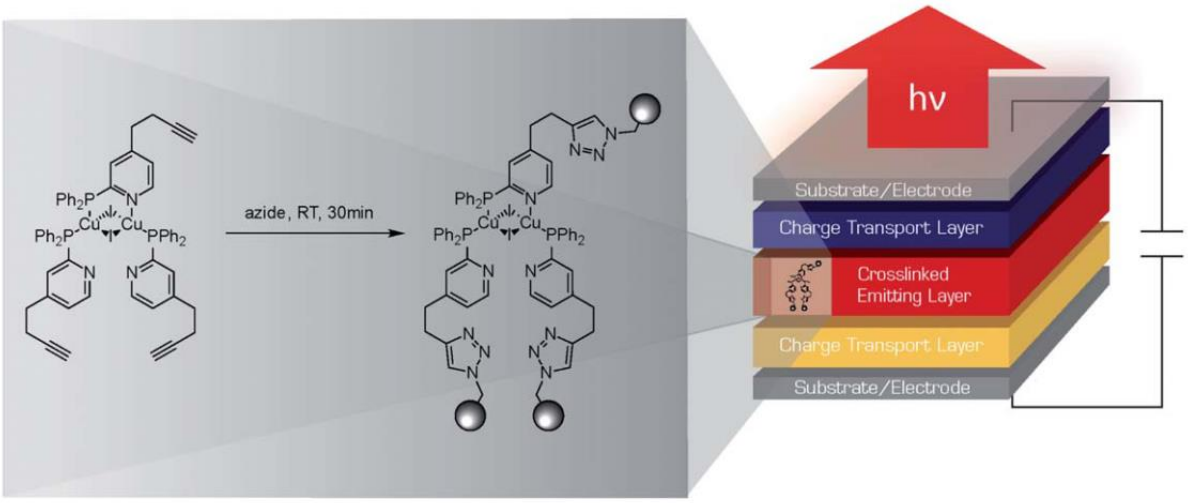

Fig. 2.3. The concept proposed by Stephan Brase et. al for an auto catalysed crosslinking of the active layer of an OLED device.[7]

A prime example of the stabilisation effect of crosslinking can be seen in the above example (see Fig. 2.3.). In this study an auto-catalysed crosslinking reaction occurs on the polymer backbone of a light emitting copper-(I)-complex. The resulting emitting layer demonstrates a drastic increase in thermal stability with only a negligible decrease in light emission. Not only was the thermal stability of these devices improved by over 100°C but the emission layer was seen to have high solvent resistance upon crosslinking. [7]

Liquid crystal co-polymers with a thiophene-thienothiophene backbone incorporate crosslinkable bromide units for photovoltaic applications. BHJ cells showed impressive thermal stability over 40 hours at 150°C while retaining 94% of the power conversion efficiency (best cells performed with 2.57% PCE). The crosslinking of alkyl bromide functionalities dispersed along the polymer backbone freezes the optimal bulk morphology. The bulk is kinetically frozen which eliminates the tendency of PCBM to migrate and crystallise (as seen by AFM below Fig. 2.4.). [8]

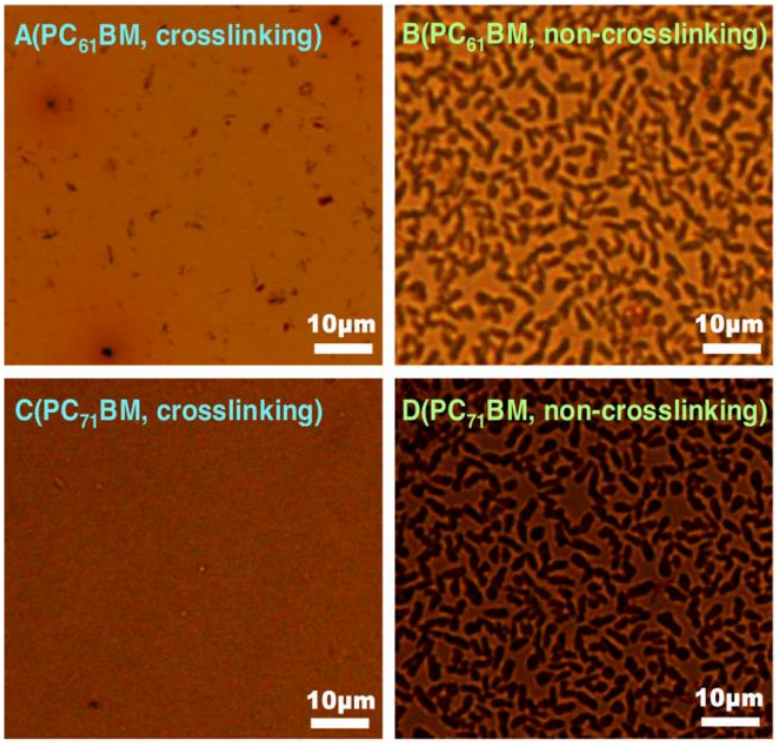

Fig. 2.4. AFM of crosslinked and non-crosslinked BHJ films. These films were subjected to thermal annealing of 150°C over 24 hours. It is evident that PCBM is crystallising in large agglomerates on the surface of the these films. [8]

Crosslinking is not only restricted to bulk heterojunction photovoltaics. The access to single material crosslinked films in OLEDs and electrochromic devices (see above[3,7,9]). The basis of this offers an interesting prospect for crosslinkable small molecules for planar bilayer devices. Not only does it appear that crosslinking affords high thermal stability but also the access to insoluble material layers.

The crosslinking approach has been made with many different functionalities and stimuli such as thermal, photo and acid catalysed crosslinking. Each approach must be tailored for specific materials during device fabrication as compatibility with other layers of the device is required. Acid induced crosslinking usually requires a sol-gel based acid generator. This system can be quite efficient in crosslinking thin layer, but it can be detrimental to semiconducting cores. The DPP core for example does not have strong acid stability. Excessive thermal treatment can also be detrimental to a film's morphology. Thermal annealing is often required to produce an ideal morphology, further treatment to initiate a crosslinking reaction can act negatively and disrupt this process.[10] UV induced crosslinking avoids this disruption to any previous thermal process although the photoinduced crosslinking may require catalytic initiators which will be trapped

within the film. Generally, crosslinking a small portion of a polymer backbone results in a significant stabilisation of a polymer BHJ morphology. The device stability is a key area of development for OPV. If the lifetime of a device is high, then the environmental payback is low as replacement of devices is required less often.

Abstract

In this chapter the development of a method for fabricating OPV devices from a series of photo-crosslinkable small molecules is explored. Initial investigation was carried out on a large series of squaraine dyes incorporating a variety of crosslinkable functionalities. This method of post deposition crosslinking benefits from the high purity, synthetic accessibility and reproducibility of a small molecule starting material. This work differs from the studies of stability for polymeric materials in that each small molecule contains two reactive crosslinkable sites. The high level of crosslinkable units will induce a phase segregation of donor and acceptor which has the potential to be controlled through intensity of light and/or concentration of photoinitiator. As such initial investigation does not concentrate on the stabilisation effects of this technique but rather on the general effect of large scale crosslinking on device performance and thin film morphology.

Squaraines

Interest in squaraine based semiconductors has peaked in the last few years. The facile synthetic routes, diverse array of structures, high absorption coefficients, low toxicity and high stability offer an attractive option for small molecule organic electronics. Squaraine dyes have been incorporated into OPVs, with fullerene derivatives as acceptor materials, recording PCEs upwards of 6.6% with tandem device architectures.[11]

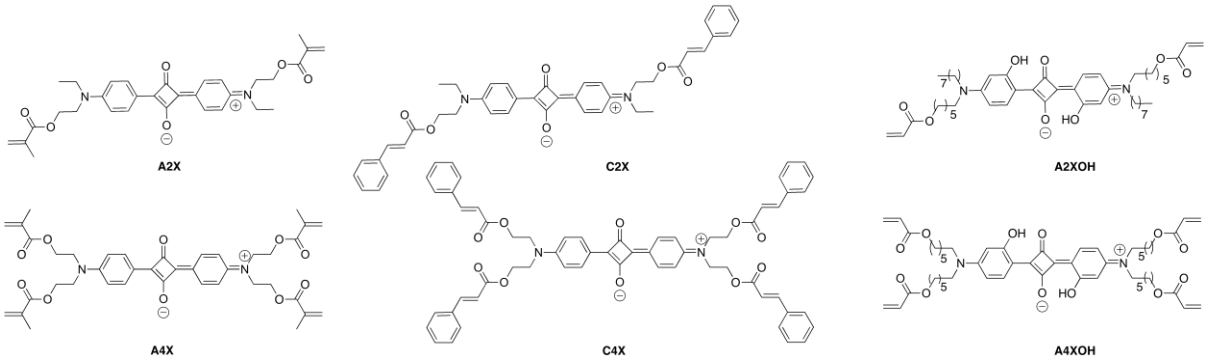

Fig. 2.5. Derivatives of squaraine with various photo-crosslinkable end groups

Squaraine dyes are an example of a material which has good absorption capabilities, short synthetic pathways, and high charge carrier mobilities. Unfortunately, squaraines also tend to have high lying HOMO levels which results in relatively low Voc in photovoltaic devices. These materials were used as a proof of concept for the photocrosslinking strategy for small molecule OPV. The high accessibility to a variety of squaraine based structures is beneficial when making comparison of potential lead functionalities for this crosslinking approach. Methacrylic, acrylate and cinnamic derivatives were synthesised with differing ratios of crosslinkable sites as a base to examine this technique. (see Fig. 2.5. for structures).

The general procedure for producing these anilino-squaraines is a straight forward condensation of a desired substrate to squaric acid in the presence of excess ethyl orthoformate in isopropanol (iPrOH). Although these highly stable squaraines have a short synthetic path they also have a relatively low synthetic yield. The highly crystalline monomer units all demonstrate typically high but narrow absorption bands between 600-650nm in solution. Significant broadening of the absorption band occurs in the solid-state due to the disorder associated with aggregation states of the material.

Initial solubility tests were carried out on thick films covering microscope slides. A solution of each Squaraine in dichloromethane with 3% by weight of 2,2-dimethoxy-1,2- diphenylethan-1-one (photoinitiator) was spread on the slide and allowed to dry. A mask was then placed over the slide and the open section was irradiated with standard laboratory UV lamp light at 365nm for 20 minutes under a nitrogen atmosphere.

The resulting film was then dipped in a solution of dichloromethane (DCM). The area that was open to the light has undergone a photocrosslinking reaction resulting in a highly solvent resistant molecular network. This is the typical effect of a negative photoresist. The resulting film showcases the high solvent resistance of the irradiated crosslinked material. This characteristic insolubility can be advantageous for processing bi-layer devices. Common processing solvents that would normally dissolve the squaraine dye act instead with a perfectly orthogonal nature. The macro structure of the film is frozen by the polymerisation process. Subsequent deposition can be carried out from the same solvent without resulting in intermixing of the squaraine layer with a subsequent material.

Squaraine device fabrication

Glass substrates with patterned ITO (150nm) anodes were deposited with a thin layer of thermally evaporated MoO_x. The surface of this film was modified by a 10-minute ozone treatment. A subsequent BHJ layer (Squaraine:PCBM 1:1) was then deposited by spincoating at 2000rpm for 30seconds from solutions of 3% photoinitiator in $CHCl_3$. The resulting films then undergo a 20-minute UV treatment at 254nm. This causes rapid polymerisation and phase segregation of squaraine and fullerene, accompanied by a large decrease in solubility. Finally, cells are transferred to a high vacuum thermal evaporator for hole blocking layer and cathode deposition.

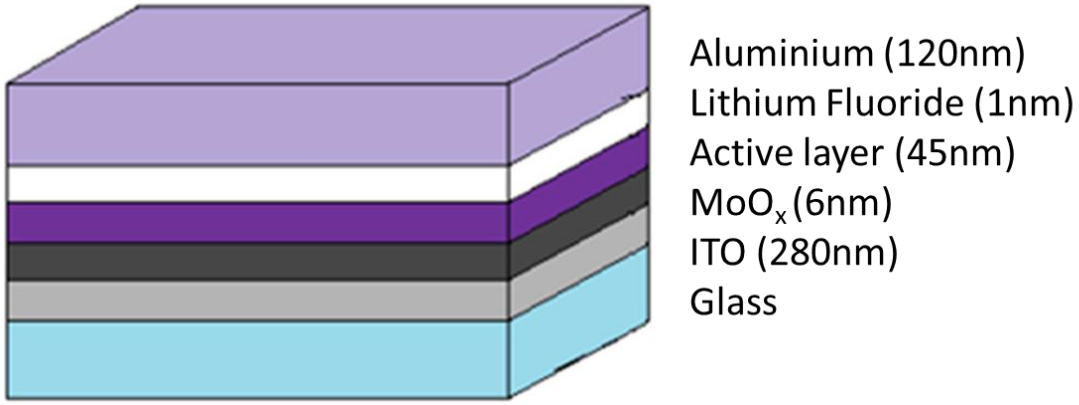

Fig. 2.6. Device structure for squaraine: PCBM bulk heterojunction solar cells.

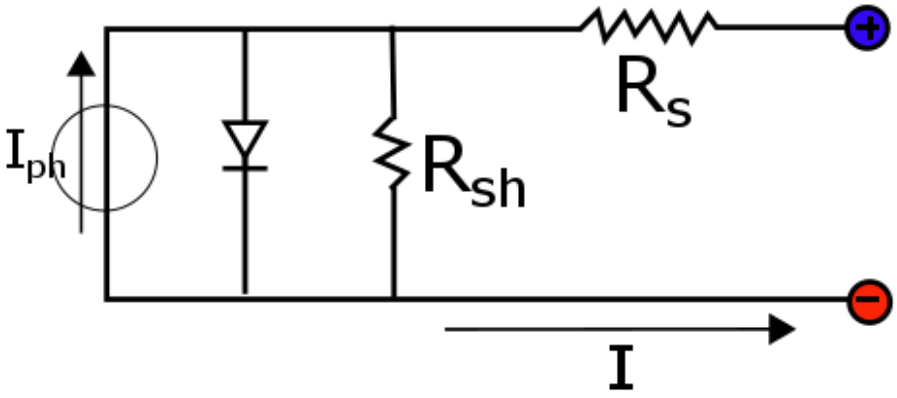

Fig. 2.7. Circuit schematic for organic solar cell Rsh=shunt resistane Rs=series resistance Iph=photocurrent

The initial results from bulk heterojunctions made with these squaraine dyes were overall quite positive (table 2.1). Generally, photovoltaic activity was retained and in some cases improved see Table 2.1. below. Close examination of the materials with AFM showed that small grain boundaries are formed upon photocrosslinking. This is due to the shrinking of the films as polymerisation occurs which induces stress on the film resulting in cracks (Fig. 2.8). These pinhole cracks have the potential to reduce the performance of a device by decreasing shunt resistance. The pinholes also act as hotspots for charge trapping and current leakage.[12]

	Ratio D/A	*Photoinitiator*	*Voc[V]*	*Jsc[mA/cm^2]*	*FF[%]*	*η [%]*
A2X	1:1	No	0.25	0.43	32	0.03
A2X	1:1	Yes	0.46	3.52	27	0.42
A2XOH	1:1	No	0.35	063	27	0.06
A2XOH	1:1	Yes	0.45	0.7	31	0.10
A4XOH	1:1	No	0.14	0.07	26	0.002
A4XOH	1:1	Yes	0.23	0.44	28	0.03

Table 2.1. IV Characterisation of squaraine dyes with comparison of crosslinked and no-crosslinked devices.

The relatively low performance of these materials before and after UV treatment is due in part to poor film quality, and in part to the high levels of insulating linear chains and restricted absorption bandwidth of these squaraine dyes. The donor acceptor ratio and film thicknesses are also most likely unoptimized.

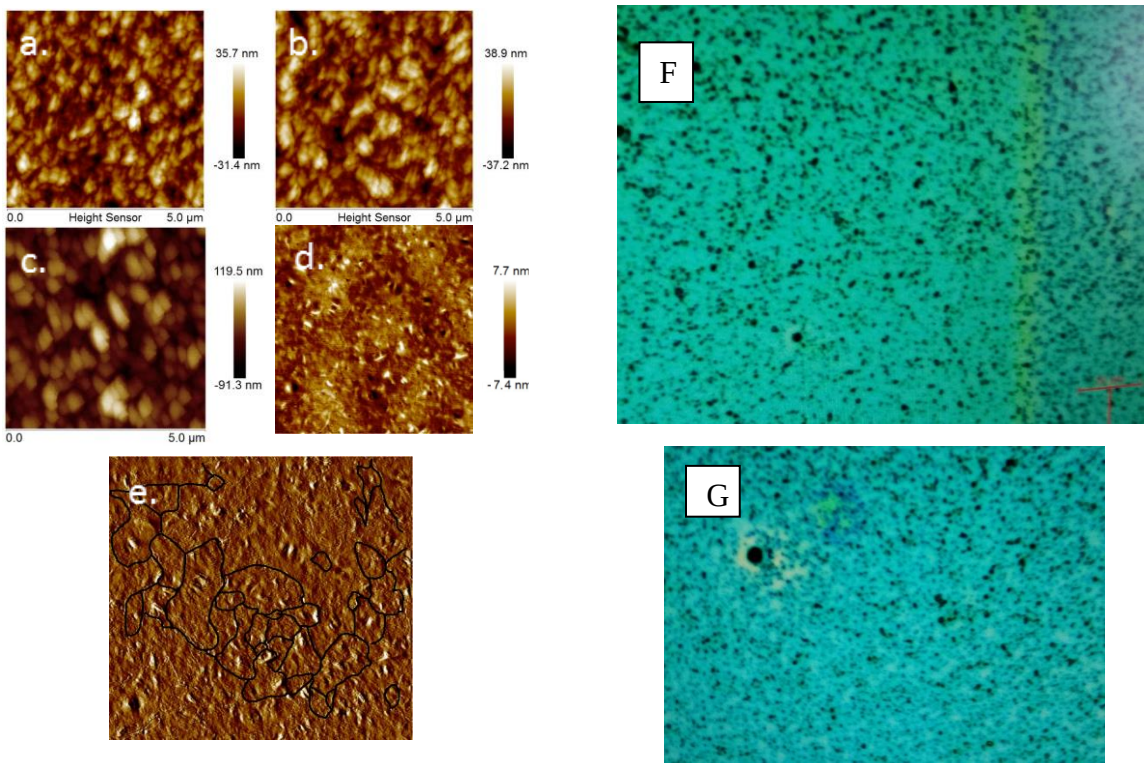

Fig. 2.8. a-e) AFM images showing grain border formation upon photocrosslinking. F-G microscope images of the complete bulk heterojunction, the ITO border can be seen and large-scale agglomeration of what is expected to be PCBM clearly seen as large dark particulates against the light blue squaraine background.

The low homogeneity seen in the macroscale morphology of these films explains the low fill factor and overall performance of these devices. PCBM and these squaraine dyes do not appear to mix very well. Regardless of the poor performance these tests have shown a good proof of concept for the use of photo-crosslinkable photovoltaics. It is seen that no significant loss in performance occurs upon crosslinking and in some cases significant performance improvements occur. It has also been reported that photo-polymerisation reduces charge mobility as a higher degree of disorder is reached within a film[13].

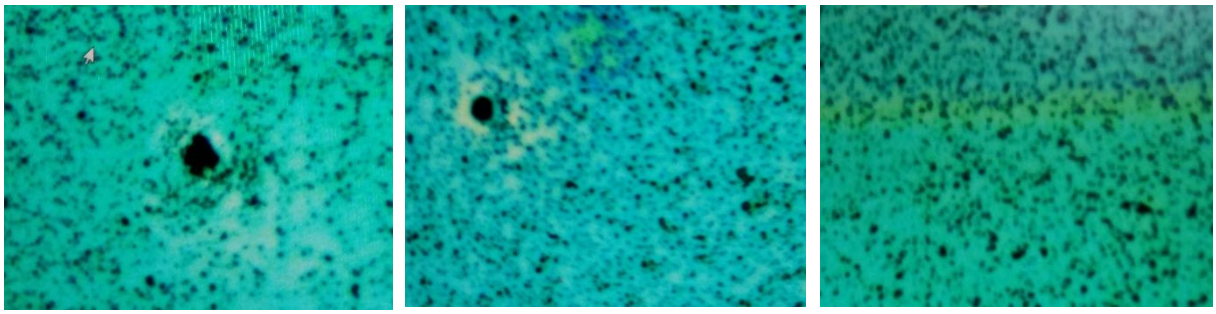

Fig. 2.9. Microscope images of squaraine A2XOH: PCBM bulk heterojunction devices, large scale agglomeration and possible phase segregation seen in both photocrosslinked (left and middle) and non- crosslinked (right) films.

From microscope images (Fig. 2.9) of the surface of a completed device with A2XOH: PCBM we can see there is a large-scale phase segregation or agglomeration of one species into very sizeable particles. This roughness in film quality result in poor performance due to pinholes, trapped charges and poor exciton splitting rates. Below we show the typical I-V curves for these devices before and after UV curing. (Fig. 2.10)

Voc	0.644579
Jsc	0.380233
FF	22.454532%
PCE	0.055034%

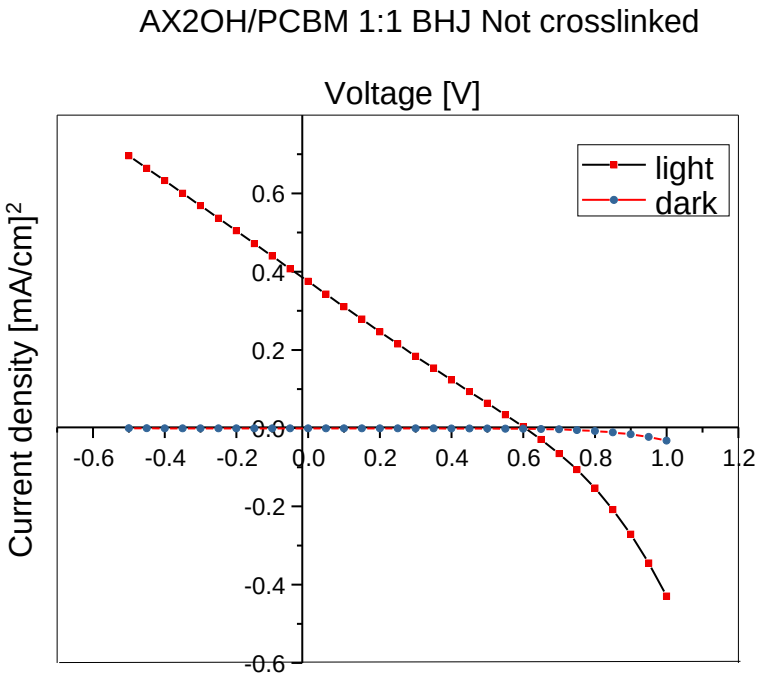

Voc	0.409583
Jsc	0.103774
FF	24.40685
PCE	0.010374

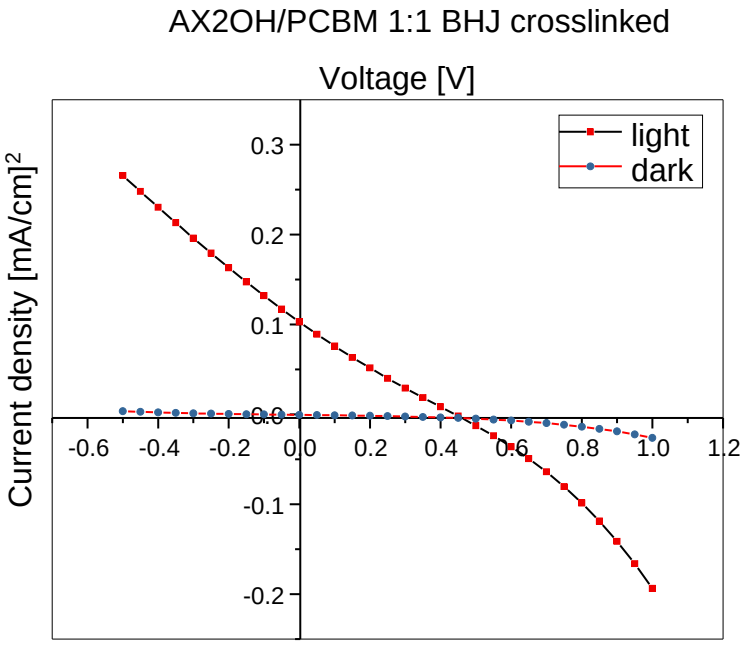

Fig. 2.10. (Top) JV-curve of non-crosslinked BHJ (bottom) BHJ made during the same batch but includes a photocrosslinking step. This cell shows evidence of pinhole formation through S shape of the curve indicating issues with leaking current seen in the shunt resistance of the cell. The majority of other cells which underwent crosslinking had higher efficiencies than the non-crosslinked counterparts. This is an output curve which shows the negative effects of the grain boundaries formed during crosslinking.

In the case of AX2OH: PCBM 1:1 devices, low shunt resistance is seen in both models. This is due to defect sites in the device which allow alternative current pathways for charges to move, thereby reducing the amount of current flowing through the heterojunction and resulting in an overall decrease in voltage within the device. In the case of the crosslinked device, the issue with shunt resistance is exaggerated with a typical S-shape I-V curve. The photocrosslinking of AX2OH results in larger phase segregation and a less desirable macro morphology as seen in the microscope images. The very low FF are also a strong indicator that large series resistance is occurring in these devices. The rough interface between metal contact and active organic layers could act as an area of high resistance with possible cracking of the active layer due to shrinking, resulting in the development of grain-boundaries which in turn promotes this issue of series at contacts.

The observed improvements in performance are possibly due to the increase in density of the films as the polymerisation occurs, resulting in a more efficient light absorption. It is also possible that the squaraines undergo a degree of rearrangement during the photo excited crosslinking leading to more efficient packing modes as individual molecules are pulled closer to one another.

Further materials

The squaraine dyes provide a facile route to test the efficiency of a variety of different crosslinking units. This is achieved due to the short synthetic procedure used to produce anilino-squaraine dyes. Of the produced materials the acrylate functionalised derivatives showed the most promise as crosslinkable small molecules. No thermal treatment and low photocatalyst loadings of 3% by weight make this photocrosslinking approach scalable and device fabrication compatible. The issues shown for this technique stem from the tendency of the films to shrink during the UV treatment. The resulting grain boundaries are detrimental to device performance.

To reduce shrinking upon photocrosslinking another set of materials with extended conjugated core was developed. It was speculated that by reducing the size ratio of the crosslinking group to the length of the conjugated core the grain boundary formation could be reduced. The steric stress created by polymerisation in the solid state is spread across the conjugated portion of the material.

Although squaraines have some of the highest absorption coefficients of organic materials, the narrow bandwidth limits the harvesting of the solar spectrum. A symmetrical

diketopyrrolopyrrole (DPP) terthiophene core was synthesised as this class of material are known to have strong absorption and comparatively broad absorption bands in comparison to typical anilino-squaraines. See appendix 2 for Experimental procedures

Material-DPP

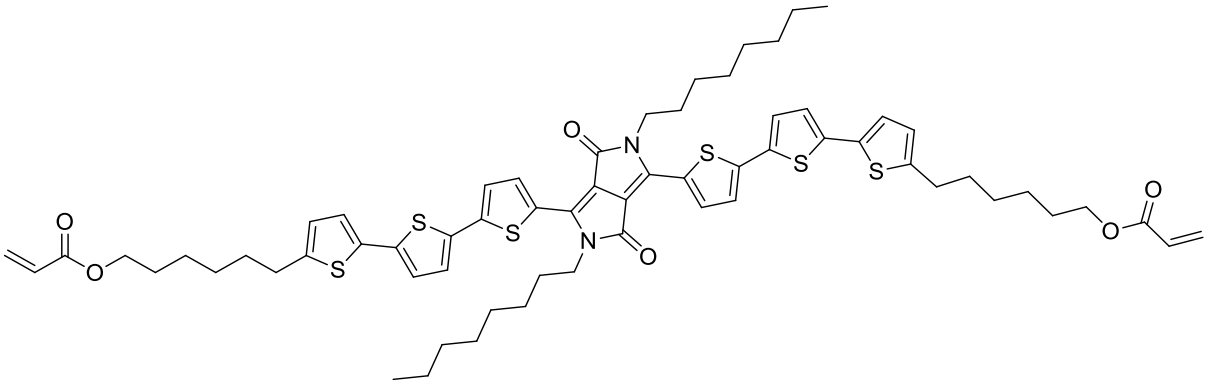

Fig. 2.11. Molecular structure of photocrosslinkable donor material DPP **11**

This material is considered a donor-acceptor-donor small molecule. Derivatives of this central core are known in literature to have impressive power conversion efficiencies of up to 7%[14]

Secondly, a non-fullerene acceptor material was also synthesised to substitute PCBM, a component which did not mix well with the squaraine dyes. PCBM is well known for its tendency to migrate through blends. The crosslinking approach can be used to reduce this effect, but the use of this approach should not be limited to controlling the aggregation of PCBM. This technique holds the potential to create stable solvent resistant layers. This in itself is a valuable asset to all multi-step fabrications.

This acceptor is a symmetrical naphthalene diimide (NDI) with extended conjugation through bithiophene groups. Similar polymer structures of the NDI have been implemented in photovoltaics with PCEs in the order of roughly 4% when used in conjunction with a PTB7-Th donor materials. [15]

Material-NDI 7.

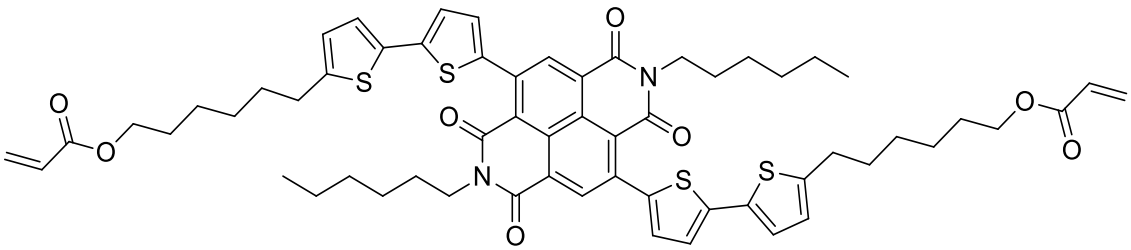

Fig. 2.12. Molecular structure of photocrosslinkable acceptor material NDI **7**

Bilayer

Initially, bilayer devices were attempted using the DPP as a donor material in conjunction with standard PCBM as an acceptor. The heterojunction cell was carried out by sequential spin coating processes with a UV treatment after deposition of the donor material.

ITO patterned glass substrates were supplied by TFD Inc. with a work function of 4.8eV. These substrates were sonicated at 50°C for 5 minutes sequentially in 1) deionised water 2) a Mucasol detergent solution 3) Acetone 4) iPrOH. Drying with a nitrogen supply line was carried out in between each washing. Substrates were then exposed to ozone treatment for 20 minutes.

Film spray coated

UV treatment with mask

Washed with DCM

*Fig. 2.13. an example of the photo patternability of DPP **11**. The film is created by airbrushing a solution of the dye with 3% by weight photo initiator from a chloroform solution. The film is then masked and irradiated with UV light under a nitrogen atmosphere. The resulting film is then washed with chloroform to reveal the crosslinked pattern.*

For photoactive solution preparation, 8mg of DPP **11** was dissolved in 1mL of a 9:1 solution of chloroform: chlorobenzene containing 3% by weight 1-hydroxycyclohexyl-phenyketone (photoinitiator). This solution was spincoated in a nitrogen filled glove box onto the previously cleaned substrates. After the films dried the substrates were treated to ultraviolet exposure 254nm by a laboratory Wood's lamp in a nitrogen atmosphere for 20 minutes.

Issues were uncovered immediately with the processing of the DPP donor. Poor wettability and a tendency to agglomerate resulted in a very rough thin film. The most homogeneous films

were achieved from spincoating with $CHCl_3$:chlorobenzene 80:20 solutions (Fig. 2.14). Average thicknesses from the best solutions were seen to be 30nm with an average of ~140nm roughness as measured by atomic force microscopy (AFM).

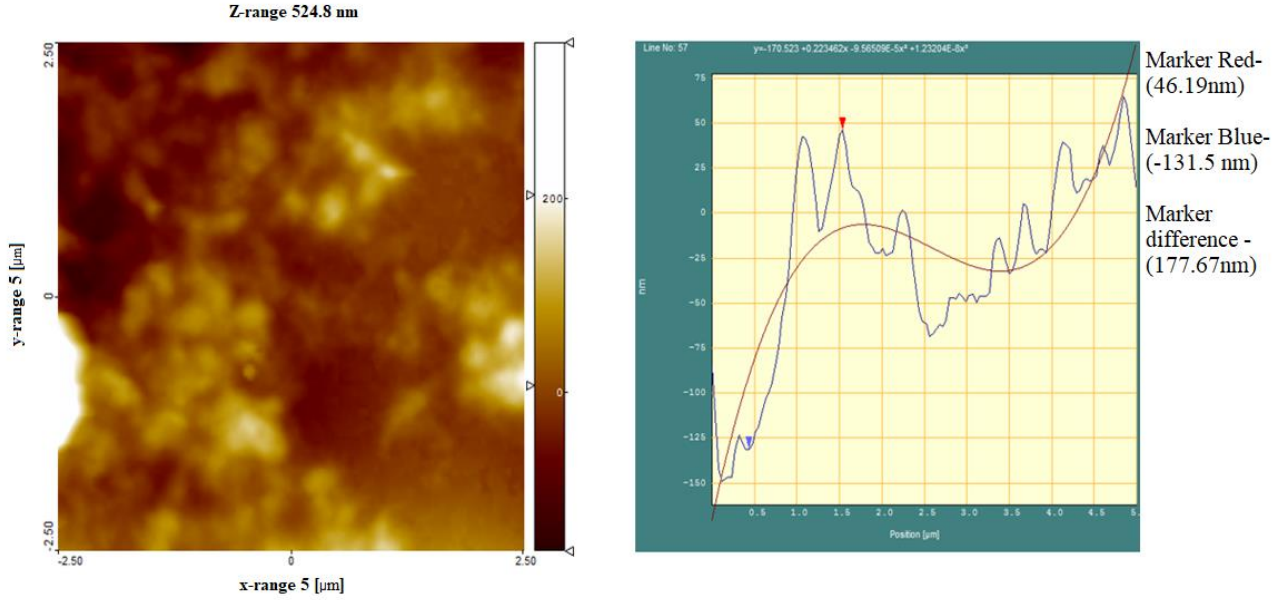

*Fig. 2.14. left) AFM image of a DPP **11** Film spincoating from $CHCL_3$: Chlorobenzene 9:1 at 1500rpm. Right) roughness average histogram for this film showing maximum roughness of 140nm.*

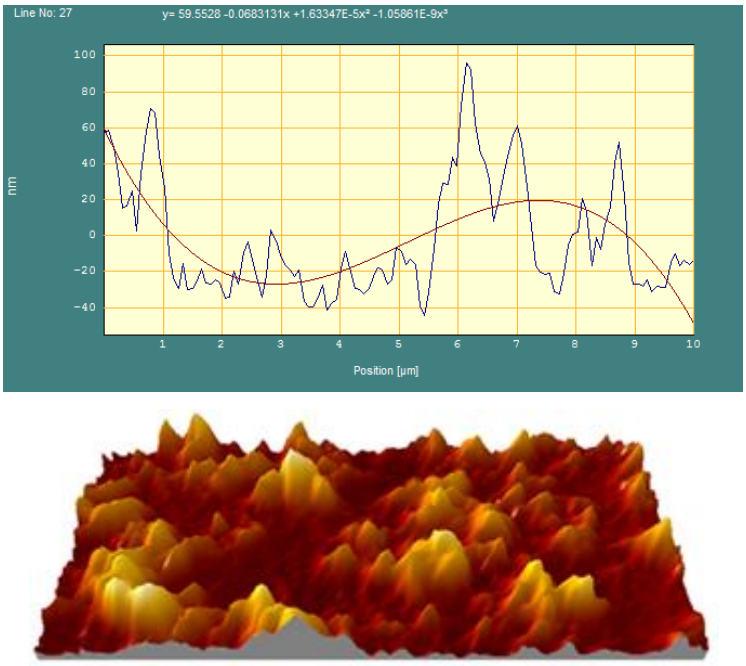

*Fig. 2.15. 3D representation for AFM image of DPP **11** film spin coated from $CHCl_3$: chlorobenzene 80:20 average film thickness 35nm. Maximum roughness 140nm.*

This film quality is non-ideal for photovoltaic devices. We moved forward regardless with solution deposition of PCBM (12mg/mL of chloroform, spincoated) and thermal evaporation of bathocuproine (a hole blocking layer) with silver contacts. The resulting cells had no photovoltaic activity and acted with resistor like characteristics. To fully examine this bilayer method, thermal evaporation of C70 fullerene was carried out, replacing the spincoated PCBM layer. This high mobility acceptor was evaporated in a relatively thick layer of 100nm to ensure good coverage of the very rough underlying donor layer. This thickness is much higher than the ideal for a bilayer device, but it was used as a compromise for the roughness of the underlying layer. The resulting cell performance showed essentially no photovoltaic activity (Fig. 2.16). The substrate wettability of this material from solution is too poor to generate useful or reproducible thin films. Surface passivation with an ozone treatment was also attempted to no avail.

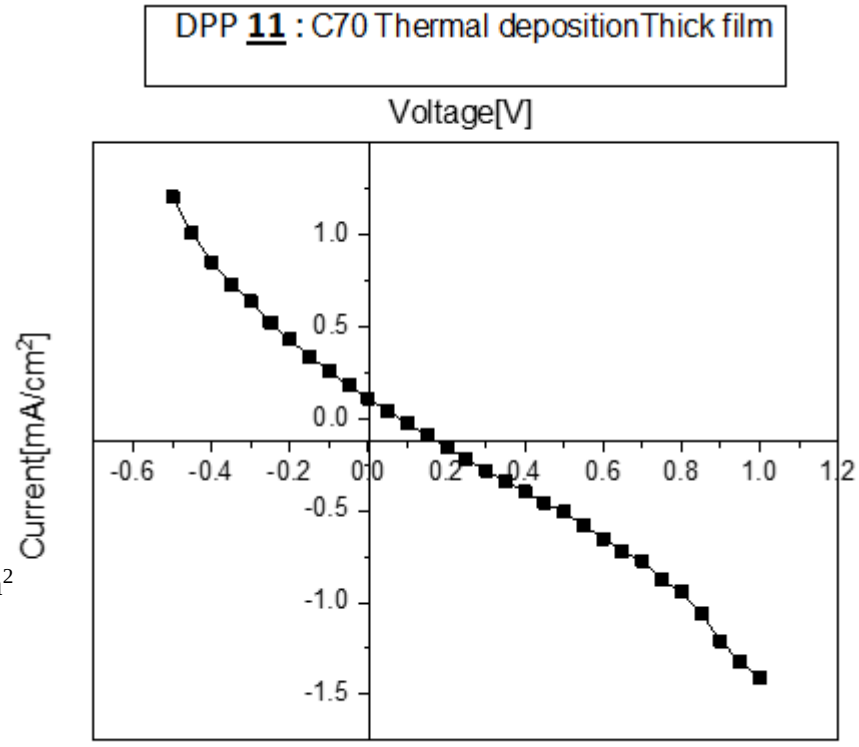

Voc	0.069673V
Jsc	0.110094mA/cm^2
FF	26.22418%
PCE	0.00201%

Fig. 2.16. I-V curve MR20/C70 100nm. The typical S-shape of this curve indicates problematic shunt resistance caused by poor film homogeneity.

Bulk heterojunction

The failure of these novel materials for use as intended in bilayer planar junction devices resulted in an attempt to incorporate them into a BHJ architecture (Fig. 2.17). The benefits of possible device stabilisation due to crosslinking remain in a BHJ format. Furthermore, as seen

with the squaraine materials, crosslinking could induce a fine phase segregation of donor and acceptor. If a crosslinkable donor material has the right miscibility with PCBM it is reasonable to believe that crosslinking could result in a stable and finely interpenetrated bulk heterojunction. The standard device architecture used is seen below in Fig. 2.17.

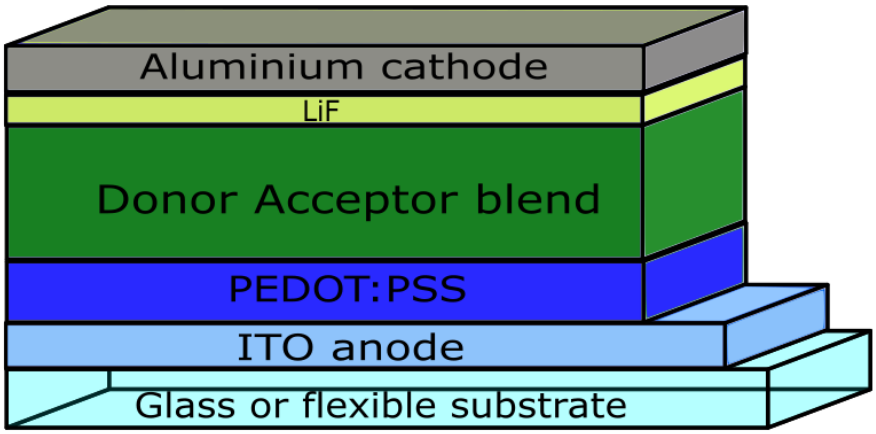

Fig. 2.17. BHJ photovoltaic cell architecture

Choosing contacts and interlayers

Lithium fluoride (LiF) was used as an interlayer between organic material and metal contact. It has been seen to lower the of workfunction the aluminium metal contact and also acts as a protective layer to reduce the penetration of the metal into the organic bulk[16]. Lithium is thought to diffuse into the aluminium resulting in the formation of aluminium-lithium clusters, aiding charge transfer to the aluminium bulk.

It has also been noted that aluminium is superior to silver as a negative contact as silver interfaces appear to lower performances in terms of device stability.[17] Aluminium is also cost effective and readily available. Annealing after evaporation of contacts has been seen to sometimes improve both fill factor and shunt resistance within photovoltaic cells[18] so we have tested completed cells where possible for such an improvement.

Unfortunately, both DPP **11** and NDI **7** have very poor miscibility with PCBM and P3HT respectively. Even with attempts to form a DPP: NDI blend poor miscibility and wettability was seen throughout. Attempts to passivate substrate surfaces with ozone was to no avail as resulting spincoated films were rough and sparse in their covering of the substrates. Attempts were made to form good films with an airbrush. This technique has the potential for creating good coverage of a substrate, but the high roughness caused by nebulised droplets of active

material solution makes this approach unsuitable for OPV thin film fabrication. However, using the airbrush to form very thick films of a donor or acceptor material which becomes completely solvent resistant has the potential to be used in the field of organic batteries.

Although BHJ films of high enough quality to fabricate photovoltaic devices could not be achieved, thick airbrushed films of both DPP **11** and NDI **7** could be successfully crosslinked and examined by cyclic voltammetry (see Fig. 2.18. below). This characterisation highlights the impressive solvent resistance of the photocrosslinked small molecules. Throughout this characterisation, materials are forced into highly oxidised and reduced states. These states typically have high solubility. In the case of DPP **11** and NDI **7** the thick airbrushed films both remained insoluble on their respective ITO substrates. This level of stability, along with the ability to form solution processed thick and rough films, makes these materials prime candidates for use in organic batteries. A difference of roughly 1ev potential between the two materials could lead to the development of a small lithium free organic battery

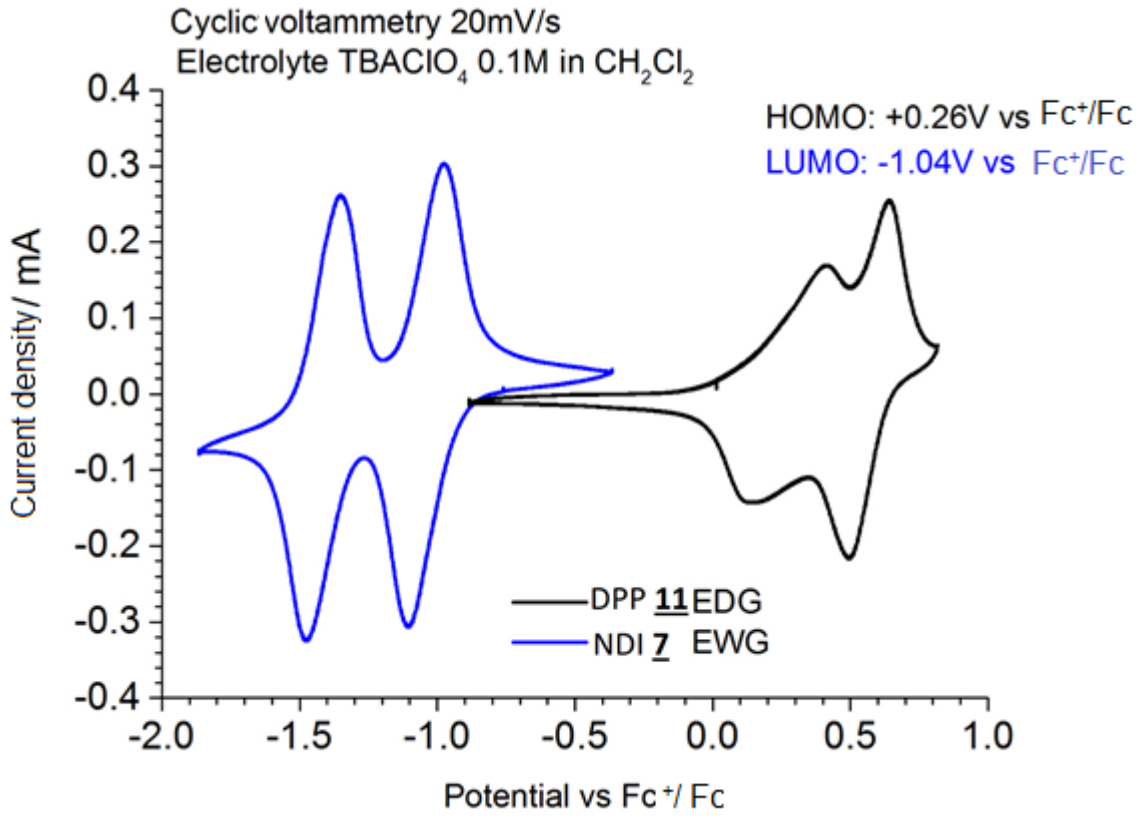

*Fig. 2.18. superimposed cyclic voltammetry's of NID **7** in blue and DPP **11** in black*

For each material DPP **11** and NDI **7** two reversible processes are observed. NDI **11** seen in Fig. 2.18. as a blue trace exhibits electrochromism from blue in the neutral state to a brown

colour in its reduced state. Good reversibility and stability is seen for both materials. The shape of the first process while cycling DPP **11**, seen as a black trace indicates a kinetically dependent swelling of electrolyte into the film with slow electron transfer occurring. A low level of solubility is also observed for the fully oxidised state of the DPP film. From further voltammetry experiments this is pertaining to an incomplete photocrosslinking process. Thicker films require longer UV exposure to ensure full polymerisation in the interior of the film. As the film swells with electrolyte during oxidation some unpolymerized monomer can leak from the interior of the film. No charge trapping states are evident within these films

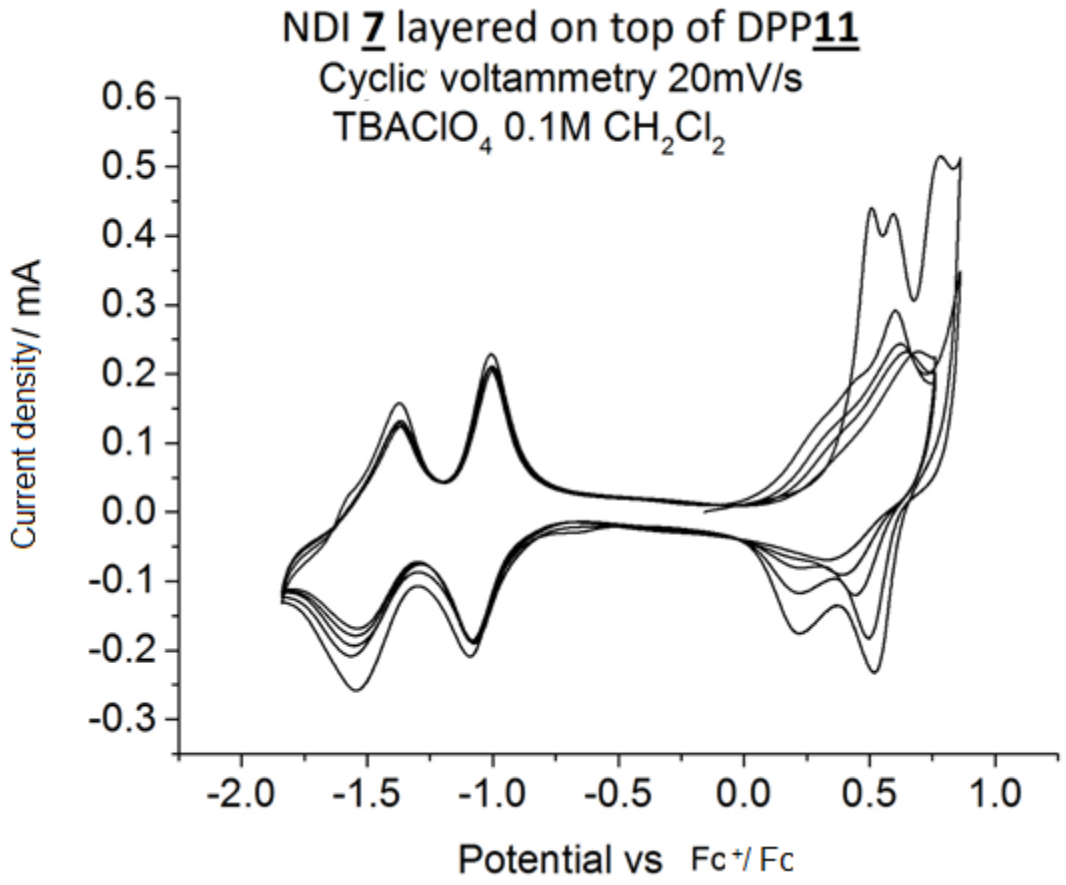

*Fig. 2.19. cyclic voltammetry of Bilayer NDI **7** coated onto a film of DPP **11***

When these materials are layered one on top of another the reversibility of the processes are preserved (Fig. 2.19). It is still evident that both materials have two redox features although the bottom layer DPP **11** has less resolution to its peaks and the dense films are not easily permeated by the electrolyte.

This system is rather robust and an investigation into the operation of such materials should be carried out with the development of coin cell batteries. For the moment this remains a work in progress.

Conclusion

Photocrosslinking offers a method for a non-invasive and scalable process to achieve insoluble photoactive films. This method has the potential to prevent and restrict PCBM agglomeration/crystallisation in a BHJ architecture through increasing the thermal stability of the phase segregated bulk. When applied to small molecules this approach offers a way to process devices in a bilayer architecture without the requirement for strict control of processing solvents for subsequent layers. Initial results for squaraine dyes showed improvements in photovoltaic performance after a photocrosslinking process for acrylate functionalised materials. Performance increases in the order of 14 times for the most improved system were recorded from 0.03% to 0.43% PCE

This approach was extended to a DPP donor material and a NDI acceptor material. Unfortunately, the low quality of the initial film depositions prevented this method from showing its true potential. Large agglomeration effects and low wettability of chosen materials on glass/ITO substrates limited this investigation. The low yield and length of synthesis for these materials also limits the upscaling of these materials. For this approach to be useful in an industrial setting simpler synthetic processes must be uncovered for similar materials with better film forming characteristics.

What has been achieved is a thorough investigation into the negative photoresist character of a variety of different small molecule organic semiconductors. Organic photovoltaics are not necessarily the best use for said materials, but it has been shown through electrochemical characterisation these materials have good potential to be developed into organic battery installations. This can be achieved through solution fabrication with the use of airbrush technologies which allow access to very thick and rough films which are desirable characteristics for this technology.

References

1. J.L.R. Williams. in *Fortschritte der Chemischen Forschung* 227–250 (2006).
2. Levinson, H. J. *Principles of Lithography*. (2011).
3. Nielsen, C. B., Angerhofer, A., Abboud, K. a & Reynolds, J. R. Discrete photopatternable pi-conjugated oligomers for electrochromic devices. *J. Am. Chem. Soc.* **130,** 9734–9746 (2008).
4. Wantz, G. *et al.* Stabilizing polymer-based bulk heterojunction solar cells via crosslinking. *Society of Chemical Industry*(2014).
5. Guerrero, A. & Garcia-Belmonte, G. Recent Advances to Understand Morphology Stability of Organic Photovoltaics. *Nano-Micro Lett.* **9,** (2017).
6. Kahle, F., Saller, C., Köhler, A. & Strohriegl, P. Crosslinked Semiconductor Polymers for Photovoltaic Applications. **1700306,** 1–10 (2017).
7. Volz, D. *et al.* Auto-catalysed crosslinking for next-generation OLED-design. *J. Mater. Chem.* **22,** 20786 (2012).
8. Yao, K., Chen, L., Hu, T. & Chen, Y. Photocrosslinkable liquid – crystalline polymers for stable photovoltaics by adjusting side-chains spacing and fullerene size to control intercalation. *Org. Electron.* **13,** 1443–1455 (2012).
9. Meerholz, K. Enlightening solutions. *Nature* **437,** 327–328 (2005).
10. Kadem, B., Hassan, A. & Cranton, W. Efficient P3HT : PCBM bulk heterojunction organic solar cells ; effect of post deposition thermal treatment. *J. Mater. Sci. Mater. Electron.* (2016).
11. Lassiter, B. E., Zimmerman, J. D., Panda, A., Xiao, X. & Forrest, S. R. Tandem organic photovoltaics using both solution and vacuum deposited small molecules. *Appl. Phys. Lett.* **101,** (2012).
12. Turrisi, R. *et al.* Synthesis and Characterization of Squaraine-Based Photocrosslinkable Resists for Bulk Heterojunction Solar Cells. *EurJOC* 4032–4040 (2016).
13. Mcculloch, I. *et al.* Polymerisable liquid crystalline organic semiconductors and their

fabrication in organic field effect transistors. *J. Mater. Chem.* (2003).

14. Zhou, J. *et al.* Solution-processed and high-performance organic solar cells using small molecules with a benzodithiophene unit. *J. Am. Chem. Soc.* **135,** 8484–8487 (2013).

15. Choi, J. *et al.* Importance of Electron Transport Ability in Naphthalene Diimide-Based Polymer Acceptors for High-Performance, Additive-Free, All-Polymer Solar Cells. *Chem. Mater.* **27,** 5230–5237 (2015).

16. Haskal, E. I. *et al.* Lithium – aluminum contacts for organic light-emitting devices Lithium – aluminum contacts for organic light-emitting devices. *Applied Physics Letters* **1151,** 14–17 (2006).

17. Reese, M. O. *et al.* Optimal negative electrodes for poly3-hexylthiophenephenyl C61-butyric acid methyl ester bulk heterojunction photovoltaic devices. *Applied Physics Letters* **53307,** 9–12 (2011).

18. Sendova-Vassileva, M. *et al.* Influence of the Type of Metal Contact and Post-deposition Treatment on the Performance of P3HT:PCBM Organic Solar Cells. *J. Phys. Conf. Ser.* **398,** 12049 (2012).

Chapter 3 Latent pigment

Introduction

In the field of organic optoelectronics, device fabrication requires the layering of multiple different materials one on top of another. Finding materials with differences in solubility remains a substantial challenge. For organic photovoltaics attempts have been made for developing roll to roll devices using orthogonal materials. These devices are made by a standard bottom up build with sequential layering of active materials. This should be achievable by standard printing methods. Generally, to achieve a good, highly resolved, and reproducible interlayer orthogonal solvent processing is used: the bottom layers of material are completely insoluble in the solvent used to process the subsequent layers. This is a very restrictive method for processing multi-layer devices. The nature of the donor and acceptor materials commonly used in OPV are such that their solubility is often similar. Completely orthogonal solvent approaches are thus quite rare. Generally, what occurs even in the case of materials which are completely orthogonal is a fine intermixing of the interface between donor and acceptor. Although this may be beneficial for device efficiencies, it is not a very controllable process. Even when completely orthogonal systems can be established, underlying layers are susceptible to swelling with the orthogonal solvent allowing for the sequential deposited materials to permeate into the bulk of the underlying layer, in effect, forming a rough interface more like a bulk heterojunction than that of the desired planar bilayer. This diffusion is an inherent problem of organic materials which is advanced by processes such as thermal annealing. Although this intermixing at the interface can often be useful for exciton splitting in photovoltaics, the resulting reproducibility and stability remain a concern. [1]

A multitude of different approaches have been devised for fabrications without the use of orthogonal solvent processing.

Vapour phase deposition

Vapour phase nanoparticle deposition of a thermo cleavable poly-thiophene/PCBM blend is a unique method for processing large scale devices from aqueous solutions while also controlling the scale of phase segregation in a film. Ya-Xiong Nan et. al successfully produced large scale devices by using an ultra micronization method to produce nanoparticles of a thermo cleavable poly-thiophene/PCBM blend. The deposition technique operates by nebulizing a micro-emulsion of the active materials into a carrier gas (in this case argon) which flows through a high temperature tubing. This thermal step dry's the nebulised materials and deprotects the

active polymer. The resulting nanoparticles then adhere to the desired substrate. This method offers an environmentally friendly method for active layer depositions without the need for orthogonal solvents.[2] This is a novel method for depositing active layers in an environmentally friendly manner with a lower influence of solvent on underlying layers. A possible downside to this method however is the high temperature used across the evaporation tubing. The thermal treatment experienced here is over 300°C. This process may stress the thermal stability of a number of common organic semiconducting materials.

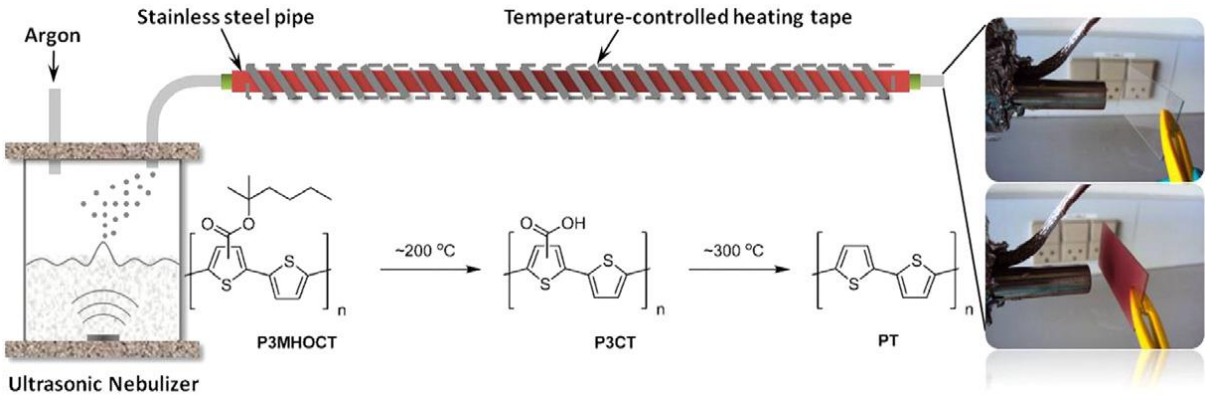

Fig 3.1. Vapour phase nanoparticle deposition technique[2]

Simultaneous deposition

Double slot dye depositions for simultaneous multilayer fabrications is possibly a viable method for the quick, low cost production of devices.[3] Attempts have been made with this technique by creating dispersions of active materials in water as a solvent. Simultaneous deposition of PEDOT: PSS in water and a P3HT: PCBM dispersion in water through two slot parallel slot dyes results in a roughly formed bilayer. Intermixing and high interface roughness results in poor PV PCE in comparison with a well-controlled single slot dye deposition.

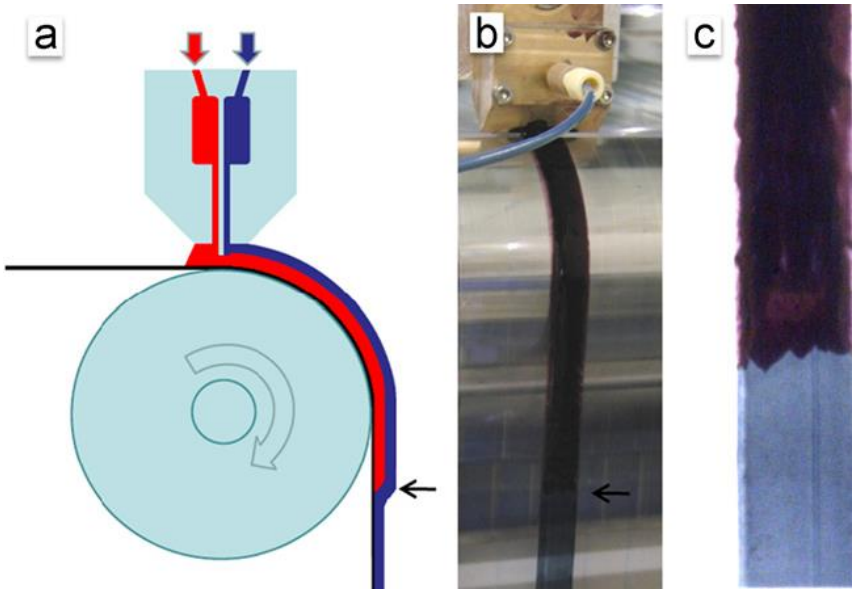

Fig. 3.2. a) schematic diagram of a simultaneous double slot dye deposition technique b) experimental photo c) close up of subsequent film.[3]

Emulsion processing

Emulsions and micellar solutions can be used to produce semiconductor films which after formation can be integrated into a multilayer device. The principle idea of this method is that hydrophobic core of micelles and emulsions provide a good environment to load organic semiconductors. This environment collapses upon the removal of the aqueous portion of the solution. In this way organic semiconductors can be deposited from water, the resulting films after evaporation of water will be completely insoluble in aqueous solutions. Emulsion cast films have been shown to have charge generation characteristics which are similar to those found in solution deposited devices [4] Frederik Krebs et. al also demonstrated 0.55% PCE roll to roll all-printed devices using an aqueous solution based method incorporating a detergent.[5] Emulsion processing gives access to nanoparticle based films with tuneable particle size (through solution concentration variation) between ~30 and 500nm.[6] This method is an area with great potential as a aqueous solution processed organic solar cell is a very appealing idea.

Vacuum deposition

Sequential vacuum evaporation deposition is a method to access planar bilayers with crisp homogenous interfaces. This technique can be considered more expensive and less scalable than solution processing which should give facile access to roll to roll processes. The level of interface control offered with this technique is clearly of higher quality than solution-based techniques. Thermally deposited films also have the benefit that they are not subject to issues

of material wettability. [7,8] The limiting factor of this technique is the low throughput potential with today's technology. A combination of solution processing and thermal evaporation is a possible compromise for organic opto-electronic device fabrication. OLED technology has seen relatively successful development with deposition of active light emitting layers being produced by solution means while subsequent electron blocking layers are thermally evaporated.[9] Photovoltaics are comparatively complex devices. Multiple layer depositions with large devices areas limits the use of thermal evaporation.

Latent pigment

To address this issue, we have investigated and developed the latent pigment approach. An organic pigment is a highly coloured organic material which has a characteristically low solubility. These materials are highly coloured due to scattering effects or selective light absorption dictated by alternating σ-π bonding networks. Pigments are generally very stable materials, with regards to temperature, solvent, and atmosphere. Furthermore, organic pigments tend to have low toxicity. Many common pigment cores are commercially available at relatively low prices due to their high demand in fabric and paint industries.[10] The intrinsic stability of organic pigments makes them a very attractive option for investigation as light harvesting donor and acceptor materials for organic photovoltaics. The only issue is that the low level of solubility makes device fabrication rather difficult as common solution fabrication techniques cannot be used. While vacuum deposited pigments can afford very high-performance devices the solution processed devices are less performing. A latent pigment approach can be successfully integrated into the fabrication of a solution processed organic device, with performances approaching that of the vacuum deposited devices.[11,12]

The principle idea of the latent pigment approach is that a pigment can be functionalised with a chemically or thermally removable solubilising functionality.[13] This results in dye-like

solubility which can be easily processed by methods such as spincoating or printing.

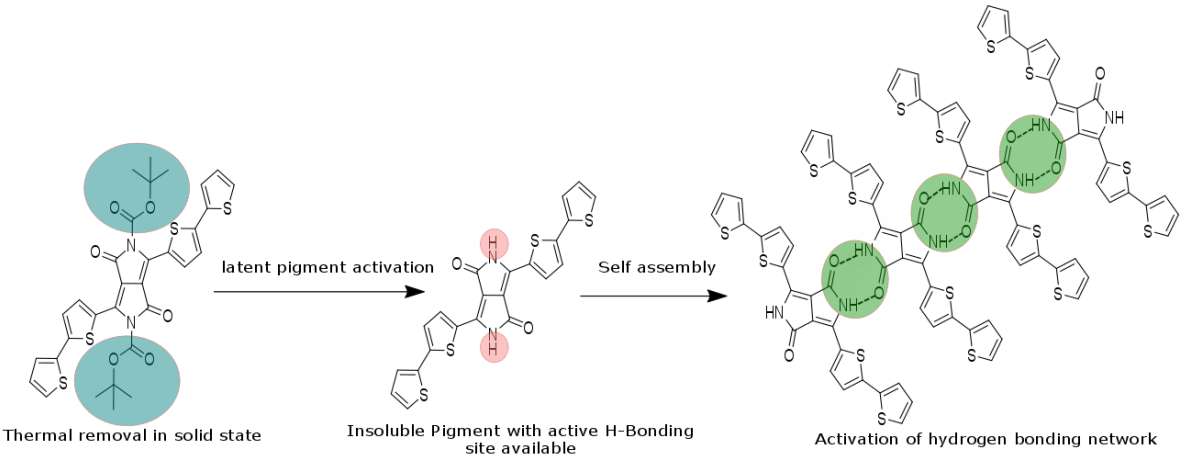

Fig. 3.3. An example of process for the deprotection of t-Boc functionality on a common DPP pigment core

The term latent indicates that the pigment is still available, lying dormant. By using common protection group chemistry, we can afford materials with good solubility that can be solution processed into thin films (Fig. 3.3). Simple post deposition treatments result in the activation of this latent pigment. The resulting removal of the solubilising protective moiety (such as the tert-butyloxycarbonyl protecting group) affords the initial pigment processed in a thin film with a complete solvent resistant character. The now insoluble stable layer of organic material is then suitable for use in electronic devices such as transistors and photovoltaics.

The basis of this approach is that organic pigment insolubility stems from intermolecular interactions such as H-bonding or π stacking[13]. Addition of chemically or thermally labile protecting groups disrupt these strong intermolecular interactions resulting in a dye-like solubility. The latent pigment approach opens a versatile avenue for affording a variety of organic electronic devices such as organic photovoltaic (OPV), organic light emitting diodes (OLED) and organic field effect transistors (OFET).

Abstract

In this chapter, the use of latent pigments as a method for providing true bilayers without the use of orthogonal solvents or vacuum evaporation is examined. Furthermore, this approach is extended to incorporate methods to provide stoichiometric solvent annealing throughout the latent pigment activation process. Diketopyrrolopyrrole based semiconductors functionalised with thiophene units were developed as efficient donor materials which incorporate thermally

labile solubilising functionalities. Two such materials were studied extensively. Both bulk heterojunction and bilayer heterojunction photovoltaics with a variety of architectures are fabricated and characterised. The morphologies of these materials were examined by X-ray spectroscopies including single crystal studies, reflectivity experiment and a Grazing incidence wide angle X-ray scattering study (GIWAXS).

Chemical design

Latent pigments have been established in a wide variety of organic devices: from patternable thermochromic time-temperature indicators for food industries[14] to luminescent solar concentrators[15] as well as being incorporated into OPV. The nature of the material crystallisation through this process with additives has been examined[16] and the possibility of creating thin single material films and BHJ films from materials of very low solubility has been exemplified through pigments such as indigo[17]

A common protection group used is di-tert-butyl dicarbonate (t-Boc protection). This group allows for facile protection of amines at near quantitative yields.[18] This functionality is sterically bulky and affords a simple and quantitative deprotection by a thermal treatment. The thermal deprotection window for this protective group is usually far below the degradation temperatures of common pigments such as diketopyrrolopyrrole (DPP), quinacridone (QC), perylenediimide (PDI) and iso-indigo.[19,20,21,] The removal of the t-Boc is observed by the evolution of two gases CO_2 and isobutylene. The functionalisation of heterocyclic amines with t-Boc can be used to disrupt H-bonding networks. The tert-butyl portion of this protection group also acts quite well to disrupt π-π stacking. In effect, t-Boc can act as an efficient functionalisation to provide a large increase in a semiconductor's solubility. An example of this is shown below with the protection of the lactamic nitrogen of a bithiophene functionalised DPP (Fig. 3.4).

Diketopyrrolopyrrole cores are recognised as high performance industrial pigments[22]. The possibility for mass production and relatively facile functionalisation through common palladium based C-C chemistries makes them an appealing prospect for industrialisation. DPP small molecules and DPP containing polymers are among the highest performance materials available for OPV and OFET applications.[23,24]

It has been recorded that in a pigment form DPP crystals have improved charge transport and mobilities over N-alkylated "dye" counterparts. This possibly corresponds to the activation of a H-bonding network resulting in more efficient π-π packing.[19]

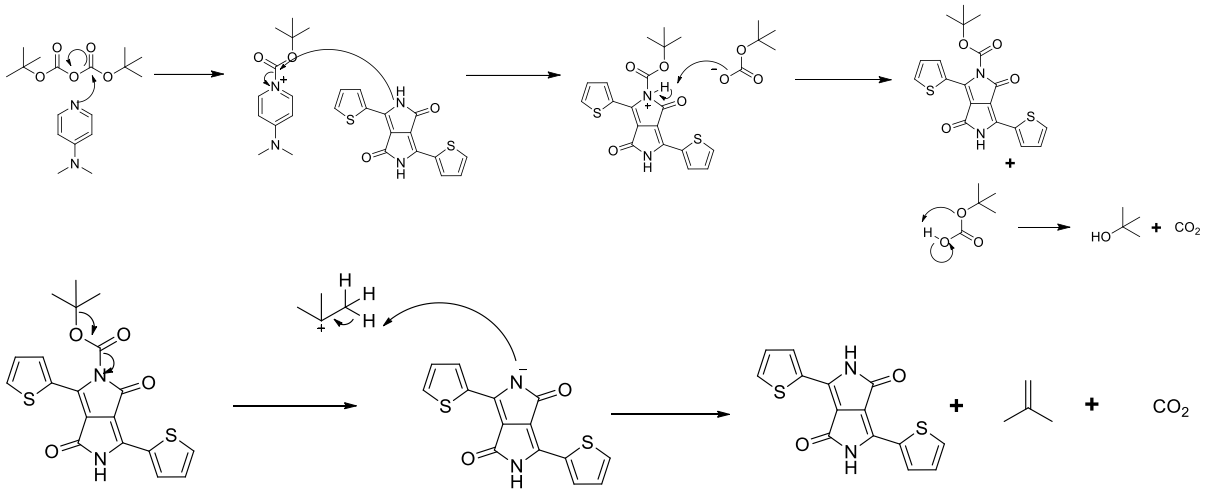

Fig. 3.4. Mechanism for chemical protection (above) and thermal deprotection (below).

A noteworthy contribution to the field of latent pigments for opto-electronics comes from the Beverina group (Fig. 3.5). A small molecule bulk heterojunction photovoltaic was developed incorporating a latent pigment Diketopyrrolopyrrole. Thermal deprotection of this DPP at 200°C resulted in the parent pigment and the activation of a hydrogen bonding network. Photovoltaic characterisation showed a remarkable increase in Jsc upon deprotection of the DPP. This resulted in a 20-fold increase power conversion efficiency to 0.15%. The increase in current is attributed to the improved charge carrier mobilities which arise from the hydrogen bonding network which improves material packing. [25]

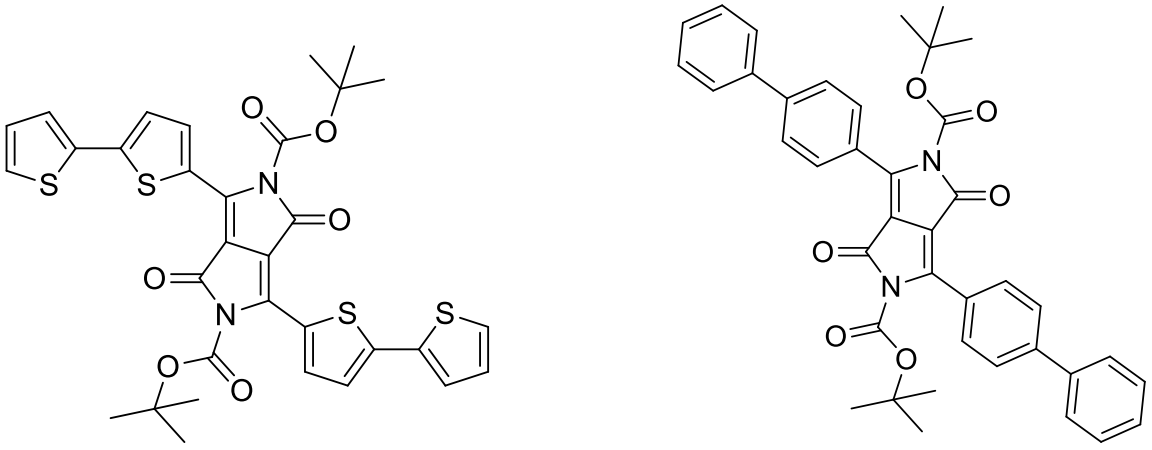

DPP **34**

DPP_H *(Beverina group)*

Fig. 3.5. Right) the structure initially proposed by Beverina et al. Left) Adjustment to the HOMO and LUMO levels of this semiconducting core is made by the replacement of phenyl functionalities with thiophene groups which have a higher donating character.

This DPP_H molecule was designed as a latent pigment for use in a BHJ as a means to control phase segregation.[25] The issues with this material was that the HOMO levels of the DPP and PCBM were misaligned, causing issues with charge separation.

To address this issue, we substituted the Phenyl rings for thiophenes in order to raise the HOMO levels of this molecule and reducing the optical gap. The resulting material DPP **34** is a t-Boc protected material. HOMO levels estimated from cyclic voltammetry (Fig. 3.6) of the protected DPP **34** have been successfully raised from the reported HOMO level of DPP_H -6.22eV to the DPP **34** HOMO level of -5.9eV. This HOMO level is much better suited for alignment with PCBM which has a HOMO level of -6.1eV. The effect of protecting with the t-Boc functionality, a strong electron withdrawing group, is the lowering of the LUMO level to -4.01eV.

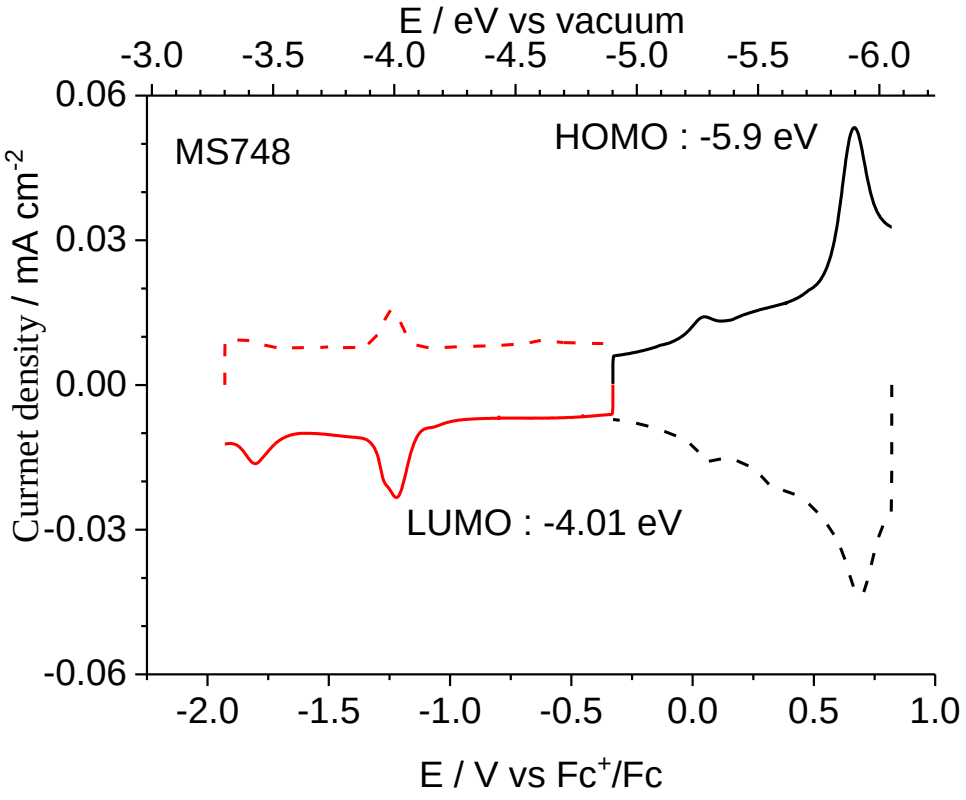

*Fig. 3.6. Cyclic voltammetery of DPP **34** reversible redox steps evaluate HOMO levels to be -5.9eV and LUMO levels of -4.01eV.*

Although the HOMO is now situated at an appropriate level, the optical band gap has also been reduced. The LUMO levels of DPP **34** now in the same region to the LUMO levels of PCBM (-3.7eV to -4.2eV). The deprotection of the electron withdrawing t-Boc groups should raise the LUMO level to a more suitable alignment between PCBM and DPP **34**, the small difference

between these levels is not ideal and results in the limitation of Voc. The cyclic voltammetry levels of the deprotected pigments cannot be measured due to the insolubility of the materials. In order to circumvent this conjugation was further extended by the addition of two more thiophene units. The solubility of this moiety comes into play so a derivative with hexyl sidechains on the ternary thiophene was synthesised DPP **27.** The extended conjugation raises the LUMO levels slightly to -3.9eV (Fig. 3.7). This is expected to rise again upon deprotection which will result in a good alignment with PCBM.

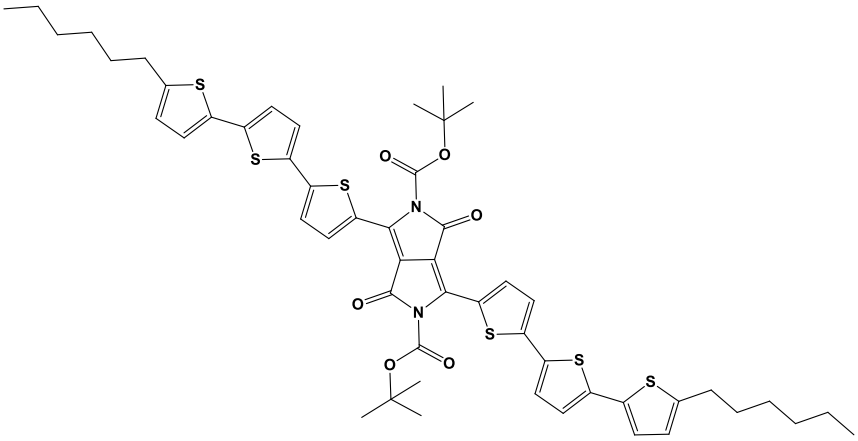

DPP **27**

Initially these two DPP materials DPP **27** and DPP **34** were synthesised by micellar coupling (see chapter 5). These relatively simple latent pigments have high yielding synthetic routes (see experimental appendix 2). The extended conjugation through thiophene sub units raises the HOMO levels so that they are compatible with standard acceptor materials such as PCBM and $PC_{71}BM$.

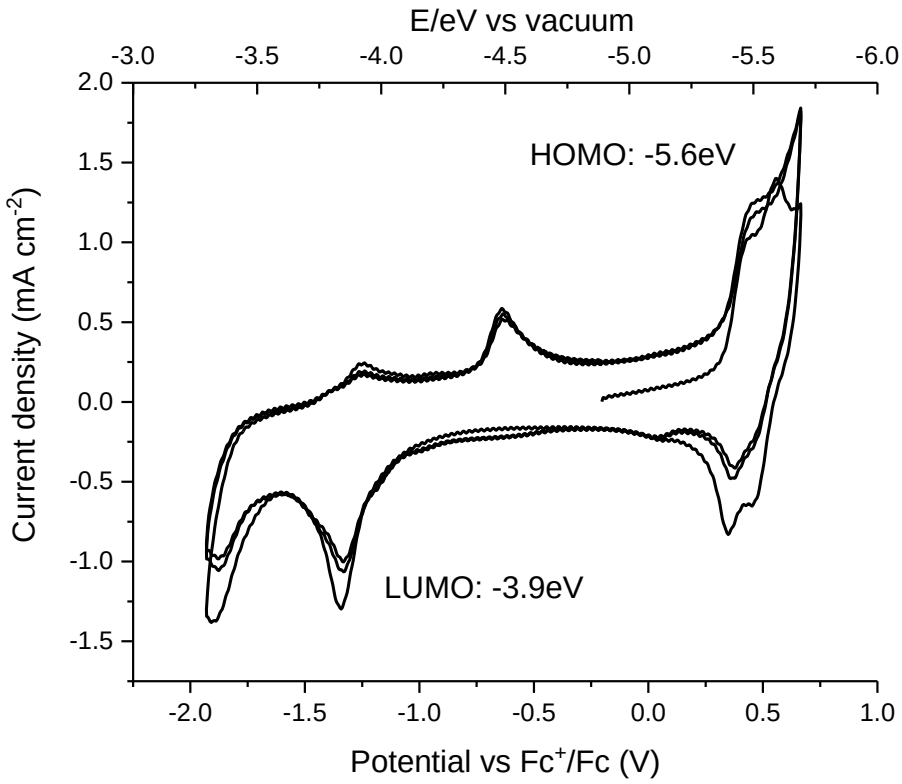

*Fig. 3.7. Cyclic voltammetry of DPP **27***

Within thin film technologies there are currently two areas of research investigated for improving efficiency in organic photovoltaics. Firstly, by improving exciton and charge carrier mobilities and diffusion lengths with molecular design. This is often achieved by fine tuning molecular structures to control molecular packing.[26,27] In regards to photoactive materials, high levels of molecular order is beneficial for efficient charge transport and extraction in many thin film organic photovoltaic devices [28,29,30]

Secondly, improving the nano-scale morphology of films to bring donor and acceptor domains within the exciton diffusion range.[31,32,33,34,35] This is usually achieved by developing materials with a tendency to phase segregate in a finely intermixed morphology with regular domain structures. These two techniques work together. An efficient device requires both an ordered molecular packing as well as an optimised nanomorphology.

In this study it is expected that the activation of latent pigment materials will result in highly crystalline domains due to the activation of H-bonding networks which become available after removal of the solubilising functionality from a relevant aryl amine. It is also possible that the evolution of gas during deprotection, from within the crystalline domains formed by spin coating active layers, could break large crystallites into a finer powdered crystal. As such an

extensive X-ray study has been carried out on DPP **27** and DPP **34**. The effect of such crystal size reduction is of importance to the nano-morphology of thin film devices.

PCBM is used as the acceptor material for the photovoltaic devices made in this chapter. This is based on the strong track record of PCBM and its derivative in the photovoltaic industry.[36] PCBM is a material which exhibits a high affinity for ITO substrates. This characteristic can disrupt the donor acceptor ratios within a film[27]. It is evident that a material's tendency to aggregate is of key importance to device performance. As such, it is necessary to examine the effects of deprotection on the density of each film. It is speculated that by activating latent pigments the strong H-bonding network will establish tight, dense packing modes. The increased density in donor material may hinder the migration of PCBM through the thin film.

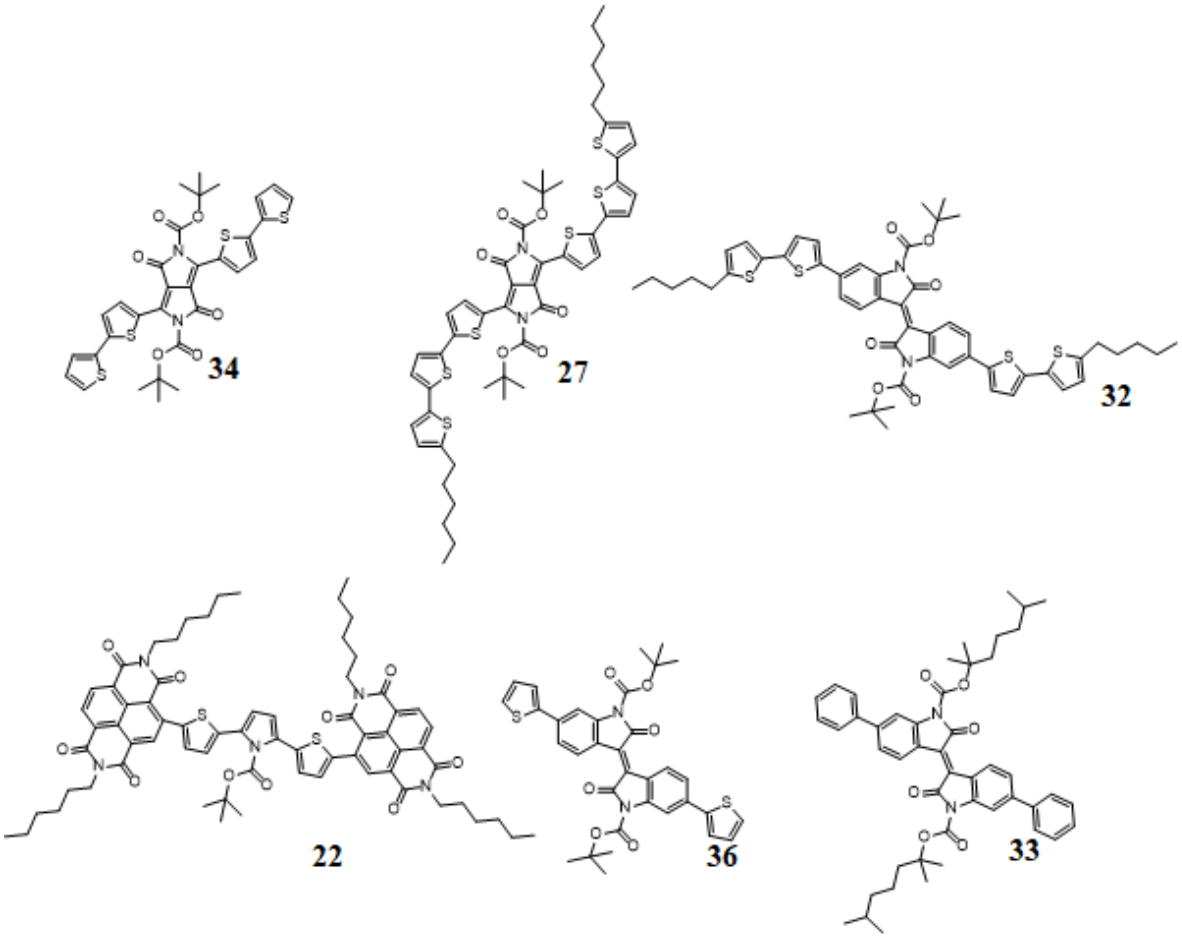

*Fig. 3.8. Examples of latent pigments. Top left to right DPP**34**, DPP **27**, and isoindigo **32** Bottom left to right NDI **22**, isoindigo**36**, and isoindigo **33***

Results and discussion

Initially DPP **34** and **27** were established in planar bilayer devices. Bilayer devices have a lower interfacial area than BHJ and thus are often less efficient. Theoretical limits of roughly 15% PCE are quoted. The benefit of this setup lies in the high accessibility and reproducibility of planar bilayer devices when accessed by roll to roll means.

DPP 34

Fabrication of planar bilayer devices was initially performed on DPP **34.** ITO substrates underwent a standard sonication for 10 minutes subsequently in 2% mucasol solution, distilled water, acetone and iPrOH. Substrates were then dried under a nitrogen flow before 10 minutes ozone cleaning. PEDOT:PSS was then spincoated at 2000rpm for 60 seconds before being annealed at 110°C for 10 minutes in a nitrogen glove box. Active layer deposition was then carried out with DPP **34** with 8.5 mg/mL solutions in chloroform spincoated at 4000rpm for 45seconds. The substrates were then placed on a hot plate for deprotection at 200°C for 7 minutes. The insolubility of this deprotected films allows PCBM to be also be spincoated from a chloroform solution of 8 mg/ml at 5000rpm for 45 seconds. The cells were then placed in a thermal evaporator where 1 nm of LiF was evaporated. The cells were closed with 90-100nm of aluminium. Each substrate contains 4 cells and 3 substrates were used per fabrication with a total of 12 cells made in tandem per fabrication. The active area of each cell is 0.2mm^2.

Interlayer choice

The interface between the active later and the electrode is of key importance for the performance of OPV.

PEDOT: PSS is the most common electron blocking layer. It is solution processable from water dispersions which make this high-performance interlayer very attractive for inclusion in photovoltaic devices. Furthermore, the acidic nature of PEDOT: PSS which is generally viewed as detrimental to device stability may aid in the deprotection of t-Boc material. LiF was initially chosen as a hole blocking layer between the photoactive semiconductors and the aluminium cathode LiF has been seen to improve the reliability of organic devices, it is thought that LiF provides an ohmic contact between semiconductor and metal contact and lowers the work function of aluminium. Lithium has also been observed migrating into active semiconductor layers, it is possible that the lithium is doping the organic layers of the cell.[37] Improvements to FF and Voc due to an optimised charge transfer across the interface is commonly seen with the

use of this interlayer.[38,39,40] This very thin buffer layer also acts to protect the organic semiconductor from the heat of evaporated aluminium.

Initial results from this architecture resulted in power conversion efficiencies in the order of 0.31%. This result is already an improvement on the values obtained for DPP_H.

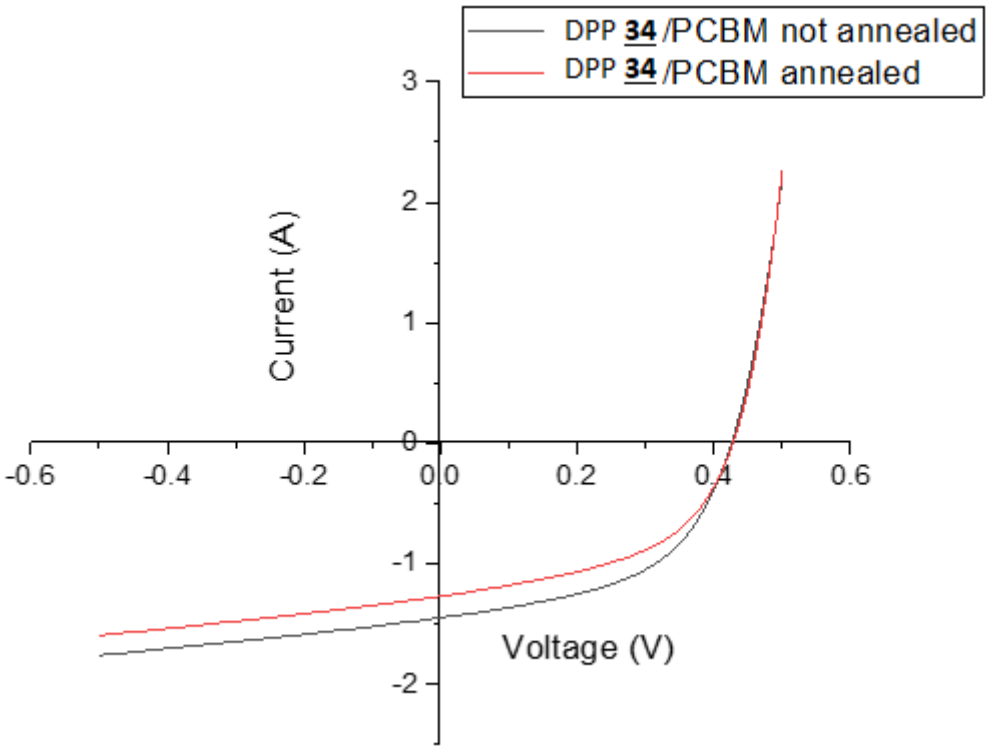

Sample	*Voc [V]*	*FF [%]*	*Jsc [mA/cm²]*	*PCE [%]*
Not annealed	0.43	0.50667	1.44	0.31%
120°C annealed (closed cell)	0.45	0.38032	1.33	0.23%

*Fig. 3.9. Initial IV curve for ITO/PEDOT:PSS/DPP **34**/PCBM/LiF/Al device. Annealing process was carried out on this cell at 120°C for 5 minutes on closed cell. The remeasured cell showed a reduction in current and fill factor.*

A short annealing of 120°C for 5 minutes was carried out on closed ITO/PEDOT:PSS/DPP **34**/PCBM/LiF/Al cells. This resulted in a noticeable reduction in short circuit current. LiF has also been seen to crystallise into plate islands on the surface of semiconductors. It is possible that the short annealing process causes the crystallisation of LiF into islands within these devices. The resulting heterogeneous interlayer may not be optimal for this device. To

investigate the possible effects of LiF dissipation during annealing, the cells were redesigned with two alternative hole blocking layers: Barium and ZnO_x. Barium was evaporated as an 8nm interlayer. ZnO_x nanoparticle films were prepared by spincoating at 1000rpm from a dispersion in ethanol and isopropanol. Both are well known hole blocking interlayer materials[41,42] The resulting device performances are seen below in table 3.1

	Voc[V]	*Jsc[mA/cm²]*	*FF[%]*	*PCE [%]*
ZnOx annealed 120C 7 min	0.45	1.64	0.450974	0.33%
Barium	0.455	0.96491	0.431655	0.0019
Barium annealed	0.441	1.254683	0.46415	0.002571
LiF	0.3975	1.4558	0.4987875	0.002882
LiF Annealed	0.436	1.295613	0.3739425	0.002117

Table 3.1. Average device data taken over 12 cells for each interlayer and annealing treatment. ZnOx film preparations always required a thermal annealing so no non-annealed devices are possible.

The ZnOx interlayer showed the most promise due to the slightly higher short circuit current of 1.64mA/cm^2. Interestingly in the case of cells fabricated with barium as a hole blocking layer the closed cell annealing improves the device performance. This is in contrast to the LiF devices.

To establish a greater understanding of the processes at play here external quantum efficiency (EQE) measurements were made on annealed and non-annealed devices. EQE measures the ratio of collected charge carriers to the external photons of a given wavelength incident on the cell. The measurements involved examining the charge carrier extraction rates at each wavelength. In this way we establish which portion of the light spectrum is causing charges to be generated within our cell.

High performance devices have recently been reported with EQE measurements showing very high charge carrier collection rates, in the order of 70%. This shows that devices are now capable of absorbing a large portion of incident light[43]. In our case, we see an unusual feature within our bilayer devices for material DPP **34**. (Fig. 3.10)

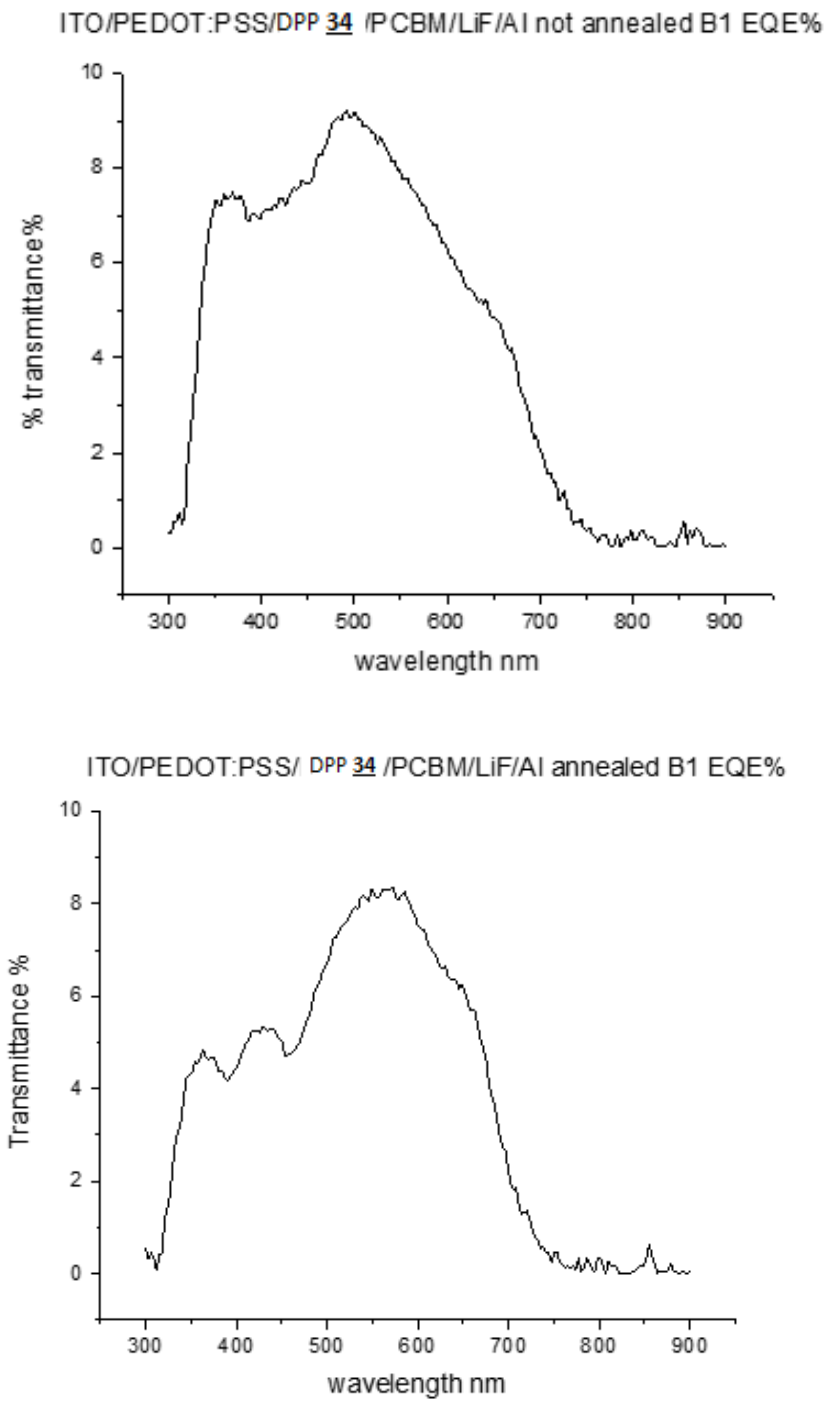

*Fig. 3.10. Above) EQE for non-annealed ITO/PEDOT: PSS/ DPP **34**/ PCBM/ LIF/ Al device. Below) EQE for annealed ITO/PEDOT: PSS/ DPP **34**/ PCBM/ LIF/ Al device.*

A short annealing of just 120°C for 5 minutes causes a significant change in charge generation. Prior to annealing the PCBM has a much larger role to play in the charge generation. A sharp strong feature is seen at 350nm. The main charge generation is occurring in the 500-550nm absorption range.

After annealing the wavelengths of absorption typical for PCBM are somewhat decreased (300-400nm). The main charge generation occurs in the region of the deprotected DPP (550-650nm). This activity is typical of a cell which shows strong migration of PCBM. This was an unexpected result as it was thought that the active deprotected layer would be very dense and unlikely to be permeable. To investigate this a thin film X-ray study was carried out.

X-ray data suggests that the process of deprotecting the highly crystalline materials causes crystallites to break apart, reducing the crystal size. This is seen as a broadening and reduction in intensity of the GIWAXS Bragg peaks (see Fig. 3.11. below for an example of this feature).

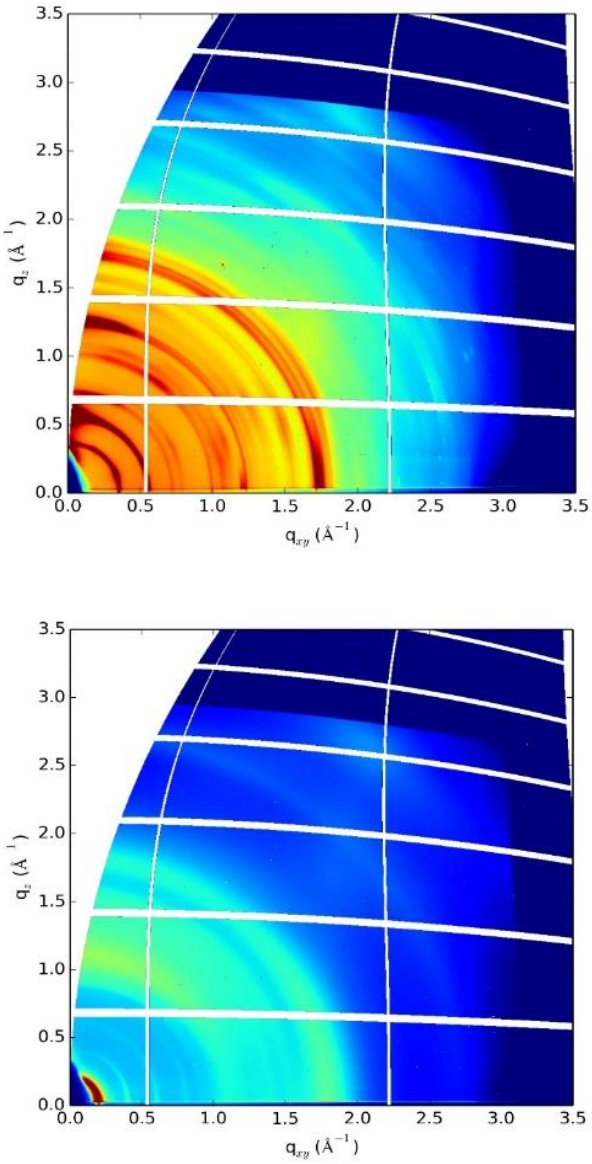

Fig. 3.11. Above) GIWAXS *of thin film of protected DPP* ***27*** *Below)* GIWAXS *of thin film of deprotected DPP* ***27.*** *Thick weak Bragg peaks seen as light blue bands indicate small crystallites with a random orientation in respect to the substrate.*

Although the deprotected film exhibits an increased density when compared to protected films, (see X-ray appendix 1, X-ray reflectivity for thorough analysis) the resulting films are powder-like in nature on the surface of the substrate. The films exhibit very small crystal structures in a random orientation with respect to the substrate. When the device is annealed percolation pathways likely appear through this very fine powder-like film. PCBM travels through these

percolation pathways. The device, in turn, becomes more like a BHJ than a bilayer and less photon absorption occurs within the now dispersed PCBM layer.

The high crystallinity of the donor material, although good for charge carrier mobilities, also results in high levels of light scattering which coupled with the tendency of the PCBM materials to agglomerate and migrate to the ITO contact significantly reduces the optical absorption and contact area of these donor pigments.

DPP 27

Initially the poor open circuit voltage of these devices was accounted for by the observed poor LUMO level alignment with PCBM materials (Fig. 3.6). The further symmetrical extension of the DPP **34** core with a further hexyl thiophene to form the DPP **27** structure was thought as a facile means to enhance the Voc. Unfortunately, the desired increase in Voc was not achieved when DPP **27** was substituted for DPP **34** (table3.2).

A variety of different film thicknesses were achieved by adapting the spincoating speed for the deposition of the donor layer. By increasing the thickness of this active layer, we see a very small improvement in the fill factor of the devices (see table 3.2. below). Further thermal annealing after deposition of PCBM at 120°C for 5 minutes does not appear to have a substantial effect on device performance.

*DPP **27** spin speed and post PCBM annealing*	*Voc [V]*	*Jsc [mA/cm2]*	*FF%*	*PCE%*
8mg/ml 2000rpm thermally annealed	0.369344	2.186748	39.21958	0.317025
8mg/ml 1000rpm thermally annealed	0.371826	2.099005	42.33023	0.329675
8mg/ml 800rpm thermally annealed	0.375439	2.10513	42.58695	0.3365
8mg/ml 1000rpm as cast	0.368743	2.277294	39.40063	0.330475
8mg/ml 800rpm as cast	0.353816	2.242067	42.23608	0.33486

*Table 3.2. Device characteristics for ITO/PEDOT:PSS/DPP **24**/PCBM/LiF/Al cells. All data is averaged over 3 substrates containing 4 cells each.*

The average short circuit current for devices fabricated with DPP **27** increases but the Voc decreases in comparison to DPP **34**.

In fact, both sets of devices (bilayer DPP **34**/PCBM and bilayer DPP**27**/PCBM) exhibit lower than expected Voc and Jsc values. The thermal treatment of these latent pigments is carried out at 200°C. It is possible that the action of this deprotection causes a delamination effect of the semiconductor from the substrate and from the individual semiconductor crystallites. In effect this would reduce the conductivity through the semiconducting core.

Possible delamination from the ITO contact and the high level of permeability of these films could be reduced by increasing the thickness of the donor layer. However, increasing the thickness is detrimental to the device efficiency as exciton diffusion lengths limit the possible thickness for bilayer devices. In order to increase the thickness of the devices a bulk heterojunction architecture can be established. Although the latent pigment method was developed to produce planar bilayer devices, the BHJ helps to establish if the low performances are caused by ITO donor interface issues or a mismatch between donor and acceptor.

Bulk heterojunction

It should also be noted that in the case of both materials a series of BHJ architectures were also attempted. The BHJ were completed and characterised with and without deprotection. Interestingly the non-deprotected BHJ had no photovoltaic activity at all. This may be due to a low level of miscibility with PCBM. Upon deprotection a low level of photovoltaic activity could be recorded (Table 3.3). This could suggest that upon deprotection the large immiscible domains of DPP break into small crystals which can be permeated by PCBM during annealing, although it should be acknowledged that these results are very poorly performing

*DPP **27** /PCBM BHJ*	*Voc V*	*Jsc mA/cm^2*	*Fill Factor*	*Efficiency*
1:1 ratio	0.332411	0.057498	23.50494	0.004493

*Table 3.3. Device characteristics for deprotected BHJ device of DPP **27** and PCBM*

(The reasoning for the low performance of these materials is further discussed in chapter 4 latent pigment transistors). Mainly, it seems as if the thermal deprotection of these materials results in a delamination and disruption of the pathways for charge gathering. It is thought that perhaps the release of two volatile gases from within a crystalline material may be an aggressive approach. As such this work has been extended to the development of latent pigments which instead of releasing gas will release a high boiling point solvent. This is achieved simply by using a protecting group which substitutes a long alkyl chain for the short tert-butyl portion of t-Boc. In doing so we have the possible access to a stoichiometric solvent annealing approach.

Long chain pyrocarbonate.

The use of a long chain pyrocarbonate to act in place of t-Boc (Fig. 3.12) provides a few benefits. Namely, the extended chain has far superior solubilising character than the tert-butyl functionality of t-Boc. This allows for larger, more complex conjugated systems to be processed through solution approaches.

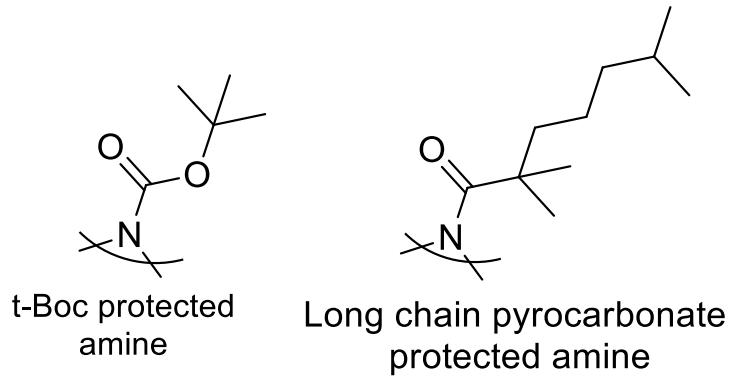

Fig. 3.12. structure of an extended chain protection group.

Another key factor when extending this solubilising chain is that the resulting deprotection affords one gas (CO_2) and one high boiling point solvent as opposed to the two gases released upon decomposition of the t-Boc. This high boiling point solvent can be very useful for film morphologies. It acts as a stoichiometric annealing solvent. Similar processing solvents used as additives such as diiodooctane (DIO) have been shown to improve film morphologies.[44] This additive has been known to enhance the edge on crystallinity of P3HT in BHJ cells. This enhancement results in an improved charge carrier transport within the cell which leads to improved device performances.[45,46]

Solvent additives can afford higher crystallinity films to form. In the latent pigment system rearrangement due to H-bond network activation may be aided by a high boiling point solvent annealing. It is expected that systems using the long chain pyrocarbonate to protect a pigment will result in a more ordered morphology with a reduction of grain boundaries throughout the film. The grain boundaries are thought to be formed by the harsh deprotection of t-Boc which produces gases that is most likely causing well-formed crystalline domains to crack.

Although this longer chain protection group affords high solubility semiconductors, synthetic processes proved difficult with this material. Standard chemical procedures such as Stille and Suzuki-Miyaura cross coupling reactions often afforded mono cross coupled products rather than the desired symmetrical cross coupling products. Iso-indigo core units protected with this long chain protection group were of very high crystallinity and struggled with compatibility in micellar cross coupling approaches as a result. Rapid deprotection on silica during material purification also caused difficulty in the synthesis of semiconductors incorporating this unique thermally sensitive protection group. A series of organic semiconductor cores could be developed successfully for this approach. Further functionalisation of these materials is necessary before incorporation into devices can be realised. This approach has interesting

potential for incorporation into copolymer structures. Latent pigment polymers could be a possible solution to the poor film quality which evolves during the activation of small molecule latent pigments. A similar approach has been investigated for thermo cleavable di-thienyl-benzothiadiazole polymers. Thermal cleavage of long chain thermo cleavable esters to afford solvent resistant bulk heterojunction solar cells. The observed effect of deprotection is a slight decrease in performance from 1.92% to 1.49%. This is most likely caused by the thermally induced phase segregation of polymer and PCBM.[47] Approaching a planar bilayer device based of thermally cleavable polymer could offer a method for access to facile device fabrication of efficient OPV.

Effects of crystallinity and agglomeration on optical properties

Some unusual behaviour was observed during device fabrication for a number of these materials. Unexpected absorption shifts and significant lowering of extinction coefficient after thermal cleavage of the t-Boc moiety was recorded. It was thought that significant change in film crystallinity could result in either significant agglomeration which results in an absorption shift or in a significant increase of light scattering throughout the film. This unexpected reduction in extinction coefficient is particularly interesting. When photovoltaic devices are made with PCBM or its derivatives the donor material used is generally expected to have good optical absorption properties. PCBM is not perceived to be a strongly absorbing material in regard to its optical properties.

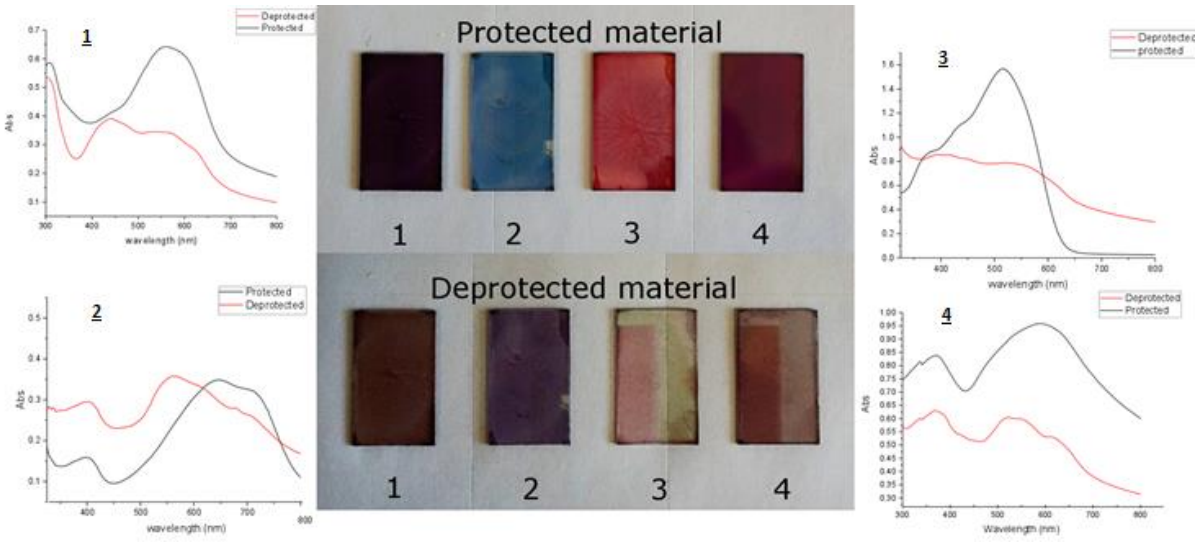

*Fig. 3.13 (central image) Thin films cast on glass/ITO substrates. Above protected below deprotected. (borders) related UV-Vis spectra of films cast on glass substrates (black) protected (red) deprotected 1=iso-indigo **32** 2=DPP **27** 3=iso-indigo **33** 4=DPP **35***

The optical shift of the DPP **34** observed in these EQE (above Fig. 3.13.) is also a further indication of material agglomeration. To examine this effect polymethylmethacrylate (PMMA) slabs were prepared where materials could be deprotected with limited crystallisation. Previous studies on latent pigment solar concentrators has reported that a fine homogeneous dispersion of latent pigment can be created in partially polymerised methyl methacrylate. As the polymerisation process progresses the latent pigment is restricted from crystallising or agglomerating. The thermal deprotection of the latent pigments can still be achieved by heating fully polymerised PMMA slabs. The highly dispersed nature of the latent pigment in the PMMA slab offers an opportunity to examine the optical properties of the material without the effect of crystallisation and agglomeration. [48]

PMMA slab preparation

100ml of freshly distilled methyl methacrylate is added to 100mg of the free radical initiator azobisisobutyronitrile (AIBN). This mixture is stirred vigorously and heated slowly until just under the boiling point. The viscosity slowly changes. Heat until the solution becomes a viscous syrup. Evolving bubbles should be slow to rise through the solution. Quench this reaction in an ice bath to 20°C. In a separate beaker dissolve 150mg of lauryl peroxide and the latent pigment of interest ($1x10^{-5}$M) in 60ml of freshly distilled methyl methacrylate. Add this solution directly to the partially polymerised syrup. Stir until homogeneous before casting into a square mould. Heat the mould in a water bath for 24hours at 58°C. Remove the slab from the mould and heat in an oven for a further 12hours at 100°C to ensure complete polymerisation. The optical absorption of a series of PMMA slabs was measured using a Jasco v-570 UV-spectrometer before and after thermal cleavage in a heated oil bath.

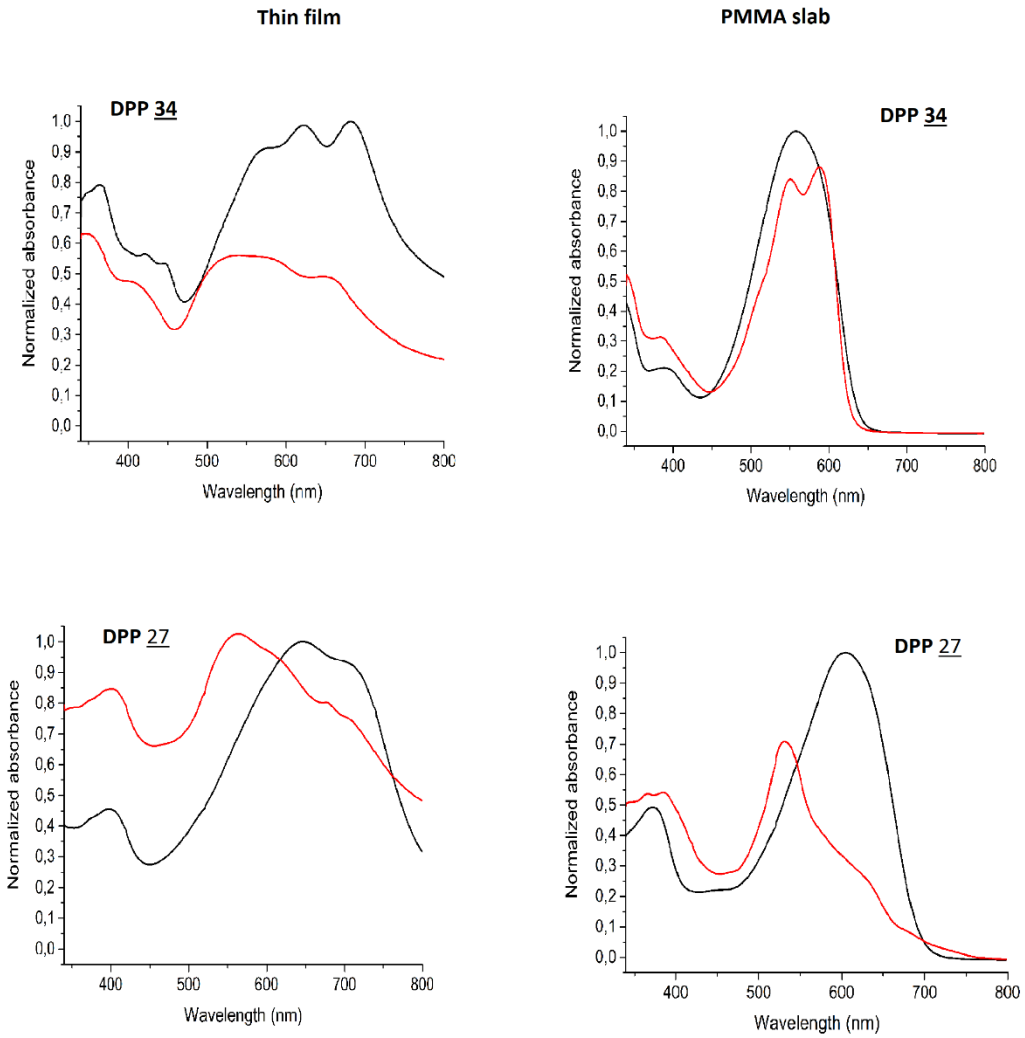

Fig. 3.14. Comparison of UV-vis of thin films (left) vs PMMA dispersions (right). Black illustrates the protected spectra and red depicts the deprotected absorption spectra.

Following the full polymerisation of methyl methacrylate (MMA) to PMMA the dispersed latent pigment shows an absorption spectrum with characteristics similar to the solution state spectra. The benefit of using PMMA is that once polymerisation is complete the PMMA slabs can be heated in an oil bath to the deprotection temperatures of the latent pigments. In fact, it has been shown that the PMMA environment facilitates the deprotection allowing the process to be carried out at lower temperatures.[15] The resulting deprotected material is somewhat frozen by the PMMA. Agglomeration effects are significantly reduced with notably different absorption characteristics in UV- spectra measured in PMMA slabs compared to thin films on glass substrates. Likewise, the sublimation effect that is seen with the lower molecular weight

iso-indigo derivatives is completely counteracted. From this short study, we examine the direct effects of deprotection on the optical properties of our materials. This experiment illuminates certain issues with the technique.

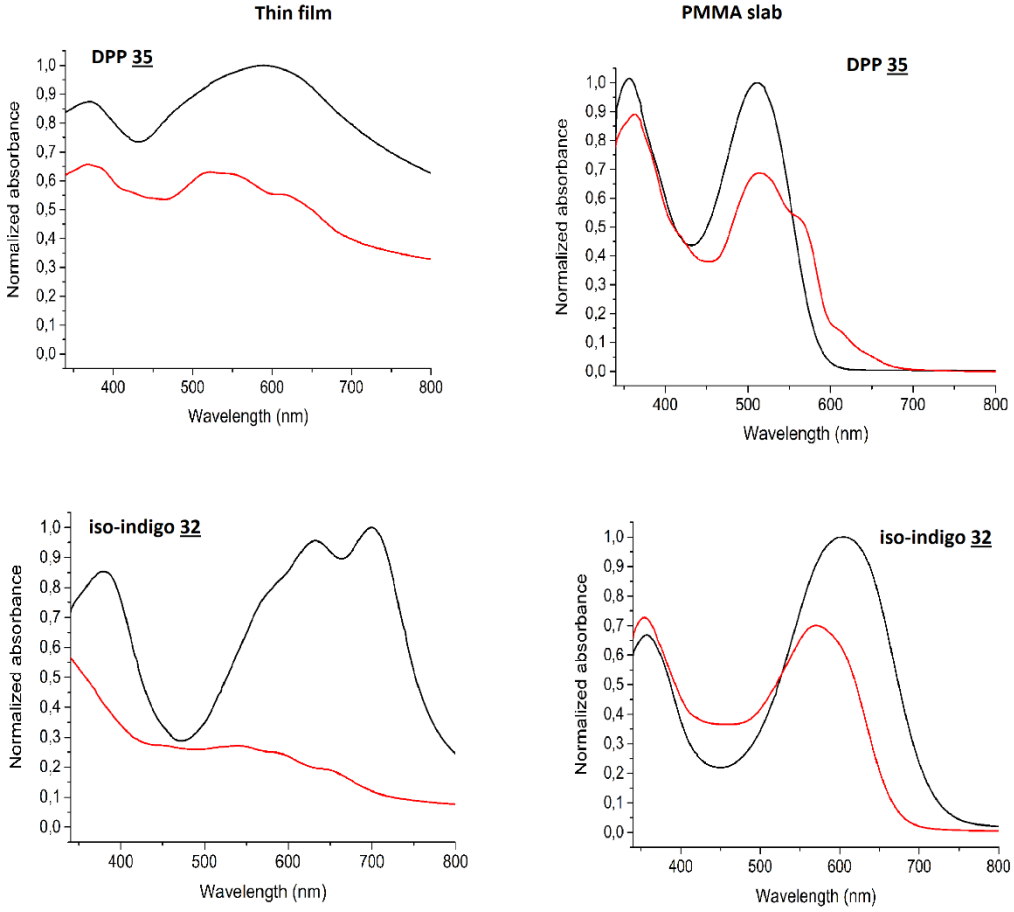

Fig. 3.15. Comparison of UV-vis of thin films (left) vs PMMA dispersions (right). Black illustrates the protected spectra and red depicts the deprotected absorption spectra. Sublimation of thin film is evident for the iso-indigo 32 latent pigment (bottom left corner)

The spectra taken of the PMMA slabs (Fig. 3.14-3.15) all have higher resolution peaks than those of the thin films. Deprotection generally results in a lowering of the extinction coefficient of the materials.

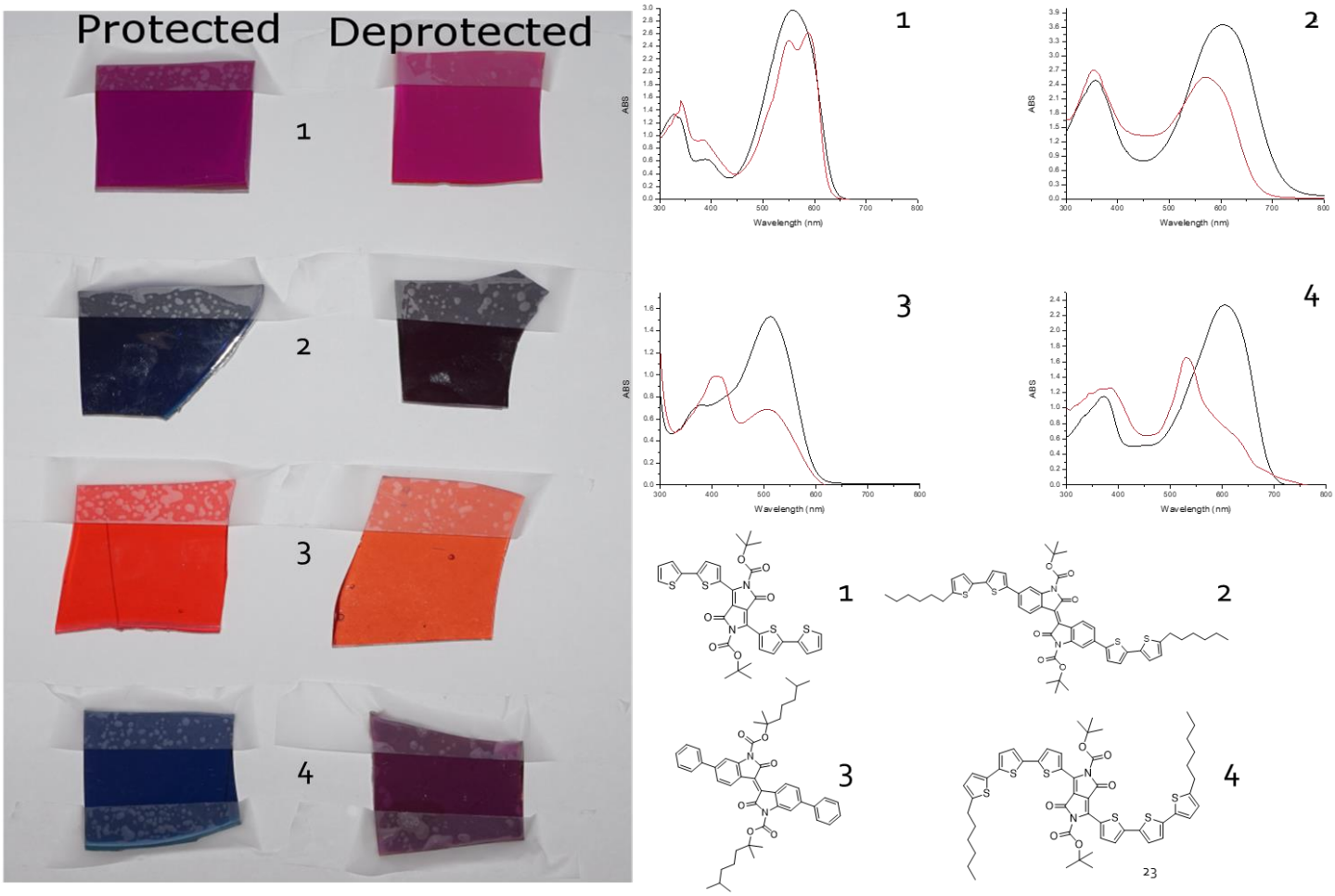

Fig. 3.16. Left) image of shards of PMMA slabs of four materials (structures bottom right) before and after deprotection. Slight colour changes can be observed during deprotection. It is possible to pattern these materials with localised heat sources. Top right) relevant UV-Vis spectra of each PMMA slab (before deprotection in black, after deprotection in red).

The 200-800nm region of a UV-spectra is the region in which photons will be absorbed by pi-electron systems or heteroatoms which have non-bonding valence shell electrons. The withdrawal of electron density from the semiconductors core lowers the HOMO levels of the material. In effect this causes the core to behave with a more acceptor-like character. All of the latent pigments studied here are donor-acceptor-donor materials. The removal of the t-Boc group reduces the acceptor strength of the semiconducting core which lead to a reduction in oscillator strength, an affect which is partially balanced by the effective planarization resulting from the activation of intramolecular hydrogen bonding.

Energetically favourable electron excitation occurs from HOMO to LUMO. The energy levels of these states are related to the wavelength of light which is absorbed by a species. The HOMO level of the material shifts during the deprotection process. As the level of conjugation

increases in a molecule the energy gap between the HOMO and LUMO decreases. This results in lower energy light being required to excite an electron within the electronic structure, absorption wavelength is increased in this was. As such, the bathochromic and hypsochromic absorption shifts observed are expected upon deprotection.

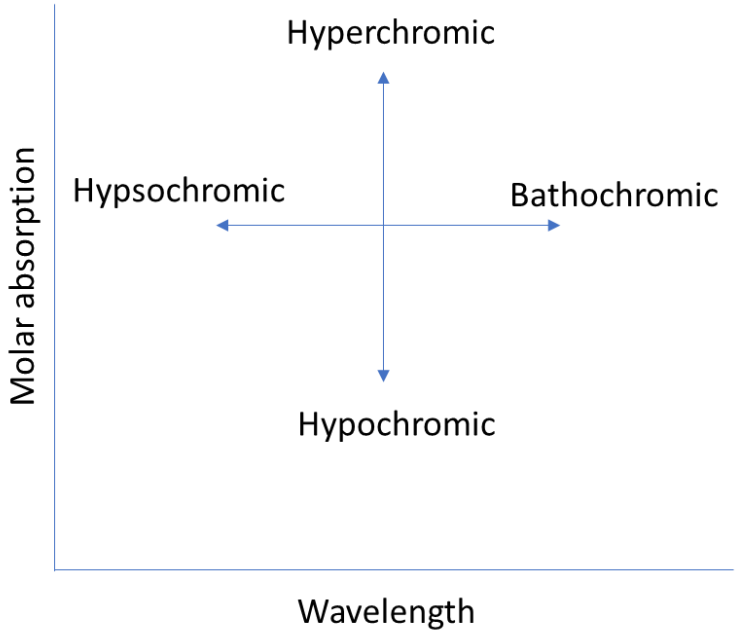

Fig. 3.17. UV vocabulary

The degree of this shift is attributed to the electronic contribution of the protection group on a molecules conjugation. The loss of extinction coefficient observed in the PMMA slabs when materials are deprotected is comparatively lower than the loss observed when the materials are deprotected as thin films on glass or ITO.

The high crystallinity of the deprotected thin films is partially responsible for this loss in absorption due to high levels of internal scattering occurs within the finely powdered material. In the case of iso-indigo derivatives **32** and **33** there is strong evidence of an unexpected sublimation process occurring (this is further observed during transistor fabrication Chapter 4) below the deprotection temperature.

From this quick experiment we can conclude that thin film agglomeration and high levels of crystallinity are having a negative impact on the quality of light absorption for deprotected latent pigment. For the field of organic photovoltaics, high optical absorption is key for high performance devices. Possible solutions for this issue may come in the form of further

processing procedures such as solvent annealing or through the addition of film additives which could reduce the effect of agglomeration within the latent pigment films.

Conclusion

A latent pigment strategy has been developed to fabricate planar bilayer organic photovoltaics. Two lead diketopyrrolopyrrole based semiconductors were chosen for a detailed study in both device characteristics and film quality. The morphologies of these materials were examined by X-ray spectroscopies including single crystal studies, reflectivity experiment and a GIWAXS study.

From this work it is established that the small molecules in question undergo a significant crystallographic rearrangement upon thermal cleavage of solubilising groups which affords the parent pigment. A significant reduction in crystal size is noted with a resulting powder-like film. No crystal orientation is observed after deprotection. This results in a disordered and possibly permeable layer of material.

The resulting device characterisations show evidence for poor charge generation and a high level of thermal instability. This is most likely attributed to the disordered morphology of the donor layer. Upon heating permeable channels are available for PCBM to migrate through causing unbalanced weakly performing devices which probably have a structure more similar to an intermixed bilayer or bulk heterojunction device. The highest performing devices for these materials was an average of 0.33% PCE. This is double the power conversion efficiency produced by a bulk heterojunction of DPP_H/ PCBM produced by Beverina et. al. The improvements in performance is account for the more appropriate alignment of HOMO and LUMO levels between donor and acceptor.

Attempts were made to extend this approach with a deprotection mechanism which provides the stoichiometric release of a high boiling point solvent which could alleviate some of the issues of morphology which arise from this approach.

PMMA slabs containing highly dispersed latent pigment were created in order to examine the optical properties of the latent pigments and the effects of agglomeration and crystallinity on the absorptive properties of these materials in thin films. A shift in the absorption spectra is accounted for by the electron withdrawing nature of t-Boc on each of the materials examined. It is established that the decrease in extinction coefficient seen during deprotection is greatly exaggerated for a thin film on a substrate compared to the highly dispersed materials trapped

within the bulk PMMA. It is evident that the crystallinity and agglomerative tendencies of the deprotected films has an adverse effect on the absorption properties of these materials

From the experience of working with small molecule latent pigments the high level of crystallinity seems to work against the device performances. Extensive device optimisation may result in useful POV devices from this approach with the use of film additives or solvent annealing. This is a situation which may undermine the original purpose of this approach as being a facile, reproducible, roll to roll compatible fabricating technique.

However, these materials are robust and designed to be compatible with a variety of different opto-electronic devices. The following chapter will investigate the incorporation of this technique into the fabrication of organic field effect transistors. This offers the possibility to examine the charge carrier mobilities of these materials and the effects of this reduced crystallite size without examining interactions with PCBM (information which could be useful in explaining the low yielding Voc and Jsc values achieved for the devices above).

References

1. Gevaerts, V. S., Koster, L. J. A., Wienk, M. M. & Janssen, R. a J. Discriminating between bilayer and bulk heterojunction polymer:fullerene solar cells using the external quantum efficiency. *ACS Appl. Mater. Interfaces* **3,** 3252–5 (2011).
2. Andreasen, B., Tromholt, T. & Andreasen, J. W. Generation of native polythiophene / PCBM composite nanoparticles via the combination of ultrasonic micronization of droplets and thermocleaving from aqueous. *Nanotechnology* **22,** (2011).
3. Larsen-olsen, T. T. *et al.* Simultaneous multilayer formation of the polymer solar cell stack using roll-to-roll double slot-die coating from water. *Sol. Energy Mater. Sol. Cells* **97,** 22–27 (2012).
4. Schwarz, K. N., Farley, S. B., Smith, T. A. & Ghiggino, K. P. Charge generation and morphology in P3HT : PCBM nanoparticles prepared by mini-emulsion and reprecipitation methods. *Nanoscale* **7,** 19899–19904 (2015).
5. Carl, J. E. *et al.* Aqueous Processing of Low-Band-Gap Polymer Solar Cells Using Roll-to-Roll Methods. *ACS Nano* **5,** 4188–4196 (2011).
6. Pecher, J. & Mecking, S. Nanoparticles of Conjugated Polymers. *Chem. Rev.* **110,**

6260–6279 (2010).

7. Kovacik, P., Assender, H. E. & Watt, A. A. R. Morphology control in co-evaporated bulk heterojunction solar cells. *Sol. Energy Mater. Sol. Cells* **117,** 22–28 (2013).

8. Kovacik, P. *et al.* Vacuum-Deposited Planar Heterojunction Polymer Solar Cells. *ACS Appl. Mater. Interfaces* **3,** 11–15 (2010).

9. Duan, L. *et al.* Solution processable small molecules for organic light-emitting diodes. *Journal of Materials Chemistry* (2010).

10. types-of-pigments @ www.dyespigments.net.

11. Sytnyk, M. *et al.* Hydrogen-bonded organic semiconductor micro- and nanocrystals: From colloidal syntheses to (opto-)electronic devices. *J. Am. Chem. Soc.* **136,** 16522–16532 (2014).

12. Głowacki, E. D. *et al.* Hydrogen-Bonded Semiconducting Pigments for Air-Stable Field-Effect Transistors. *Adv. Funct. Mater.* **25,** 1563–1569 (2013).

13. J. S. Zambounis, Z. Hao, A. I. Latent pigments activated by heat. *Nature* **388,** 131–132 (1997).

14. Galliani, D. *et al.* Thermochromic Latent-Pigment-Based Time – Temperature Indicators for Perishable Goods. *Adv. optical materials* 1164–1168 (2015)

15. Mattiello, S., Sanzone, A., Brazzo, P., Sassi, M. & Beverina, L. First Demonstration of the Applicability of the Latent Pigment Approach to Plastic Luminescent Solar Concentrators. *EurJOC* 5723–5729 (2015)

16. Liu, T. H., Cheng, W. T. & Huang, K. T. Crystallization and morphology of indanthrone converted from latent pigment in the solution with photo acid generator. *Dye. Pigment.* **105,** 137–144 (2014).

17. Online, V. A. *et al.* A facile protection–deprotection route for obtaining indigo pigments as thin films and their applications in organic bulk heterojunctions †. *Chem. Commun.* **49,** 6063–6065 (2013).

18. Wuts, P. G. M. *Protective Groups in Organic Synthesis*. (1999).

19. Głowacki, E. D. *et al.* Hydrogen-bonded diketopyrrolopyrrole (DPP) pigments as organic semiconductors. *Org. Electron.* **15,** 3521–3528 (2014).

20. Jones, F. & Okui, N. The Thermal Stability of Linear Trans-quinacridone Pigments. *Soc. Dye. Colour.* **91,** 361–365 (1975).

21. Moreno-lo, J. C., Grizzi, O. & Sa, E. A. Thermal Stability of N,N′-Bis(1-ethylpropyl)perylene-3,4,9,10-tetracarboxdiimide Films on Cu(100). *J. Phys. Chem. C* **120,** 19630–19635bro (2016).

22. Chandran, D. & Lee, K. Diketopyrrolopyrrole : A Versatile Building Block for Organic Photovoltaic Materials. **21,** 272–283 (2013).

23. Arias, A. C., Mackenzie, J. D., Mcculloch, I., Rivnay, J. & Salleo, A. Materials and Applications for Large Area Electronics : Solution-Based Approaches. *Chem. Rev.* **110,** 3–24 (2010).

24. Vezie, M. S. *et al.* Exploring the origin of high optical absorption in conjugated polymers. *Nat. Mater.* **15,** (2016).

25. Bruni, F. *et al.* Post-deposition Activation of Latent Hydrogen-Bonding : A New Paradigm for Enhancing the Performances of Bulk Heterojunction Solar Cells. *Adv. Funct. Mater.* 1–10 (2014).

26. Cnops, K. *et al.* 8.4% Efficient Fullerene-Free Organic Solar Cells Exploiting Long-Range Exciton Energy Transfer. *Nat. Commun.* **5,** 1–6 (2014).

27. Matthew T. Weintraub, Enia Xhakaj, Ashli Austina, J. M. S. The effects of donor:acceptor intermolecular mixing and acceptor crystallization on the composition ratio of blended, spincoated organic thin films. *Mater. Chem. C* **4,** 7756–7765 (2016).

28. Karak, S. *et al.* Crystallinity and Morphology Effects on a Solvent-Processed Solar Cell Using a Triarylamine-Substituted Squaraine. *Applied materials and interfaces* (2014).

29. Saeki, H., Kurimoto, O., Nakaoka, H. & Misaki, M. Effect of crystallinity in small molecular weight organic heterojunction solar cells. *Journal of materials chemistry C* 5357–5364 (2014).

30. Schoonbeek, F. S. *et al.* Efficient intermolecular charge transport in self-assembled fibers of mono- and bithiophene bisurea compounds. *Angew. Chemie - Int. Ed.* **38,** 1393–1397 (1999).

31. Riede, M., Mueller, T., Tress, W., Schueppel, R. & Leo, K. Small-molecule solar cells — status and. **424001,** (2008).

32. Szarko, J. M., Guo, J., Rolczynski, B. S. & Chen, L. X. Nanoscale structure, dynamics and power conversion efficiency correlations in small molecule and oligomer-based photovoltaic devices. *Nano Rev.* **2,** 1–17 (2011).

33. Lee, K. H. *et al.* Morphology of All-Solution-Processed 'Bilayer' Organic Solar Cells. *Adv. Mater.* **23,** 766–770 (2011).

34. Dolores Perez, M., Borek, C., Forrest, S. R. & Thompson, M. E. Molecular and morphological influences on the open circuit voltages of organic photovoltaic devices. *J. Am. Chem. Soc.* **131,** 9281–9286 (2009).

35. Liu, Y. *et al.* Aggregation and morphology control enables multiple cases of high-efficiency polymer solar cells. *Nat. Commun.* **5,** 1–8 (2014).

36. Bauer, N. *et al.* Comparing non-fullerene acceptors with fullerene inpolymer solar cells: a case study with FTAZ and PyCNTAZ. *J. Mater. Chem. A Mater. energy Sustain.* **5,** 4886–4893 (2017).

37. Bruder, F. & Brenn, R. Photoelectron Spectroscopy of the Contact between the Cathode and the Active Layers in Plastic Solar Cells : The Role of LiF. *Jpn. J. Appl. Phys.* **44,** 3695 (2005).

38. Brabec, C. J. *et al.* Effect of LiF / metal electrodes on the performance of plastic solar cells. *Appl. Phys. Lett.* **80,** 1288 (2002).

39. Lee, S., Jeong, S., Kim, D., Kim, C. & Han, Y. Inverted Polymer Solar Cells with an Ultrathin Lithium Fluoride Buffer Layer. *J. Nanosci. Nanotechnol.* **12,** 3205–3209 (2012).

40. Ahlswede, E. *et al.* Comparative study of the influence of LiF , NaF , and KF on the performance of polymer bulk heterojunction solar cells bulk. *Appl. Phys. Lett.* **90,** (2007).

41. Cells, B. S. *et al.* Barium : An Efficient Cathode Layer for. *Sci. Rep.* **3,** 1–7 (2013).

42. Manor, A., Katz, E. A., Tromholt, T. & Krebs, F. C. Enhancing functionality of ZnO hole blocking layer in organic photovoltaics. *Sol. Energy Mater. Sol. Cells* **98,** 491–

493 (2012).

43. He, Z. *et al.* Enhanced power-conversion efficiency in polymer solar cells using an inverted device structure. *Nature photonics* 1–5 (2012)

44. Fan, X. *et al.* 1,8-Diiodooctane as the processing additive to improve efficiency of P3HT: PCBM solar cells. *J. Nanosci. Nanotechnol.* **14,** 3592–3596 (2014).

45. Rogers, J. T., Schmidt, K., Toney, M. F., Bazan, G. C. & Kramer, E. J. Time-Resolved Structural Evolution of Additive-Processed Bulk Heterojunction Solar Cells. *JACS* (2012).

46. Rogers, J. T., Schmidt, K., Toney, M. F., Kramer, E. J. & Bazan, G. C. Structural Order in Bulk Heterojunction Films Prepared with Solvent Additives. *adv. mater.*2284–2288 (2011)

47. Helgesen, M., Bjerring, M., Nielsen, N. C. & Krebs, F. C. Influence of the Annealing Temperature on the Photovoltaic Performance and Film Morphology Applying Novel Thermocleavable Materials. *Chem. Mater.* **22,** 5617–5624 (2010).

48. Turrisi, R. *et al.* Stokes shift/emmision efficiency trade-off in donor-acceptor perylenemonoimides for luminescent solar concentrators. *J. Mater. Chem. A* 8045–8054 (2015).

Chapter 4- Latent Pigment Field-Effect Transistors.

Introduction

Standard transistors found in today's technologies are generally made from inorganic materials such as silicon or germanium. These materials afford reliable, high performance devices. In this respect, organic materials may be limited to market sectors such as integrated optoelectronic devices in displays or for light emission and sensor applications. The first transistor devices were developed by John Bardeen, William Shockley and Walter Brattain working for bell labs between 1944-1948 during a war time effort to produce high purity germanium crystals. The team worked together to develop this first transistor from germanium crystals sandwiched between gold contacts.[1]

The possibility to develop organic devices on flexible substrates is a main marketable aspect of these devices. The future of organic field effect transistors (OFET) looks bright with a lot of research currently concentrating on developing further understanding of charge carrier recombination rates and light emission properties in organic materials. Advanced displays, microelectronics, portable electronics and optical communications are but a few areas sorely in need of the development of advanced OFET.[2,3,4,5] Whether acting as an amplifier (always on with varying current levels resulting in varying voltages) or as an on/off switch (on with maximum current or off with no current) transistors play a hugely important role in all modern circuitry.

Conceptually patented by Lilienfeld et.al in 1930,[6] an FET is essentially a capacitor with a conducting channel between two contacts. A modulation of charge is created by an applied voltage to the capacitor. The first organic polymeric field effect transistors came into existence in the mid to late 80's with the development of a polythiophene based device in 1987 (Fig. 4.1).[7,8]

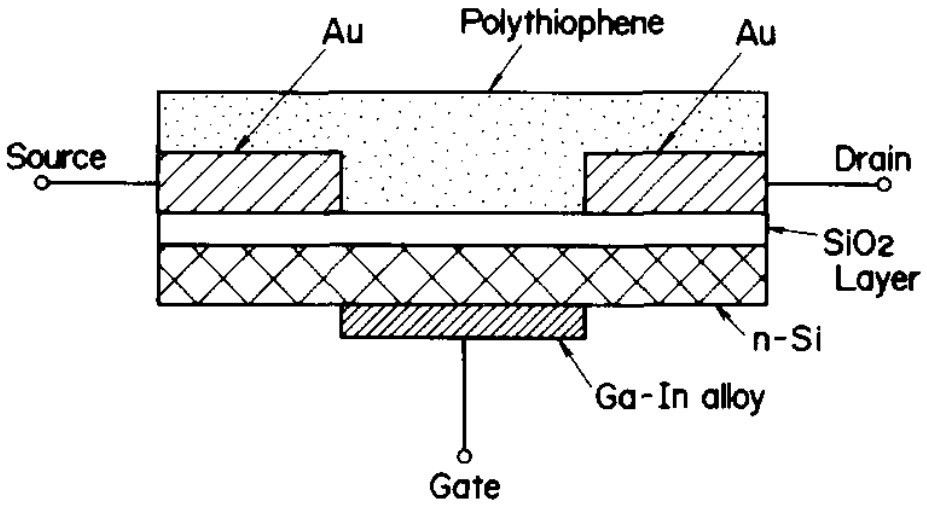

Fig. 4.1. Schematic diagram of the first generation of polymer FET devices.[8]

The development of the first OFET started a new field of research which quickly gathered interest due to the possible technological benefits of such devices. In recent years this field has continued to expand with increasing numbers of publications in the area of organic thin film transistors. Remarkable improvements to charge carrier properties has been seen over the years with modern materials performance beginning to challenge amorphous silicon devices with alternating donor acceptor polymer FETs surpassing $10cm^2V^{-1}s^{-1}$. This high molecular weight DPP-dithienylthieno[3,2-b]thiophene polymer was solution processed and integrated on flexible substrates to develop reproducible high mobility devices.[9]

The development of high mobility polymer and small molecule materials is attributed to the design of increasingly planer ordered materials with close π-π stacking and high levels of crystallinity. Field effect mobility has a close relationship molecular order.

Rigorous studies of conjugation length engineering show the importance of molecular order for thin film OFETs. One such study examines high mobility DPP copolymers. With conjugation length engineering it is possible to achieve edge on alignment of thiophene bridged DPP copolymers. Solution processing of these highly crystalline materials results in impressive hole mobilities of over $4cm^2V^{-1}s^{-1}$. By varying the conjugation length and donating level of this copolymers bridge units the HOMO and LUMO levels can be tuned and optimised.[10]

As always, small molecules have benefits over the high-performance polymers. High purity, reproduceable synthesis and easy access to functionalisation's makes the development of high performance small molecules essential.

Field effect transistors working principles.

The field effect is the phenomenon of an external electric field changing the conductivity of a semiconductor. In an organic field effect transistor (Fig. 4.2), a voltage is applied to a metallic gate electrode which controls the current between drain and source electrodes. A voltage is also applied between source and drain. For an OFET to operate this voltage must be above a value known as the threshold voltage. When the voltage is applied to the gate electrode, electrons or holes (depending on whether the semiconductor is a p or n material) accumulate along the semiconductor/dielectric interface. This is known as the "on state" of the transistor. Initially, a linear response in current is seen when increasing the voltage between source and drain (V_{SD}) and the voltage between source and gate (V_{SG}). This is known as the transistors linear current regime. A second effect is seen when the drain voltage begins to exceed the gate voltage, this is a nonlinear current regime known as the saturation region.[11] If the voltage used to turn on the transistor is negative the semiconductor is said to be a p-type device as holes are the majority carrier. This is the most common type of organic device.[12,13]

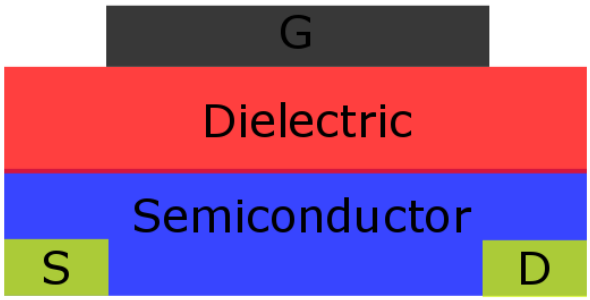

Fig. 4.2. Schematic diagram of transistor in top gate bottom contact configuration. S =source D=drain G= gate.

When the current travels positively from source to drain in the presence of a positive voltage the semiconductor is considered to be an n-type semiconductor. In n-type devices, electrons are the main charge carrier. N-type materials are usually less stable (due to reactivity with radical anions in air) than p-materials and electrons tend to have lower mobilities than holes. Ambipolar devices are also possible where one semiconducting material can have both p and n-type character. [14]

Two important features of an OFET are the carrier mobility and the on/off ratio. The carrier mobility is a measure of the performance of the device. This parameter is proportional to the semiconductors conductivity. The switch like behaviour of an OFET is also very important. The on/off ratio is the ratio of the saturation current, when the voltage between the gate and source is high, to the leak current that is recorded when the voltage between gate and source is low. Generally speaking, the higher this ratio the better.

Efficient charge transport in a semiconductor is desirable for good OFET device performance. For efficient transistor performance a good ohmic contact must be established between the semiconductor and the source/drain. A major determining factor in charge mobilities is the inter-molecular π-π bond distance of the organic semi-conductor.[15] Ideally molecules will orient themselves parallel to each other with close π-π interaction, optimising the charge transport through the semi conductor. This is a reason why most of the more effeicient charge transporting materials are highly planar materials which affords close π-π packing.[16,17,18] Smooth films and interfaces between semiconductor and dielectric are also desirable as interface roughness can affect the charge carrier mobility. The film quality is of great importance. Uniform, smooth films should ideally form a continous network between drain and source.[19] The dielectric should also be smooth and uniform as pinholes in this layer result in undesirable leak current.

Although simpler in architecture than OPV's, the OFET still relies on a bottom up build. The layered structure of these devices still requires sequential deposition steps. The similar solubility characteristics of independent materials within a multi-layer stack reduces the flexibility of processing significantly. The use of orthogonal solvents or evaporation techniques is often required for sucessful device fabrication. The field of solution-fabricated transistors is in need of a novel method which allows the deposition of semiconductor layers that can readily become insoluble post deposition.

Fig. 4.3. Microscope image of a complete device with a very thin layer of semiconductor. A measuring probe is seen touching the gate contact.

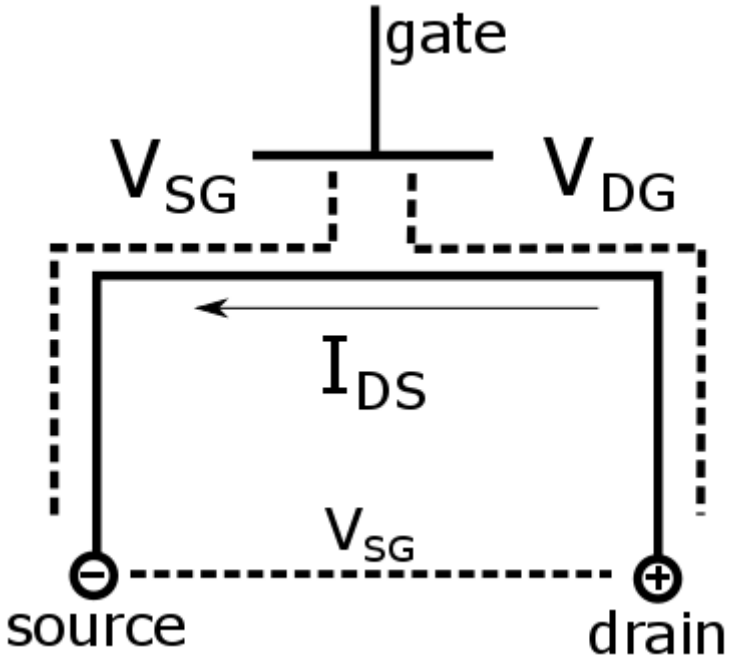

Fig. 4.4. Circuit schematic of organic field effect transistor

$$I = \frac{1}{2}\mu; C_i \frac{W}{L}(V_{GS} - V_T)^2$$

The equation used for measuring the field effect mobility in the saturation region.

I=drain to source current μ=mobility C_i=capacitance of dielectric W=channel width L=channel length V_{Gs}=gate voltage V_T=threshold voltage.

Materials for OFET

A diverse array of organic semiconducting materials have been shown to be suitable for OFET applications.

Pentacene and TIPS-pentacene

Fused ring acene materials are prominent in OFET research. Pentacene is one such material which has shown high performance as an active layer for OFET. It has been established that the charge carrier transport in field effect transistors occurs within the first few nanometres of the semiconductor layer. As such the crystallisation of these layers is very important for device performance. Pentacene is a highly planar and rigid material which has undergone extensive optimisation in this respect.

Optimisation of thermal deposition rates, underlying surface energies, annealing temperatures and cooling rates of the active semiconducting layers and subsequently deposited dielectric layer have also been extensively studied for this material.[20,21,22,23,24] Highly optimised pentacene devices can result in charge carrier mobilities as high as 2.02$cm^2V^{-1}s^{-1}$.[25]

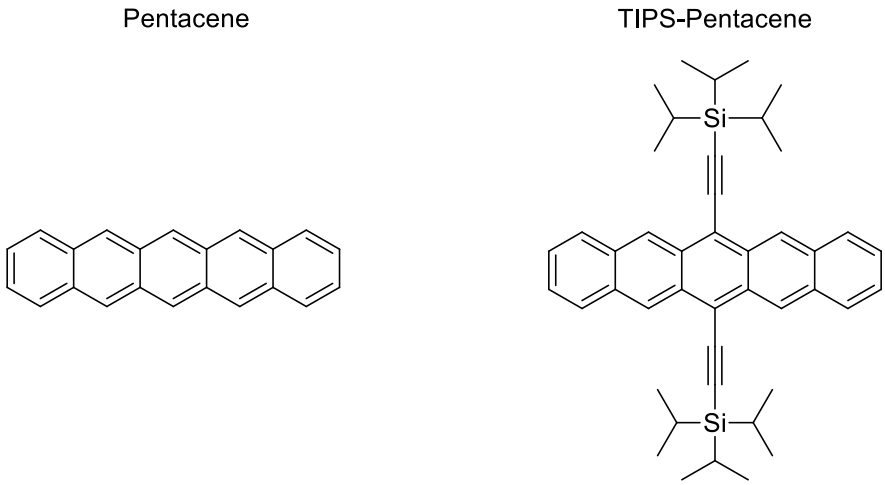

Fig. 4.5. Chemical structure of pentacene and TIPS-pentacene

The development of TIPS-pentacene enabled the solution processing of this high performance semiconducting core.[26,27] Films of TIPS-pentacene with high levels of molecular alignment have resulted in OFET devices with hole mobilities as high as 3.8 $cm^2V^{-1}s^{-1}$.[28]

Rubrene

Another well documented acene semiconductor is rubrene. Rubrene is an example of wide-band-gap semiconductor which can be grown as single crystals that exhibit good ambipolar behaviour[29]

Rubrene

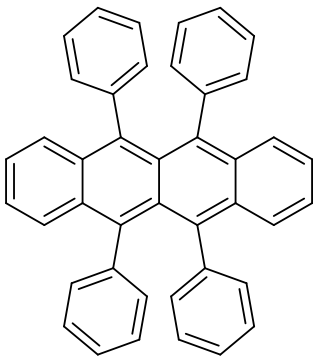

Fig. 4.6. chemical structure of Rubrene

This material holds the record for the highest hole mobility observed in an organic small molecule. Single crystal platelets of high purity rubrene transferred to silicon dioxide gates have established incredible hole mobilities ranging between 10-40$cm^2V^{-1}s^{-1}$.[30,31]

This material represents the cutting edge of small molecule and illuminates the potential for small molecules to establish themselves competitively with inorganic materials

Benzothieno[3,2-b]benzothiophene BTBT

BTBT and its derivatives are gaining attention as high performance materials for OFET applications. The developing chemistry for this material is leading to a diverse array of molecular analogues of this highly planar and crystalline material.

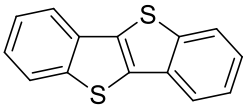

Fig. 4.7. Chemical structure of 1-benzothieno[3,2-b]benzothiophene

This material is comparatively more chemically stable than acene materials such as pentacene.[32] BTBT materials have low-lying HOMO levels good chemical stability and high p-type charge carrier mobilities in the order of 2$cm^2V^{-1}s^{-1}$.[33] The chemical adaptability of this material allows access to alkylated BTBT or even integration into a high performance co-

polymer[34,35] Impressive mobilities of 10 $m^2V^{-1}s^{-1}$ were demonstrated for a symmetrical C8-BTBT material which was epitaxially grown as few layer molecular crystals from 2D materials graphene and boron nitride which shows the potential of BTBT materials as high performance semiconductors.[36]

Diketopyrrolopyrrole

Diketopyrrolopyrrole semiconductors are well known p-type cores used in a variety of different opto-electronic devices such as organic photovoltaics and organic field effect transistors. Such examples as dimeric thiophene functionalised DPP small molecule materials have demonstrated mobilities 0.07 for holes and 0.03 for electrons. Side chain engineering has seen the development of donor acceptor DPP materials with field effect mobilities as high as 3.04 $cm^2\ V^{-1}\ s^{-1}$.[37,38]

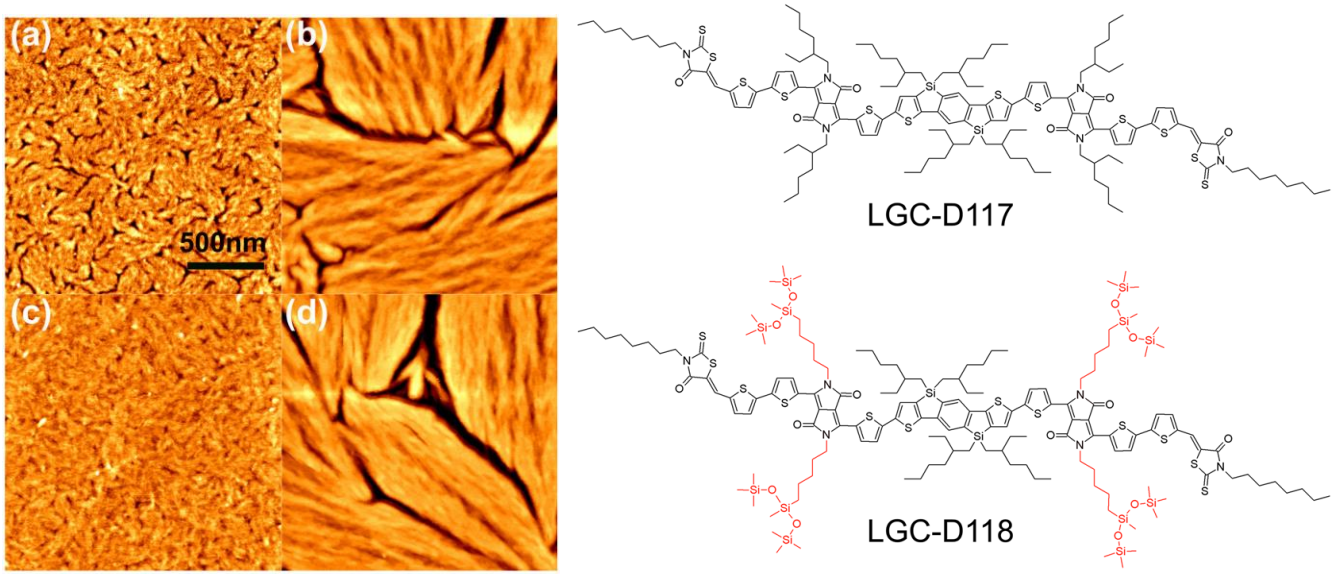

Fig. 4.8. AFM images of morphology upon thermal annealing of DPP small molecules a-b) LGC-D117 and LGC-D118 unannealed c-d) LGC-D117 and LGC-D118 annealed.[38]

Furthermore, polymeric derivatives of DPP with thiophene side groups having p-type mobilities in the order of 10 cm^2/Vs from solution have been reported, showing some of the highest performances for solution processed devices to date.[9]

Perylene diimide

PDI materials are also well-known n-type materials. Notable works coming from the Facchetti group report electron mobilities of up to 0.15 $cm^2\ V^{-1}\ s^{-1}$ from solution after a thermal annealing process. The air stability shown for this material (more than 20 days in air) is quite rare for an n-type OFET. N-type devices are notoriously environmentally unstable. [39]

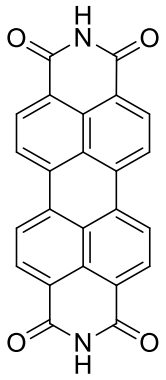

Fig. 4.9. Perylene diimide

This semiconducting core can be readily functionalised on the nitrogen of the cyclic imide as a method to access soluble derivatives which are suitable for OFET devices. [40]

Abstract

Within this chapter the unique effects of latent pigment activation for several materials on the device characteristics of organic field effect transistors is examined. The work is initially carried out on two materials, a tert-butyloxycarbonyl (t-Boc) functionalized diketopyrrolopyrrole and a perylene-diimide based semiconductor. The mobilities of these materials are examined before and after deprotection in air and in nitrogen. This work is extended through the fabrication of four other latent pigment devices. The development of this method for fabricating field effect transistors gives an insight into effects of deprotection on semiconductor mobilities. These results can also be used to illuminate some reasoning on the photovoltaic activity seen in the previous chapter.

The bottom up build of these devices usually requires the use of orthogonal solvents. Practical aspects of fabrication are often complicated due to the similar solubility profiles of subsequent layers. The latent pigment approach may be well suited for addressing such an issue. The benefit of insoluble semiconductor layers can be complimented with the access of these latent pigment systems to H-bonding networks. The use of the t-Boc radical also reduces the levels of electrical insulation which would normally incur from the presence of the dense, electronically inactive solubilising chains normally found in semiconductor material design. The stability of latent pigments throughout the fabrication process is also of key interest in this study. FET properties were examined to understand the complex changes of film morphology and the effect these changes incur on the charge carrier properties of the material.

Device fabrication.

All transistor data is from a top gate bottom contact architecture. Source and drain were patterned by lithography from 40nm of gold with channel lengths of 20, 10, 5 and 2.5µm. The semiconductor was deposited by spin coating 5mg/ml in chloroform at 1000rpm for 60seconds. The substrates are dried for 10 minutes at 70°C. Transistors were always made in pairs with one half being deprotected at 200°C for 7 minutes. The dielectric poly(methylmethacralate) (PMMA) was then spincoated in a thick layer from n-butyl acetate. The PMMA layer was dried over 45 minutes before 50nm of aluminium was deposited as a top contact by thermal evaporation under vacuum.

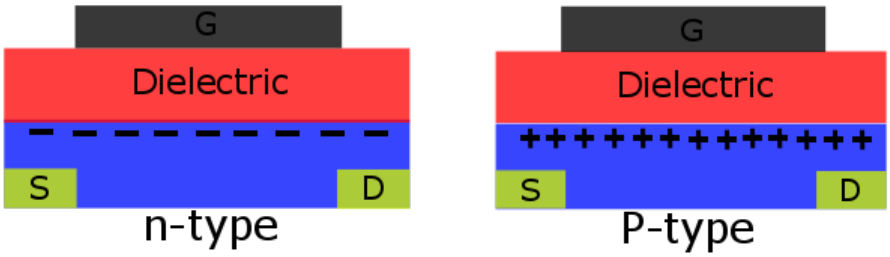

Fig. 4.10. N-type and p-type thin film transistors. S= source D=drain G=gate

The electrical characteristics of transistors were measured in a nitrogen glovebox with a Semiconductor Device Analyser (Agilent B1500A) and a Wentworth Manual Probe Station.

Results

The first two materials used to fabricate OFETS were a ter-thiophene functionalised DPP (**27)** core as a p-material and a perylene-diimide (**PDI)** material (Fig. 4.11) (synthesised according to the reported procedure by Mattiello et al.)[41] for fabricating an n-type device, both parent pigments were protected with t-Boc radicals. [42]

Field effect currents were measured for both materials in the top gate bottom contact configuration as this architecture is thought to optimize the charge injection and energetics at the interface.

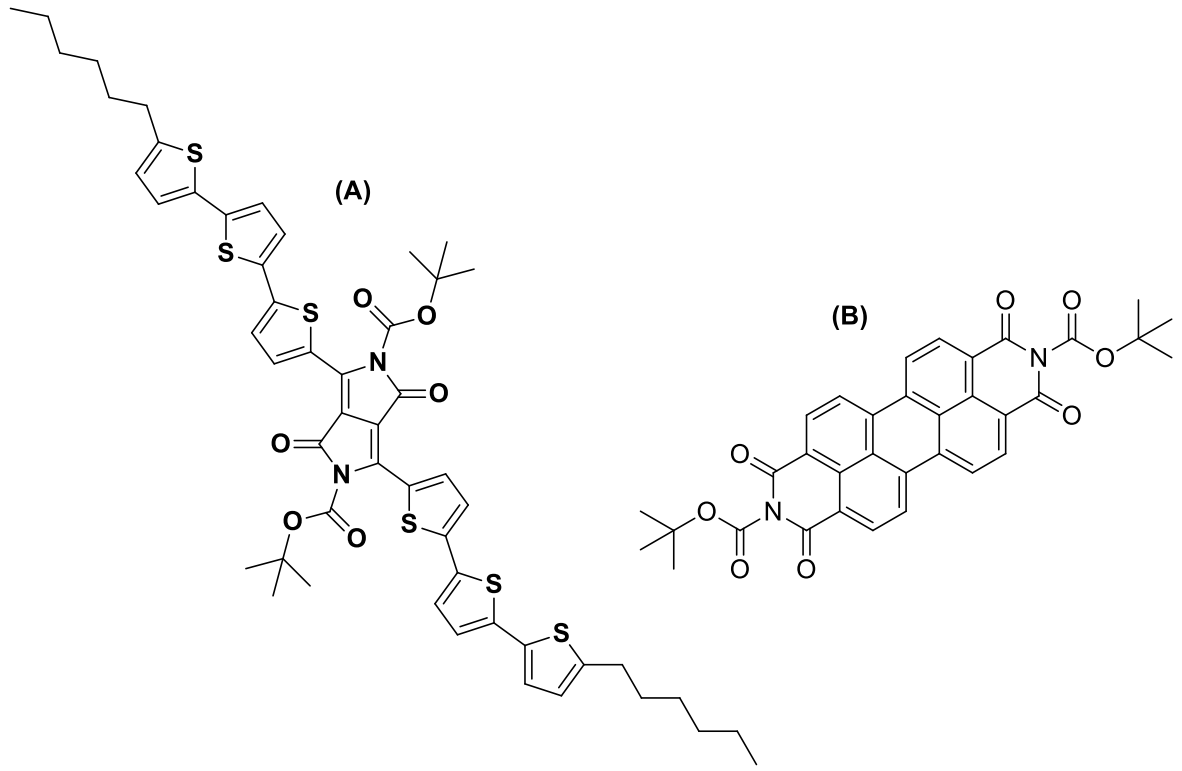

Fig. 4.11. ***(A)=DPP 27*** *p-type material,* ***(B)=PDI*** *n-type material. For synthesis see experimental procedures* ***appendix 2***

As with the OPVs the thermal process used to cleave the t-Boc was a 200°C thermal annealing for 7 minutes. This temperature was chosen as TGA analysis of **27** shows deprotection initiating at roughly 160°C (Fig. 4.12). This is seen as a reduction of roughly 20% of the materials mass, corresponding to the loss of two t-Boc moieties per molecule in the form of CO_2 and iso-butene. Meanwhile, specular X-ray analysis shows the onset of the deprotection of DPP moieties beginning around 160-170°C (Fig. 4.13). The higher temperature was chosen as standard to ensure full deprotection within a suitable timeframe for processing. It was noted the thermal stability of this pigment extends to 380°C.

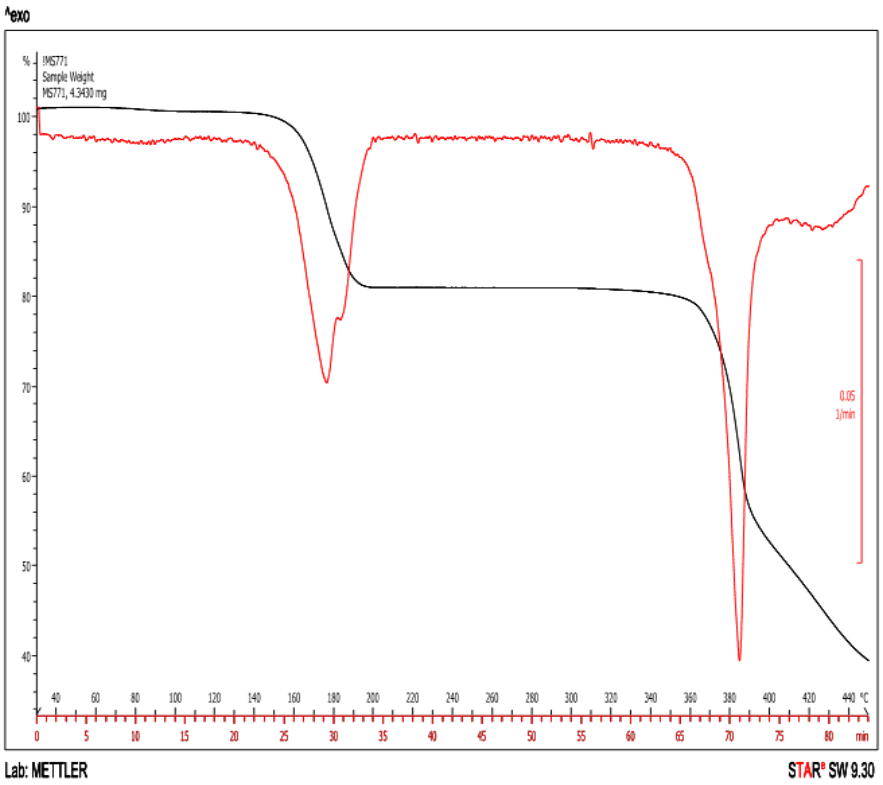

Fig. 4.12. TGA of 27. Initial deprotection occurs at roughly 160°C-170°C

It could be argued that 200°C is an unnecessarily high temperature as deprotection is seen during a 160°C specular scan. The deprotection is seen in real time during a thermal gradient specular scan of **27** where full specular X-ray scans were carried out on a thin film with 10°C intervals. Each scan takes roughly 5 minutes. As 160°C is reached the sample is allowed to equilibrate in temperature for 3 minutes before the scan is started. The scan begins at a low 2 theta value and slowly increases over a large 2 theta range. In the first portion of the scan there appears to be no change in phase but as the scan progresses we notice the second Bragg reflection has been reduced significantly. This indicates the process is almost complete at 160°C. By 170°C it appears that the thermal deprotection is already complete. This type of characterisation is important for new materials as it is possible a lower deprotection window may be less aggressive and result in a more desirable final film uniformity.

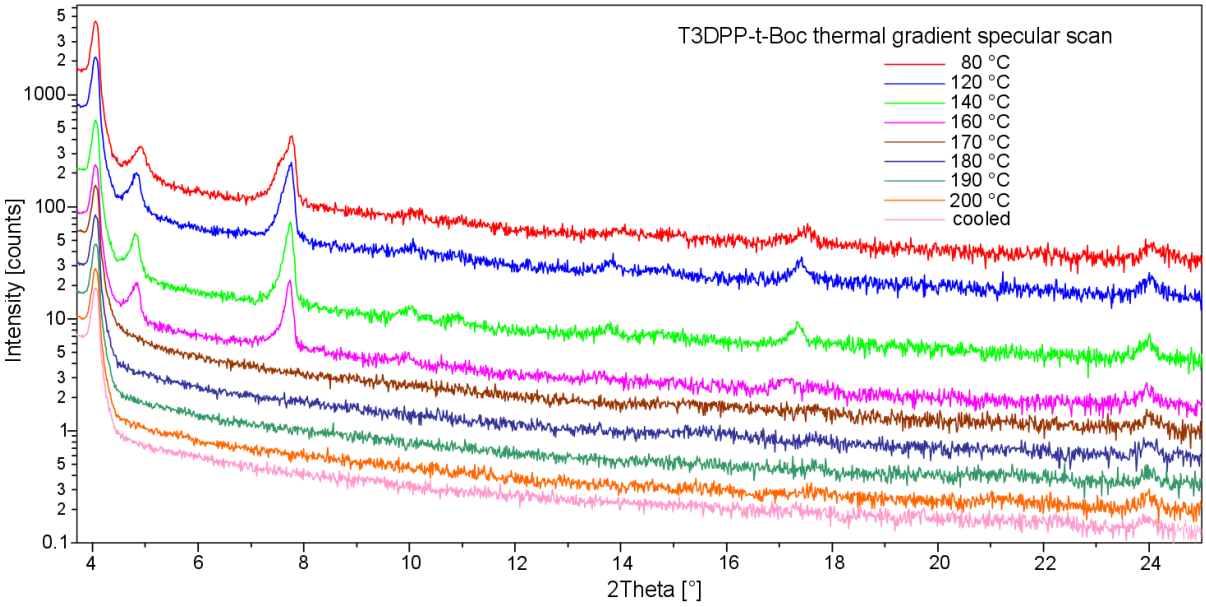

*Fig. 4.13. Thermal gradient specular scan of **27** with background subtractions measured with CuKα specular radiation source. Change in crystalline phase begins during the 160°C specular scan. Scan timescale is ~5minutes.*

The deprotection of PDI occurs at a lower temperature of ~120°C (Fig. 4.14). The thermal stability of the parent PDI pigment, however, extends beyond 500°C. As such, it was decided that to have a strong comparison between the two materials the same deprotection temperature of 200°C would be used for device fabrication. This temperature ensures full deprotection of both model materials and also surpasses a temperature that is typically used to thermally anneal both classes of material.

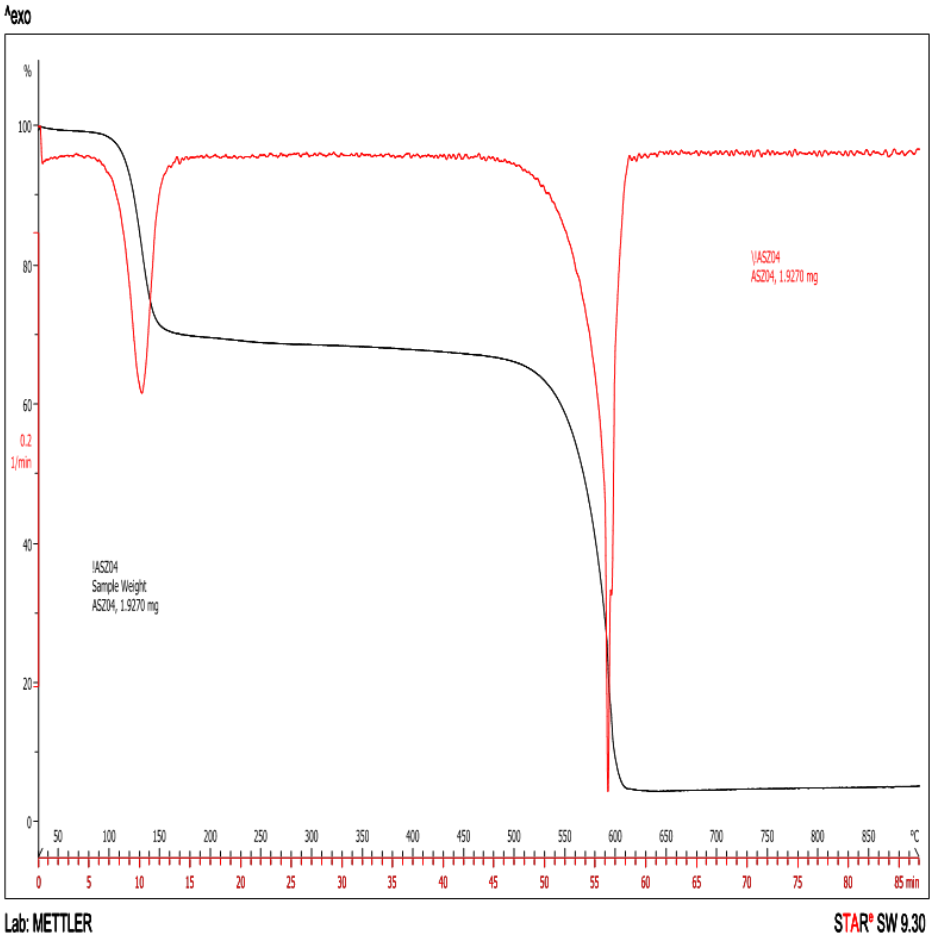

*Fig. 4.14. TGA of **PDI** deprotection commences at 120°C and is complete by 155°C*

Full X-ray characterisation of DPP **27** thin films was carried out, including grazing incidence wide angle X-ray (GIWAXS) at the DIAMOND synchrotron source in England. This investigation was required as it offers a unique insight into the crystallinity of a film. Structure activity relationships are key areas for explaining device characteristics. By performing GIWAXS at synchrotron sources we can attempt to establish a relationship between a molecules order and the charge carrier characteristics of a film (Fig. 4.15).

During this study, thin films of **27** with known thickness and roughness were spincoated from 7mg/ml chloroform solutions on thermally grown silicon dioxide on silicon substrates. A thermal gradient was applied to this substrate in situ on the beamline. GIWAXS measurements were recorded at every 10 degrees increase in temperature. An annealing process is recorded at 140°C where the initial crystalline phase seen from spincoating becomes more resolved. As the temperature increases this crystalline phase remains clear and obvious until 160°C upon

which time deprotection initiates. There is a clear and obvious molecular rearrangement throughout this film. As full deprotection is achieved Bragg peaks broaden and lose intensity with the formation of more obvious ring structures. This is a strong indication that a significant reduction in crystallite size occurs during the deprotection process. The very small crystallites sit in a powder-like confirmation on the surface of the substrate. The crystallite orientation is random as evidenced by the ring-shaped Bragg peaks rather than the hemi-circle or broken band like structures seen in pre-thermally treated scans, indicating a small degree of crystallite orientation most likely due to the direction of spinning while coating the films. It is possible that the release of two volatile gases (see mechanism of deprotection in section 3.2 chemical design of latent pigments) from the inside of a crystal result in a cracking and breaking of the crystals into a very fine powder. Meanwhile the activation of the H-bonding networks and loss of steric groups during a thermal process could give the system energy to rearrange with stronger π-π stacking interactions and a denser crystalline structure.

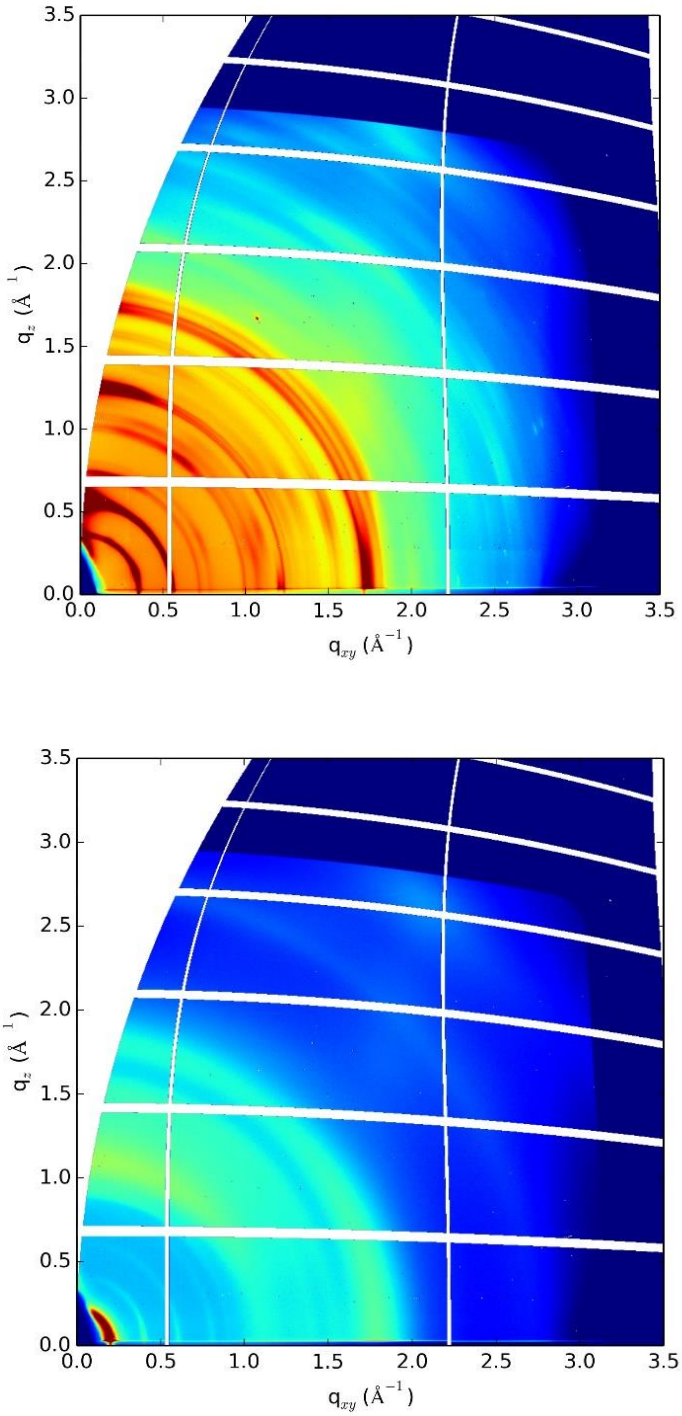

Fig. 4.15. GIWAXS *data converted to Q-space of DPP* ***27*** *above show pre-thermal treatment. The intense clear bands indicate good crystallite quality and size. Below is an example of the film post thermal treatment and cooled to room temperature. The broad thick bands with low intensity are indicative of small powder-like crystallites.*

Strong π-π stacking and dense crystalline structure should result in improved transistor performance, as it is generally thought close packing and high crystallinity is favourable for intermolecular charge transfer. The overall aim of this technique is to provide a method for creating insoluble semiconductor layers which establish good charge transfer pathways for high mobility transistors. To accomplish this goal, charge transfer properties were measured on devices that were made in tandem, with one half being fabricated with thermally deprotected pigment and another half containing the protected soluble dye. To achieve useable transistors for the protected material an orthogonal solvent n-butyl acetate (in which the latent pigment is not soluble) was used to spincoat the subsequent dielectric layer.

In the case of protected DPP **27**, a strong unbalanced ambipolar character is observed. Linear regime on-off ratios are recorded in the order of 10^4. In comparison with deprotected samples the hole current is much lower for devices incorporating the protected dye. Thermal deprotection in air prior to the dielectric deposition affords an increase in hole current by more than an order of magnitude. Meanwhile, the ambipolar character is significantly reduced with the n-channel becoming completely suppressed. The DPP **27** transistors, after deprotection, have a higher mobility and a more pronounced p-type character. The suppression of the electron channel seen in deprotection in air is not seen when deprotection is carried out under a nitrogen atmosphere. Ambipolar character is still seen with nitrogen deprotected devices.

This is possibly due to the kinetics of the deprotection process which may be accelerated by moisture in air. The latent pigment cleavage can be an acid catalysed process. Absorbed moisture in the film from air, at high temperature will accelerate the deprotection process. This will be even more evident with materials processed on a polar surface. A resulting Debye layer with acidic character in close proximity to t-Boc functionalities is probable under air atmosphere deprotection conditions. Alternatively, there may be a degree of oxygen and CO_2 doping of the film before deposition of the dielectric. CO_2 capture by similar structures such as quinacridone has been previously documented. [43]

The levels of CO_2 or O_2 permeating the film can affect the HOMO/LUMO levels of the pigment in question. This activity would be suppressed under a N_2 atmosphere. This reasoning remains speculative.

As we increase the gate voltage we can switch the transistor on. By fixing the gate voltage we can vary the drain voltage. The drain voltage increases causing the current to increase linearly. The transistor is resistor like, this phase is called the linear regime. As the gate voltage increases

the channels eventually become saturated (indicating the onset value), the current remains constant with increasing voltage. Changing the gate voltage changes the effective resistance of the transistors linear regime. By measuring the source drain current and voltage over a number of different constant gate voltages we can produce an output curve which can be used to recover output characteristics from an OFET. The region in which the gate voltage results in a negligibly small drain current is known as the cutoff region. A switch transistor is in the off position when operating in the cutoff region.

The device output curves for DPP **27** (Fig. 4.16) indicate that, although deprotection in N_2 results in higher a hole mobility, a better injection operation is seen in the devices deprotected in air. Field effect transistor hole mobilities are extracted from the saturation regime with an increase upon deprotection observed from $2x10^{-5}cm^2/Vs$ to 0.01 cm^2/Vs and 0.03 cm^2/Vs in air and nitrogen respectively. The ambipolar devices show that electron mobilities are not increased in the same manner as the hole mobilities for this material.

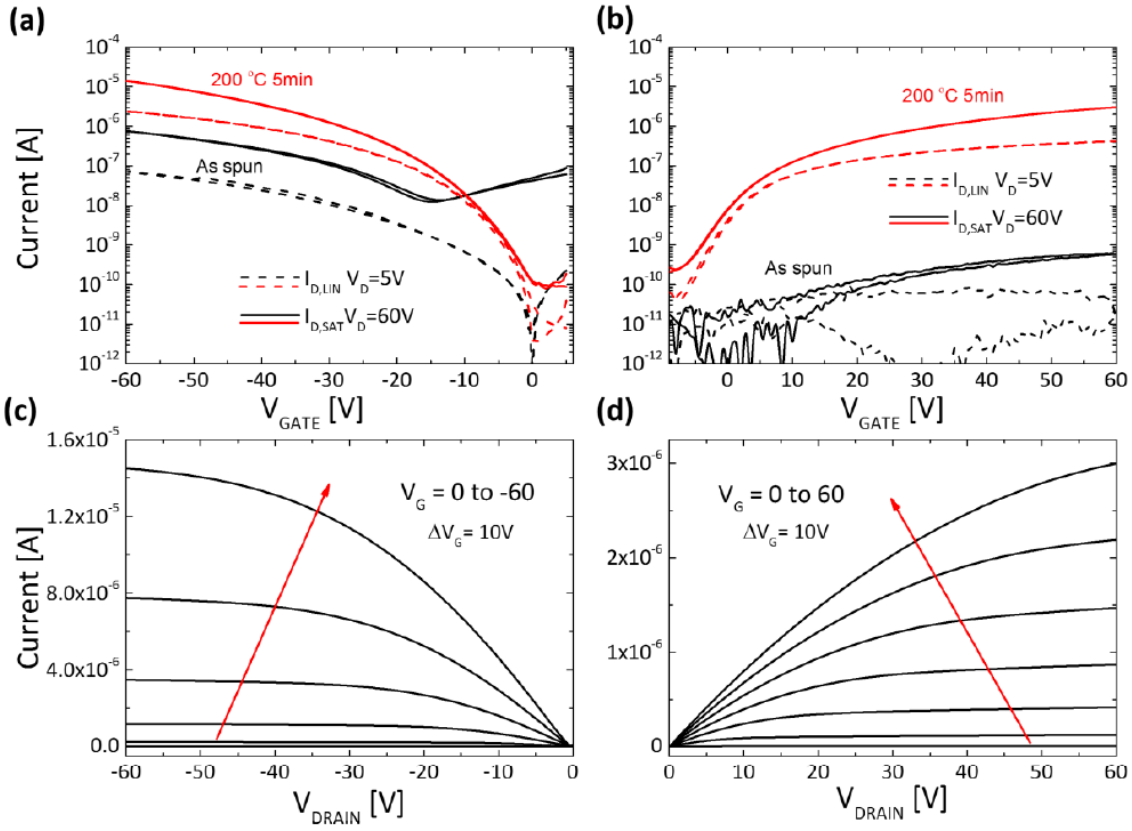

*Fig. 4.16. Transfer curves for a) protected (in black) and deprotected (in red) DPP **27** b) protected and deprotected PDI. Related output curves c) DPP d) PDI*

In the case of the protected PDI material, very low performances are seen with initial electron mobilities in the order of $1x10^{-7}$ cm^2/Vs in the saturation regime. This poor performance is typical of a material with an undesirable crystalline packing regime. Interestingly, upon deprotection in air this PDI material has an increase in performance by almost 4 orders of magnitude, raising to electron mobilities of $4x10^{-4}$. This substantial increase is most likely due to a strong molecular rearrangement with the removal of the sterically bulky t-Boc moieties with transport properties being greatly improved after rearrangement. In the case of PDI, no ambipolarity was observed before or after deprotection, the material is a low performance n-type material. This is the first case of an n-type latent pigment being used in an OFET device. Whereas similar methods have already been provided for P-type DPP materials.[44]

It should be noted that n-type materials generally have strong interactions with oxygen which leads to instability of n-type OFETs in air. In the case of the activated PDI pigment stability is donated by the strong H-bonding network throughout the film. During gate bias stress tests (Fig. 4.17) in air and nitrogen the PDI material showed outstanding stability in comparison to standard PDI materials in literature. A current reduction of only 19% over a 2-hour bias stress test was recorded. This was increased by a further 15% with testing in air for 2-hours. This level of stability is respectable for an n-type small molecule and is most likely related to the dense packing of the film which slows the permeation of reactive species such as oxygen and water in the device.

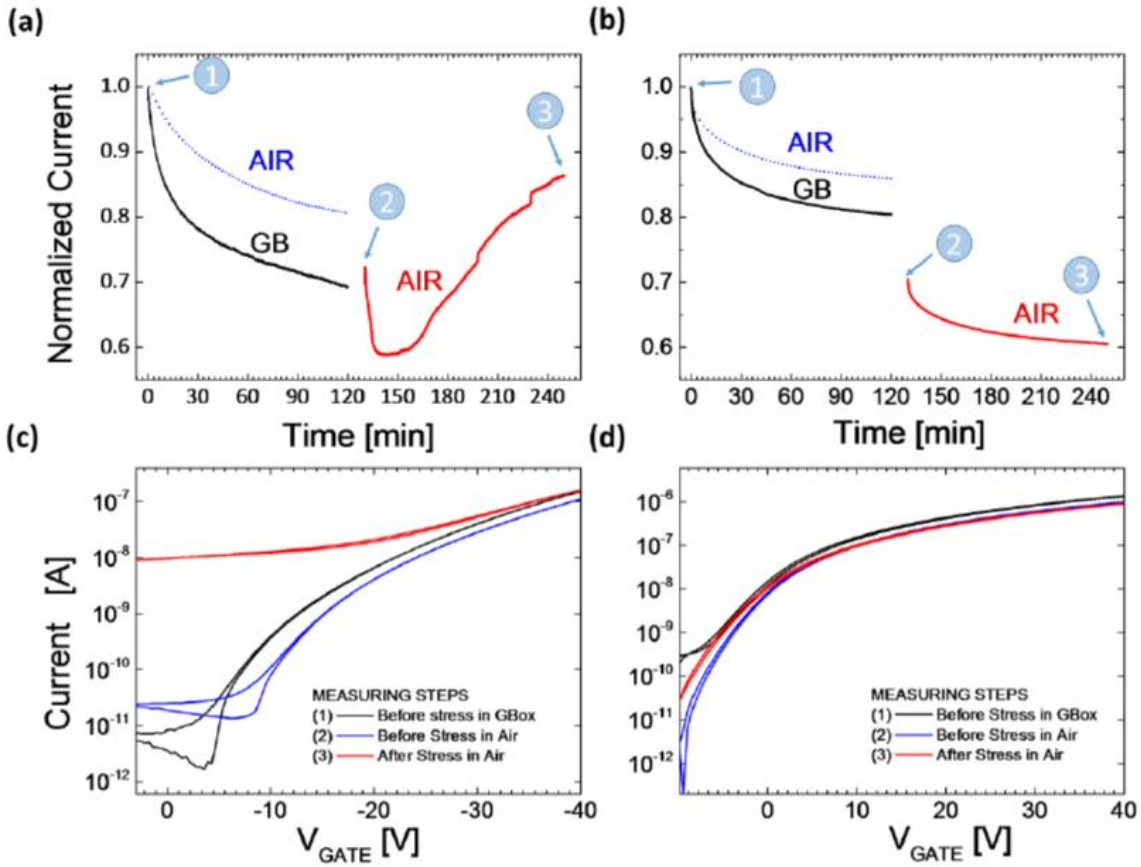

Fig. 4.17. Stress test of DPP ***27 (a)*** *and* ***PDI (b)*** *under nitrogen atmosphere (black tracer) followed by a sequential test in air (red tracer), blue tracer corresponds to a standard stress test in air. Output is a measurement of Drain-Source current every second for two hours with gate-source and drain-source voltages both equalling 40V.* ***(c)*** *and* ***(d)*** *are transfer curves taken before (black) in air (blue) and after the stress test in air (red) for* ***27*** *and* ***PDI*** *respectively.*

In general, we have observed that through the removal of electronically inactive solubilizing chains and the activation of H-bonding networks we can create dense films with close packing modes. In doing so, we improve the charge transport characteristics of small molecule FET's. Initially, only one p and n-type material were tested for this application (table 4.1). To extend this study a further three latent pigment materials were developed (Fig. 4.18). These new materials were designed with the principle idea that their synthesis would be facile and scalable (see appendix 2 experimental procedures). Dense conjugated cores with low levels of permanent solubilising chains were chosen to investigate this unique method of OFET fabrication.

	DPP 27	DPP 27	PDI
Mobility	μ_{hole} [cm^2/Vs]	$\mu_{electron}$ [cm^2/Vs]	$\mu_{electron}$ [cm^2/Vs]
Protected	$2x10^{-4}$	$4x10^{-4}$	10^{-7}
Deprotected in air	0.01	-	$4x10^{-4}$
Deprotected in Nitrogen	0.03	$4x10^{-5}$	-

Table 4.1 charge mobilities Hole/Electron for DPP27 and PDI

As a standard comparison an iso-indigo material **31** with standard solubilising chains was used to compare the effects of thermal annealing vs thermal deprotection to a second iso-indigo **32** with the same structure replacing solubilising chains with t-Boc.

A similar material to DPP **27** was developed removing the tertiary hexyl chains from the thipohene units to create a material that upon deprotection would have no insulating, solubilising chains contained within the structure **34**.

Finally, a further iso-indigo analogue **33** was designed with a replacement of t-Boc with an extended pyrocarbonate chain. Instead of producing two gases upon deprotection this long chain material is cleaved into a high boiling point solvent and CO_2. This high boiling point solvent has the possibility to create a stoichiometric solvent annealing process which may allow smoother rearrangement of the crystalline film. This longer chain also gives a much higher level of solubility to the semiconducting core.

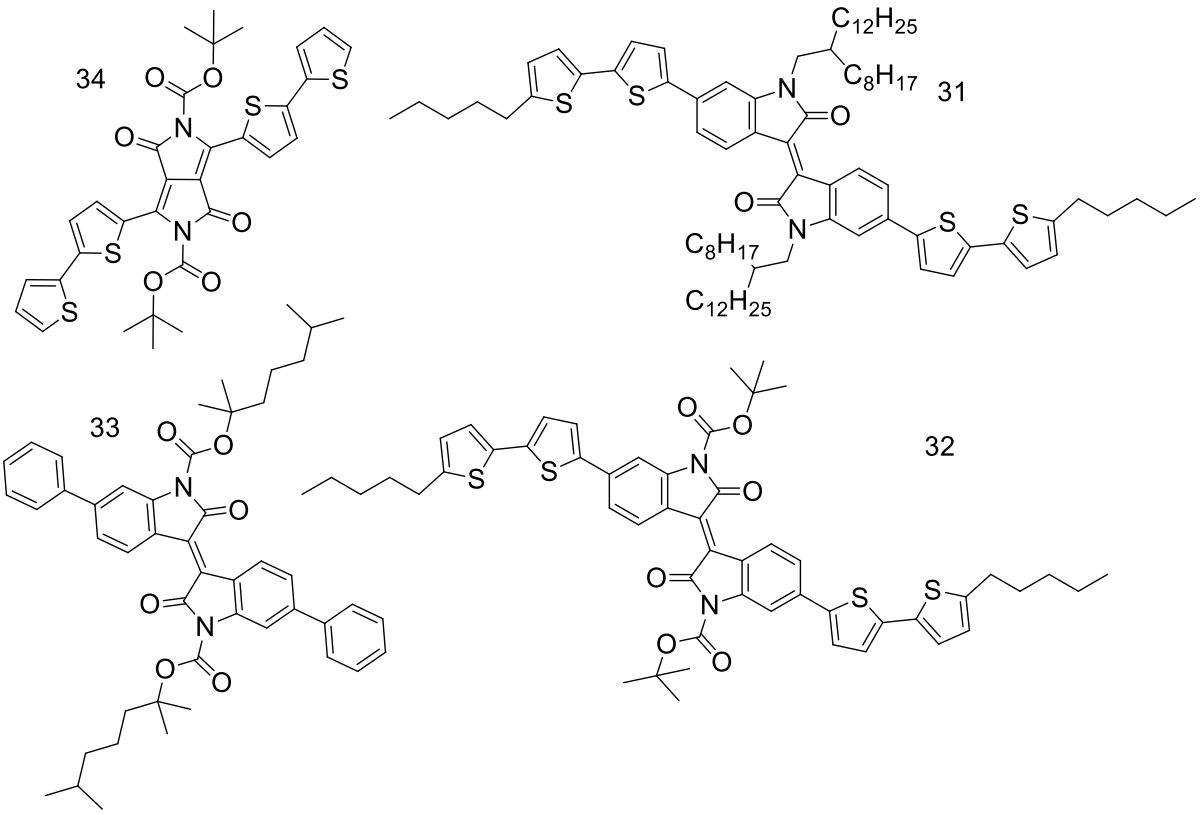

*Scheme 4.18. Molecular structure of materials used in OFET fabrication, top left **34**, Top right= **31**, bottom left= **33**, bottom right=**32***

From these four materials, the initial films were of good quality and appropriate thickness for OFET fabrication as measured by X-ray reflectivity experiments (see appendix 1 X-ray data). Issues arose throughout the thermal deprotection of these latent pigments. Both protected iso-indigo materials **32** and **33** underwent a sublimation process. The resulting films were very thin and un-homogeneous by visual inspection. Once dielectric was spun on top of the remaining materials areas of low thickness were filled forming pathways through the dielectric to the underlying contacts. In effect these two materials created pinholes for current to leak through and as a result the transfer curves were essentially unmeasurable. Extension of the conjugated core will, in the future, control this issue. It is also possible that a gentler deprotection (lower temperature for a longer period) may improve this issue. It was also observed that of the protected material remaining on the substrate, upon spincoating of PMMA, most of the material was washed free of the substrate. This is an unusual feature as the material should be insoluble in n-butyl acetate and PMMA. It is likely that we are observing a delamination effect. As seen by GIWAXS (Fig. 4.15.) these latent pigments become a very fine powder-like material upon deprotection. As the initial large crystals split and fragment it is acceptable to believe these materials break away from the substrate, which in turn leaves these materials susceptible to

being washed away by the force of a spin coated solution. This is also a reasonable explanation for why we have low performance in photovoltaic cells as the contact between photoactive material and the electrode is lower than expected.

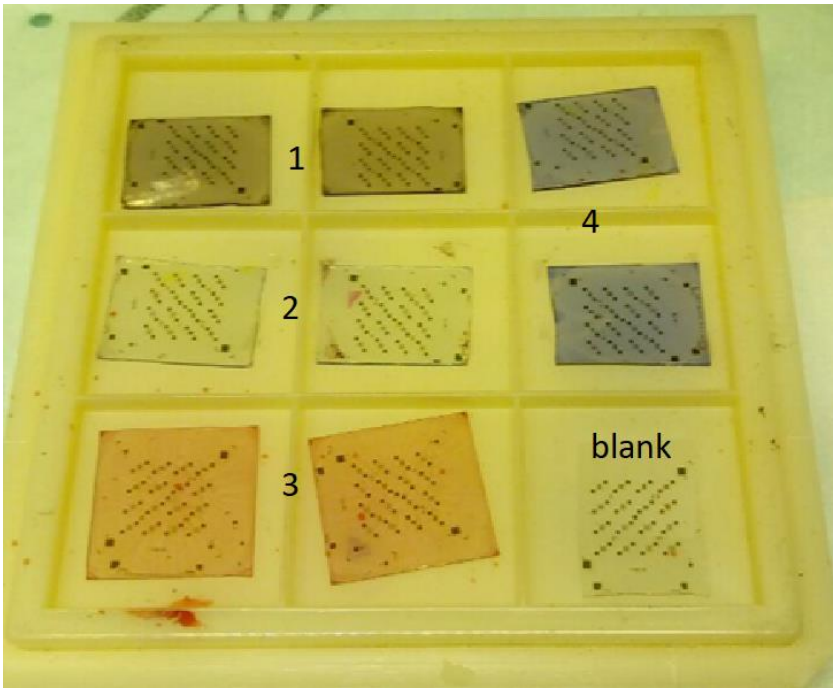

*Fig. 4.19. Transistors made in tandem with materials 1= **31** 2=**32** 3=**33** 4= **34***

Material **31** is an iso-indigo with extended branched chain structure. This material did not sublime in the manner of **31** and **32**. After thermal treatment the film looked unchanged by visual inspection to the sample cell which had not undergone 200°C annealing. Interestingly, as PMMA was spincoated onto these films the heat-treated sample was completely washed away. The thermally treated sample may have undergone polymorphic transition, or the thermal treatment may be detrimental to the binding of **31** to the surface of the substrate. This material exhibits a strongly ambipolar character, with the p-type channel being very noisy with a level of leak current occurring. The n-type channel is slightly smoother but lower performing with mobilities in the order of $\mu_{n,sat} \approx 10^{-5}$ $cm^2V^{-1}s^{-1}$ rather than $\mu_{p,sat} \approx 10^{-4}$ $cm^2V^{-1}s^{-1}$. These output curves (Fig. 4.20) are non ideal and are an example of a material with poor injection characteristics. These measurements were taken only in nitrogen atmosphere.

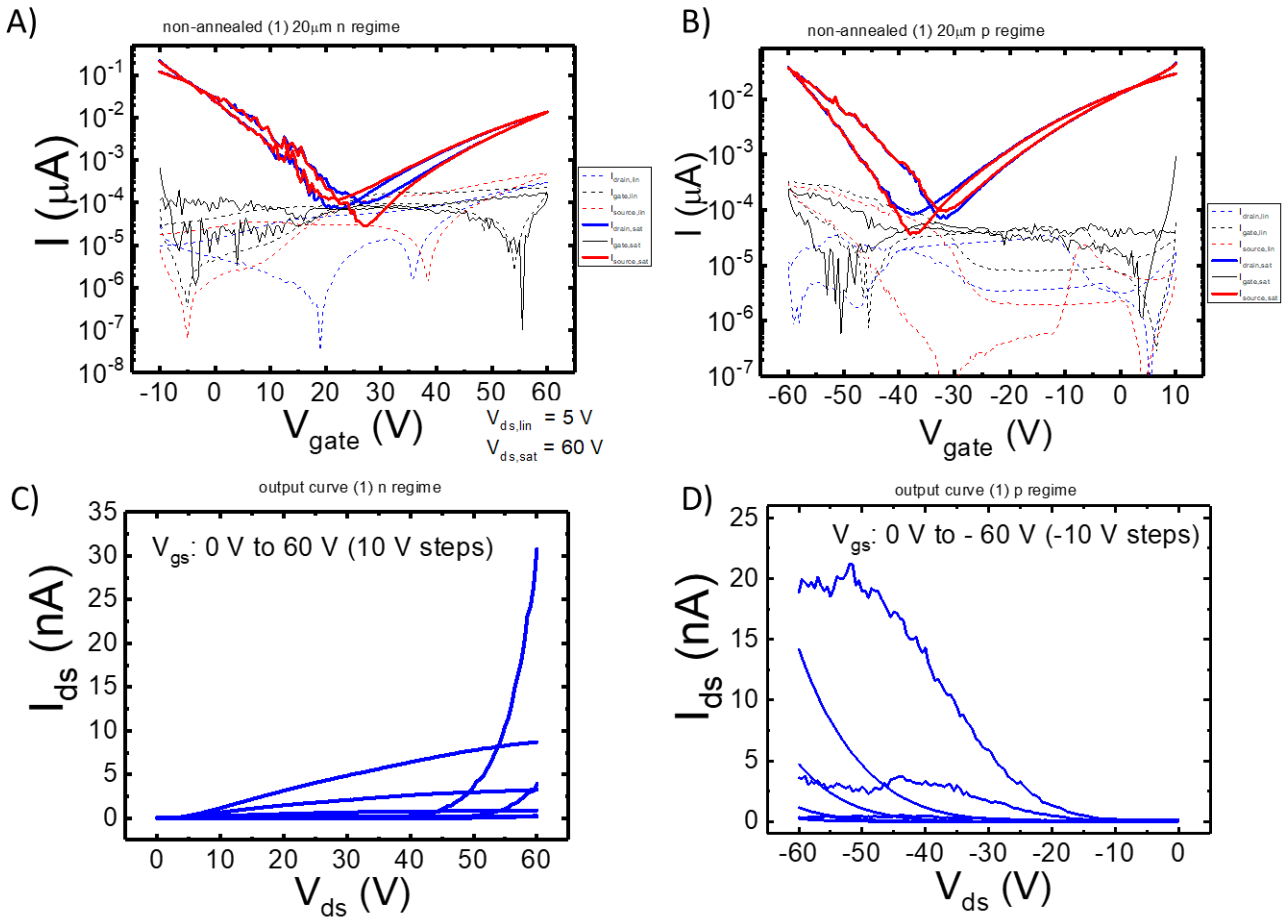

*Fig. 4.20. A) n channel transfer curve of pigment **31** measured in a nitrogen atmosphere B) p channel transfer curve of pigment **31** measured in nitrogen. C) n channel output curve D) p channel output curve*

DPP 34

In moving from a large length 20µm channel length to a small length 5µm channel we see a good improvement of current by the expected factor of 4. This indicates that the low current rates are not associated with contact resistance or poor frontier orbital level alignment with the contacts. This instead, indicates that the charge carrier mobility of this material is low.

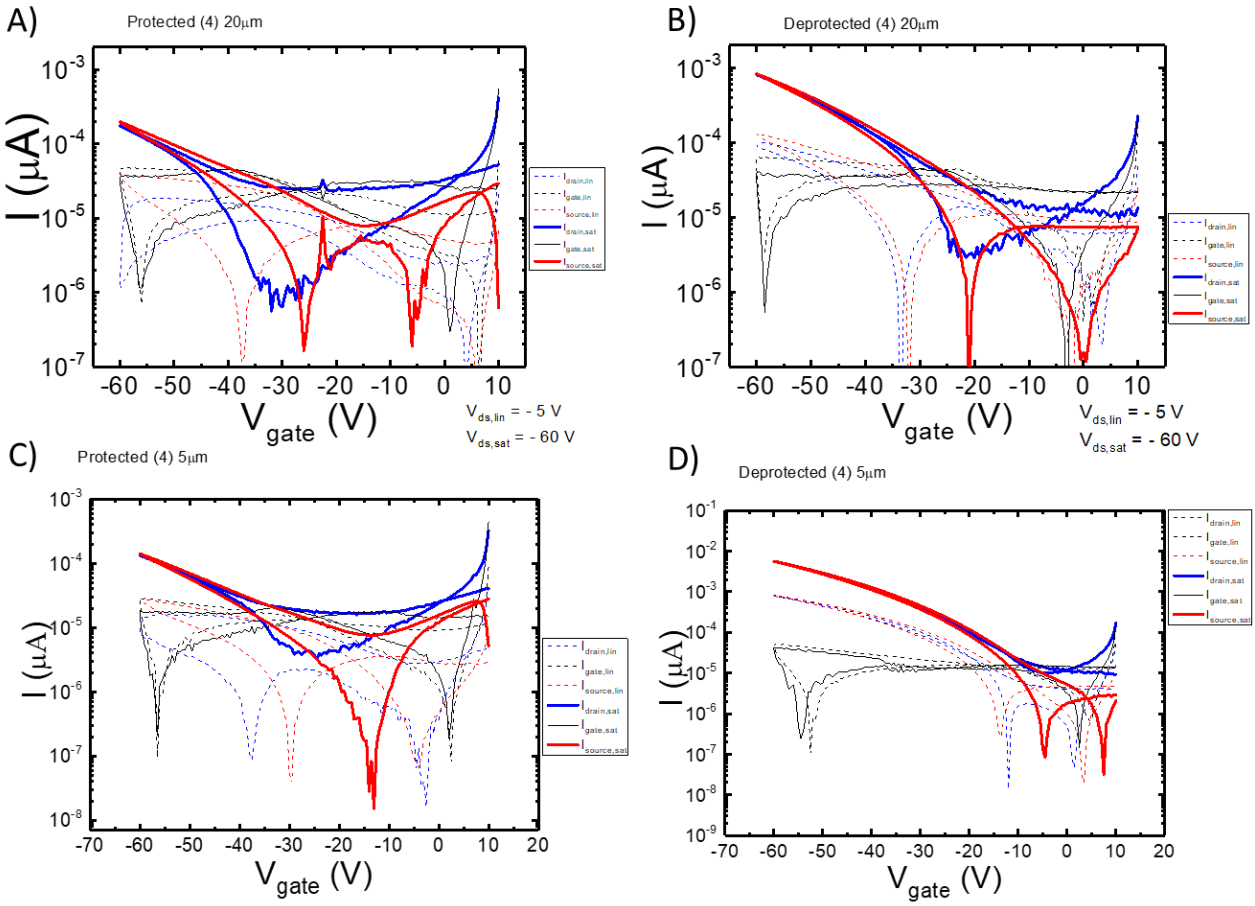

*Fig. 4.21. A) protected **34** 20µm length cell B) Deprotected **34** 20µm length cell C) Protected **34** 5µm length cell D) deprotected **34** 5µm length cell*

For these cells a strong hysteresis is seen as the voltage returns. Although these devices show a much lower mobility than the DPP **27** we can still see that the deprotecting results in an improvement in device performance of roughly an order of magnitude.

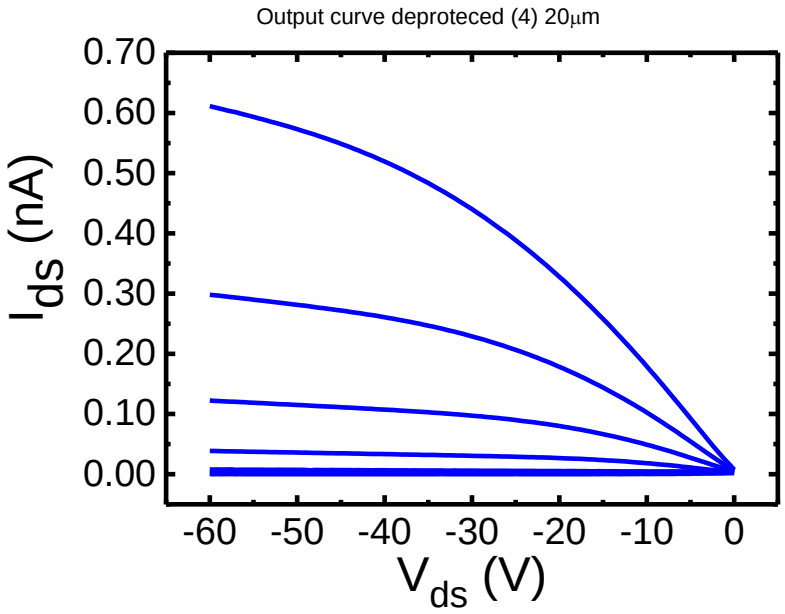

Fig.4.22. Output curve for deprotected ***34***

Conclusions

The increased density and high crystallinity of the activated pigment has now been recorded in three separate materials. Two p-type DPP materials and one n-type PDI were successfully fabricated into functioning devices. Further materials designed for this application underwent an unexpected sublimation at temperatures approaching the deprotection target of 200°C. A comparative device was fabricated from a branched chain iso-indigo, processing with similar temperatures resulted in delamination and a subsequent washing from the substrate upon addition of dielectric. Non-thermally treated samples remained on the substrate and showed strongly ambipolar character.

In conclusion, the latent pigment strategy has been successfully incorporated into OFET devices. The thermal cleavage results in improved mobilities for both p and n-type materials. The dense films and strong H-bonding networks result in stable devices which function in air and under inert conditions.

By elucidating the charge mobilities from these devices we can relate this study to the disappointing results found in the photovoltaic section of this thesis. The same materials DPP **27** and **34** were used in both BHJ and Bilayer devices. Low open circuit voltage and low short circuit current may perhaps be explained by the delaminating effect occurring during deprotection. Relatively large crystals break into small particulates leading to poor charge extraction/injection properties. Poor observed charge transport properties of the organic

semiconductor may be misleading. Further optimisation to the thermal cleaving process is required. A detailed study of the effective deprotection rate compared to crystal size and quality of ohmic contact could be particularly useful. The issues of this approach for fabricating organic optoelectronic devices in general, most likely arise from contact semiconductor interfaces and the low levels of film continuity that was seen in the photovoltaic chapter where PCBM can seep through channels formed in the fine powder-like films after deprotection. These issues are not necessarily associated with the principle idea of latent pigments but rather in the aggressive high temperature approach to cleaving these groups. Optimisation of this method can be easily achieved with a thorough study of the interfaces during cleavage and optimisation of the cleavage temperature for each individual material. The long chain pyrocarbonate solubilising material also has the potential to reduce these issue, this is a powerful solubilising unit that could see useful incorporation into latent pigment polymers in the future.

The FET device performances reported in this chapter are far from competitive with the most efficient materials seen in literature. Bearing that in mind, this method has shown its potential. A number of latent pigments have been incorporated successfully into FET devices acting as semiconductors. Upon removal of the protective t-Boc functionality an improvement in mobility was observed in all materials tested. A comparison has been made with a more standard molecular structure **31** which underwent a similar heat process. This heating test shows that it is possible that high temperature annealing could have a negative effect on contact quality. Never the less, deprotected materials are higher performing and have promising stability in both air and nitrogen atmospheres.

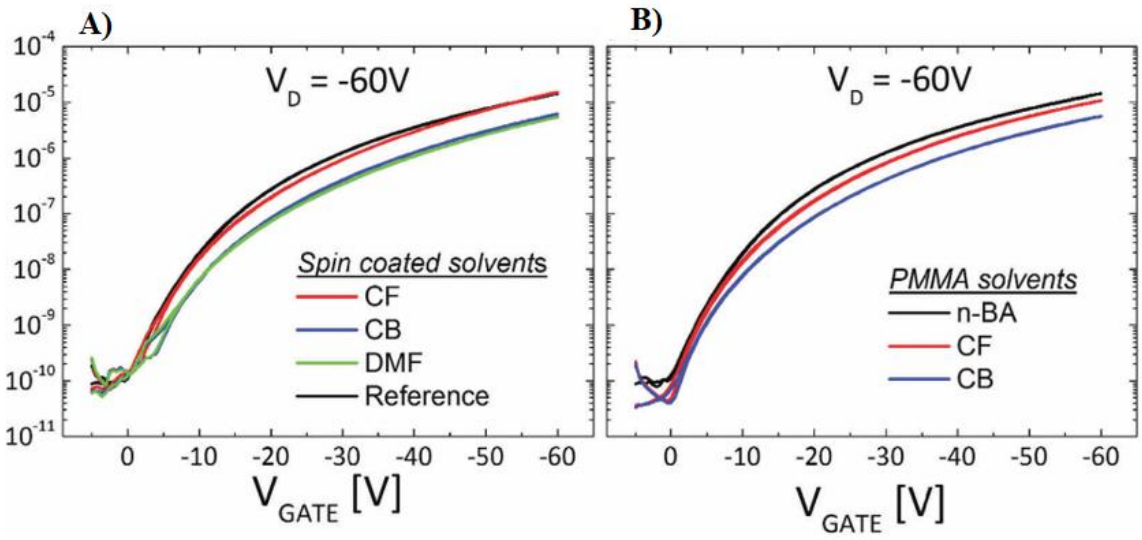

*Fig. 4.23. Device characteristics of latent pigment transistors A) deprotected DPP **27** device subject to subsequent spincoating of solvents chloroform, chlorobenzene and Dimethyformamide. B) Deprotected DPP **27** with subsequent deposition of dielectric from a variety of different solvents n-butyl acetate, chloroform and chlorobenzene.*

The Semiconductor layer is highly solvent resistant (as seen in Fig. 4.23) and allows a further degree of freedom to the device fabrication process. This method is a promising start to obtaining complex multilayer architectures which are not achievable by standard methods.

Very recently Yu Zhu et. al have released a work where three very simple latent pigment cores, including an isoindigo and a DPP material were integrated into a OFET device. Similar deprotection was carried out and studied. An increase of one to two orders of magnitude in charge carrier mobility was recorded for these materials. Thin films formed by solution processing resulted in the formation of microcrystals upon deprotection. This is concurrent with our results both in device characterisation and in x-ray analysis.[45]

References

1. http://www.computerhistory.org/atchm/who-invented-the-transistor/.

2. Caironi, M. & Noh, Y.-Y. *Large Area and Flexible electronics*. (2015).

3. Han, B., Li, J. & Liao, J. A New Highly Sensitive Sensor for Detecting Glucose Concentration. *Chem. Eng. Trans.* **46,** 313–318 (2015).

4. Torsi, L., Magliulo, M., Manoli, K. & Palazzo, G. Organic field-effect transistor sensors: a tutorial review. *Chem. Soc. Rev.* **42,** 8612–8628 (2013).

5. Zhang, C., Chen, P. & Hu, W. Organic field-effect transistor-based gas sensors. *Chem. Soc. Rev.* **44,** 2087–2107 (2015).

6. Edgar, L. J. Method and apparatus for controlling electric currents US1745175 A. (1930).

7. Koezuka, H. Field-effect Transistor for Polythiophene Thin Film. *Synth. Met.* **18,** 699–704 (1987).

8. Polythiophene Field-Effect Transistor : Its Characteristics and Operation Mechanism. *Synth. Met.* **25,** 11–23 (1988).

9. Lim, S. H., Zhou, Y., Su, H. & Ong, S. A stable solution-processed polymer semiconductor with record high-mobility for printed transistors. *Sci. Rep.* **2,** 1–10 (2012).

10. Cho, M. J. *et al.* Diketopyrrolopyrrole-based copolymers bearing highly pi-extended donating units and their thin-film transistors and photovoltaic cells. *Polym. Chem.* **6,** 150–159 (2015).

11. Kymissis, I. *Organic Field Effect Transistors: Theory, Fabrication and Characterization*. (2009).

12. Sirringhaus, B. H. Device Physics of Solution-Processed Organic Field-Effect Transistors. *Adv. Mater.* **17,** 2411–2425 (2005).

13. Natali, D. & Caironi, M. Charge Injection in Solution-Processed Organic Field-Effect Transistors : Physics , Models and Characterization Methods. *Adv. Mater.* **24,** 1357–1387 (2012).

14. Zaumseil, J. & Sirringhaus, H. Electron and Ambipolar Transport in Organic Field-Effect Transistors. *Chem. Rev.* **107,** 1296–1323 (2007).

15. Nan, G., Shi, Q. & Li, Z. Influences of molecular packing on the charge mobility of organic semiconductors : from quantum charge transfer rate theory beyond the first-order perturbation. *Phys. Chem. Chem. Phys.* **20,** 9736–9746 (2011).

16. Odajima, T., Ashizawa, M., Konosu, Y., Matsumoto, H. & Mori, T. The impact of molecular planarity on electronic devices in thienoisoindigo-based organic semiconductors. *J. Mater. Chem. C* **2,** 10455–10467 (2014).

17. Yoon, W. S. *et al.* High-Mobility n-Type Organic Transistors Based on a Crystallized Diketopyrrolopyrrole Derivative. *Adv. Funct. Mater.* **23,** 3519–3524 (2013).

18. Zhong, W. *et al.* High-Performance Organic Field-Effect Transistors Fabricated Based on a Novel Ternary π - Conjugated Copolymer. *ACS Appl. Mater. Interfaces* **9,** 7315–7321 (2017).

19. Shao, W., Dong, H. & Hu, W. Morphology control for high performance organic thin film transistors. *Chem. Sci.* **2,** 590–600 (2011).

20. Ling, H., Zhang, C., Chen, Y., Shao, Y. & Li, W. Engineering the mobility increment in pentacene-based field-effect transistors by fast cooling of polymeric modification layer. *J. Phys. D. Appl. Phys.* **50,** (2017).

21. Wang, Y. *et al.* Effect of the phenyl ring orientation in the polystyrene buffer layer on the performance of pentacene thin-film transistors. *Org. Electron.* **11,** 1066–1073 (2010).

22. Rao, I. V. K., Mandal, S. & Katiyar, M. Effect of pentacene deposition rate on device characteristics of top contact organic thin film transistors. *Proc. 14th Int. Work. Phys. Semicond. Devices* 1–3 (2007).

23. Guo, D., Ikeda, S. & Saiki, K. Effect of annealing on the mobility and morphology of thermally activated pentacene thin film transistors. *J. Appl. Phys.* **99,** 1–7 (2006).

24. Ruzgar, S. & Caglar, M. Use of bilayer gate insulator to increase the electrical performance of pentacene based transistor. *Synth. Met.* **232,** 46–51 (2017).

25. Biring, S. *et al.* The effect of gate dielectric deposition at different vacuum conditions on the field-effect mobility of pentacene based organic field effect transistors. *Thin Solid Films* **636,** 485–489 (2017).

26. Park, S. K. *et al.* High mobility solution processed 6,13-bis(triisopropyl-silylethynyl) pentacene organic thin film transistors. *Appl. Phys. Lett.* **91,** (2007).

27. Kim, J., Jeong, J., Cho, H. D., Lee, C. & Ong, S. All-solution-processed bottom gate organic thin-film transistor with improved subthreshold behaviour using functionalized pentacene active layer. *J. Phys. D. Appl. Phys.* **42,** (2009).

28. Li, H., Tee, B. C., Giri, G., Chung, J. W. & Lee, S. Y. High-Performance Transistors

and Complementary Inverters Based on Solution-Grown Aligned Organic Single Crystals. *Adv. Mater.* **24,** 2588–2591 (2012).

29. Takahashi, T., Takenobu, T., Takeya, J. & Iwasa, Y. Ambipolar organic field-effect transistors based on rubrene single crystals. *Appl. Phys. Lett.* **88,** (2006).

30. Takeya, J. *et al.* In-Crystal and Surface Charge Transport of Electric-Field-Induced Carriers in Organic Single-Crystal Semiconductors. *Phys. Rev. Lett.* **98,** 1–4 (2007).

31. Takeya, J. *et al.* Very high-mobility organic single-crystal transistors with in-crystal conduction channels. *Appl. Phys. Lett.* **90,** (2007).

32. Takimiya, K., Osaka, I., Mori, T. & Nakano, M. Organic Semiconductors Based on [1] Benzothieno [3,2-b][1] benzothiophene Substructure. *Acc. Chem. Res.* **47,** 1493–1502 (2014).

33. Takimiya, K. *et al.* 2,7-Diphenyl[1]benzothieno[3,2-b]benzothiophene, A New Organic Semiconductor for Air-Stable Field-Effect Transistors with Mobilities up to 2.0cm^2 V-1 s-1. *J. Am. Chem. Soc.* **128,** 12604–12605 (2006).

34. Nair, V. S. *et al.* Conjugated Random Donor −Acceptor Copolymers of [1]Benzothieno[3,2-b]benzothiophene and Diketopyrrolopyrrole Units for High Performance Polymeric Semiconductor Applications. *Macromolecules* **49,** 6334–6342 (2016).

35. Matsushima, T., Sandanayaka, A. S. D., Esaki, Y. & Adachi, C. Vacuum-and-solvent-free fabrication of organic semiconductor layers for field- effect transistors. *Sci. Rep.* 1–9 (2015).

36. He, D. *et al.* Two-dimensional quasi-freestanding molecular crystals for high-performance field-effect transistors. *Nat. Commun.* **5,** 1–7 (2014).

37. Wang, L. *et al.* A cyano-terminated dithienyldiketopyrrolopyrrole dimer as a solution processable ambipolar semiconductor under ambient conditions. *Chem. Comm* **49,** 11272–11274 (2013).

38. Lim, B., Sun, H., Lee, J. & Noh, Y. High Performance Solution Processed Organic Field Effect Transistors with Novel Diketopyrrolopyrrole-containing Small Molecules. *Sci. Rep.* **7,** 1–8 (2017).

39. Piliego, B. C. *et al.* High Electron Mobility and Ambient Stability in Solution-Processed Perylene-Based Organic Field-Effect Transistors. *Adv. Mater.* **21,** 1573–1576 (2009).

40. Singh, T. B., Erten, S. & Gu, S. Soluble derivatives of perylene and naphthalene diimide for n-channel organic field-effect transistors. *Org. Electron.* **7,** 480–489 (2006).

41. Mattiello, S., Sanzone, A., Brazzo, P., Sassi, M. & Beverina, L. First Demonstration of the Applicability of the Latent Pigment Approach to Plastic Luminescent Solar Concentrators. *EurJOC* 5723–5729 (2015).

42. Maqueira-albo, I. *et al.* Latent Pigments Strategy for Robust Active Layers in Solution-Processed, Complementary Organic Field-Effect Transistors. *J. Mater. Chem. C* (2017).

43. Apaydin, D. H., Głowacki, E. D. & Portenkirchner, E. Direct Electrochemical Capture and Release of Carbon Dioxide Using an Industrial Organic Pigment : Quinacridone. *Angew. Chemie - Int. Ed.* **53,** 6819–6822 (2014).

44. Suna, Y., Nishida, J., Fujisaki, Y. & Yamashita, Y. Ambipolar Behavior of Hydrogen-Bonded Diketopyrrolopyrrole- Thiophene Co-oligomers Formed from Their Soluble Precursors. *Org. Lett.* **14,** 3356–3359 (2012).

45. Zhang, H. *et al.* Crystalline Organic Pigment-Based Field-Effect Transistors. *App. Mater. and Interfaces* (2017).

Chapter 5-Green Chemistry Media and Micellar Synthesis

Introduction

Organic electronics claims to hold a number of unique benefits over their inorganic counterparts. Primarily, the cheap, facile accessibility of the organic materials used in these devices is regularly boasted. Synthetic organic methods lead to reliable and reproducible products for scalable production processes. The rapid and "low cost" nature of organic chemistry is quoted to outweigh the slow, time and energy consuming process of purifying and refining inorganic materials. Organic materials are often championed as the future of electronics in this way. Not to mention the benefit that organic materials are light weight and can be consolidated into flexible devices.

The reality is quite different to this biased review of organic materials. Yes, organic materials have the potential to be cheaper and more environmentally friendly than highly processed silicon. The fact is that the silicon industry is fully developed. Silicon devices whether they are transistors, photovoltaic cells or light emitting diodes are all fabricated in a mature industry setting. The devices are comparatively high performing and cheap for the average consumer. For organic materials to compete the realisation of novel forms of synthesis must be developed. Green chemistry must be developed so that environmentally and financially cheap processes can be established to produce tuneable organic materials.

The abundance of carbon based materials is of course a very attractive feature of organic materials. A bottleneck to upscaling of organic materials for electronics is that high performing materials do not necessarily have facile synthetic routes nor are they environmentally friendly simply by definition of being organic. One of the key areas of concern with large scale organic synthesis is the environmental impact of common organic solvents and reagents.[1]

Here we describe a green method for carrying out palladium catalysed C-C bond forming chemistries, such as Suzuki and Stille couplings in an aqueous, benchtop environment. Not only does this method drastically improve the environmental effects of our chemistry but also substantially lowers the cost of semiconductor production through the removal of solvent and the requirement for inert reaction conditions. Cost reduction is an important step required for the successful industrialisation of organic electronics.

Micellar couplings

Surfactants are surface active agents that reduce the surface tension of a liquid or interface. They are commonly found in detergents and are used industrially as drug excipients, cleaning agents and emulsifiers. Surfactants are amphiphilic, generally consists of two portions, a hydrophilic (head group) and a hydrophobic portion (tail group) (Fig. 5.1). The surfactants are classed into three groups based on the type of head groups used: anionic/cationic, non-ionic and amphoteric.[2]

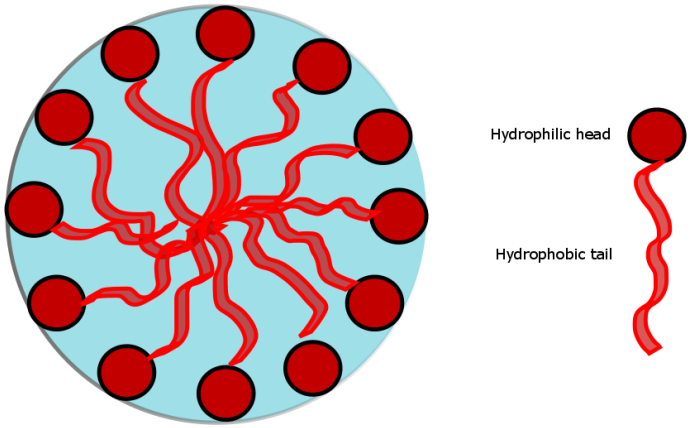

Fig. 5.1. schematic diagram of a micelle

High concentrations of surfactants in solution tend to form macrostructures called micelles. This formation is driven by the difference in hydrophobicity between the head and tail of a surfactant.[3,4] These structures breakdown the surface interaction at water /oil interfaces and help to solubilise hydrophobic components in aqueous suspensions. The water-insoluble materials in suspension are known to pass into the micelle as they tend to congregate in the hydrophobic portion of the micelle.[5] This concentrated hydrophobic core environment is a well-suited medium for performing organic chemistries. This reaction medium can be recycled, and often work up involves only a simple filtration. In turn we have shown that this technique can provide a method with comparable yields to standard synthetic techniques, in the case of Suzuki-Miyaura we can even show vastly improved yields with lower bi-product production.[6]

Abstract

We have investigated the common drug excipient and surfactant, Kolliphor El, as a new micellar medium to investigate palladium (Pd) catalysed cross coupling reactions. Initially a series of simple small molecule structures were tested as substrates for Suzuki-Miyaura couplings to optimise a procedure. This method was then applied to extending conjugation in

a series of complex organic semiconductors. For the fully optimised system a small aliquot of co-solvent is required. This establishes an emulsion based system which provides a highly efficient oxygen free medium for carrying out cross coupling chemistries with yields in excess of 80% within a 2 hour reaction time.

Results and discussion

Kolliphor El is a non-ionic surfactant consisting of polyethylene glycol ricinolate with a hydrophobic tail made from polyethylene glycol fatty acid esters and a hydrophilic head group consisting of polyethylene glycols and ethoxylated glycerol.

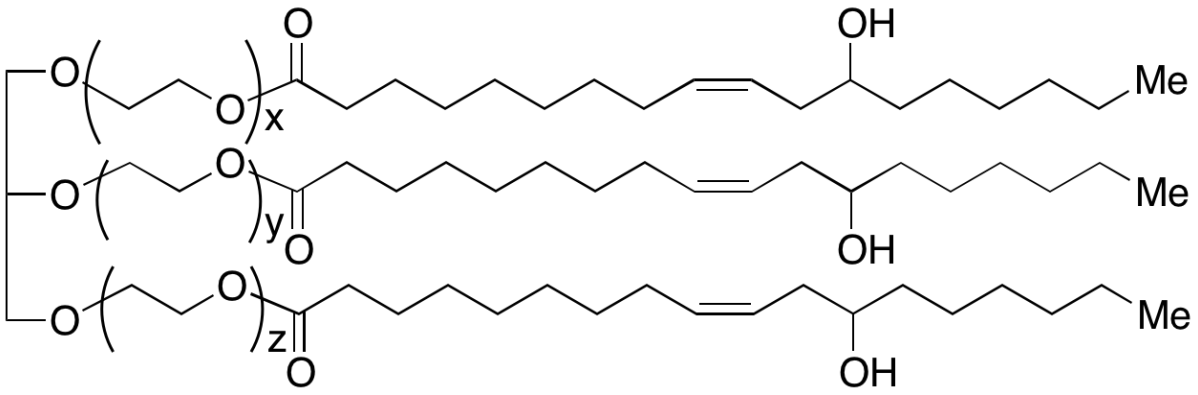

Fig. 5.2. General structure of polyoxyl castor oil, trade name Kolliphor EL[7]

The benefit we have found with Kolliphor El over other designer surfactants, such as the costlier Lipshutz groups surfactant TPGS-750-M, is that Kolliphor EL micelles appear to provide oxygen free core environments in the order of 7-9nm in diameter.[8] This results in a complete reduction of homocoupling bi-products (a common bi-product from standard procedures) in Suzuki-Miyaura reactions when performed in air.

Experimental

For this work to be directly comparable with other reported surfactants from literature we have used the standard accepted conditions for micellar couplings (room temperature, 2%wt surfactant solution in distilled water, 0.5M halide, 2%mol Pd catalyst with respect to halide and triethylamine acting as a base). The difference between our procedure and the respected literature methods is that we have performed all micellar couplings in air without degassing with nitrogen or inert atmospheres.

Range of synthesis

A comparative experiment was run with the coupling of 3-thiopheneboronic acid and 3-bromoquinoline (Fig. 5.3) with known high performance micellar forming surfactants TPGS-750-M [9] and Triton X-100.[10] It was seen that when the reaction was run in air, Kolliphor El outclassed both of these surfactants with high yields of 90%. TPGS-750-M and Triton X-100 had more modest yields of 69% and 68% respectively.

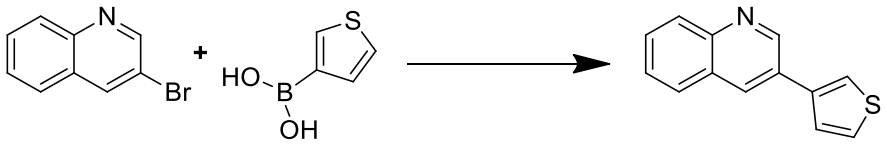

Fig. 5.3. Initial comparative reaction performed in an open benchtop vessel

Initially, this new method for open vessel benchtop coupling reactions was carried out on 1ml scale of 2% Kolliphor EL solution. A broad series of simple aryl bromides were coupled with aryl-boronic acids (in slight excess), using Pd(dtbpf)Cl_2 as a catalyst and 1.5 equivalents of triethylamine in respect to the bromide. This method proved to be very efficient resulting in high yields ~90%, with short reaction times of 2 hours or less (Fig.5.4).

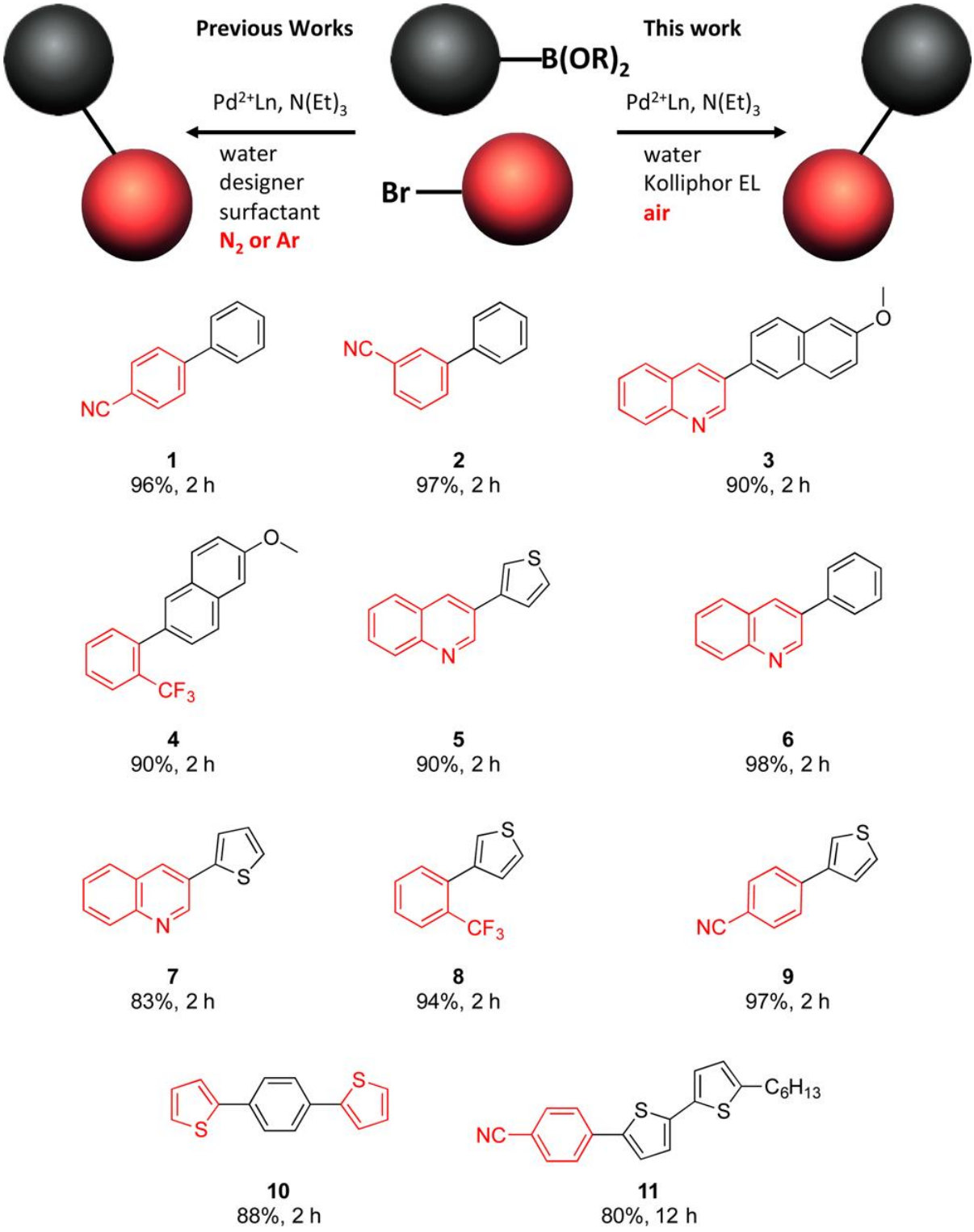

Fig. 5.4. Table of initial Suzuki-Miyaura cross coupling reactions carried out with 2% Kolliphor EL solutions as the reaction medium. Bromide materials are shown in black while relevant boronic substituents are shown in red. All yields were calculated after workup and purification after 2 hours of reaction time.

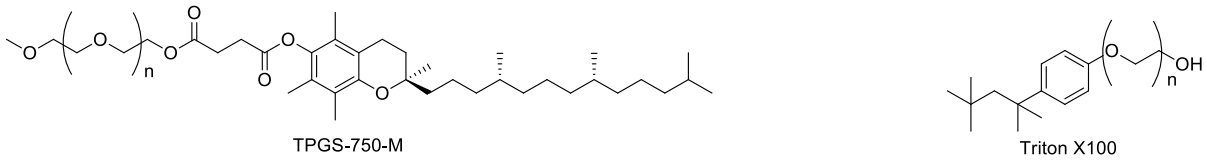

Fig. 5.5. Chemical structure of designer surfactants TPGS-750-M and Triton X100

The effect of oxygen on Suzuki-Miyaura cross couplings is substantial as reactions run with these designer surfactants under nitrogen atmosphere showed improved yields of 95% and 80% respectively. The high yield of the reaction run in TPGS-750-M shows that this is a very efficient designer surfactant well optimised for palladium cross couplings. The main point of difference in this study is that Kolliphor EL provides an efficient medium for performing these cross couplings regardless of atmosphere. Kolliphor EL reactions carried out in air and under inert conditions have identical reaction yields. It was also found that if the product of the coupling is crystalline it can be readily isolated by filtration. The filtrate can then be reused without the addition of fresh base or catalyst. In effect this method can be used as a recyclable medium for palladium cross couplings.

To investigate the theory that Kolliphor EL micelles create an oxygen free core several solutions of Tetrakis(triphenylphosphine)palladium(0) were prepared (Fig.5.6). This is an air sensitive palladium catalyst. 10mg of this catalyst was added with stirring to two separate vials, one containing 2% solutions of Kolliphor El and the other containing the same concentration of TPGS-750-M. The typical yellow colour of fresh Pd tertrakis is initially observed. It is seen that in after 24hours of stirring in Kolliphor EL in air the catalyst remains stable where as in the TPGS-750-M we see significant degradation of the catalyst due to the presence of oxygen. 6-methoxynaphthalene-2-boronic acid, 9-bromoanthracene, and $N(Et)_3$ were added to each solution after 24 hours. The reaction could be successfully carried out in the Kolliphor EL solution with high yields, whereas the TPGS-750-M solution showed negligible desired product formation by GC-MS which is consistent with the breakdown of catalyst.

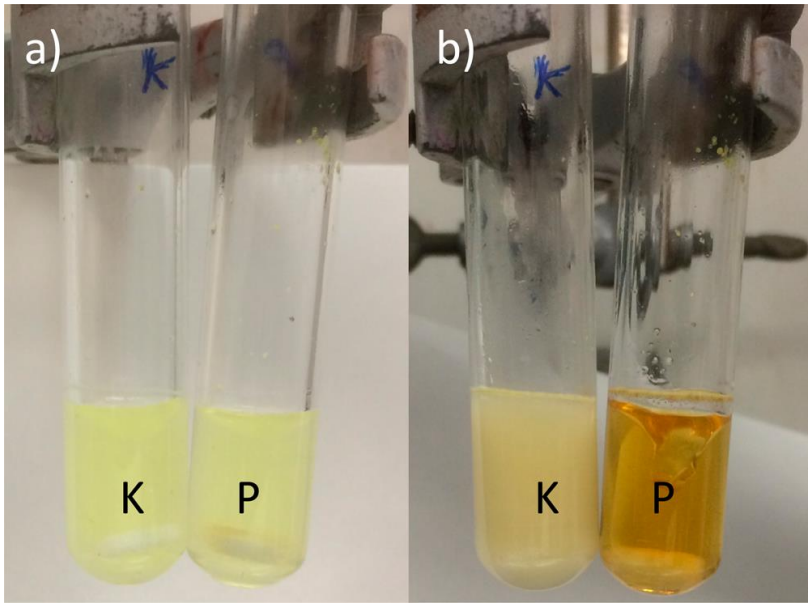

Fig. 5.6. K denotes Kolliphor solution, P denotes TPGS-750-M a) immediately after addition of Pd b) 24 hours past

Issues and limitations of technique

Reactions carried out on the simple small molecules above (see Fig. 5.4.) readily afford good yields. The late stage functionalisation of organic semiconductor materials for opto-electronics is often more complex. Limited solubility, poor miscibility and steric hindrance result in lower yielding reactions and longer reaction times with standard chemical approaches.

To fully test the capabilities of Kolliphor El, we have synthesised a large series of materials which have been recognised in literature to be high performance organic semiconductors. The Bromides tested in this case include diketopyrrolopyrroles, diarylbenzothiadiazoles, isoindigos, perylenediimides and 9,10-diarylanthracenes, all of which are common semiconducting cores for various devices.[11,12]

It was necessary to re-optimise our method due to the size and complexity of some of these materials. To do this we performed several reactions of varying concentration with respect to the semiconducting core bromides.

With several of these more crystalline starting materials a number of issues were revealed. The quality of the dispersion with crystalline materials can be very low, resulting in poor mixing with a magnetic stirring bar. High crystallinity with low density result in solid agglomerations resulting in no reagent entering the micelle. In some cases, changing shape of the reaction vessels was enough to reduce this agglomeration.

The main issue is the ability to stir these mixtures. It was thought that sonication of the mixture might prove to be an efficient method for mixing these sticky reaction mediums. Unfortunately, sonication of the reaction mixture resulted in the destruction of the micelles.

A more thorough stirring can be achieved by mechanical stirrer but the scale and volume of solvent limits this use.

The most successful manner to stir these mixtures was found to be a peristatic pump (Fig. 5.7). Solid reagents are added directly to tubing for this pump. An appropriate amount of Kolliphor EL solution is then added. The solution is pumped through the tubing due to pressure applied through a constrictive motor. This method offers a very efficient way to finely mix the resulting viscous mixture. The solid material is essentially milled and mixed simultaneously.

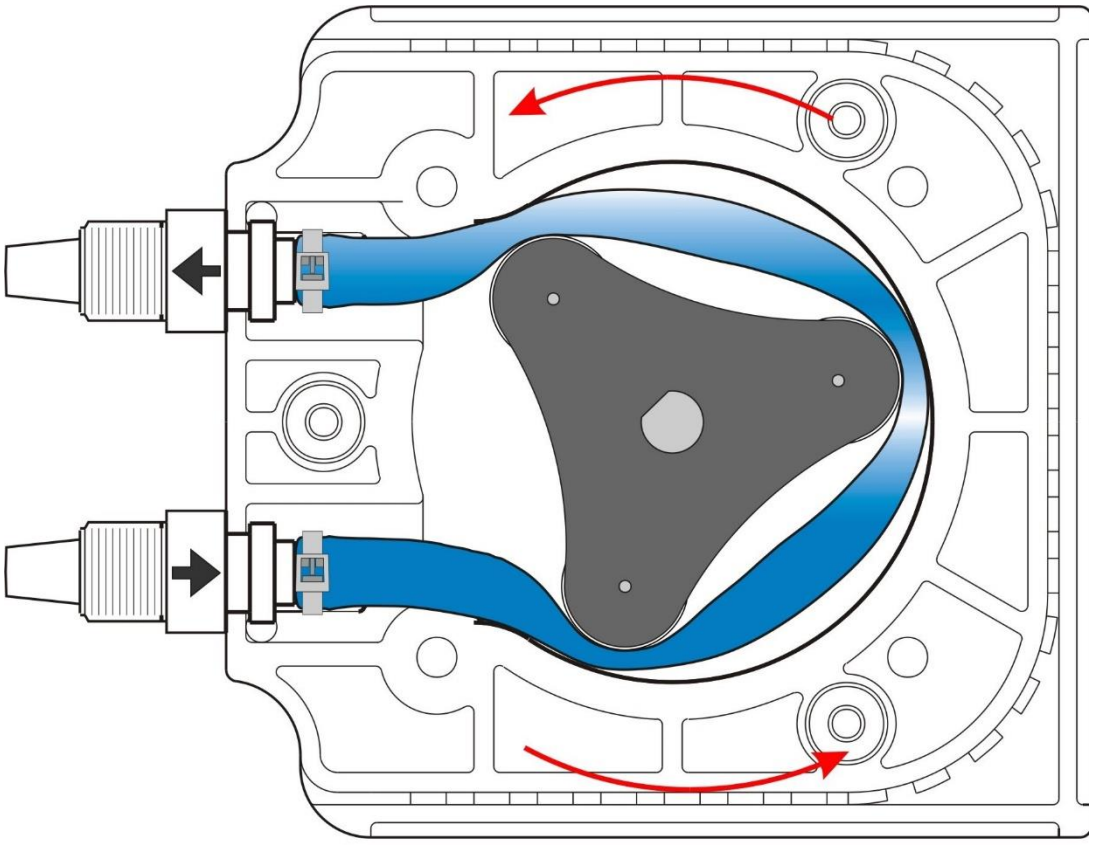

Fig. 5.7. Schematic diagram of peristatic pump.[13]

With these complex materials, we have found that higher yields can be achieved by increasing the concentration of the mixture. Kolliphor EL by itself forms two shells: one that is oxygenated (the outer core) and one that is oxygen free (inner core). When dilute samples are run, homocoupling products are seen to form. This would suggest that at weaker concentrations the micelles are not saturated; active materials are not forced into the interior core of the micelle but rather remain in the oxygenated outer core. We speculate that the diffusion of the boronic

acid from the polar un-oxygenated outer core into the inner core is concentration dependant. Furthermore, it is likely that the palladium catalyst and bromide, both of which are non-polar, have an affinity for the unoxygenated core. This explains the high stability of the system.

It should also be noted that in all cases, no mono-cross coupling product was recovered. This also indicated that we have a concentrated compartmentalised reaction. The mono-cross coupled product remains as a quite non-polar species. It is reasonable to believe that this material will remain in the micelle core until the second cross coupling process occurs. The now higher polarity product will be removed from the inner core allowing fresh unreacted material to enter the core.

Increasing the concentration of the micellar mixture to 1M of boronic acid results in a significant increase in yield and a reduction of homocoupling bi-products. This higher concentration mixture, of course, creates more difficulties in homogenisation of the mixture so a balance must be achieved.

Further issues were seen when using material functionalised with t-Boc and pyro-carbonate functionalities. Reactions with simple boronic acids proved unsuccessful. Originally, we postulated that the strongly electron withdrawing ester functionality may be binding to the active Pd centre of the catalyst.

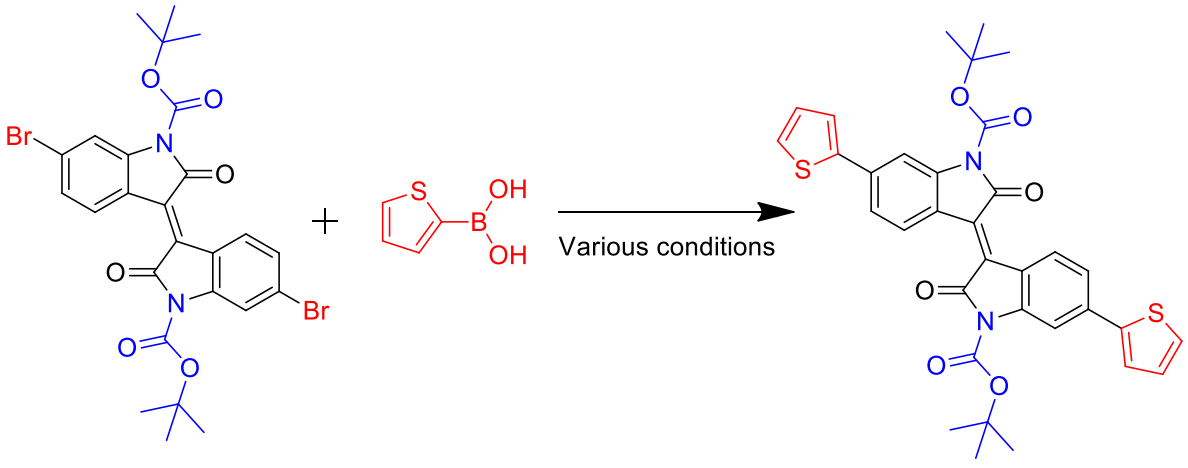

Fig. 5.8. Reaction od thiophene-2-boronic acid and t-Boc protected 6,6'-dibromoisoindigo used for screening reaction condition.

To test this hypothesis the cross coupling of a dibromo isoindigo with t-Boc protection on the lactamic nitrogen was examined (Fig. 5.8). Numerous catalysts and phosphines were screened to identify the most efficient non-coordinating catalyst (see table 5.1. below). The result of this test showed that no combination of Pd species and phosphine resulted in the desired product. This would suggest that a binding of t-Boc to a palladium centre is unlikely to be the cause of

stunted reactivity. Instead, we could rationalise that the issue is due to a reduced tendency of this functionality to enter the micelle.

N°	Medium	catalyst	Atm	Time/temperature	Yield
1	Kolliphor EL (2%)	$Pd(dppf)Cl_2$	air	24/r.t.	-
2	Kolliphor EL (2%)	$Pd(dtpbf)Cl_2$	air	12/r.t.	-
3	Kolliphor EL (10%)	$Pd(dtpbf)Cl_2$	air	12/r.t.	-
4	TPGS-750-M (2%)	$Pd(dtpbf)Cl_2$	N_2	12/r.t.	-
5	TPGS-750-M (2%)	$Pd(dtpbf)Cl_2$	N_2	12/r.t.	-
6	Kolliphor EL (2%)	$Pd(AcO)_2$/ CyJohnphos	air	24/r.t.	-
7	Kolliphor EL (2%)	$Pd_2(dba)_3$/ri(o-tolyl)phosphone	N_2	24/r.t.	-
8	Kolliphor EL (2%)	$Pd_2(dba)_3$/dppf	air	24/r.t.	-
9	Kolliphor EL (2%)	$Pd_2(dba)_3$/Tris(2-methoxyphenyl) phonsphine	N_2	24/r.t.	-
10	Kolliphor EL (2%)	$Pd_2(dba)_3$/XPhos	N_2	24/r.t.	-
11	Kolliphor EL (2%)	$Pd_2(dba)_3$/CyJohnphos	N_2	24/r.t.	-
12	Kolliphor EL (2%)/toluene 9:1 (vol)	$Pd(dtpbf)Cl_2$	air	1/60°C	80%
13	Kolliphor EL (2%)/THF 9:1 (vol)	$Pd(dtpbf)Cl_2$	air	2/60°C	38 %
14	Kolliphor EL (2%)/acetone 9:1 (vol)	$Pd(dtpbf)Cl_2$	air	2/60°C	42 %

Table 5.1.Table of attempted reaction conditions for the cross coupling of thiophene-2-boronic acid and t-Boc protected 6,6'-dibromoisoindigo.

A more in-depth examination of the hydrophilic-lipophilic balance (HLB) value would indicate that perhaps this functionality is not well suited for diffusion through Kolliphor El'a outer micelle core. The HLB value of the Kolliphor EL micelle solutions can be adjusted with the addition of organic co-solvent which also helps to swells the micelles.[14]

Co-solvent/ emulsion method

Issues arising from the use of highly crystalline materials or highly polar materials restricts the use of this green chemistry method. The use of co-solvents in micellar systems has been documented to improve the versatility of this approach. It has been reported that 5-20% of a water miscible organic solvent such as acetone or tetrahydrofuran (THF) can help improve reaction rates and yields. Small quantities of co-solvent can stabilise the suspension and reduce the influence of agglomeration which inhibits mixing.

An addition of ten percent of co-solvent can be added to a micellar solution to swell the micelle cores of Kolliphor El. This allows efficient C-C coupling to occur with materials that have slow transition rates through the micelle shells. [14]

Initially, when incorporating a co-solvent into the Kolliphor EL micelle, trace quantities of mono-cross coupling product were observed. This leads us to speculate that this reaction may go through a completely different mechanism of entry into the hydrophobic core of the micelle when co-solvent is present as no mono-cross coupling product could be isolated from standard 2% surfactant reactions.

The trace mono cross coupling product could be explained by a reduced surface tension between phases when the micelle core is swollen. This would reduce the energetic barrier for the more polar mono-cross coupling products to leave the inner micelle core. The reactions in which mono-cross coupling products were isolated the reaction reaches an equilibrium point where addition of excess boronic acid does not result in further reaction processes.

By increasing the concentration of Kolliphor EL in water from 2% to 10% and 20% we can observe dynamic changes to the mean micelle diameter using dynamic light scattering techniques. The results of these experiments indicate that the micelle size has very little dependence on Kolliphor EL concentration once the critical concentration for forming these micelles has been achieved. Average diameter of micelle increases from 11.17nm for 10% (Fig.5.9) concentrations to 12.73nm for 20% (Fig.5.10) concentrations of Kolliphor EL in purified water. For higher concentrations there is a higher standard deviation in the micelle size

but generally the system has a stable average micelle size between 10-15nm over a concentration range of 2-20%.

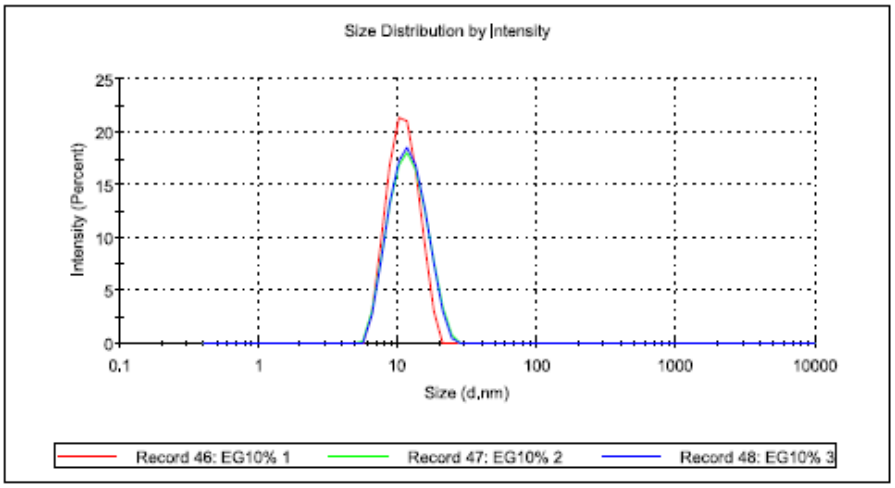

Z-Average (d. nm)	Peak 1 Size (d. nm)	Peak 1 std. deviation (d. nm)	Temperature	Duration (s)
10.85	11.17	2.733	25°C	80

Fig. 5.9. Dynamic light scattering measurement of a Kolliphor EL 10% solution

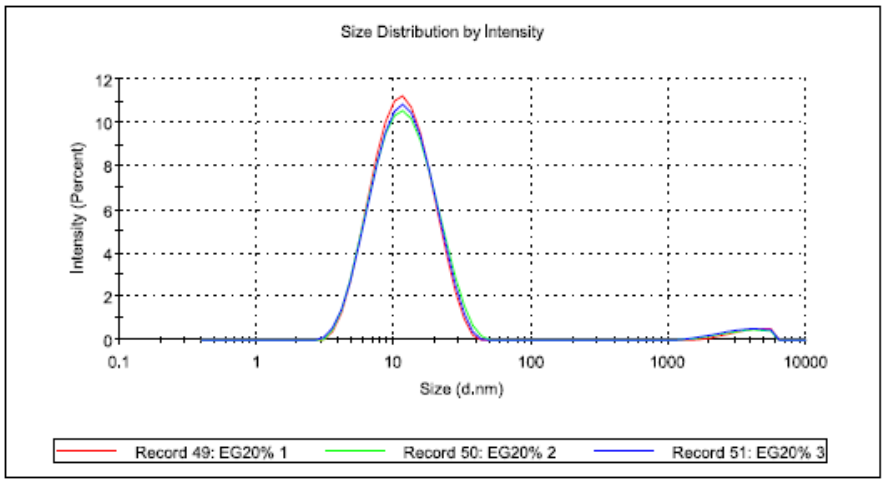

Z-Average (d. nm)	Peak 1 Size (d. nm)	Peak 1 std. deviation (d. nm)	Temperature	Duration (s)
10.76	12.73	6.055	25°C	80

Fig. 5.10. Dynamic light scattering measurement of a Kolliphor EL 20% solution

It has been previously stated by Lipshutz et. al that introduction of a co-solvent results in the swelling of micelles. This is indeed the case in Kolliphor EL when acetone or THF are used as co-solvent (as seen in Fig. 5.11. below). A small increase in average micelle diameter is observed. However, the use of toluene as a Co-solvent in a 9:1 ratio, Kolliphor EL 2%: toluene, creates a unique environment which behaves in an entirely different manner to instances previously reported in literature.

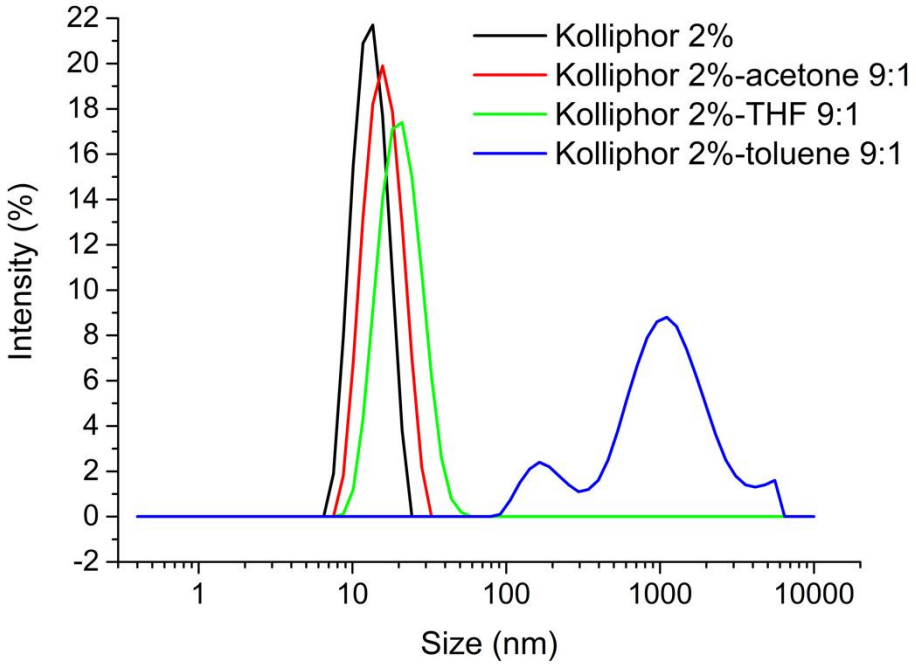

Fig. 5.11. DLS spectra of Kolliphor EL 2 % by weight in water (black) and of the corresponding 10 % by volume mixtures with acetone (red), THF (green) and toluene (blue).

Dynamic light scattering measurements of Kolliphor EL 2%, 10% toluene solutions indicate that the average particle size in solution has increased to 1016nm. There is no evidence of micelle size particles remaining in this solution. It appears that the addition of toluene as 10% co-solvent results in an emulsion which is thermodynamically stable for an extended period of time.

The formation of this emulsion has a profound effect on the cross-coupling chemistries involved. Without co-solvent, we appear to have a strong interaction between t-Boc protecting groups and the micelle. This interaction completely limits the use of micellar chemistry for latent pigments protected with t-Boc or similar analogues. When we introduce toluene as a co-

solvent we no longer observe this inhibition of t-Boc protected materials. In fact, with the implementation of toluene as a co-solvent we observe increased reaction rates for standard cross-coupling reactions and a broader scope in reaction substrates which allows for the incorporation of the t-Boc protected latent pigments.

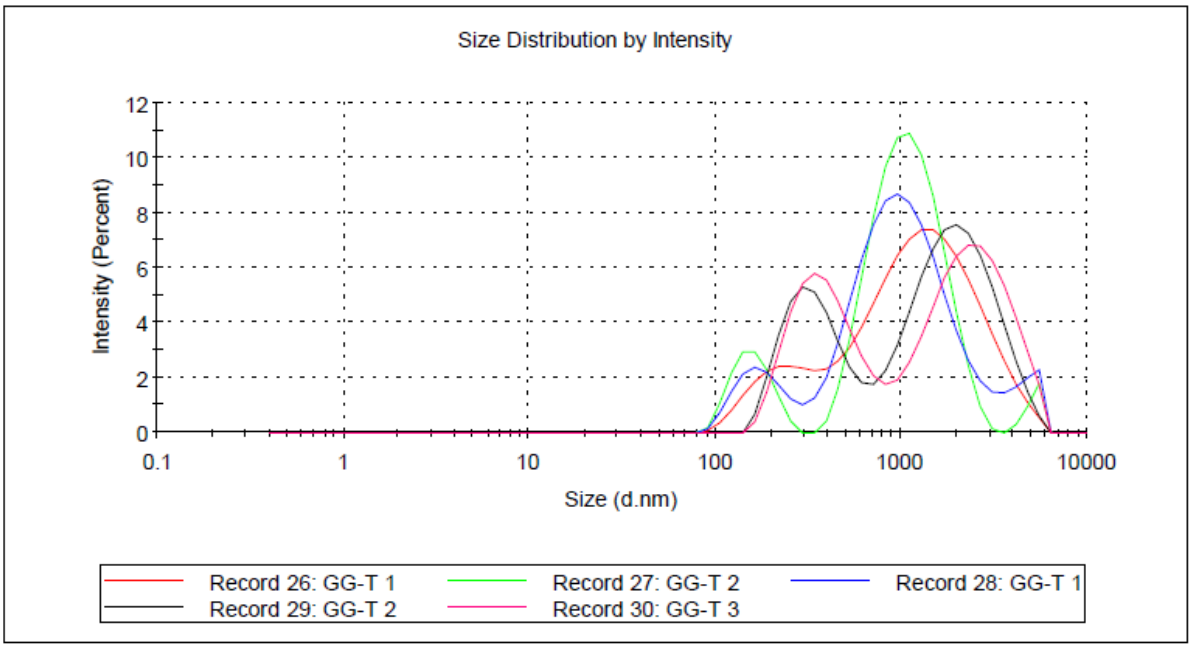

Z-Average (d. nm)	Peak 1 Size (d. nm)	Peak 1 std. deviation (d. nm)	Peak 2 size (d. nm)	Peak 2 std. deviation (d. nm)
705.1	*1576*	*1016*	*227.9*	*69.98*

Fig. 5.12. Kolliphor 2% toluene 10% DLS data

A speculative reasoning for this increased reactivity is that in a micellar system, the rate of the reaction is limited somewhat to the diffusion rate of the semiconducting core across the micelles outer membrane. In the case of the emulsions it is reasonable to believe that the rate is not limited in this manner. Large emulsion barriers with low surface tension will internalise the semiconductor core at a high rate, resulting in a high concentration of semiconductor into the hydrophobic regions of this diverse reaction media. The lower surface tension reduces the diffusion barrier resulting in a rapid reaction rate. One curiosity of this system is the ability to retain an oxygen free reaction environment in an emulsion state. All reactions were run with standard bench top solvents, no removal of oxygen or water was carried out before use. Toluene, which has good oxygen solubility, can be used to carry out efficient Suzuki-Miyaura cross couplings with no formation of homo-products. This indicates that Kolliphor EL may

have a unique mechanism for the segregation of oxygen from the hydrophobic portion of the surfactant.

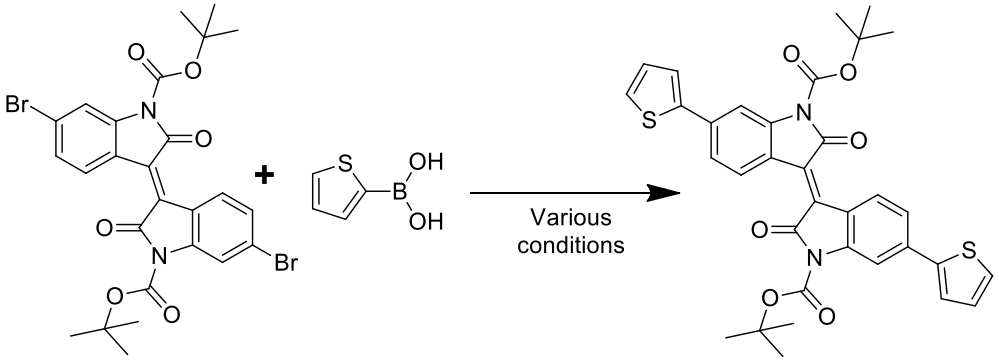

n°	medium	catalyst	atm.	time, h/temperature, °C	yield
1	Kolliphor EL /acetone 9:1	$Pd(dtbpf)Cl_2$	Air	2/60	**42**
2	Kolliphor EL /acetone 9:1	$Pd(dtbpf)Cl_2$	N_2	2/60	**40**
3	Kolliphor EL /THF 9:1	$Pd(dtbpf)Cl_2$	Air	2/60	**38**
4	Kolliphor EL /THF 9:1	$Pd(dtbpf)Cl_2$	N_2	2/60	**39**
5	Kolliphor EL /toluene 9:1	$Pd(dtbpf)Cl_2$	Air	1/60	**80**
6	Kolliphor EL /toluene 9:1	$Pd(dtbpf)Cl_2$	N_2	1/60	**79**

Fig. 5.13. Optimisation table of co-solvent with relating yields for cross coupling of thiophene-2-boronic acid and t-Boc protected 6,6'-dibromoisoindigo.

Emulsions are metastable dispersions of one immiscible liquid in another. Surfactants such as Kolliphor EL can act as emulsifiers. The addition of a co-solvent to a surfactant solution propagates a biphasic emulsion which is separated by Kolliphor EL.

In an emulsion the reaction medium is biphasic, the surfactant constitutes the separation layer between phases. In a micellar approach the inner core of the surfactant formed micelle acts as the reactive medium. This is not the case for emulsion based chemistries. Emulsions have a large reactive medium separated from the oxygenated atmosphere by a surfactant bi-layer.

The reduced bromide concentration (due to the relatively larger reactive environment volume) within this oxygen free area of the emulsion results in a higher tendency for mono cross coupling to occur over the standard micelle approach.

Still with this co-solvent approach we see no homo coupling products, indicating that the system still operates through an oxygen free mechanism. The appearance of the Kolliphor EL solution when 10% co-solvent is added is that of an emulsion. A cloudy white, opaque solution which remains stable for an extended period of time. Emulsions are generally observed as cloudy white dispersions. Light is evenly scattered at the interphases of the two liquids components of the emulsion. This light scattering effect is not seen in micelle dispersions due to the small diameter of the micelles. This micelle solution of Kolliphor EL 2% in water gives a clear solution. There is a strong dependence on the concentration of co-solvent on the particle size of these dispersions[15]

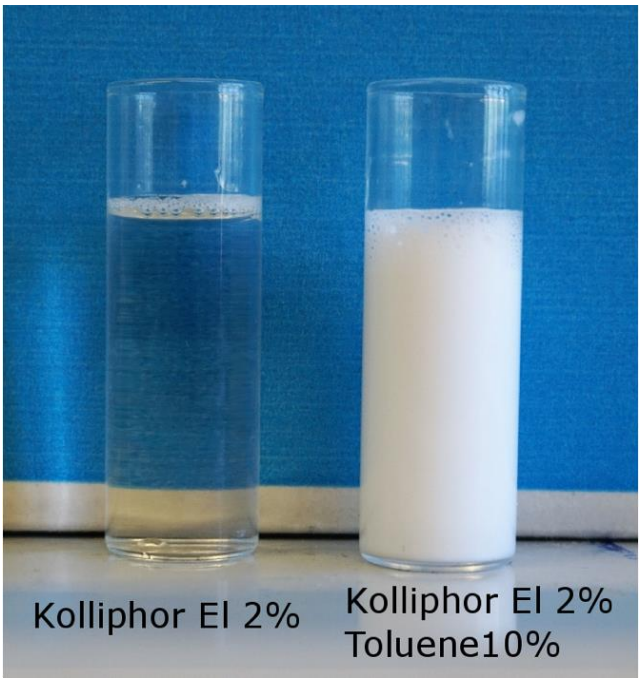

Fig. 5.14. Left) Kolliphor EL 2%. Right) Kolliphor 2% 9:1 water: toluene solution

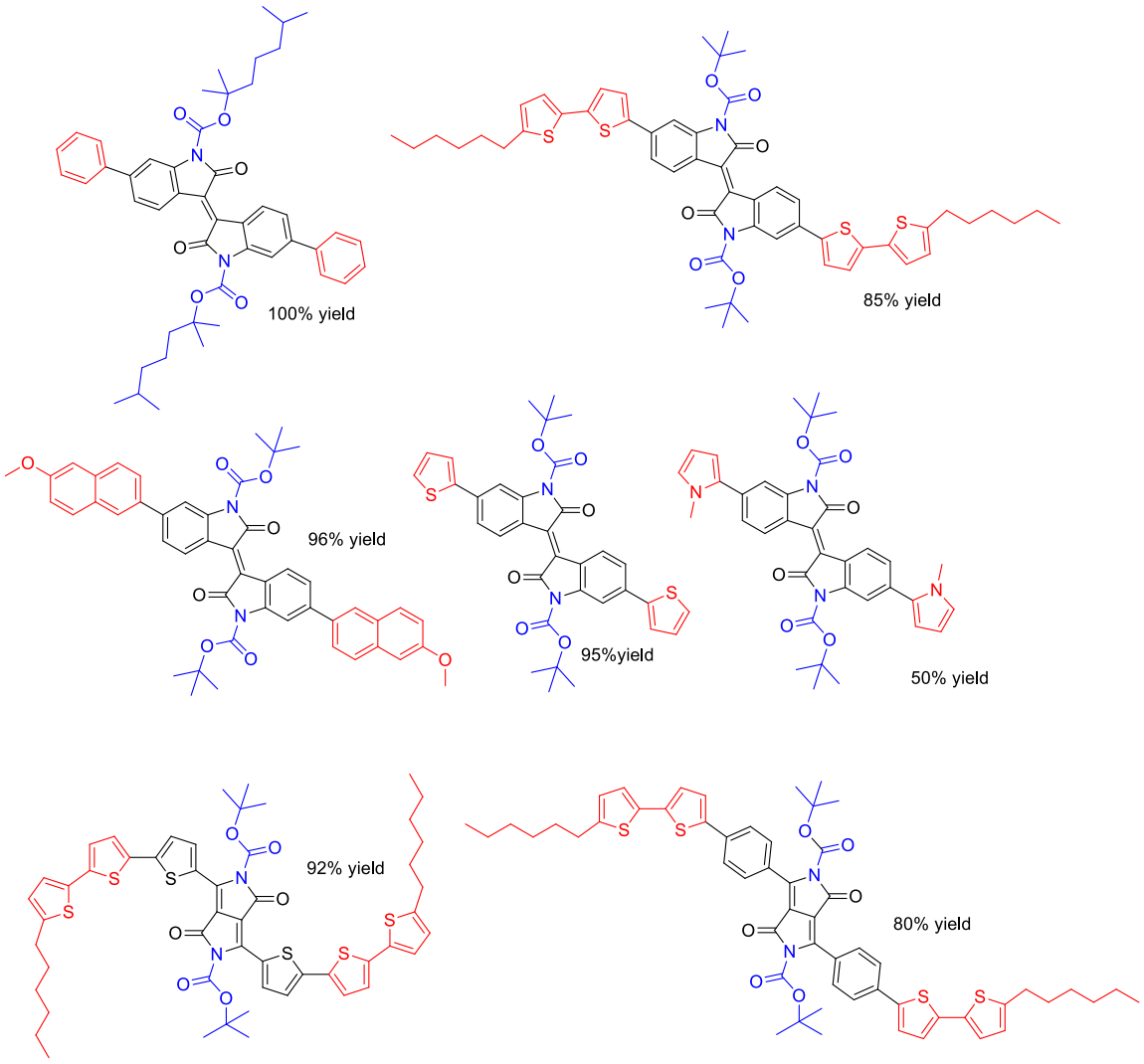

Fig.5.15. A variety of latent pigments were successfully prepared by the emulsion technique, the structures and yields are reported above. Protection group is seen in blue, the semiconducting core in black and the boronic substituent in red.

Reported yields for standard synthetic approaches are in the order of 25-30% for Suzuki-Miyaura cross couplings involving t-Boc protected semiconducting cores.[16] We have seen comparable yields in our own attempts with standard conditions. However, after extensive optimisation the power of the co-solvent micellar couplings can be seen. Reaction yields in the order of 80-95% can be achieved for the same reactive species used in standard approaches.

The optimized system for micellar couplings consists of 1ml of a 9:1 mixture by volume of 2 % by weight Kolliphor EL solution in deionized water and toluene. 0.5mmol of aryldibromide, 1.5mmol of desired arylboronic acid, 3 mmol of $N(Et)_3$ base and 0.03mmol Pd(dtbpf)Cl with vigorous stirring at 60°C in ambient atmosphere. The average reaction time for the materials in Fig. 5.15. above was 2 hours.

Conclusion

Kolliphor EL a cheap, commercially available drug excipient has been used as a surfactant to create a novel micellar reaction medium.

This surfactant creates a highly efficient medium for C-C bond forming chemistries which are essential for the functionalisation of common semiconducting cores. In a comparative study with the state of the art designer surfactants, TPGS-750-M and Triton x100, Kolliphor EL outperforms both in terms of effective reaction yield while equalling their selectivity for the desired cross-coupling products

Furthermore, the unique ability of Kolliphor EL to provide an oxygen free reaction environment even in an open reaction vessel in air sets this surfactant apart from the top of the line designer surfactants. Possibly attributed to reactivity of oxygen with a double bond in the structure of polyoxyl castor oil which is a main component of Kolliphor EL.

Kolliphor EL accommodates a broad variety of molecular structures as a reactive medium. One exception was discovered when attempts to perform Suzuki-Miyaura cross couplings on semiconducting cores functionalised with tert-butyloxycarbonyl protecting groups resulted in deprotection or no reaction.

It is speculated that this particular chemical functionality did not diffuse across the micelles outer core. Lead by research previously carried out on designer surfactants the addition of a variety of co-solvents was carried out in an attempt to understand if swelling the micelles inner core could aid in diffusing t-Boc protected materials into the reactive environment of the inner micelle core.

The addition of 10% THF and acetone co-solvent had the desired effect of swelling the micelle core and indeed successful formation of t-Boc protected cross-coupling products was achieved for these systems, albeit in low yields 40-45%.

The addition of 10% of toluene as co-solvent however resulted in an entirely unique reaction medium. This addition resulted in the formation of a long-lasting emulsion. In comparison to swollen micelles the bi-phasic emulsion has a much larger particulate size. Materials were observed to have high transition rates across the phases, observed as a high reaction rate compared to standard conditions. Interestingly no homo-coupling products were observed in the reactions carried out in emulsion. This indicates that there is a very low concentration of oxygen in the region where the coupling reaction is carried out which reinforces the idea that

Kolliphor has a mechanism for reacting with dissolved oxygen rather than and seclusion process by the formed micelles. This unusual phenomenon is still unexplained and disserves further study.

Facile access to organic semiconductor materials in an open benchtop manner could prove very useful in the field of organic electronics. Oftentimes material costs and environmental risks associated with synthetic procedures limits the access of the marketplace.

The emulsion based media outlined here provides a comparatively Green method for production of a versatile array of organic semiconductors. This method is entirely scalable, the possibility to carry out these complex C-C bond forming reactions in air in a very cheap and available solvent (water) is extremely valuable for industrial applications. Kolliphor El is a cheap and commercially available surfactant. Micelle and emulsion based chemistry is not restricted to Suzuki-Miyaura reactions, the robust environment provided by Kolliphor micelles is ideal for performing reactions such as Stille couplings, Buchwald–Hartwig, Heck and Sonogashira to name but a few.

References

1. Roy, W. R. Environmental Impact of Solvents. *Illinois state Geol. Surv.* (1990).
2. Muthuprasanna, P. *et al.* Basics and Potential Applications of Surfactants - A Review. *J. PharmTech Res.* **1,** 1354–1365 (2009).
3. Heinzelmann, G., Jr, P. S. & Figueiredo, W. Dynamics of micelle formation from temperature-jump Monte Carlo simulations. *Phys. Rev. Lett.* **92,** 1–9 (2015).
4. Chandler, D. Interfaces and the driving force of hydrophobic assembly. *Nature* **437,** (2005).
5. Torchilin, V. P. Micellar Nanocarriers : Pharmaceutical Perspectives. *Pharm. Res.* **24,** (2007).
6. Mattiello, S. *et al.* Suzuki − Miyaura Micellar Cross-Coupling in Water, at Room Temperature, and under Aerobic Atmosphere. *Org. Lett.* 22–25 (2016).
7. Kolliphor-EL @ pharmaceutical.basf.com.
8. Mattiello, S. *et al.* Self-Assembled Dual Dye-Doped Nanosized Micelles for High-contrast Up-conversion Bioimaging. *Adv. Funct. Mater.* (2016).

9. Lipshutz, B. H. & Ghorai, S. Designer surfactant-enabled cross-couplings in water at room temperature. *Aldrichimica Acta* **45,** (2012).

10. Patel, N. D. *et al.* Effective BI-DIME Ligand for Suzuki–Miyaura Cross-Coupling Reactions in Water with 500 ppm Palladium Loading and Triton X. *Asian J. Org. Chem.* **6,** 1285–1291 (2017).

11. Lin, Y., Li, Y. & Zhan, X. Small molecule semiconductors for high efficiency organic photovoltaics. *Chem. Soc. Rev.* **41,** (2012).

12. Mishra, A. & Bäuerle, P. Small Molecule Organic Semiconductors on the Move : Promises for Future Solar Energy Technology. *Angew. Chemie Int. Ed.* **51,** 2020–2067 (2012).

13. http://blue-white.com/peristaltic-pump-wear-factors/.

14. Gabriel, C. M. *et al.* Effects of Co-solvents on Reactions Run under Micellar Catalysis Conditions. *Org. Lett.* **19,** 194–197 (2017).

15. Muenmart, D. *et al.* Conjugated Polymer Nanoparticles by Suzuki − Miyaura Cross-Coupling Reactions in an Emulsion at Room Temperature. *Macromolecules* (2014).

16. Online, V. A. Air-stable organic semiconductors based on 6,6'-dithienyindigo and polymers therof. *J. Mater. Chem. C* **2,** 8089–8097 (2014).

Final Conclusions

An attempt has been made to develop two methods for controlling the morphology of thin film organic small molecules electronic devices. The methods were developed with industrial applications in mind, where high through put processing for solution is a requirement. The two methods developed both use facile post deposition processes which are used to control or freeze the as cast thin film.

Of the two methods developed, the first technique was the development of a series of soluble negative photoresists which after a photo-initiated crosslinking would form an insoluble film of organic semiconductor which can be used in the fabrication of multi-layer organic electronics. The photocrosslinking process is robust and achieves the desired level of insolubility after a short UV-cure. These materials were incorporated into organic photovoltaic devices (both BHJ and bilayer). Photocrosslinkable squaraine based BHJ cells showed promise with improved performances seen upon photocrosslinking. This is generally attributed to an improved phase segregation with PCBM acceptor materials. The materials are generally stable but overall the performances are disappointing. Upon close examination under microscope and atomic force microscopy it is evident that the photocrosslinking process can create grain boundaries in the film as it shrinks. This results in pinholes, charge leak sites and site for charge trapping to occur. The bilayer devices were fabricated with two large cores to crosslinking site ratio materials. It was thought that extended conjugation could alleviate the issues of film shrinkage. Unfortunately, the casting of these materials proved to be difficult. The low wettability of these materials resulted in extremely rough films which were unsuitable for thin film OPV. The tuneable HOMO/LUMO levels of organic materials coupled with the insolubility of photocrosslinked materials even in fully oxidised or reduced states is perhaps suited better to incorporation into organic batteries. A new PhD project is branching from the seminal results described here

The second method for controlling nano-morphologies of thin films is using the latent pigment. This method uses thermally labile protection group chemistries to donate a soluble characteristic to otherwise insoluble pigments by disrupting H-bond networks. This work culminated in the development of two novel DPP semiconductors. These materials while completely soluble in the protected latent pigment form can be processed into thin film devices. Upon deposition a short 7-minute thermal treatment afford the parent pigment. This pigment

has a strong H-bonding network in its deprotected form. The density of the films increases and the material forms nano-crystals (as seen by an extensive X-Ray thin film study) which are essentially insoluble in organic solvents. These materials were designed specifically for planar bilayer OPV. The most successful device was a deprotected and annealed bilayer with the device architecture as ITO/ PEDOT: PSS/ DPP **34**/ PCBM/ ZnOx/Al. This device afforded a PCE of 0.33% which was stable in air over 24hours. The low Voc and Jsc of these materials led to the incorporation of these materials into OFET devices. By developing OFET devices the charge carrier mobility can be studied before and after thermal annealing. Remarkable improvements to charge mobility was recorded upon deprotection of the latent pigments. All latent pigments tested showed some improvement in mobility but the material DPP 27 stood out with an increase in mobility over three orders of magnitude. This result is most likely due to an improved crystalline packing as the H-bonding network initiates. The high temperature of 200°C for deprotection provides the thermal energy for molecular rearrangement in the thin film. The dense packing of these small crystallites then facilitates charge mobilities in the film.

These approaches aim to provide a variety of methods for industrial applications. Organic opto-electronic industries require cheap and large-scale production of organic semiconductors. The environmental impact of largescale synthesis with the use of large volumes of organic solvents must be addressed as a result. As such, the development of a highly efficient micellar system for carrying out C-C bonding chemistries has been achieved. The use of a very cheap and readily available surfactant called Kolliphor EL affords a micellar reaction medium in water. Common synthetic methods such as Suzuki-Miyaura, Stille and Heck reactions can be carried out in ambient temperatures and atmospheres. This method is compatible with open vessel reactors and requires low loading of metallic catalysts to result in high yielding reactions. This method was originally not applicable to latent pigment synthesis as there was an unusual interaction between t-Boc protected materials and the Kolliphor EL micelle. It appears that the HLB is not aligned to allow these protected materials into the hydrophobic oxygen free core of Kolliphor El micelles. The addition of water miscible co-solvent alleviated this issue, but yields remained in the order of 40-50%. The use of 10% by volume of Toluene as a co-solvent results in an emulsion. The synthesis of complex latent pigment semiconductors was successfully carried out in this emulsion. The emulsion retains a oxygen free character and allows Suzuki-Miyaura cross coupling reactions to be carried out in air in water with yields in excess of 90% (compared to 20-30% for standard organic solvent based procedures). This novel synthesis medium is highly efficient with short reaction times, high synthetic yields and low side-product

production. This method has the potential to be incorporated as a versatile tool for large scale production of organic semiconductors, resulting in cheaper high volume and environmentally friendly materials.

Appendix 1- x-ray characterisation

Structure within thin films has a massive effect on the physical properties of that film, such as the electrical and magnetic properties. This is especially true for modern electronics which rely heavily on the tuning of electrical conductivity and transport by adjusting structures and adding dopant impurities into the nano-structures formed when fabricating devices. Therefore, it is important to undergo an investigation of thin film structures so that we can relate the properties of our devices to the structure of the bulk and surface of the material and not just to the molecular structure.

X-ray characterisation offers one of the most sensitive methods for investigating not only the surface but also the bulk and interfaces of thin films. Generally, X-ray characterisation of thin films is a non-destructive method to give structural information for thin films and multilayers (although degradation can be seen at high intensity at synchrotron sources). The techniques are not only limited to single crystalline materials but can be used to investigate various parameters of poly crystalline and amorphous films too.

The reason X-rays are so useful for structural characterisation is because they are electromagnetic radiation with a wavelength approaching interatomic distances. The interatomic spacing of atoms, which are well ordered in a crystal lattice, act as a diffraction grating for the X-rays causing scattering patterns to appear when the x-rays strike a crystal. From the diffraction pattern it can be calculated where constructive and destructive interference occurs which in turn gives structural information.

X-ray reflectivity

One type of X-ray diffraction technique that is especially useful for studying thin films is x-ray reflectivity. This technique is especially useful for analysing film thickness, roughness and electron density within a film. It gives information about interface roughness and wetting layers which is unobtainable by other techniques such as atomic force microscopy. X-ray radiation is focused on a thin film sample at a grazing angle the detector records the reflected beam is specular conditions (equal but opposite angle to the incoming beam) over a small angle e.g. 0°-5°. Total Reflection occurs below the critical angle of the material, as the incident angle is increased beyond αc (the critical angle) x-rays begin to penetrate into the material and refraction occurs, the intensity of the reflected beam is decreased significantly this is why only small angles can be used to measure the reflectivity of a material.

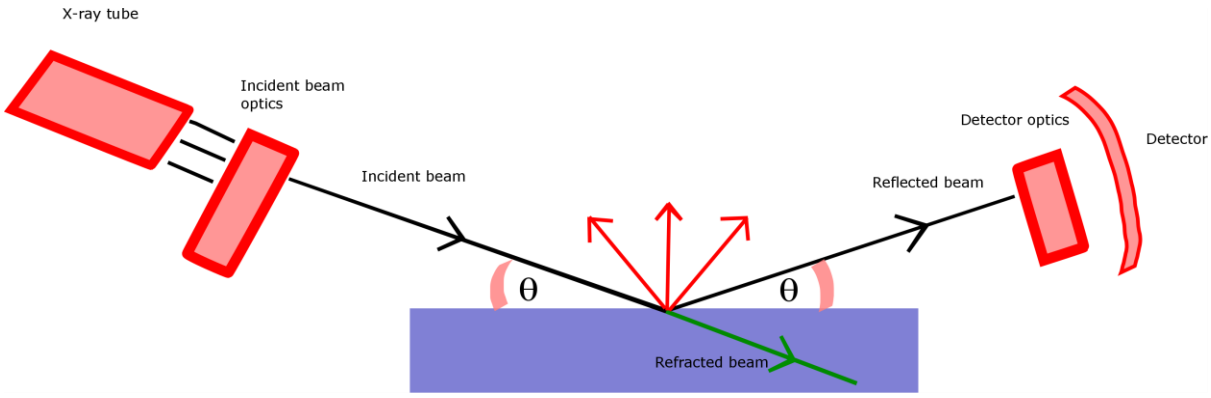

Fig. 6.1 Schematic of reflection experiment showing reflected and refracted beam including diffuse reflections (seen in red).

A portion of the x-rays are reflected at the interface of materials with different electron densities, the interference of these reflected beams gives us the reflectometry pattern. For example, a silicon substrate coated with a uniform organic substance as seen below. Reflection occurs at the organic layer but also at the interface between the silicon and the organic layer the interference between the two reflected beams causes oscillations in the reflectivity profile, these were first seen by Kiessig in 1931 and are therefore called Kiessig fringes. These fringes can tell us the thickness of the layers of each material by studying the frequency of the fringes, thick films will have shorter oscillations.

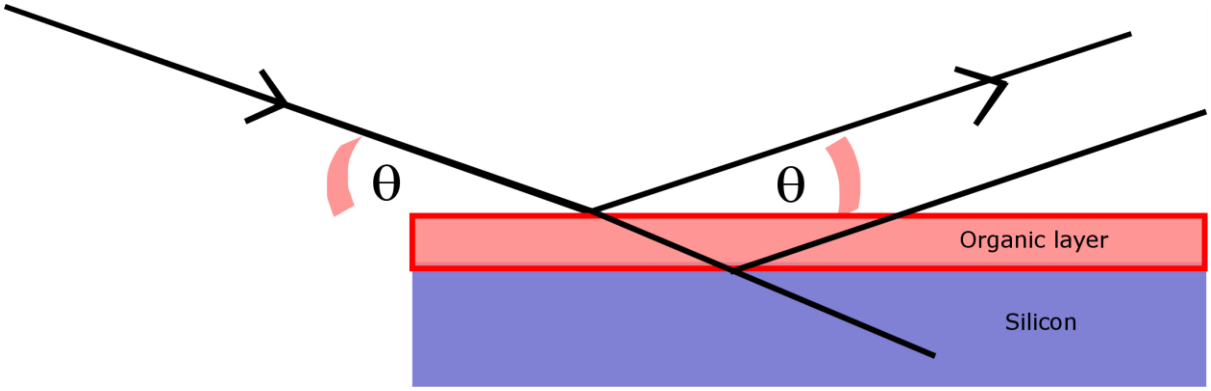

Fig. 6.2 Schematic of reflections caused by a thin organic film on top of a Silicon substrate.

Another piece of information we can gather from the reflectivity experiment is the Density of the material. This is related to the Critical angle of the material and can also be calculated from the density contrast of the substrate as the measured amplitude of the Kiessig fringes. The higher the difference in density of substrate and film the leger the oscillations.

A very important factor for organic devices is film roughness, X-ray reflectivity offers a unique tool for viewing the overall surface roughness of a sample and not just a localised position like in AFM. The rate of decay of the X-ray determines the roughness of the film, a high rate decay relates to a high roughness, the high rate of decay of the intensity of Kiessig fringes indicates high interface roughness.[1]

Today there are a number of programs which can be used to fit theoretical parameters to experimental data allowing for the facile determination of each of the film properties (thickness, roughness, density etc.) the programs used in this work were X'Pert Reflectivity and an XRD Data Viewer from Panalytical.

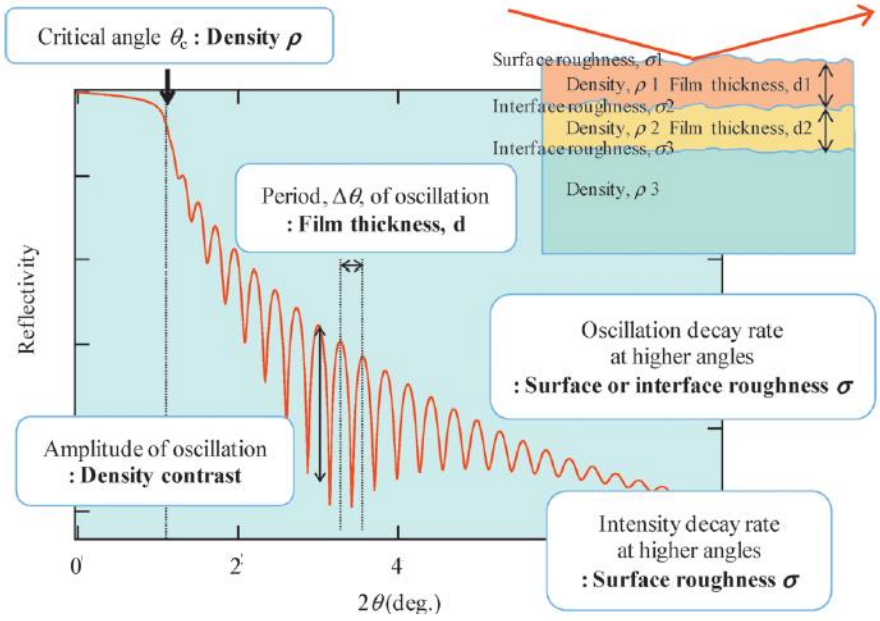

Fig. 8. Information provided by X-ray reflectivity profile.

*The Rigaku Journal, **26**(2), 2010*

Fig. 6.3. Overview of the effects of film parameters on x-ray reflectivity.

The radiation source used for all specular and reflective investigations in this thesis was a Cu-Kα source. X-ray reflectivity measurements were carried out on an Empyrean Panalytical with an attenuator, $\frac{1}{32^\circ}$ divergence slit, a 10mm beam mask, a 0.1 anti-scatter mask and a 0.02radian Solar slit.

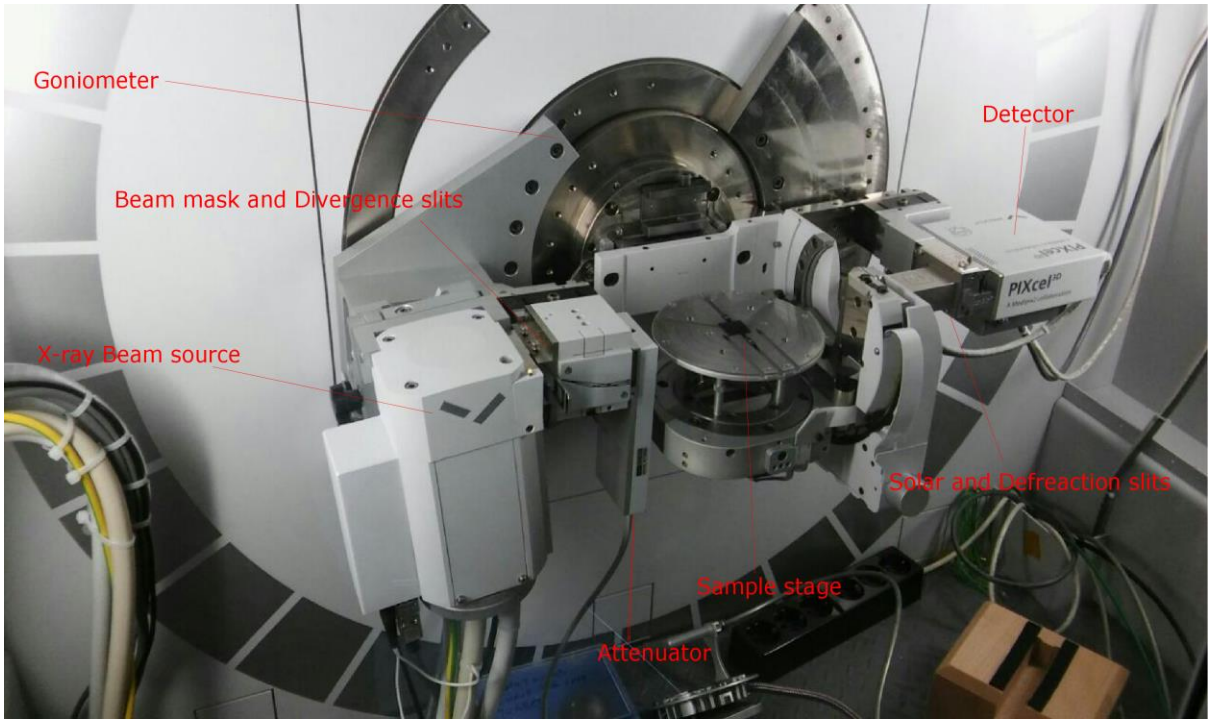

Fig. 6.4 Empyrean Panalytical X-ray reflectivity and specular setup at TU Graz, Austria.

Films tested for x-ray reflectivity were prepared by spincoating 8mg/ml in chloroform at 4000rpm for 40seconds onto cleaned silicon dioxide 1x1cm substrates. The samples were made in tandem with one half being either treated thermally in an oven at 200°C for 7 mins or with UV exposure 254nm for 30 mins. The experiments test between θ=0.05-5.9°

Macroscopic	Shape	Layer thickness
	Composition	Structural phase
		Elements present

		Phase extent
	Form	Amorphous
		Polycrystalline
		Single crystal
	Orientation	General preferred texture
		Layer tilt
	Distortion	Layer strain tensor
		Warping
	Homogeneity	Between analysed regions
	Interfaces	Interface spreading
	Density	Porosity
		Coverage
Microscopic	Shape	Average crystallite size
		Crystallite size distribution
	Composition	Local chemistry
	Orientation	Crystallite tilt distribution
	Distortion	Crystallite lattice strain
		Crystallite strain distribution
		Dislocation strain fields
		Point defects
		Cracks
		Strain from precipitates
	Interfaces	Roughness
	Homogeneity	Distribution within region of sample studied

Table 6.1. examinable parameters by X-Ray spectroscopy[2]

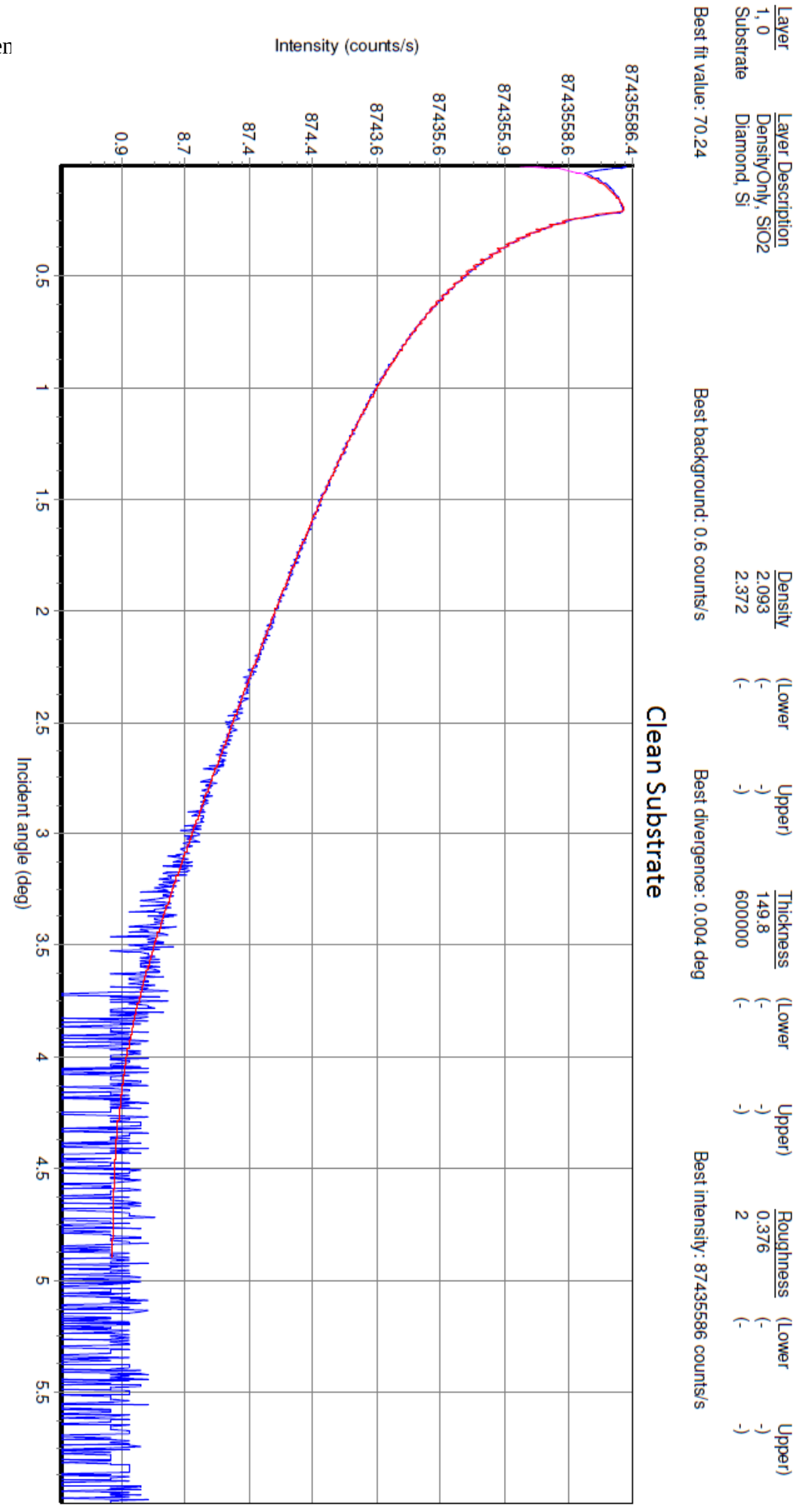
Clean Substrate
Intensity (counts/s)
87435586.4
87435586.4
87435586.4
87435586.4
87435586.4
87435586.4
87435586.4
Incident angle (deg)
0.5
1
1.5
2
2.5
3
3.5
4
4.5
5
5.5
Best fit value: 70.24
Best background: 0.6 counts/s
Best divergence: 0.004 deg
Best intensity: 87435586 counts/s
Layer
1, 0
Substrate
Layer Description
DensityOnly, SiO2
Diamond, Si
Density
2.093
2.372
(Lower
(-
(-
Upper)
-)
-)
Thickness
149.8
600000
(Lower
(-
(-
Upper)
-)
-)
Roughness
0.376
2
(Lower
(-
(-
Upper)
-)
-)

Appendix 1- X-Ray characterisation

The first Reflectivity experiment was on a freshly cleaned substrate, sonicated for 5mins in acetone followed by Isopropyl alcohol. These are manufactured with specification of 150nm of thermally grown silicon di-oxide upon an amorphous silicon substrate 1x1cm. From the reflectivity investigation we see that the actual thickness is 149.8nm with a roughness of 0.376nm. From this result we can state that we have chosen the correct optics and aligning practices for accurate thickness and roughness measurements.

Layer	Layer Description	Density	(Lower	Upper)	Thickness	(Lower	Upper)	Roughness	(Lower	Upper)
2, 0	DensityOnly, Cellulose	1.1	(-	-)	40	(-	-)	1.25	(-	-)
1, 0	DensityOnly, SiO2	2.2	(-	-)	149.8	(-	-)	0.245	(-	-)
Substrate	Diamond, Si	2.372	(-	-)	600000	(-	-)	2	(-	-)

Best fit value: 137.16 Best background: 0.6 counts/s Best divergence: 0.004 deg Best intensity: 69551049 counts/s

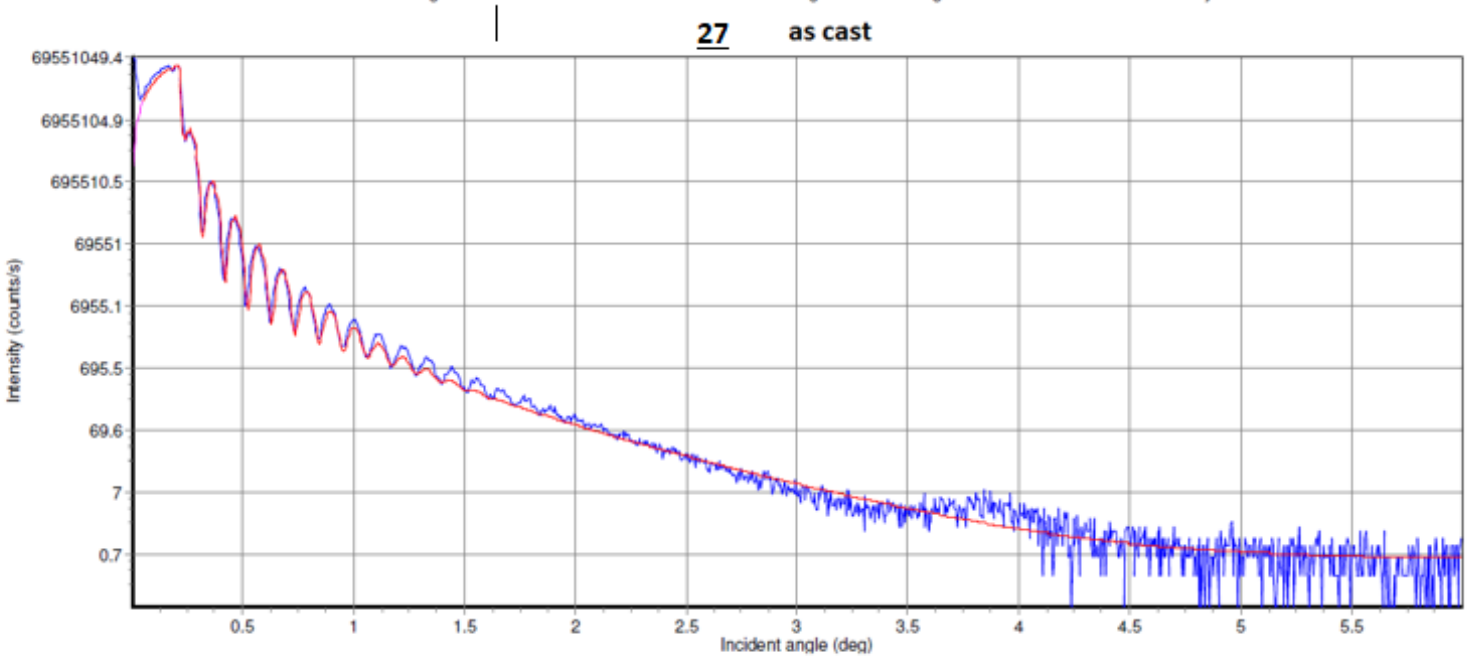

Layer	Layer Description	Density	(Lower	Upper)	Thickness	(Lower	Upper)	Roughness	(Lower	Upper)
2, 0	DensityOnly, Cellulose	1.1	(-	-)	29.645	(-	-)	3.015	(-	-)
1, 0	DensityOnly, SiO2	2.2	(-	-)	149.8	(-	-)	0.245	(-	-)
Substrate	Diamond, Si	2.372	(-	-)	600000	(-	-)	2	(-	-)

Best fit value: 114.6 Best background: 0.6 counts/s Best divergence: 0.004 deg Best intensity: 64883725 counts/s

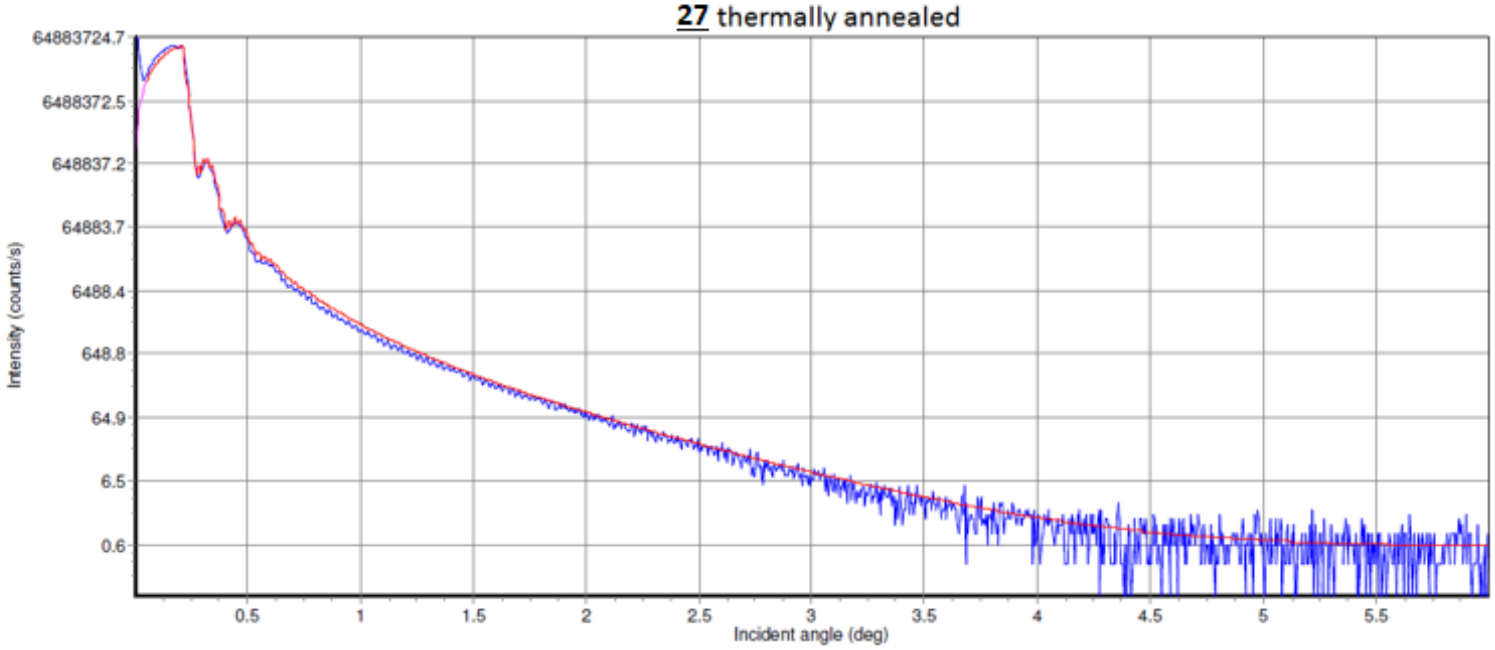

Appendix 1- X-Ray characterisation

Reflectivity	**DPP 27**	**DPP 27 annealed**
αc SiO2	0.225	0.2252
αc organic layer	0.1746	0.18495
Organic electron density	435.3nm^{-3} (electrons per nm$^{3)}$	488.44nm^{-3}
Roughness (δ)	1.3nm	3nm
Thickness (d)	40nm	29nm
d-spacing (of Bragg peak)	1.14nm (typical of edge on alignment)	No Bragg peak seen
Vertical crystal size	≈13nm	N/A

Upon activation of the latent pigment by thermal annealing an increase in the critical angle of the DPP 27 layer occurs. This is related to the increased density of the material; this is an indicator that perhaps the hydrogen bonding network that becomes activated after thermal annealing results in a denser packing of material or may just be due to the loss of insulating chains. The density is calculated with the formula

$$\rho_c = \frac{\theta c^2 \pi}{\lambda^2 \gamma_c}$$

Where ρ_c= electron density θ_c =critical angle in radians λ= the wavelength of radiation (0.15418 nm for Cu-Kα) and γ=the classical electron radius 2.8179x10^{-6}nm

There is a significant decrease in film thickness from 40 to 29nm and an increase in surface roughness from 1.3 to 3nm this indicates that there is a significant change occurring within the film. The film thickness can be almost directly related to the loss of material as the tert-butyloxycarbonyl groups are removed.

$$\frac{797.17\ g/mol}{997.4 g/mol} x \frac{100}{1} = 79\%\ of\ mass\ remaining\ after\ deprotection$$

$$\frac{29nm}{40nm} x \frac{100}{1} = 72\%\ of\ film\ thickness$$

The disappearance of the Bragg peak can also be a strong indication of structural change but more likely if we have smaller crystal sizes the signal would be weaker and hidden by backround. The film does not necessarily become less crystalline as this form of measurement only shows the in-plane crystallinity.

The d-spacing can be calculated from the Bragg equation: nλ=2dsinθ

Where λ is wavelength d is lattice spacing and θ is the angle of the Bragg peak in degree

$$d = \frac{0.15418}{2\sin(3.865)} = 1.14nm$$

Crystallite size can be determined using the Scherrer equation $\tau = \frac{K\lambda}{\beta cos\theta}$

τ= average size of crystallite K=shape factor (typically taken as 0.9) β=FWHM of the peak in radians θ=Bragg angle λ= X-ray wavelength (0.15418 nm for Cu-Kα)

when determining Crystallite size using the Scherrer equation it must be noted that instrumental broadening is not taken into consideration so in reality this is just a method to obtain a rough estimate of crystallite size.

Appendix 1- X-Ray characterisation

Layer	Layer Description	Density	(Lower	Upper)	Thickness	(Lower	Upper)	Roughness	(Lower	Upper)
2, 0	DensityOnly, Cellulose	1.2	(-	-)	46.288	(-	-)	1.997	(-	-)
1, 0	DensityOnly, SiO2	2.24	(-	-)	151.125	(-	-)	0.27	(-	-)
Substrate	Diamond, Si	2.561	(-	-)	600000	(-	-)	1	(-	-)

Best fit value: 133.81 Best background: 0.53 counts/s Best divergence: 0.015 deg Best intensity: 92849771 counts/s

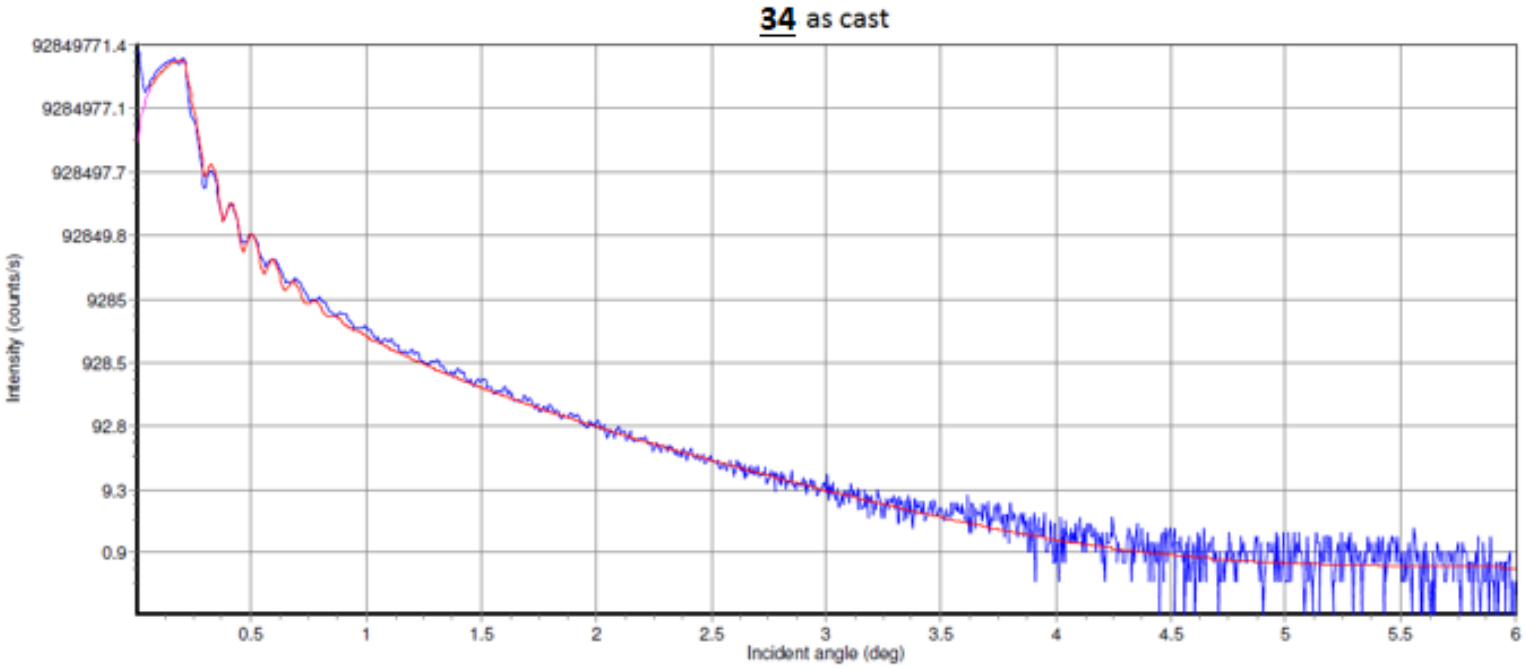

Layer	Layer Description	Density	(Lower	Upper)	Thickness	(Lower	Upper)	Roughness	(Lower	Upper)
2, 0	DensityOnly, Cellulose	1.2	(-	-)	37.226	(-	-)	2.14	(-	-)
1, 0	DensityOnly, SiO2	2.21	(-	-)	151.125	(-	-)	0.27	(-	-)
Substrate	Diamond, Si	2.36	(-	-)	600000	(-	-)	1	(-	-)

Best fit value: 99.65 Best background: 0.53 counts/s Best divergence: 0.005 deg Best intensity: 99207806 counts/s

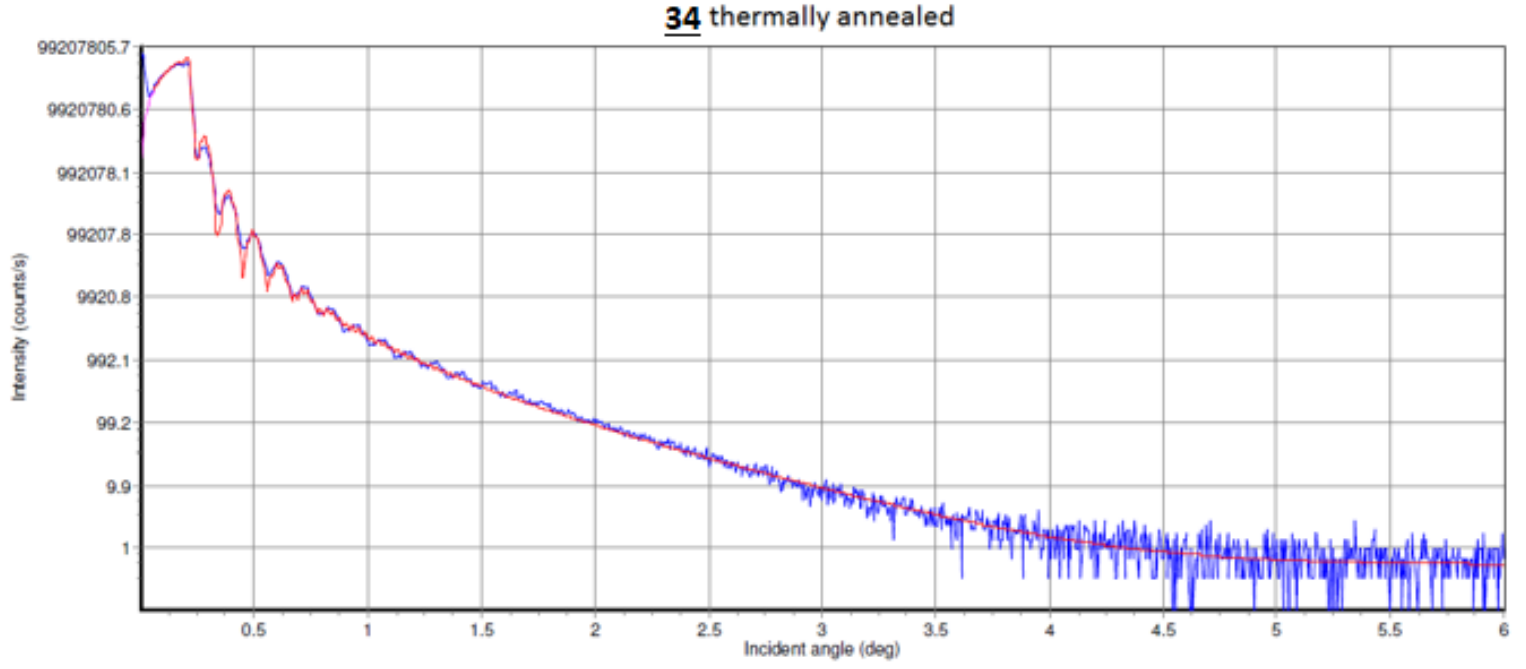

Reflectivity	**Spin coated DPP 34**	**Annealed DPP 34**
α c organic=	0.175	0.18
α c silicon	0.221	0.221
Organic electron density	437.521 nm^{-3}	462.80 nm^{-3}
d organic	46.3nm	37nm
d silicon	151nm	151nm
δ silicon	0.27nm	0.27nm
δ organic	1.9nm	2.1nm
d Bragg	1.18 nm	-
Vertical crystallite size	-	-

The crystal size could not be determined as the Bragg peak has low resolution in comparison to the background. Again, we see a similar reduction in the film thickness with a slight increase in film roughness as expected. Disappearance of the Bragg peak is also noted

Layer	Layer Description	Density	(Lower	Upper)	Thickness	(Lower	Upper)	Roughness	(Lower	Upper)
2, 0	DensityOnly, Cellulose	1.962	(-	-)	5.116	(-	-)	0.376	(-	-)
1, 0	DensityOnly, SiO2	2.64	(-	-)	151	(-	-)	0.16	(-	-)
Substrate	Diamond, Si	2.328	(-	-)	600000	(-	-)	1.5	(-	-)

Best fit value: 15.53 Best background: 5.12 counts/s Best divergence: 0.004 deg Best intensity: 25412088 counts/s

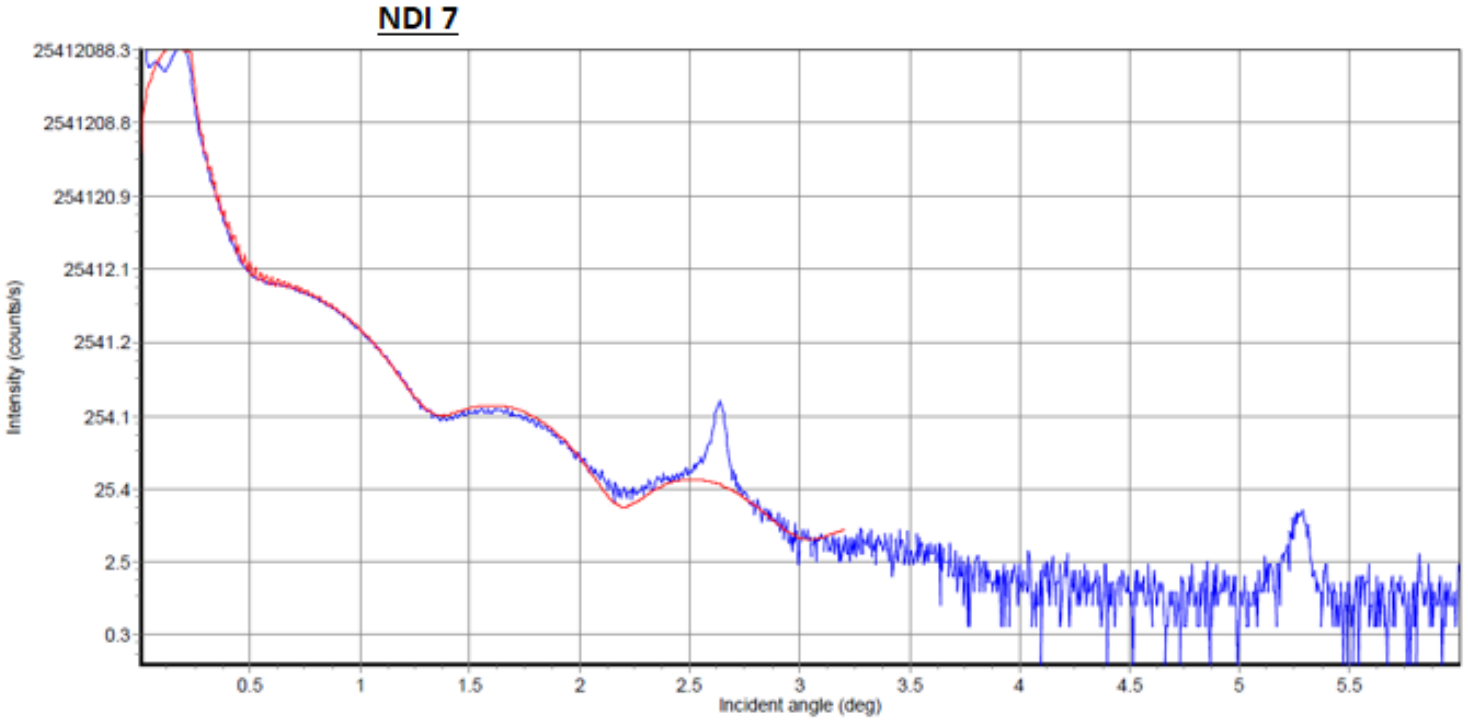

Layer	Layer Description	Density	(Lower	Upper)	Thickness	(Lower	Upper)	Roughness	(Lower	Upper)
2, 0	DensityOnly, Cellulose	1.968	(-	-)	5.084	(-	-)	0.322	(-	-)
1, 0	DensityOnly, SiO2	2.64	(-	-)	151	(-	-)	0.318	(-	-)
Substrate	Diamond, Si	2.328	(-	-)	600000	(-	-)	1.5	(-	-)

Best fit value: 107.92 Best background: 0.93 counts/s Best divergence: 0.004 deg Best intensity: 17978020 counts/s

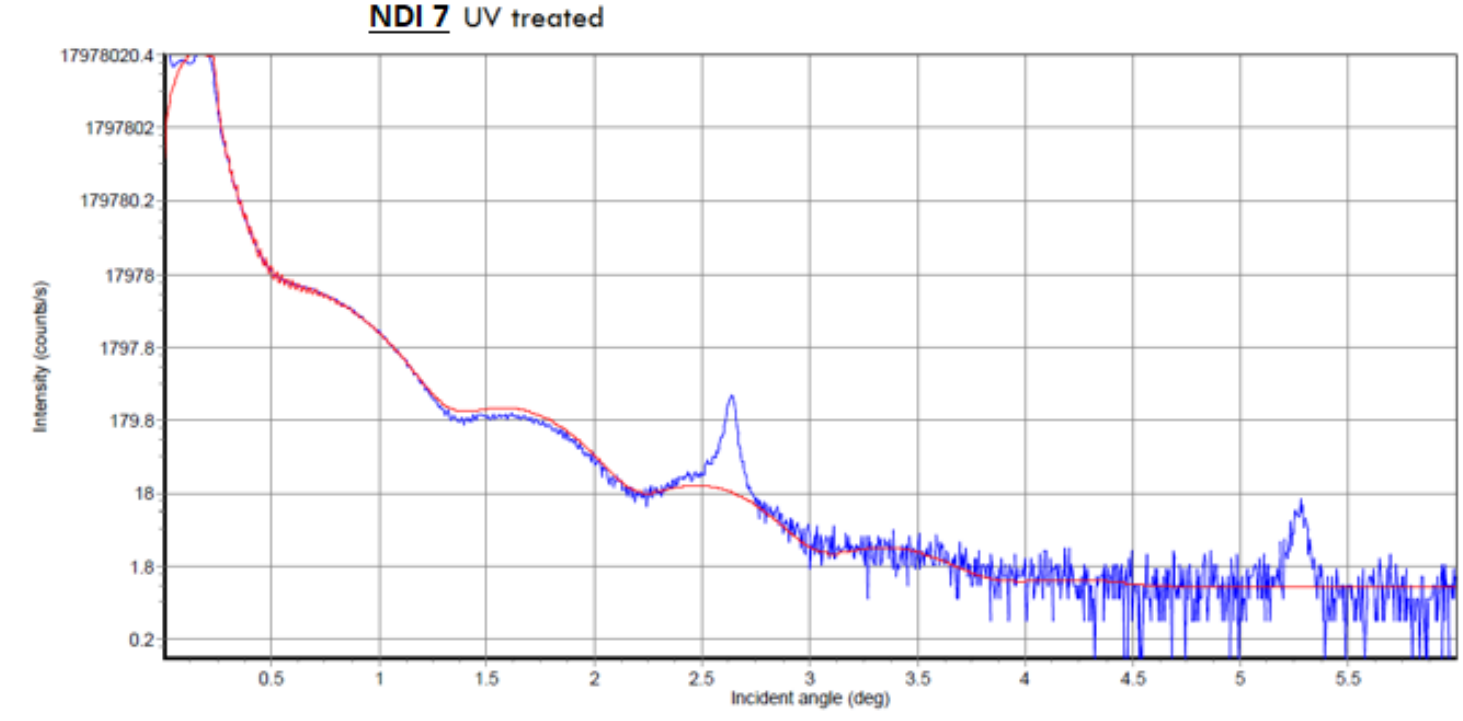

Reflectivity	**Spin coated NDI 7**	**Uv treated NDI 7**
α c organic=	0.09	0.1036
α c silicon	0.217	0.215
Organic electron density		
d organic	5.116nm	5.084nm
d silicon	151nm	151nm
δ organic	0.376nm	0.322nm
δ silicon	0.16nm	0.318nm
d Bragg 1	1.67nm	1.68nm
d Bragg 2	0.837nm	0.839nm

This material has very poor wetting on Silicon dioxide the sample has a baseline thickness of 5nm but in reality there are areas of the film with thicknesses in the order of 100nm, severe agglomeration of the material results in sparsely spread island formations on the film with a very thin surface all over the low critical angle of the organic material indicates a very low density layer that cannot be regarded as the actual density of the material in the film due to its large inhomogeneity. The overall poor quality of the films makes it difficult to give any definitive analysis in regards to film thickness, roughness, material density or crystallite size, but we can still acknowledge qualitatively the crystallinity of the material as Bragg peaks are seen in both as cast and UV cured samples indicating a degree of order in the material.

Appendix 1- X-Ray characterisation

Layer	Layer Description	Density	(Lower	Upper)	Thickness	(Lower	Upper)	Roughness	(Lower	Upper)
2, 0	DensityOnly, Cellulose	1.76	(-	-)	2.178	(-	-)	0.001	(-	-)
1, 0	DensityOnly, SiO2	2.64	(-	-)	149.856	(-	-)	1.3	(-	-)
Substrate	Diamond, Si	2.328	(-	-)	600000	(-	-)	0.493	(-	-)

Best fit value: 3.59 Best background: 10 counts/s Best divergence: 0.004 deg Best intensity: 15985349 counts/s

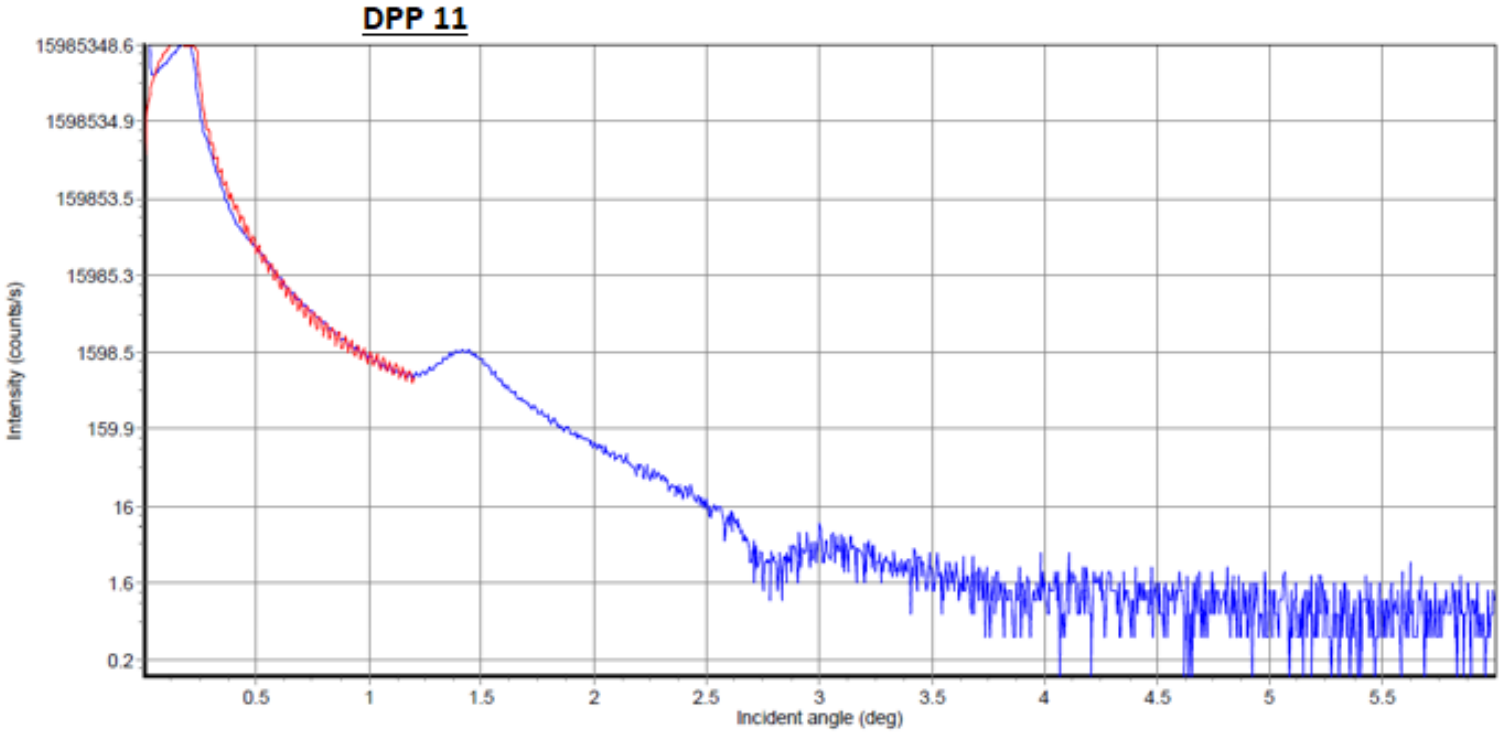

Layer	Layer Description	Density	(Lower	Upper)	Thickness	(Lower	Upper)	Roughness	(Lower	Upper)
2, 0	DensityOnly, Cellulose	2	(-	-)	2.277	(-	-)	0.414	(-	-)
1, 0	DensityOnly, SiO2	2.64	(-	-)	151	(-	-)	0	(-	-)
Substrate	Diamond, Si	2.328	(-	-)	600000	(-	-)	0.645	(-	-)

Best fit value: 21.31 Best background: 4.26 counts/s Best divergence: 0.004 deg Best intensity: 24259077 counts/s

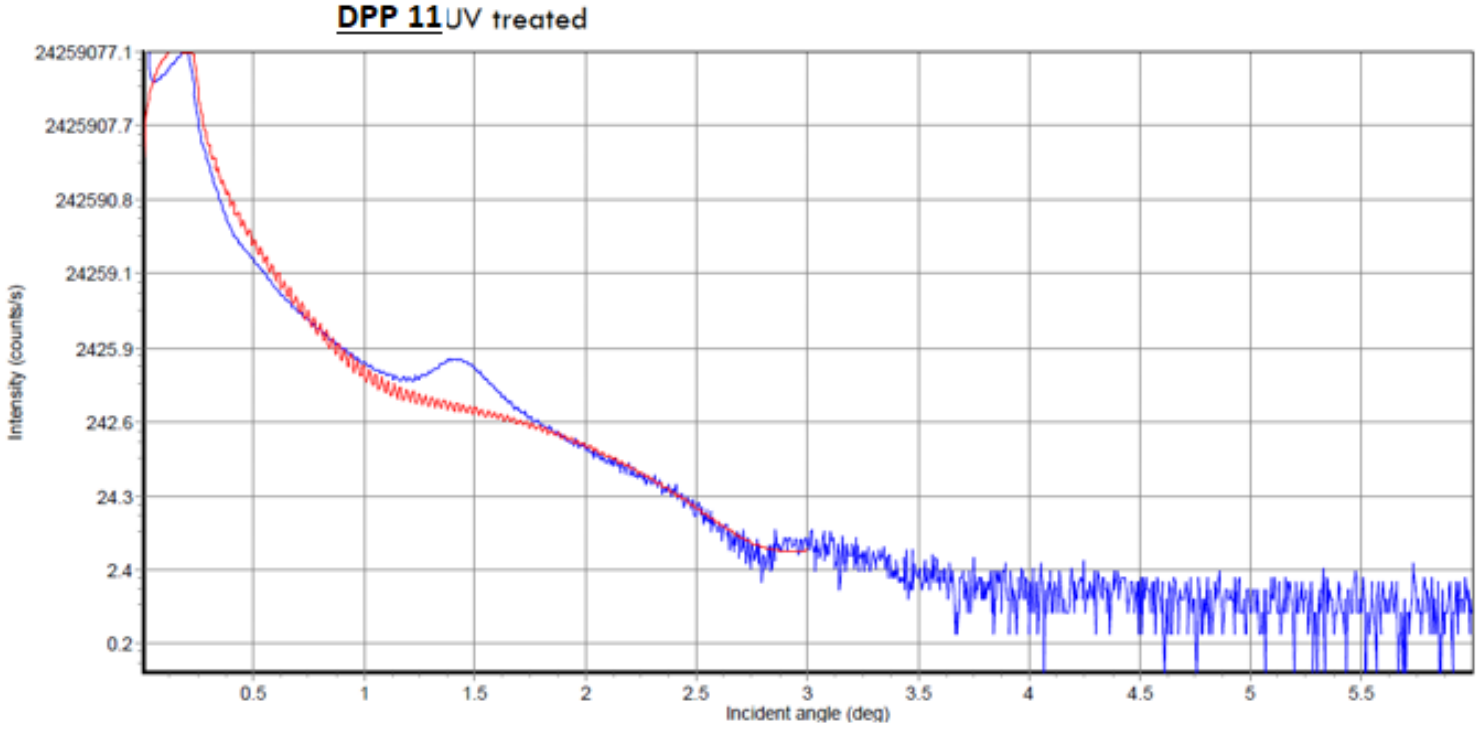

Reflectivity	**Spin coated DPP 11**	**Uv treated DPP 11**
α c organic=	-	-
α c silicon	0.218	0.217
Organic electron density	-	-
d organic	2.178nm	2.277nm
d silicon	149.85nm	151nm
δ organic	0.001nm	0.414nm
δ silicon	1.3nm	0
d Bragg 1a	3.11nm	3.11nm
d Bragg second order	1.47nm	1.472nm

Again, we see a film with very poor wetting, in this case the inhomogeneity is so high that we cannot determine a critical angle for the organic phase. It is also difficult to determine any real film parameters as X-ray reflectivity gives an average of thickness over a large area on the film, the roughness is too high for proper correlation to be extrapolated. Similar to NDI 7 Bragg information can still be analysed from this film. One Bragg peak is seen at 1.4θ this has a less intense second order peak seen at double the angle of the first Bragg peak.

Appendix 1- X-Ray characterisation

Layer	Layer Description	Density	(Lower	Upper)	Thickness	(Lower	Upper)	Roughness	(Lower	Upper)
2, 0	DensityOnly, MRPyrrole	1.1	(-	-)	51.49	(-	-)	4.598	(-	-)
1, 0	DensityOnly, SiO2	2.25	(-	-)	152	(-	-)	0.364	(-	-)
Substrate	Diamond, Si	2.3	(-	-)	600000	(-	-)	0.084	(-	-)

Best fit value: 1.07 Best background: 2 counts/s Best divergence: 0.0044 deg Best intensity: 46201935 counts/s

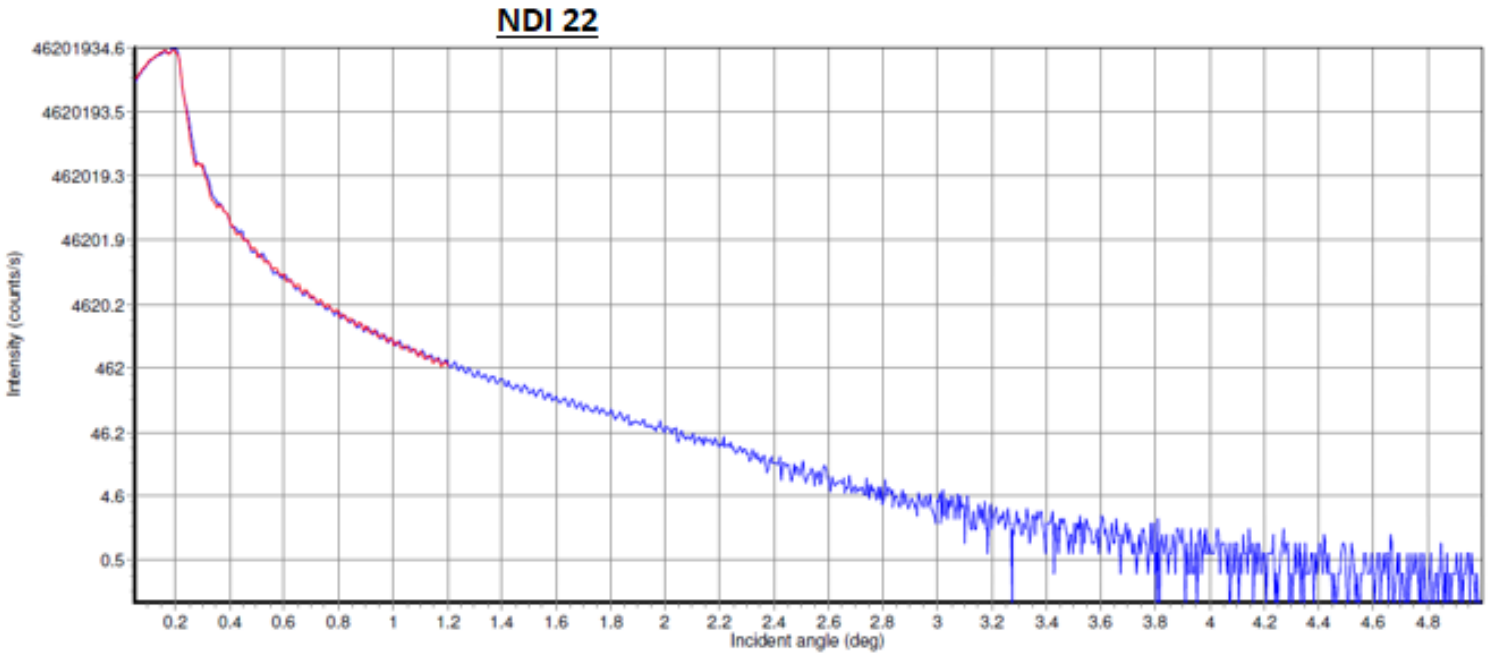

Layer	Layer Description	Density	(Lower	Upper)	Thickness	(Lower	Upper)	Roughness	(Lower	Upper)
2, 0	DensityOnly, Cellulose	1.71	(-	-)	45	(-	-)	7.311	(-	-)
1, 0	DensityOnly, SiO2	2.64	(-	-)	152	(-	-)	0	(-	-)
Substrate	Diamond, Si	2.328	(-	-)	600000	(-	-)	2	(-	-)

Best fit value: 5.6 Best background: 10 counts/s Best divergence: 0.0036 deg Best intensity: 35905123 counts/s

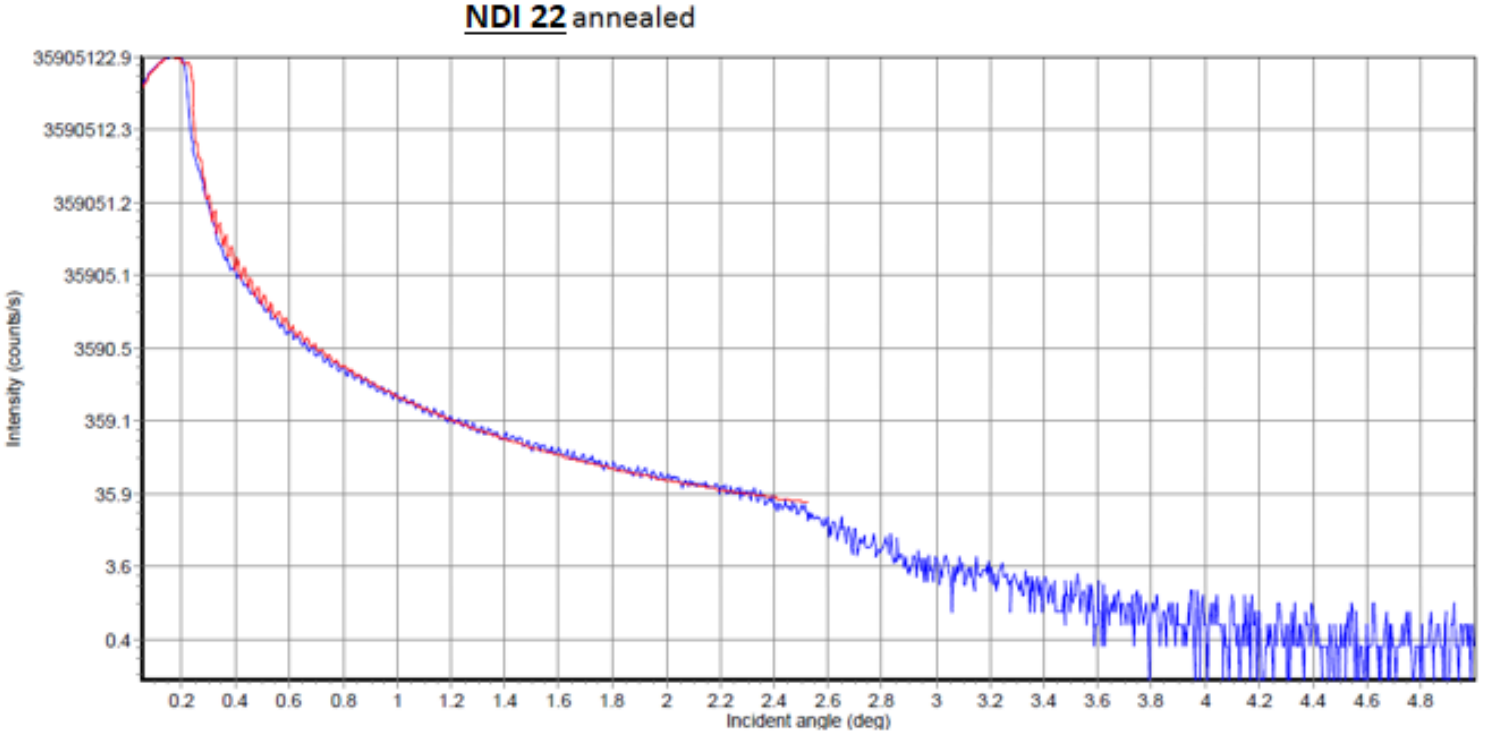

Appendix 1- X-Ray characterisation

Reflectivity	**Spin coated NDI 22**	**Annealed NDI 22**
α c organic	0.175	0.171
α c silicon	0.22	0.264
Organic electron density	437.521	417.74
d organic	50nm	45nm
d silicon	151nm	152nm
δ silicon	0.36nm	0.nm
δ organic	4.6nm	7.3nm
d Bragg	1.96nm	1.8nm

Specular X-ray Diffraction

Specular scans over a wide 2θ range 5-40° were measured for spin cast samples. The beam setup was as follows $\frac{1}{8^\circ}$ divergence slit, a 4mm beam mask, a 7.5mm anti-scatter mask and a 0.02rad Solar slit. This set up uses more pixels on the detector than the Reflectivity experiments allowing for images of a number of degrees to be taken at each goniometer position.

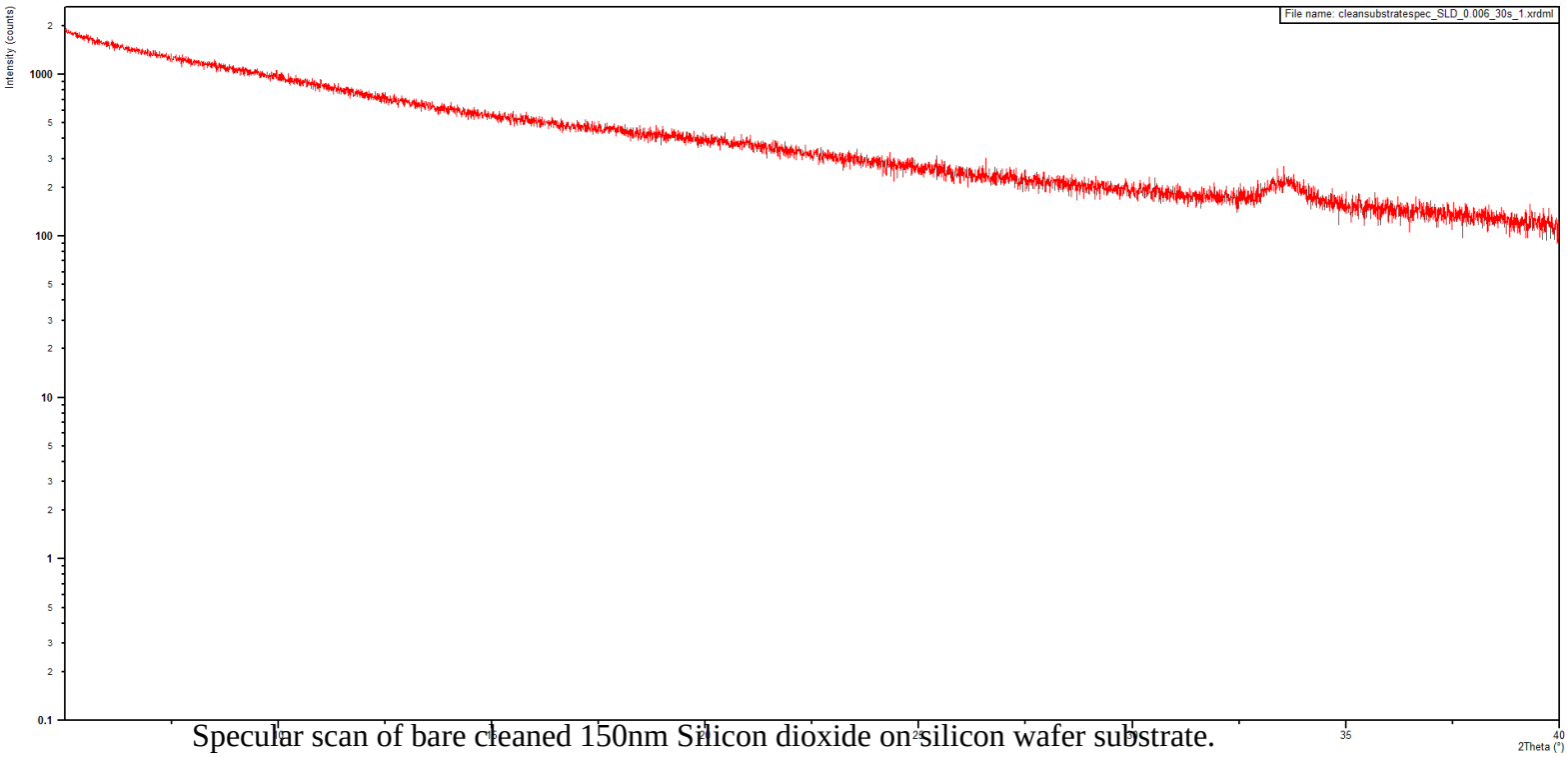

Specular scan of bare cleaned 150nm Silicon dioxide on silicon wafer substrate.

Appendix 1- X-Ray characterisation

NDI 7

Blue= UV cured Red= as cast

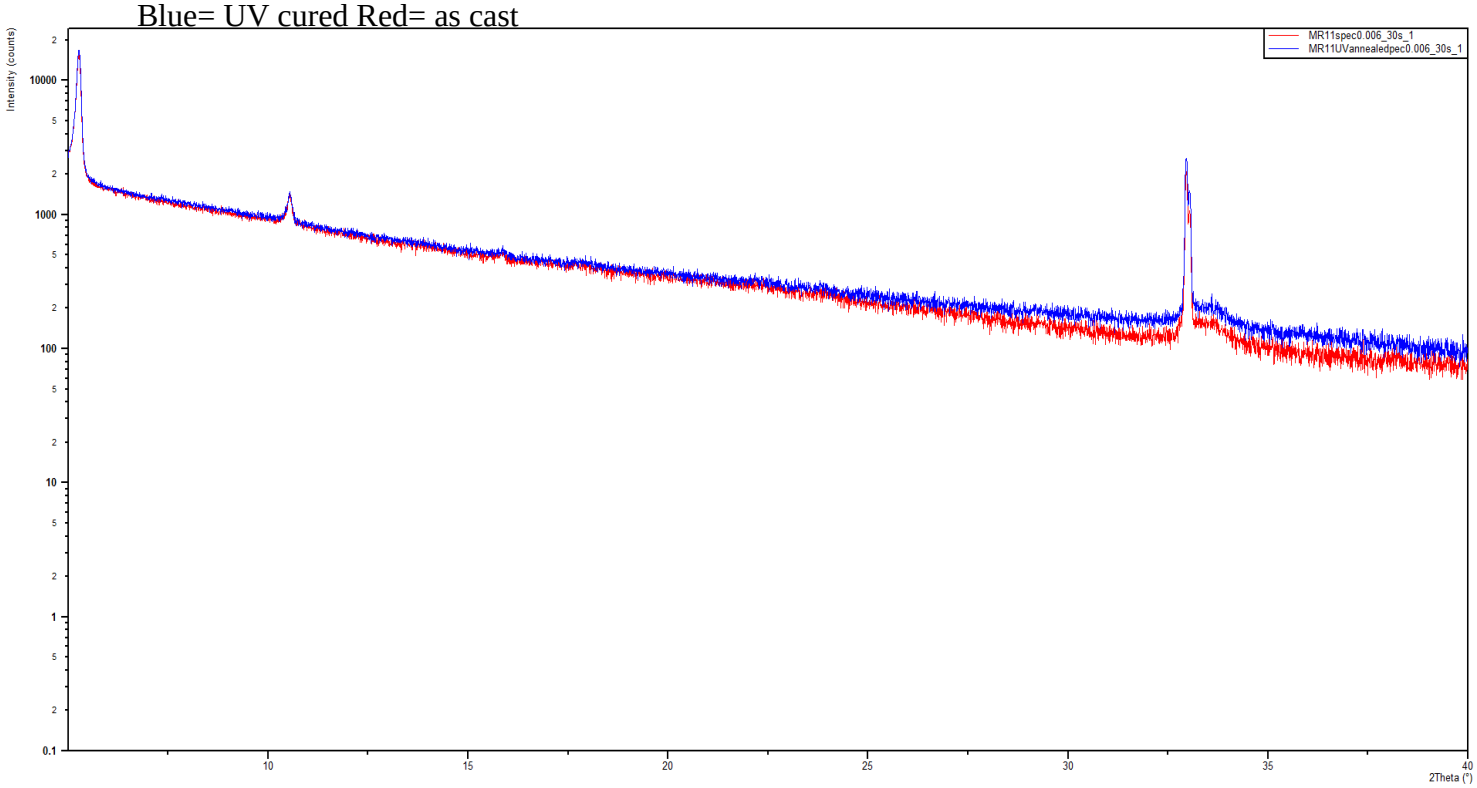

DPP 11

Blue= as cast Red=UV cured

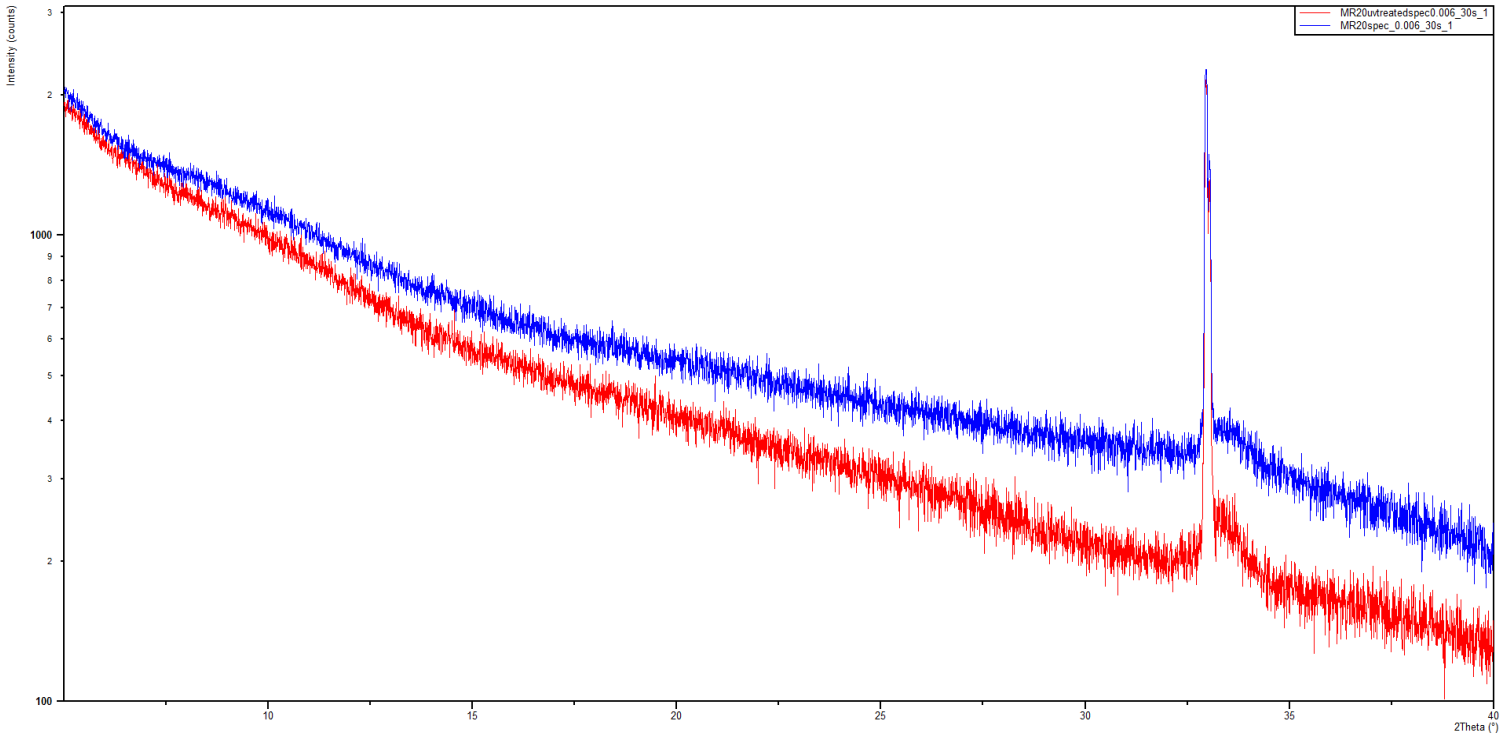

Appendix 1- X-Ray characterisation

NDI 22

Red= annealed blue=as cast

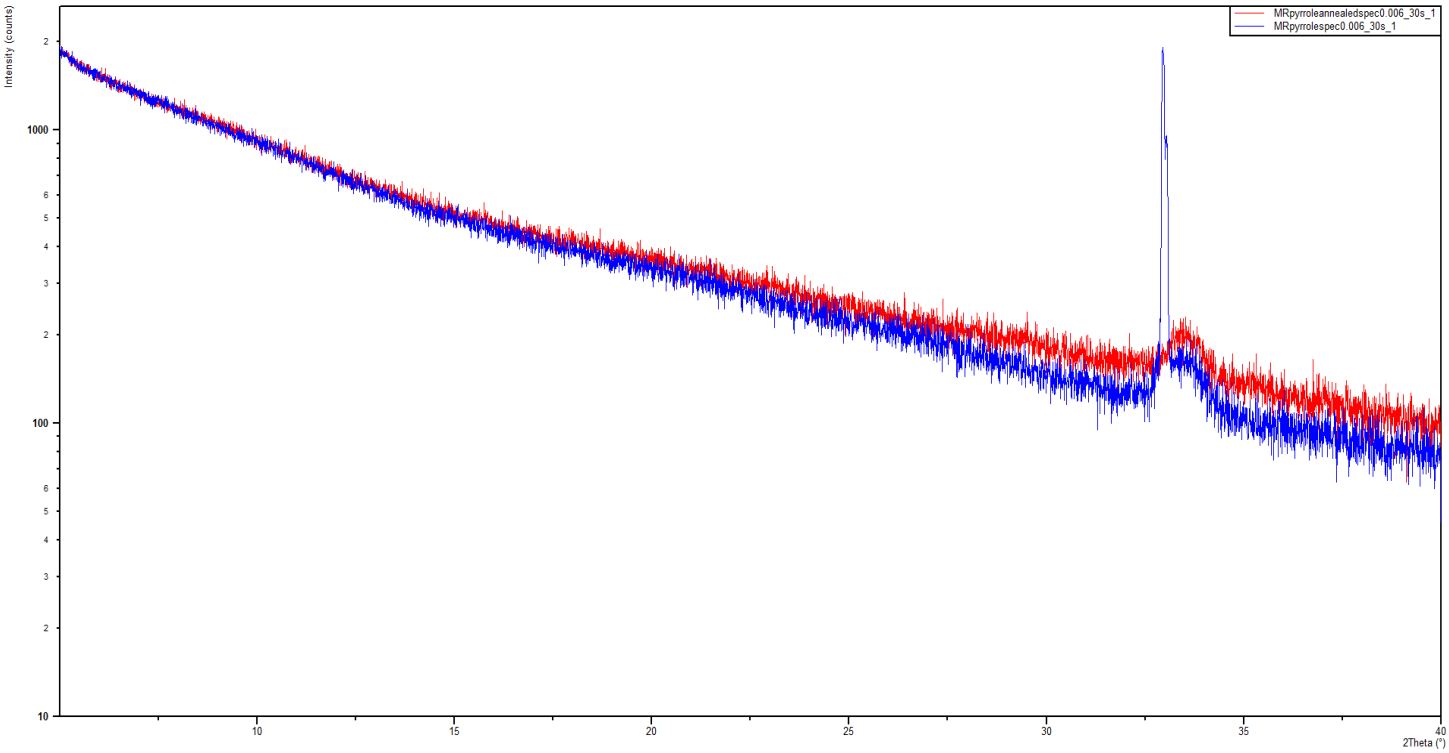

DPP 27

Red= annealed Blue= as cast

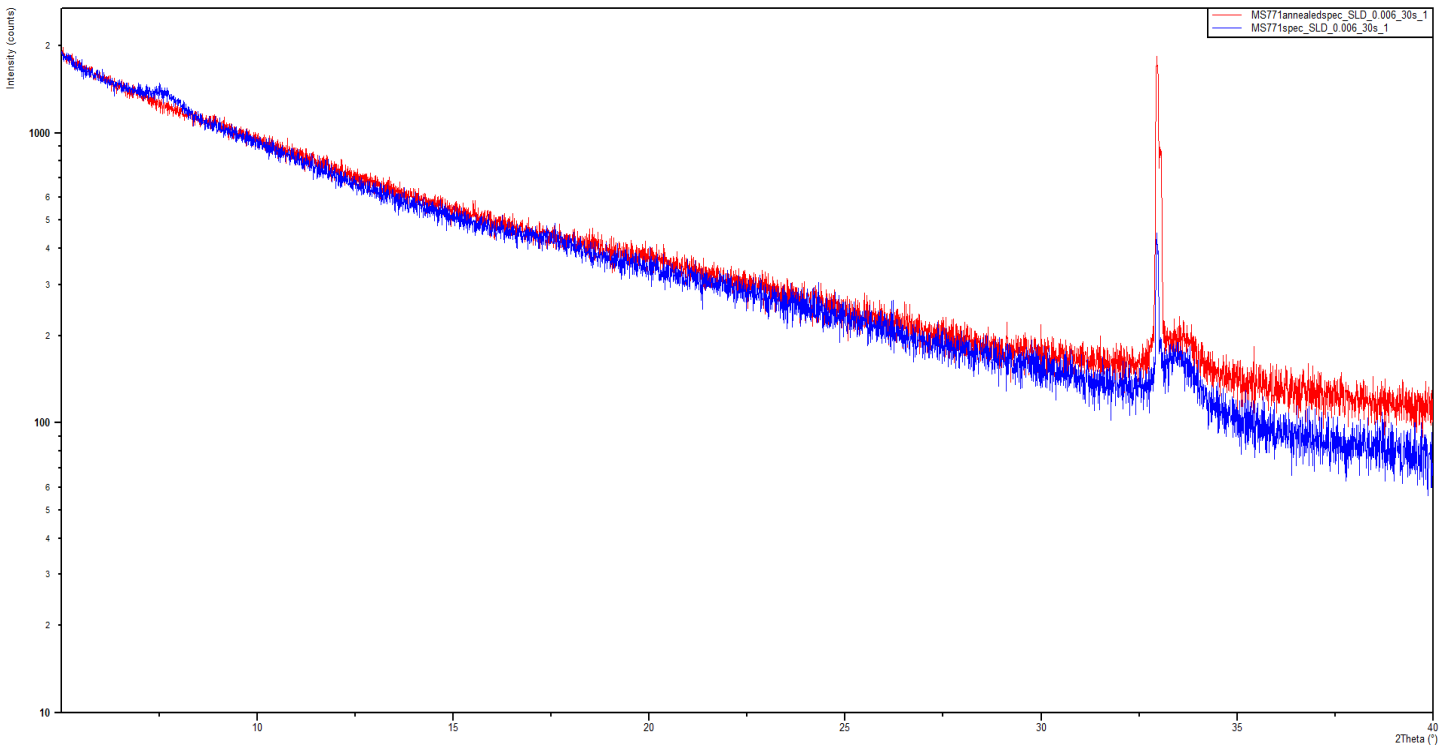

Appendix 1- X-Ray characterisation

DPP 34

Red= annealed Blue=as cast

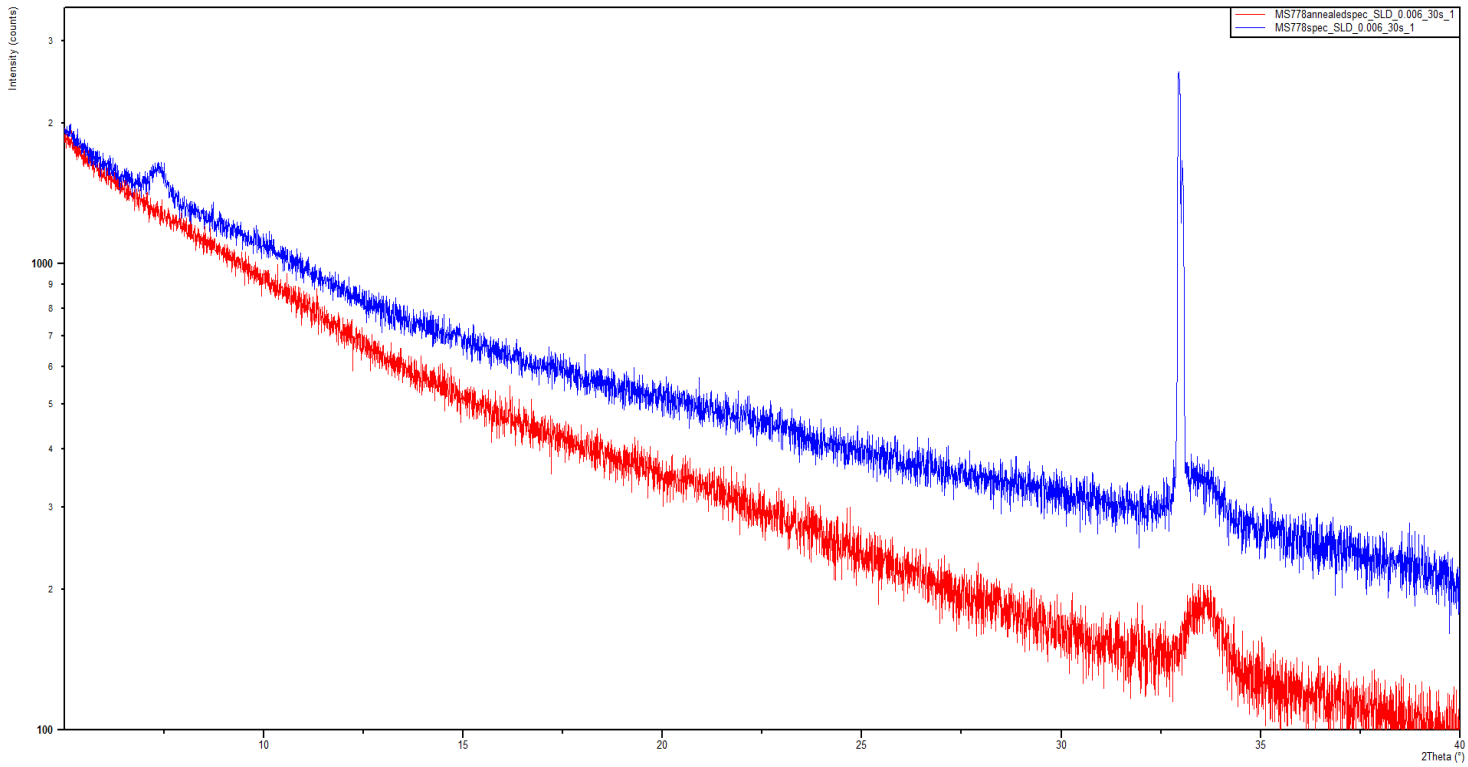

Thermal Gradient studies were performed on DPP 34 drop cast films from chloroform and chlorobenzene. The Empyrean Panalitical was fit with a heating stage and thermal experiment was performed. Inline scans were performed at incremental temperatures from 30-200°C in air. The samples were let sit at each set temperature for 5mins before the scan was performed between 2θ=3.7-25°. Alignment of samples was performed with $\frac{1}{32°}$ divergence slit, a 10mm beam mask, a 0.1 anti-scatter mask and a 0.02radian Solar slit.

The full scan was performed with $\frac{1}{8°}$ divergence slit, a 10mm beam mask, a 7.5mm anti-scatter mask and a 0.02radian Solar slit.

DPP 34 chloroform

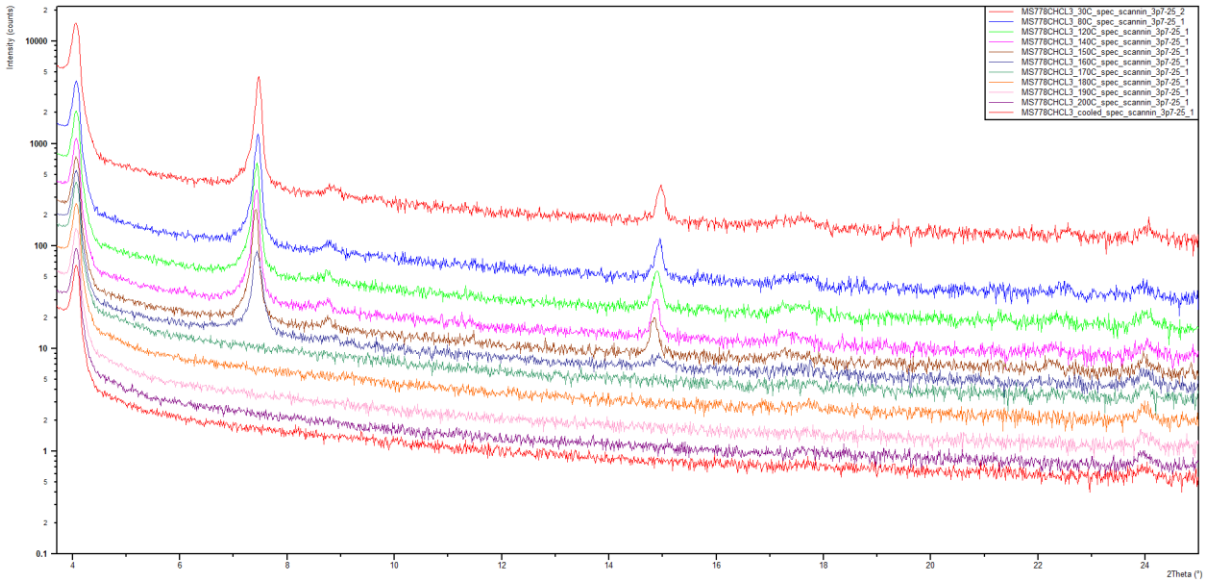

DPP 34 Chlorobenzene

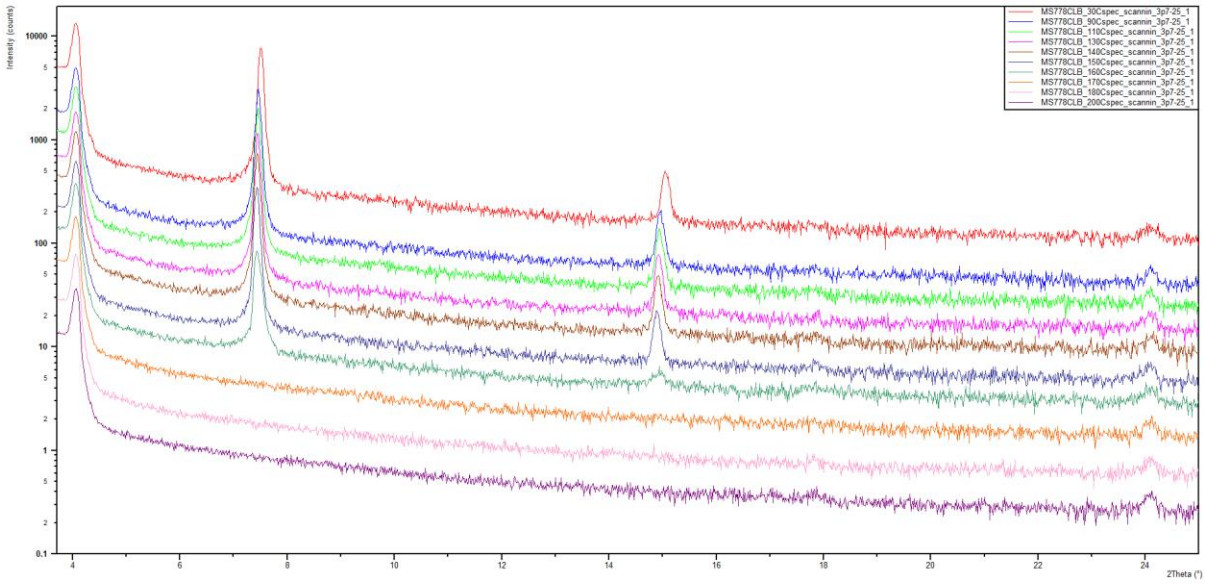

Grazing Incidence X-ray Diffraction

In this thesis, all diffraction plots have been converted into the scattering vector q space so that they are independent of wavelength of x-ray source. $|q| = \frac{4\pi sin\theta}{\lambda}$

This formula gives a q spacing in nm^{-1}, GIXD (grazing incidence x-ray diffraction) performed at BESSY II and DIAMOND have q values reported in $angstroms^{-1}$ 1 nm^{-1}=0.1$Å^{-1}$

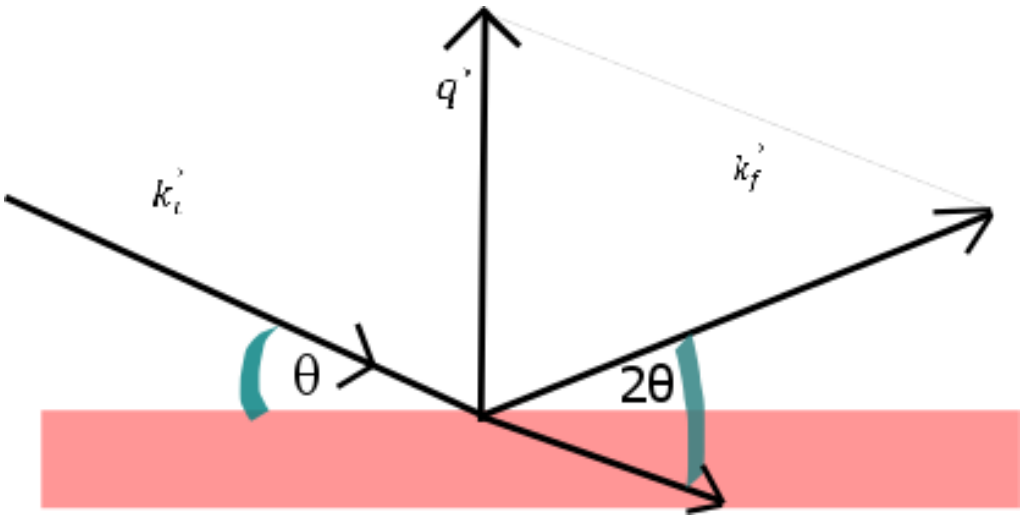

Fig. 6.5. schematic diagram of beam diffraction for wide angle x-ray

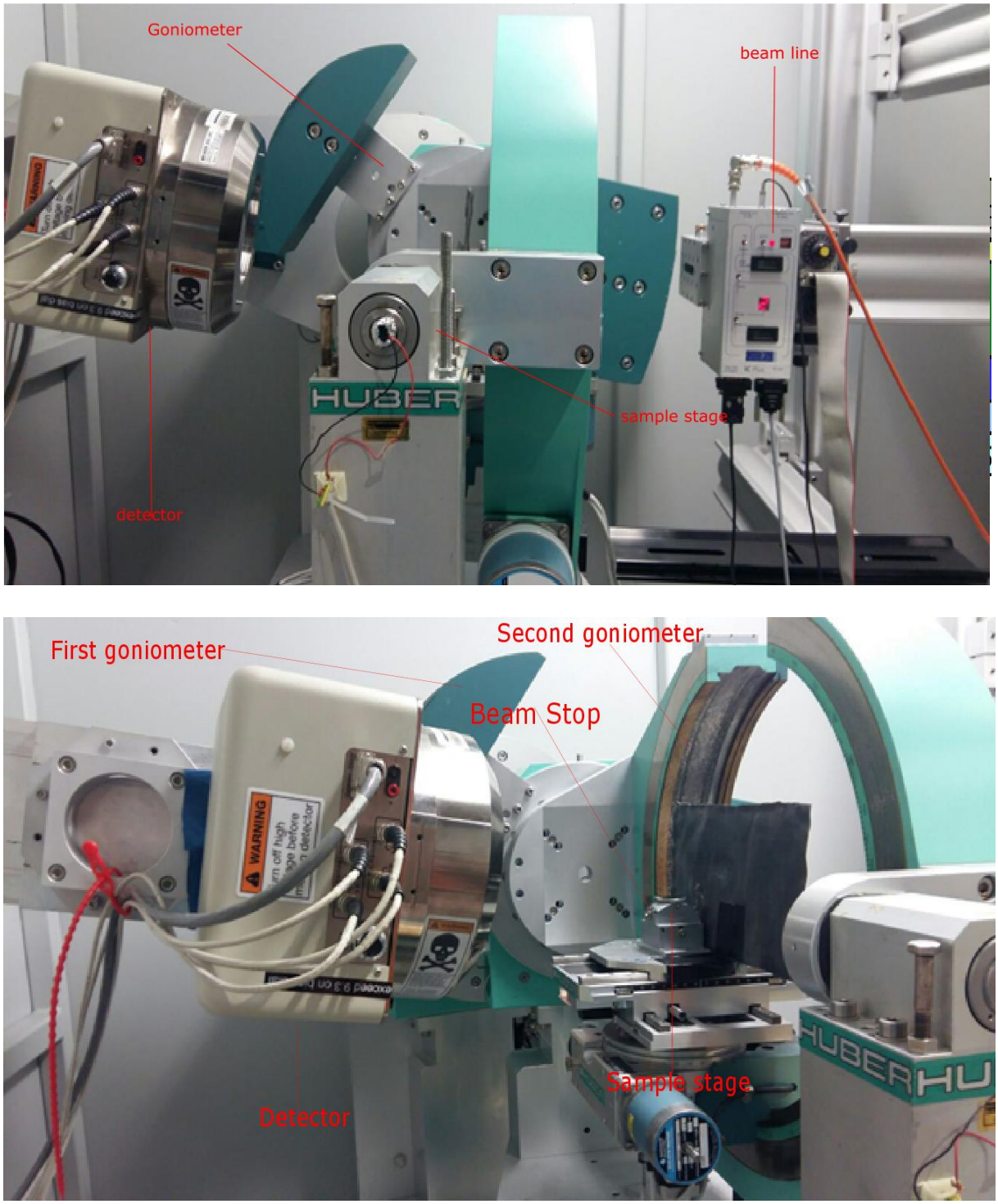

Fig. 6.6. GIWAXS setup at BESSY II Berlin.

Grazing incidence wide angle X-Ray diffraction was carried out in BESSY II synchrotron in Berlin. This setup measured dropcast samples of semiconductor 7mg/ml cast from Chloroform and Chlorobenzene on thermally grown silicon dioxide on bulk silicon substrates. A large

curved detector was aligned on a goniometer to a sample stage with lead beam stop. Attenuator was attached to beam line. No device was put in place to reduce air scattering. The resulting diffraction patterns have a lot of background noise and irradiation times were in the order of 20 minutes leaving possibility of x-ray decomposition of semiconductor in question. This system is not ideal for measuring thin films but can still be a useful indicator to levels of crystallinity in the film and a qualitative indicator of structural rearrangement due to thermal or Photocrosslinking processes.

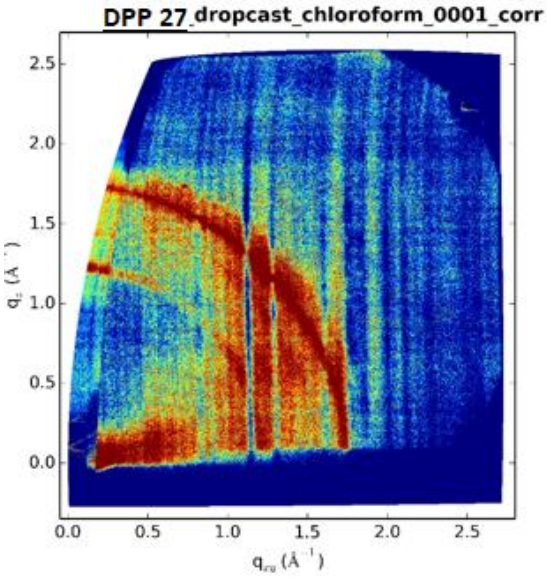
DPP 27_dropcast_chloroform_0001_corr
2.5
2.0
1.5
1.0
0.5
0.0
q_z (Å^{-1})
0.0
0.5
1.0
1.5
2.0
2.5
q_{xy} (Å^{-1})

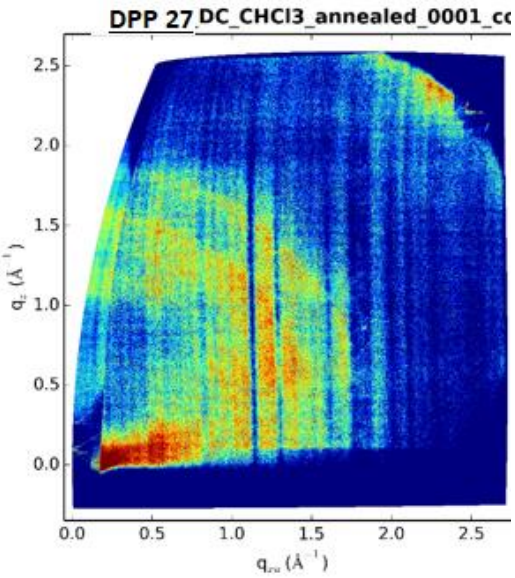
DPP 27_DC_CHCl3_annealed_0001_cc
2.5
2.0
1.5
1.0
0.5
0.0
q_z (Å^{-1})
0.0
0.5
1.0
1.5
2.0
2.5
q_{xy} (Å^{-1})

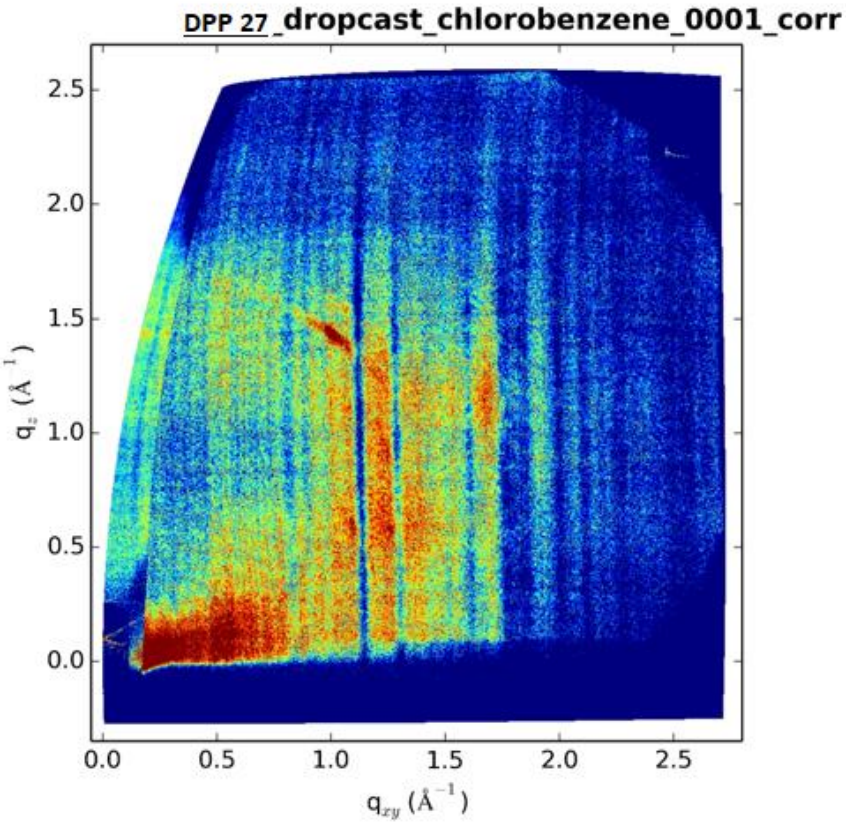
DPP 27_dropcast_chlorobenzene_0001_corr
2.5
2.0
1.5
1.0
0.5
0.0
q_z (Å^{-1})
0.0
0.5
1.0
1.5
2.0
2.5
q_{xy} (Å^{-1})

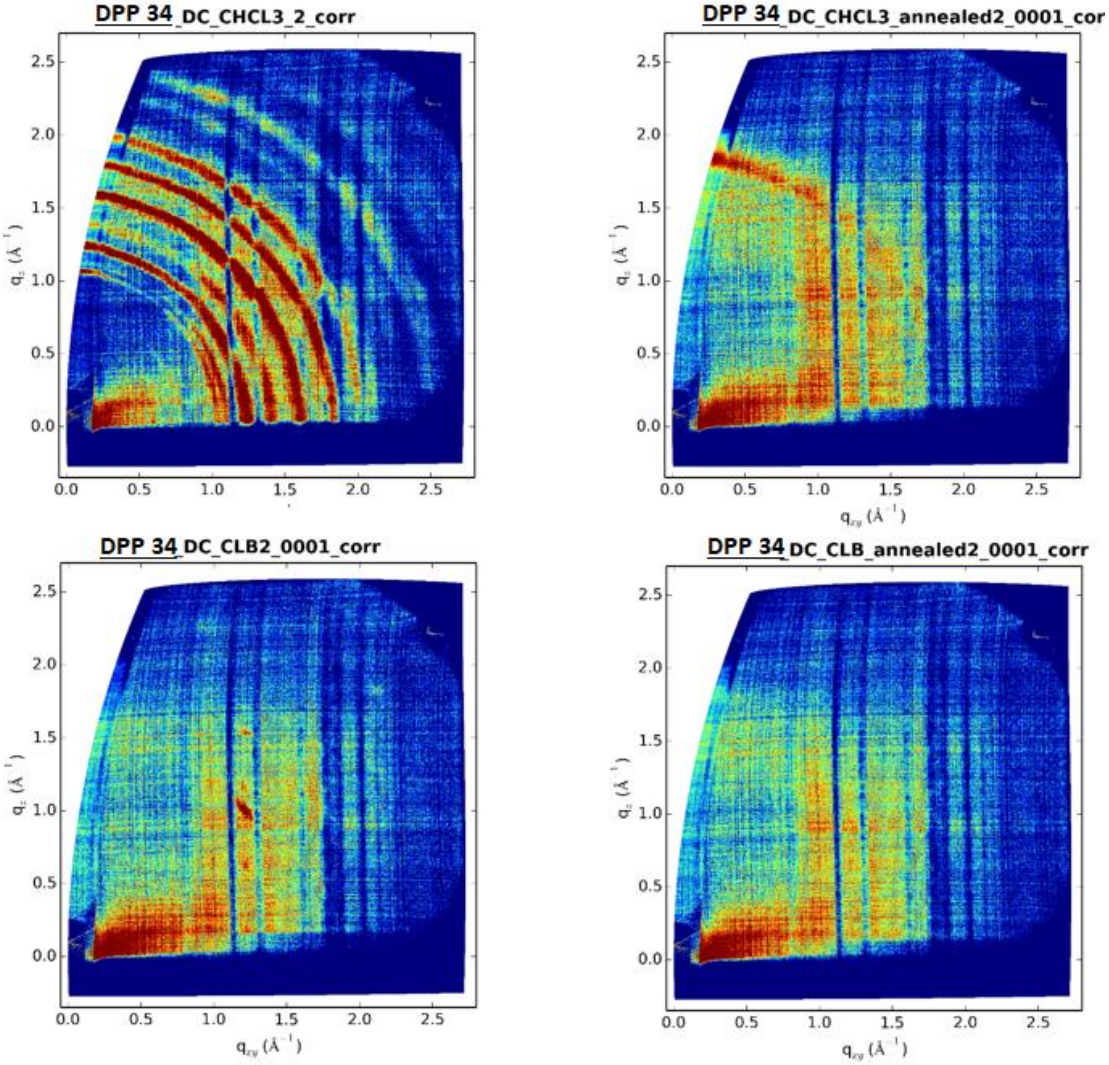

Single crystal

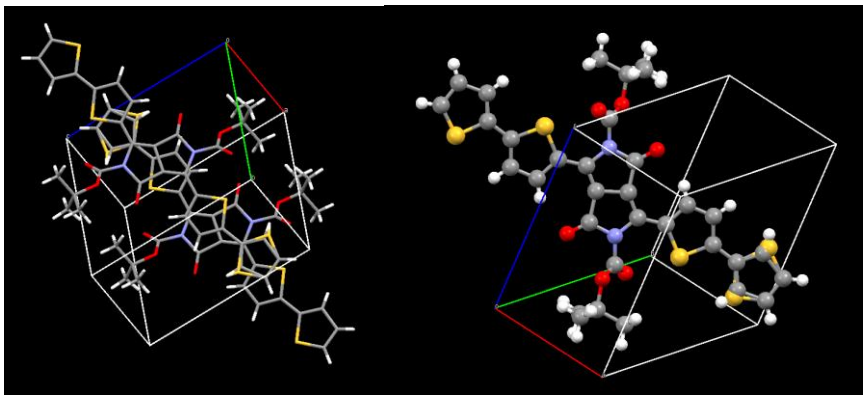

A single crystal of DPP 34 was grown by slow evaporation of a concentrated Chloroform solution. The lattice parameters overlay the spincoated and drop casted GIWAXS samples from BESSY and DIAMOND. This indicates that we have the same crystal structure in thin film as

we do in single crystal grown from chloroform. Strong π-π stacking occurs that appears displaced by the bulky t-Boc units. The single crystal of the deprotected material was not achieved.

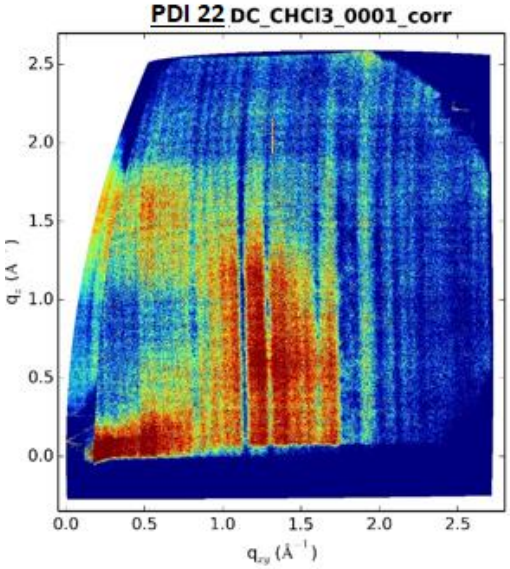

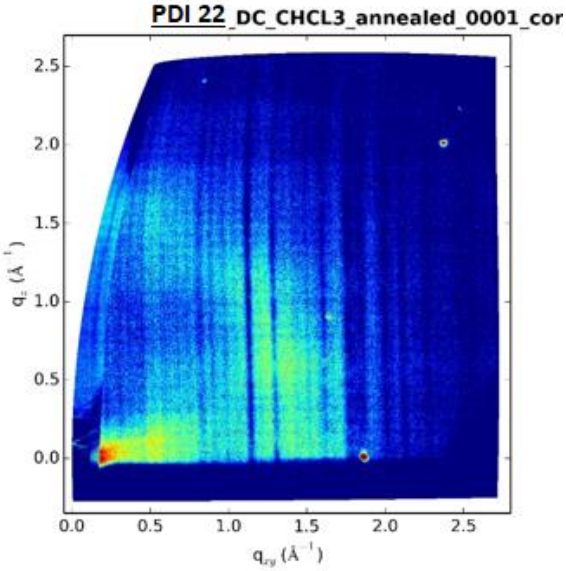

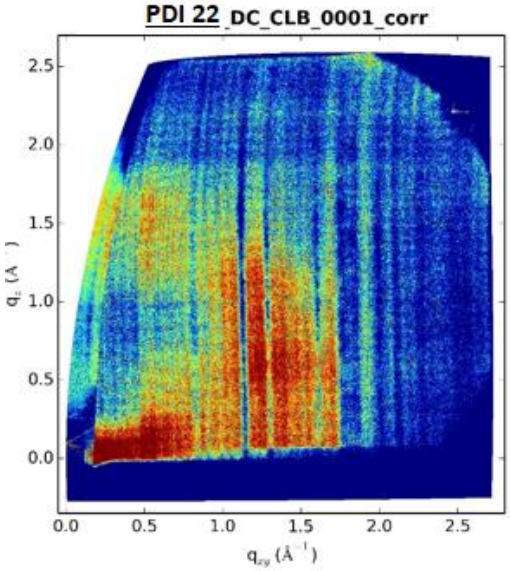

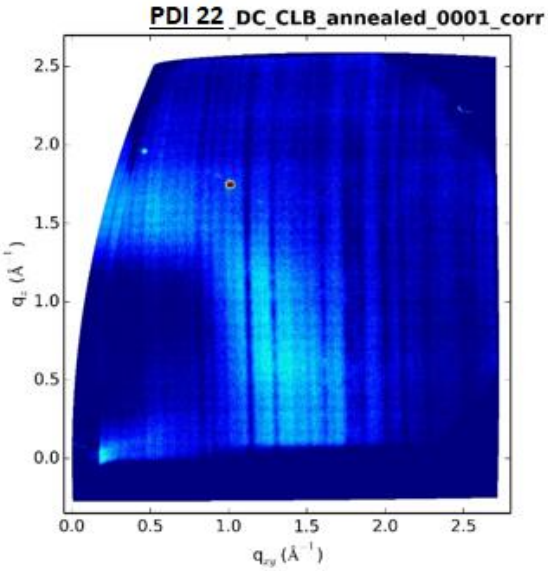

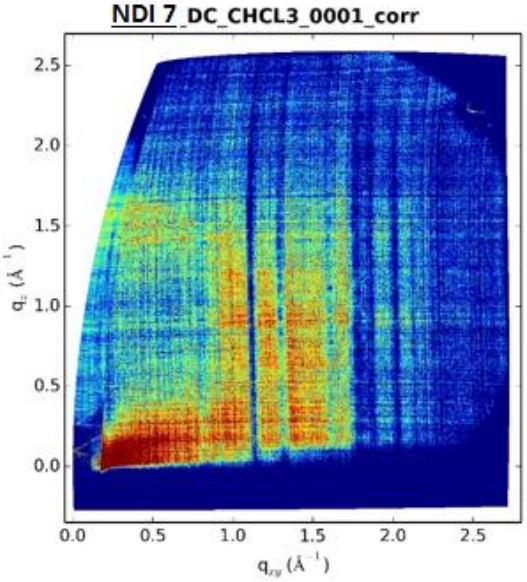
NDI 7_DC_CHCL3_0001_corr
2.5
2.0
1.5
1.0
0.5
0.0
q_z (Å^{-1})
0.0
0.5
1.0
1.5
2.0
2.5
q_{xy} (Å^{-1})

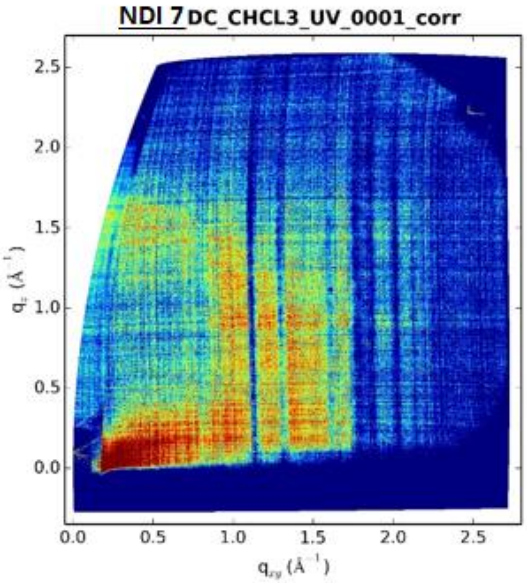
NDI 7DC_CHCL3_UV_0001_corr
2.5
2.0
1.5
1.0
0.5
0.0
q_z (Å^{-1})
0.0
0.5
1.0
1.5
2.0
2.5
q_{xy} (Å^{-1})

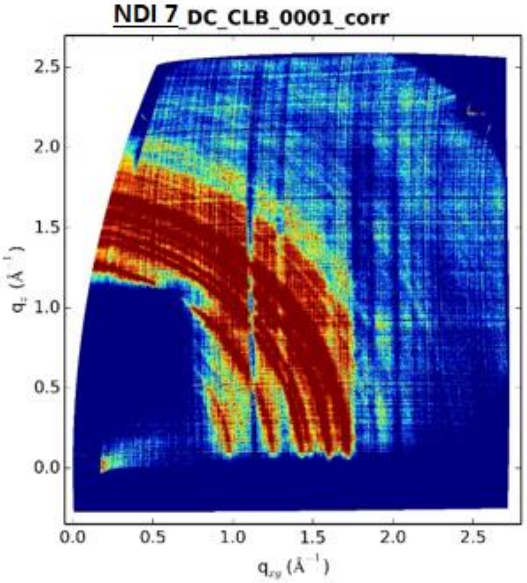
NDI 7_DC_CLB_0001_corr
2.5
2.0
1.5
1.0
0.5
0.0
q_z (Å^{-1})
0.0
0.5
1.0
1.5
2.0
2.5
q_{xy} (Å^{-1})

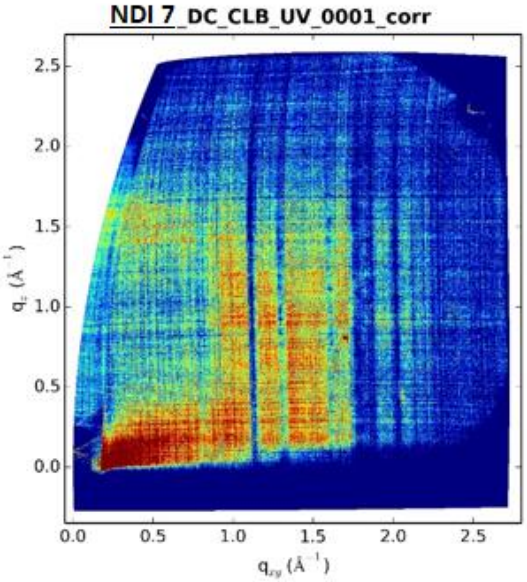
NDI 7_DC_CLB_UV_0001_corr
2.5
2.0
1.5
1.0
0.5
0.0
q_z (Å^{-1})
0.0
0.5
1.0
1.5
2.0
2.5
q_{xy} (Å^{-1})

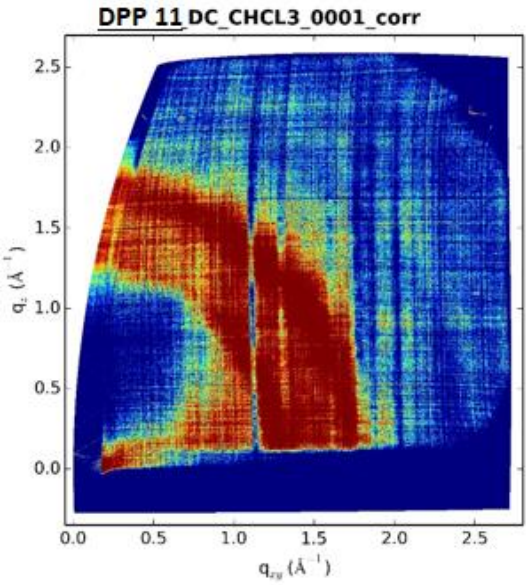
DPP 11_DC_CHCL3_0001_corr
q_z (Å^{-1})
q_{xy} (Å^{-1})
0.0
0.5
1.0
1.5
2.0
2.5

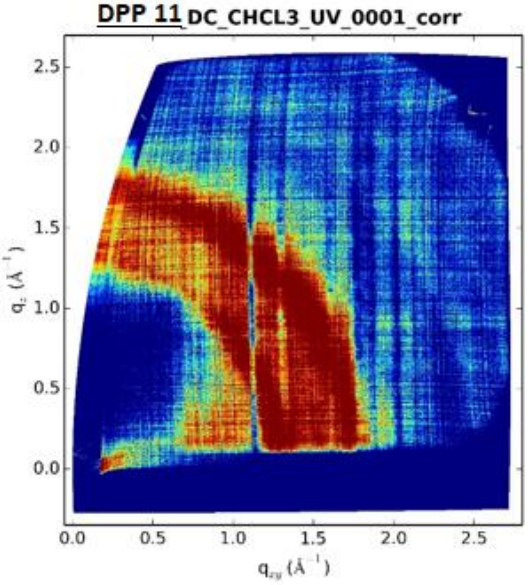
DPP 11_DC_CHCL3_UV_0001_corr
q_z (Å^{-1})
q_{xy} (Å^{-1})
0.0
0.5
1.0
1.5
2.0
2.5

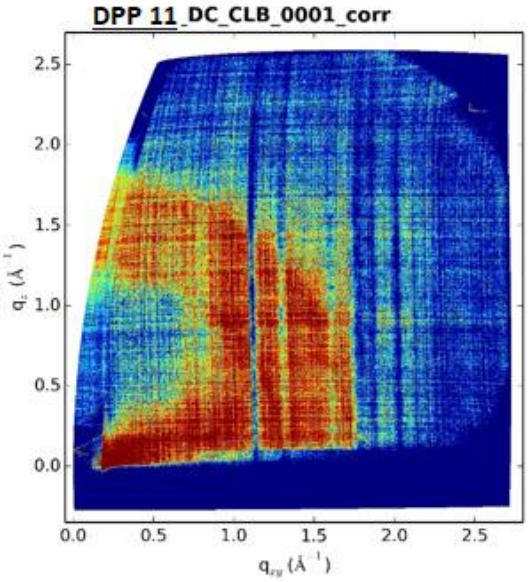
DPP 11_DC_CLB_0001_corr
q_z (Å^{-1})
q_{xy} (Å^{-1})
0.0
0.5
1.0
1.5
2.0
2.5

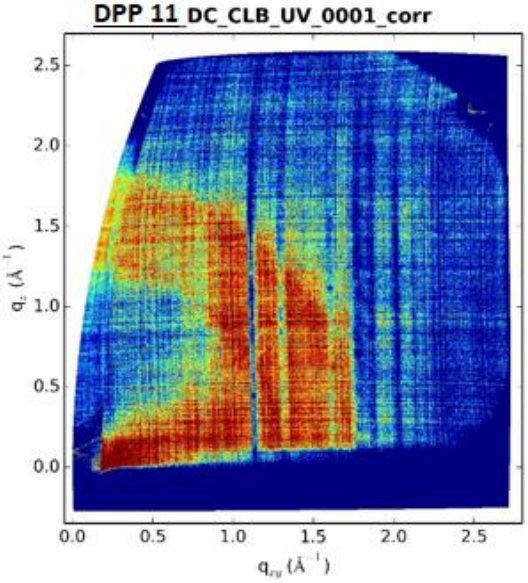
DPP 11_DC_CLB_UV_0001_corr
q_z (Å^{-1})
q_{xy} (Å^{-1})
0.0
0.5
1.0
1.5
2.0
2.5

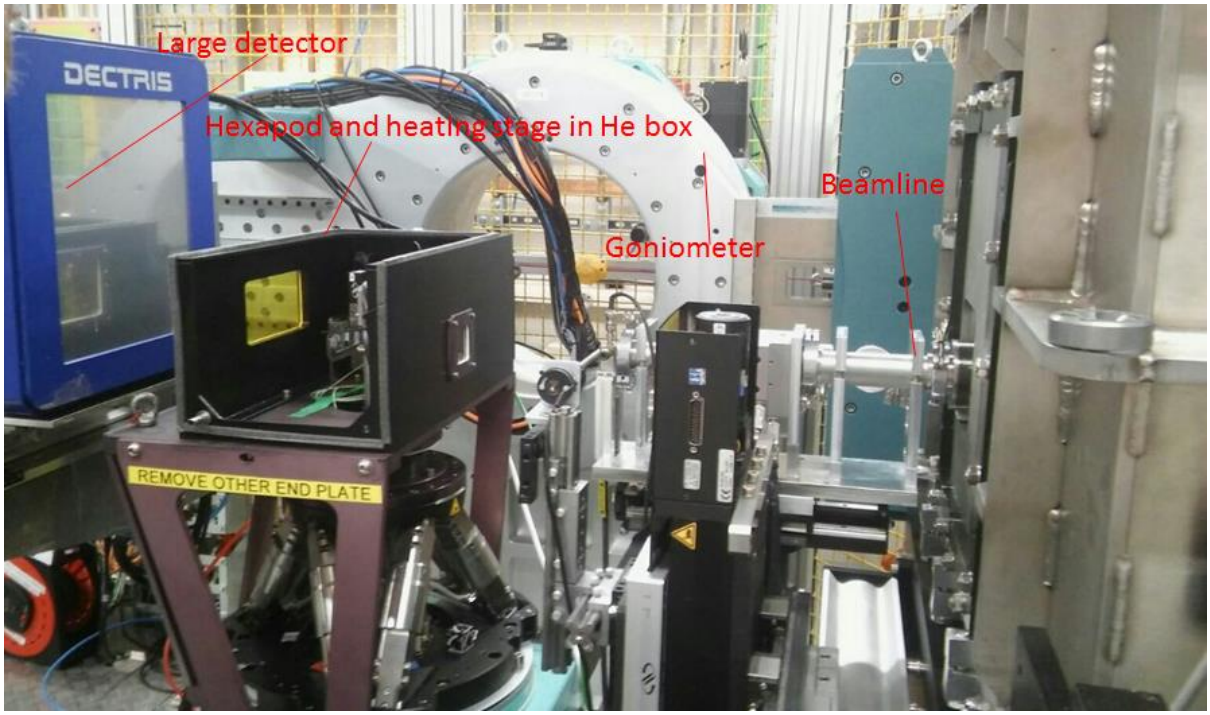

Fig. 6.7. Diamond beam source in England.

Diamond beamline is fully optimised for the study of thin films. A large square detector is made from many high-resolution detector pieces a hexapod with heating plate allows for very fine alignment and in-situ thermal studies the Helium chamber significantly reduces air scattering and an automated beamline block reduces the time that the intense x-ray beam is incident on the semiconductor.

Appendix 1- X-Ray characterisation

DPP 27 protected

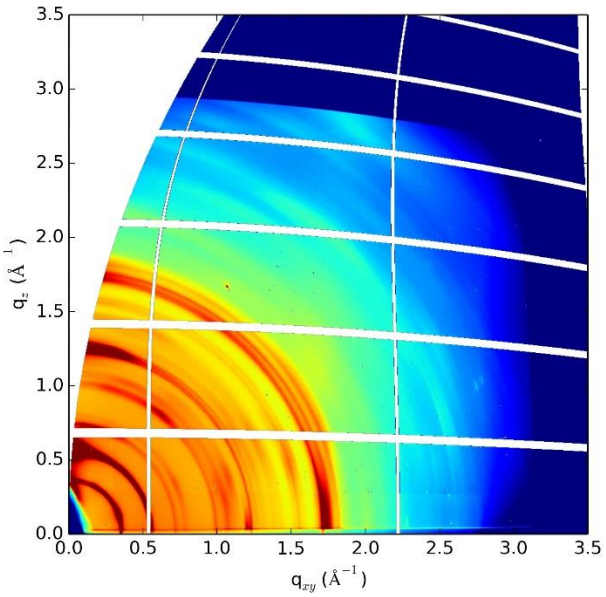

DPP 27 deprotected

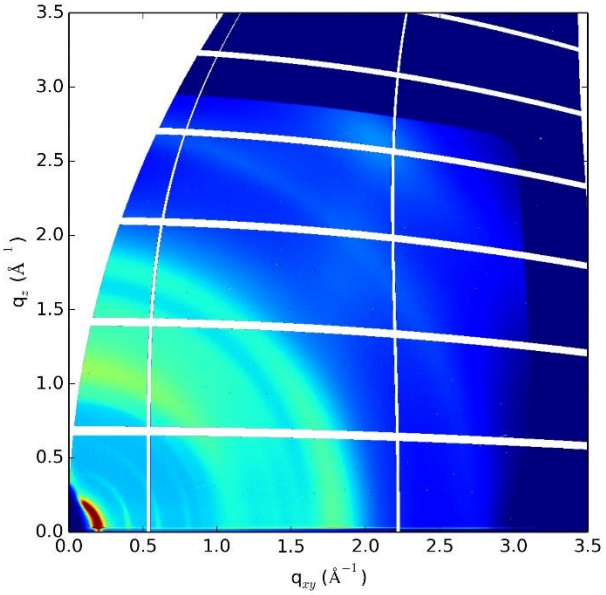

Appendix 1- X-Ray characterisation

DPP 34 protected

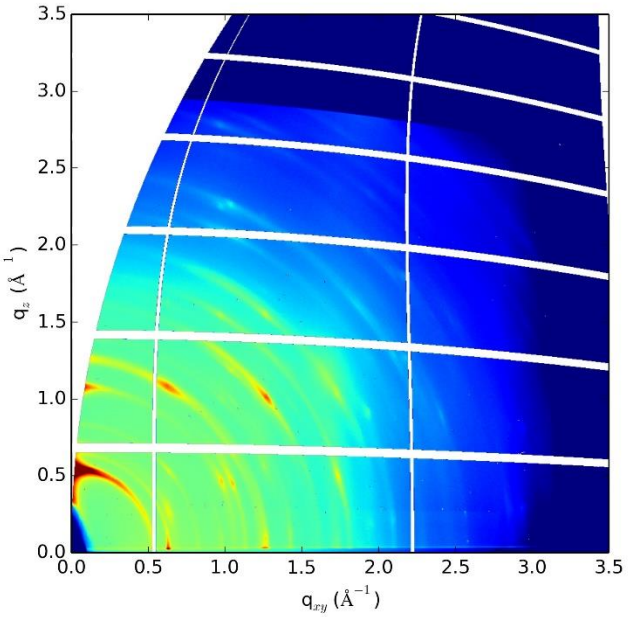

DPP 34 deprotected

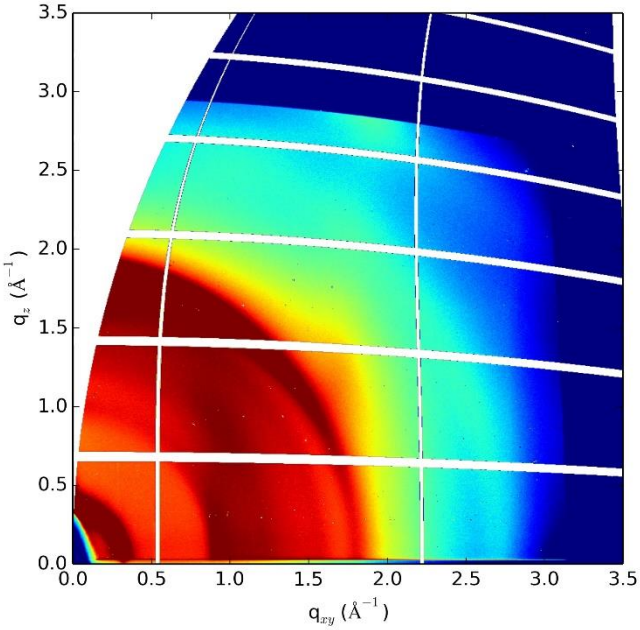

PDI 22 pre-thermal treatment

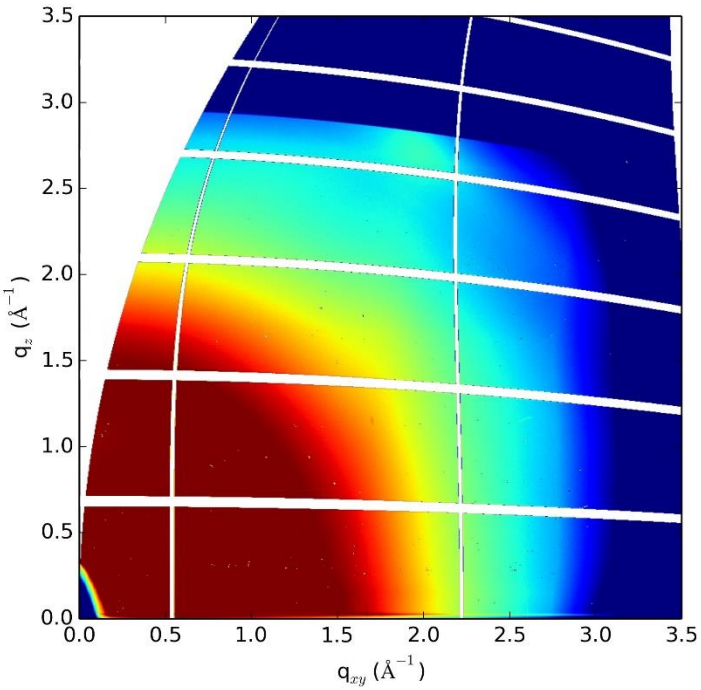

PDI 22 post-thermal treatment

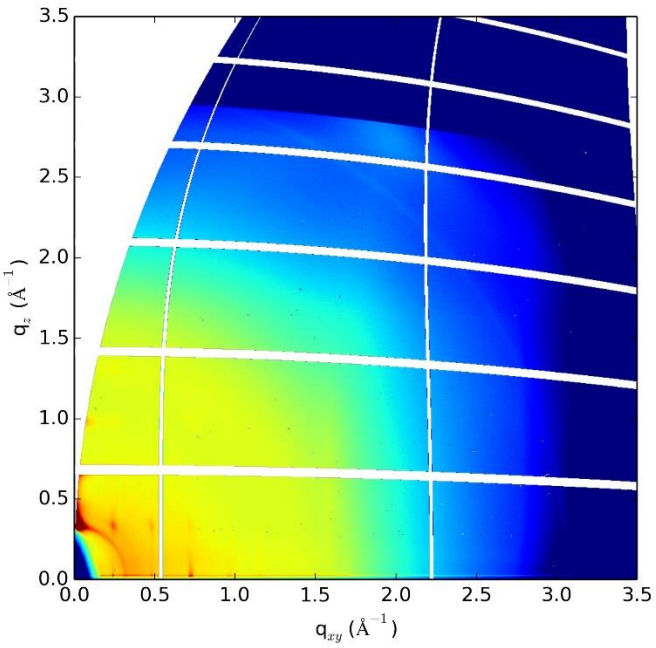

Amorphous film pre-treatment. Low levels of order seen after treatment. Pyrrolic bridge unit potentially decomposes under the high temperatures required for deprotection.

NDI 7 pre-Photocrosslinking

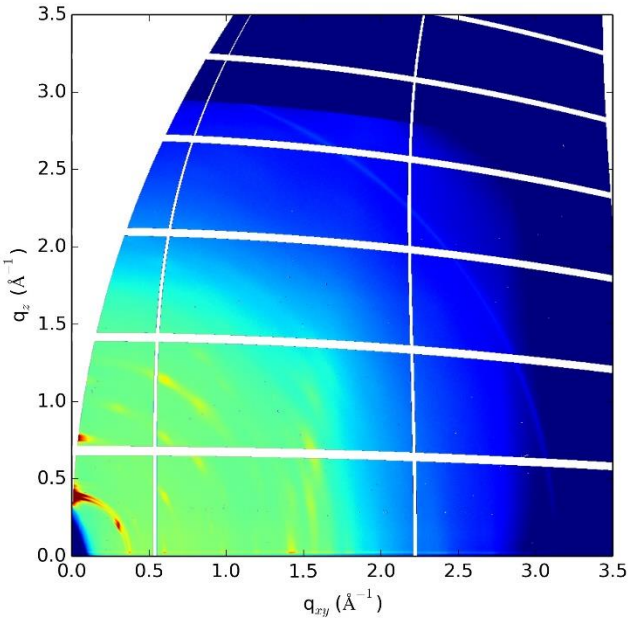

NDI 11 post-Photocrosslinking

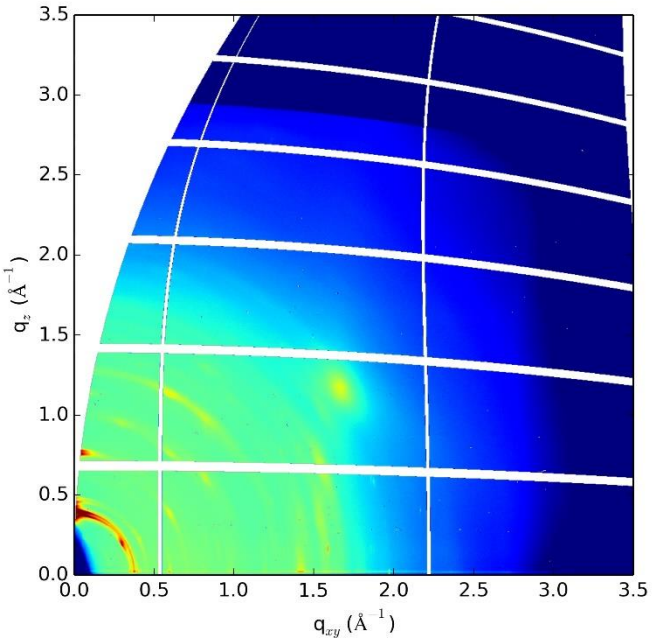

Appendix 1- X-Ray characterisation

DPP 11 pre-Photocrosslinking

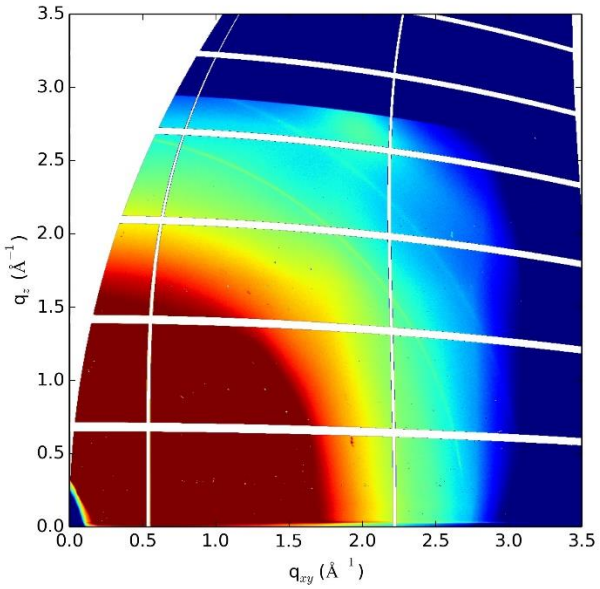

DPP 11 post-Photocrosslinking

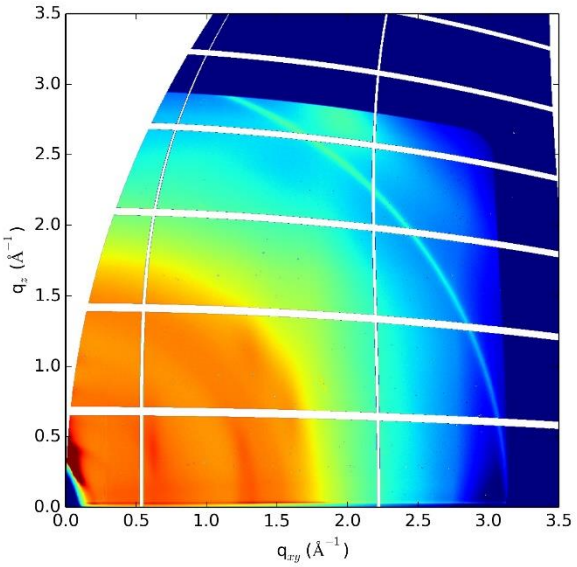

Spincast from chloroform MR20 initially shows an amorphous state. After Photocrosslinking a level of order can be seen with the cores perhaps orienting themselves perpendicular to the substrate.

References

1. Yasaka, M. X-ray thin-film measurement techniques. *V. X-ray reflectivity Meas. Rigaku J.* **26,** 1–9 (2010).

2. Fewster, P. F. X-ray analysis of thin films and multilayers. **59,** 1339–1407 (1996).

Experimental.

Synthesis of 3,6-di(thiophen-2-yl)pyrrolo[3,4-c]pyrrole-1,4(2H,5H)-dione **(1)**

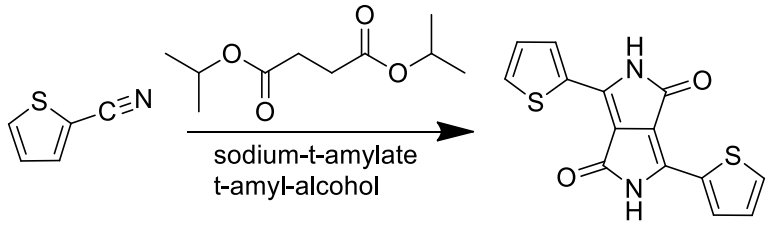

1

In a RBF with condenser and dropping funnel, add 80ml of t-amyl alcohol to sodium-t-amylate (32.87g, 298.5mmol) under inert atmosphere. It may be required to gently heat this mixture to fully dissolve the sodium-t-amylate. Using a syringe inject 2-cyanothiophene (25g, 299mmol) and bring to reflux. The reaction turns a brown colour. To the dropping funnel add 20ml t-amyl alcohol and di-isopropyl succinate (20.1g, 99.5mmol). allow dropwise addition over 1 hour. Reflux for 3 hours before cooling to 50°C. Add 85ml isopropanol followed by 150ml water to protonate the lactamic Nitrogen. The colour chances from a deep purple to red. Cool to Room temperature and gravity filter. Subsequent thorough washing with boiling 1:1 isopropanol: water affords the pigment. No NMR can be performed due to complete insolubility of pigment. Dry in vacuum oven at 50°C overnight (16.86g, 56%yield)

Synthesis of 2,5-dioctyl-3,6-di(thiophen-2-yl)pyrrolo[3,4-c]pyrrole-1,4(2H,5H)-dione **(2)**

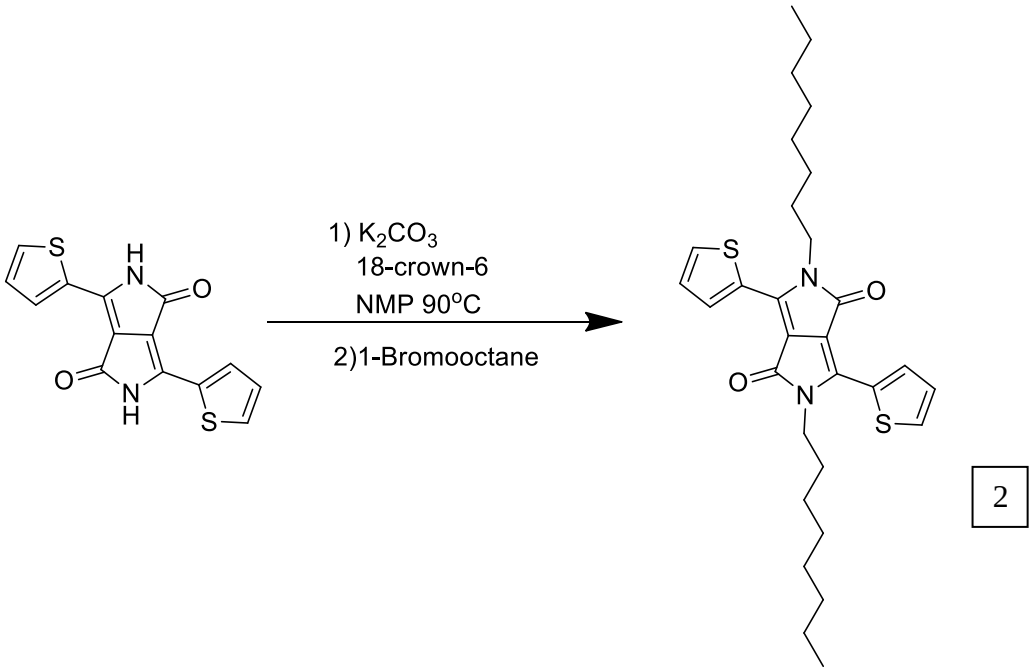

2

In a two neck round bottom flask with magnetic stirrer, add K_2CO_3 (13.66g, 98.9mmol), 18-crown-6 (1.04g, 3.97mmol) and 3,6-di(thiophen-2-yl)pyrrolo[3,4-c]pyrrole-1,4(2H,5H)-dione (10g, 33mmol) under inert atmosphere. Charge the reaction vessel with 200ml anhydrous NMP. Stir for1 hour at 90°C. Dropwise addition of 1-Bromooctane (25.47g, 132mmol) was carried out at a rate of 1ml/hour using and automated syringe pump. The reaction mixture was stirred overnight at 90°C. The reaction is quenched with 10% by weight NaCl solution and extraction with diethyl ether. Filter directly to was through soluble bi-products and excess bromooctane. Take up solid in filter paper and perform hot filtration in toluene. Remove solvent under reduced pressure. Collect and wash with methanol to afford dark shiny powder. (10.52g, 20mmol, 61% yield.)

^{1}H NMR ($CDCl_3$, 500Hz): δ[ppm.] 8.91(d, J=3.73Hz, 2H) 7.64(d, J=5.03Hz, 2H) 7.28(t, J=4.1Hz, 2H) 4.06 (t, J=7.6Hz, 4H) 1.74(q, J=7.8Hz, 4H) 1.41(q, J=7.064Hz, 6H) 1.28(m, 1.64) 0.86(t, J=6.8Hz, 6H)

Synthesis of 2-((6-([2,2'-bithiophen]-5-yl)hexyl)oxy)tetrahydro-2H-pyran **(3)**

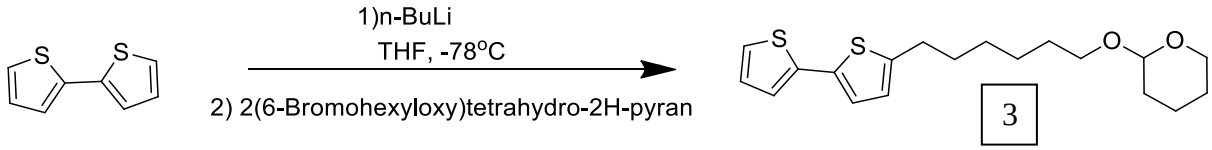

To a tri necked 500ml round bottom flask with thermometer bi-thiophene (5g, 30mmol) under nitrogen. Add 200 ml of dry THF and cool to -80 in bath of liquid nitrogen and ethyl acetate. Slowly add 15 ml(24mmol) of 1.6M butyl lithium dropwise monitoring colour fluctuations (green to yellow) as equilibrium is found. Monitor the temperature of reaction upon addition. A Yellow Precipitate forms Stir at this temperature for 1 hour before adding 2(6-bromohexyloxy)tetrahydro-2H-pyran (5.15g, 19.4mmol) dissolved in 30ml Dry THF. Allow mixture to come to room temperature and stir overnight. Colour changes to dark orange, precipitate dissolves. Pour onto ice and stir before extracting with diethyl ether. Organic layer washed with brine and water, dried over $MgSO_4$. Filter and remove Solvent under reduced pressure. Purify using silica column 50:50 Heptane: DCM. Remove unreacted alkylating agent through steam distillation. (4.95g, 14mmol, 72% yield)

^1H NMR ($CDCl_3$, 500Hz) : δ[ppm.] 7.16(dd, J=5.2Hz, J=1.6Hz, 1H) 7.09(dd, J= 3.4Hz,J= 1.6Hz, 1H) 6.9(m, 2H) 6.67(d, J=3.4Hz, 1H) 4.38(t, J=3.68Hz, 1H) 3.87(m, 1H) 3.75(m, 1H) 3.50(m, 1H) 3.39(m, 1H) 2.79(t, J=7.6Hz, 2H) 1.8(m, 1H) 1.709(m, 3H) 1.41 (m, 7H) 1.40(q, J=3, 4H)

Synthesis of tributyl(5'-(6-((tetrahydro-2H-pyran-2-yl)oxy)hexyl)-[2,2'-bithiophen]-5-yl)stannane **(4)**

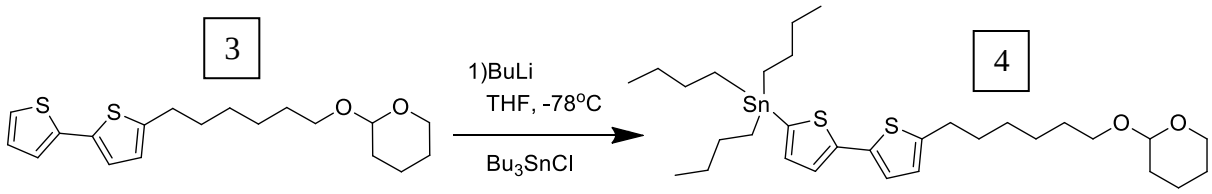

In a two neck RBF charge Bithiophene (0.351g, 1mmol) under inert conditions. Dissolve in 15ml dry THF. Cool to -80°C. Dropwise add BuLi (1.6M 1.75ml, 2.8mmol). Stir at -80°C for 15 minutes allow to come to room temperature for 30 minutes before re-cooling to -80°C. Slowly add tributyltin chloride (0.82ml, 3.03mmol). Stir at room temperature for three hours before removing solvent under reduced pressure on manifold. Product is kept under nitrogen and is used directly in subsequent Stille coupling.

Synthesis of 2,7-dihexyl-4,9-bis(5'-(6-((tetrahydro-2H-pyran-2-yl)oxy)hexyl)-[2,2'-bithiophen]-5-yl)benzo[lmn][3,8]phenanthroline-1,3,6,8(2H,7H)-tetraone **(5)**

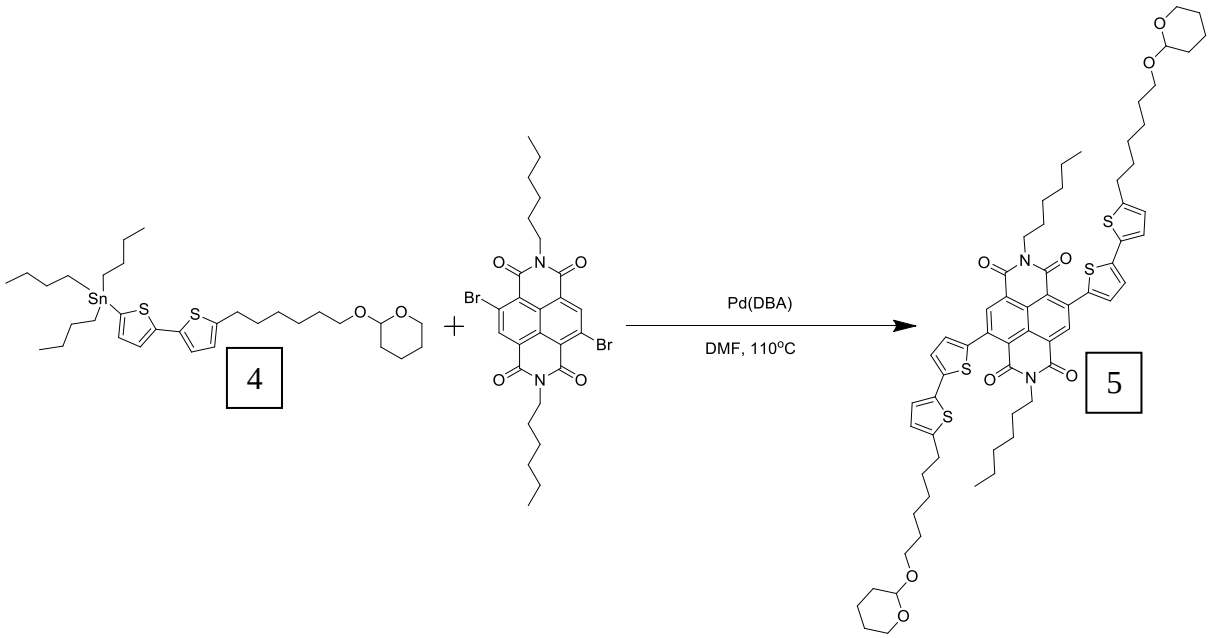

In a three neck RBF with condenser, charge 4,9-dibromo-2,7-dihexylbenzo[lmn][3,8]phenanthroline-1,3,6,8(2H,7H)-tetraone (0.36g, 0.607mmol) and Tris(dibenzylideneacetone)dipalladium(0) (100mg) under inert conditions. Take up the Stannly residue **4,** which is being kept under a nitrogen atmosphere, with 15 ml of dry DMF. Using a syringe transfer this to the main reaction vessel. Heat to 110°C and stir vigorously for

12 hours. Remove solvent under reduced pressure and take up dark oil with methanol. Filter to afford a dark blue material. Product washed through a silica filter to remove inorganic materials. Dark blue powder recovered after recrystallization in acetonitrile (66% yield)

^{1}H NMR ($CDCl_3$, 500Hz) : δ[ppm.] 7.1561(d, J=5Hz, 2H) 7.08(d, J=4.14Hz, 2H) 6.97(m, 4H) 6.6(d, J=4.1Hz, 2H) 4.5(t, J=3.2Hz, 2H) 3.86(m, 2H) 3.7(m, 2H) 3.5(m, 2H) 3.38(m, 2H) 2.79(t, J=7.36Hz, 4H) 1.83(m, 3H) 1.72(m, 8H) 1.61(m, 11H) 1.48(m, 67H) 1.32(m, 82H) 0.9(m, 94H) 0.86(m, 41.7) 0.7(m, 6H)

Synthesis of 2,7-dihexyl-4,9-bis(5'-(6-hydroxyhexyl)-[2,2'-bithiophen]-5-yl)benzo[lmn][3,8]phenanthroline-1,3,6,8(2H,7H)-tetraone **(6)**

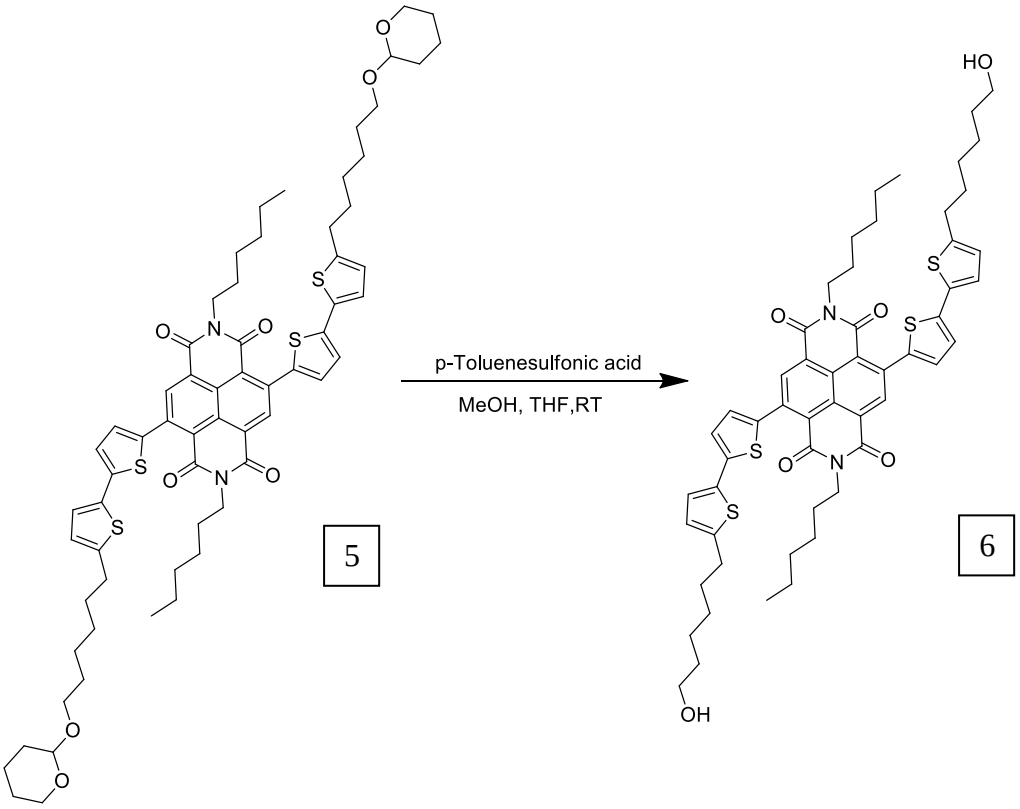

To a RBF with condenser charge **5** (0.59g, 0.52mmol) to 40ml MeOH and 10ml THF. Stir vigorously until well dispersed. Add 10% by weight p-toluenesulphonic acid (0.059g). Reflux and monitor by TLC with a 1:1 THF:Heptane eluent. When reaction is complete remove solvent under reduced pressure. Wash and filter residue with water. Quantitative yields achieved

^{1}H NMR ($CDCl_3$, 500Hz) : δ[ppm.] 8.77(s, 2H) 7.27(d, J=3.6Hz, 2H) 7.17(d, J=3.8Hz, 2H) 7.07(d, J=3.6Hz, 2H) 6.7 (d, J=3.6Hz, 2H) 4.13(t, J=7.8Hz, 4H) 3.66(t, J=7.27Hz, 4H) 2.83(t, J=7.27, 4H) 2.496(m, 2H) 2.30(m, 2H) 1.889(s, 1H) 1.71(m, 10H) 1.42(m, 16H) 0.87(t, J=6.3Hz, 12H)

Synthesis of (5',5'''-(2,7-dihexyl-1,3,6,8-tetraoxo-1,2,3,6,7,8-hexahydrobenzo[lmn][3,8]phenanthroline-4,9-diyl)bis([2,2'-bithiophene]-5',5-diyl))bis(hexane-6,1-diyl) diacrylate **(7)**

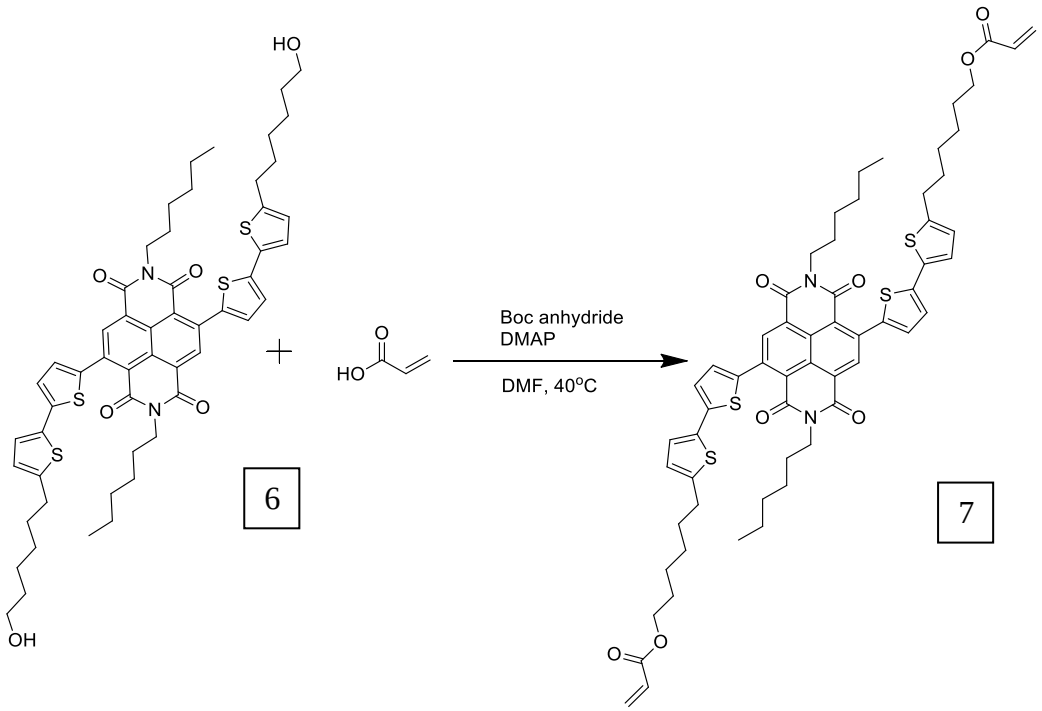

In a RBF add **6** (0.1g, 0.1mmol), Acrylic acid (0.0144g, 0.2mmol), dimethyl aminopyridine (0.001g, 0.01mmol) and Di-tert-butyl dicarbonate (0.045g, 0.2mmol) to 3ml of DMF. Stir at 40°C for 72 hours. The reaction is slow and comes to a point of equilibrium where no further reaction occurs. Dilute with CHCL3 and wash with water. Separate fractions dry with $MgSO_4$ and remove solvent under reduced pressure. Silica column with 3:1 ethyl Acetate: Heptane. Three fractions recovered, first fraction recovered is the desired product. 54% yield.

^{1}H NMR ($CDCl_3$, 500Hz) : δ[ppm.] 8.775(s, 2H) 7.27(d, J=4.6Hz, 2H) 7.17(d, J=3.5Hz, 2H) 7.072(d, J=4.09Hz, 2H) 6.71(d, J=2.9Hz, 2H) 6.403(d, J=18Hz, 2H) 6.13(dd, J=18Hz, 2H)

5.82(d, J=12Hz, 2H) 4.172(t, J=7.3Hz, 4H) 2.83(t, J=8.7Hz, 4H) 1.7(m, 14H) 1.43(m, 14H) 1.25(m, 19H) 0.87(t, J=7.2Hz, 12H)

13C NMR (CDCl3, 125.7 MHz): δ[ppm.] 167.23, 163.06, 146.9, 142.14, 140.41, 139.48, 137.43, 135.11, 131.42, 130.81, 129.47, 128.38, 126.23, 125.95, 125.08, 124.13, 123.48, 65.43, 42.07, 32.39, 32.29, 30.98, 30.53, 29.52, 29.40, 28.86, 27.63, 26.38, 23.44, 14.95, 1.89

Synthesis of 3,6-bis(5-bromothiophen-2-yl)-2,5-dioctylpyrrolo[3,4-c]pyrrole-1,4(2H,5H)-dione **(8)**

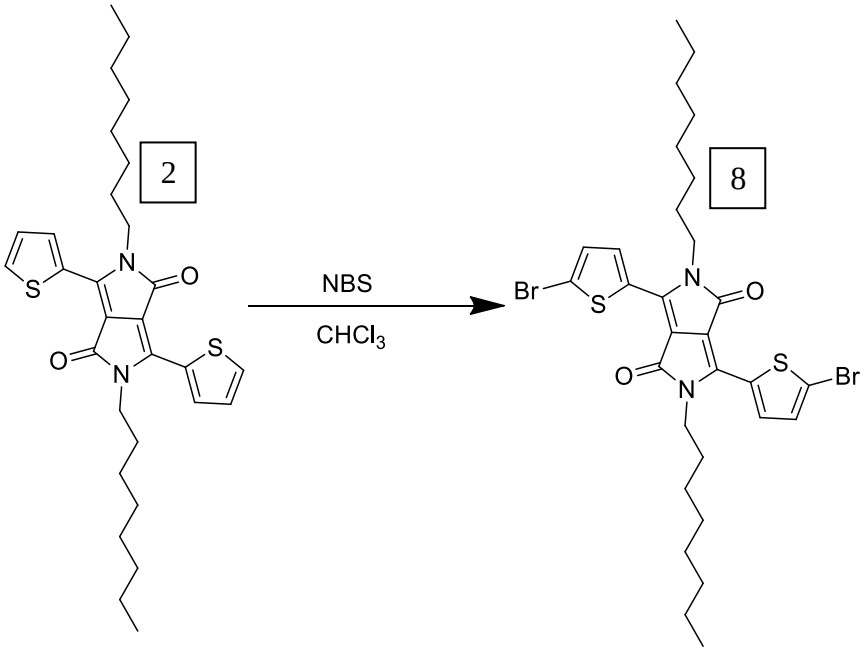

In a brown RBF add **2** (1g, 1.9mmol) under inert conditions. Add 50ml anhydrous $CHCl_3$ and cool to -10°C with a salt and ice bath. In a separate flask charge n-bromosuccinimide (0.75g, 4.18mmol) and dissolve in the minimum amount of dry solvent. Take up the n-bromosuccinimide in a syringe and slowly add this to the solution of **2** over 10 minutes. Allow to slowly come to room temperature. Stir for 24hours. Solution turns from a bright orange to a dark purple/red. Wash solution with 10% NaOH 100ml followed by 2x100ml washings with water. Dry over $MgSO_4$ and remove solvent under reduced pressure. Purify with silica column and Recrystallize in toluene to afford product. (67% yield)

^{1}H NMR ($CDCl_3$, 500Hz) : δ[ppm.] 8.68(d, J=4.2Hz, 2H) 7.24(d, J=3.81Hz, 2H) 3.98(t, J=7.7Hz, 4H) 1.71(m, 4H) 1.4(m, 4H) 1.28(m. 18H) 0.87 (t, J=3.9Hz, 6H)

Synthesis of 2,5-dioctyl-3,6-bis(5"-(6-((tetrahydro-2H-pyran-2-yl)oxy)hexyl)-[2,2':5',2"-terthiophen]-5-yl)pyrrolo[3,4-c]pyrrole-1,4(2H,5H)-dione **(9)**

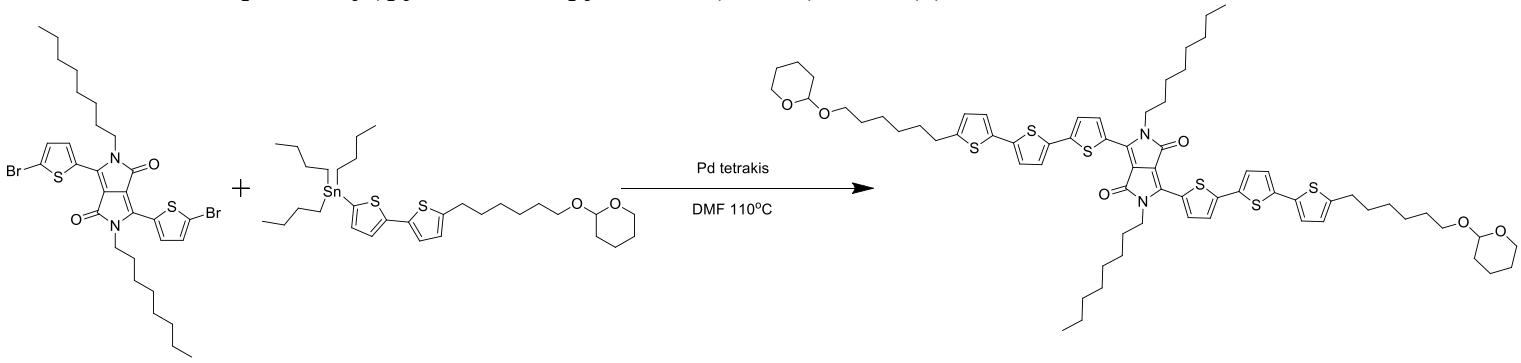

8 4 9

In a three neck RBF with condenser, add **8** (0.8g, 1.17mmol) and palladium tetrakis (100mg) under inert conditions. Add 15ml dry DMF. Take up the freshly prepared Stannly residue **4,** which is being kept under a nitrogen atmosphere, with 15 ml of dry DMF. Using a syringe transfer this to the main reaction vessel. Heat to 110°C and stir vigorously for 12 hours. A solid crystalline material precipitates. Filter and wash with methanol and water. Product washed through a silica filter with $CHCl_3$ to remove inorganic materials. (79%Yield)

^{1}H NMR ($CDCl_3$, 500Hz) : δ[ppm.] 8.91(d, J=3.9Hz, 2H) 7.21(d, J=4.2Hz, 2H) 7.15(d, J=3.8Hz, 2H) 6.9(dd, J=3.1Hz, 2.8Hz, 4H) 6.67(d, J=3.6Hz, 2H) 4.57(t, J=3.87Hz, 2H) 4.05(t, J=7.65Hz, 4H) 3.8(m, 2H) 3.74(m, 2H) 3.49(m, 6H) 3.38(m, 2H) 2.78(t, J=7.4Hz, 4H) 1.76(m, 13H) 1.86(m, 14H) 1.42(m, 16H) 1.28(m, 13H) 0.87(t, J=7.15Hz, 6H)

Synthesis of 3,6-bis(5"-(6-hydroxyhexyl)-[2,2':5',2"-terthiophen]-5-yl)-2,5-dioctylpyrrolo[3,4-c]pyrrole-1,4(2H,5H)-dione **(10)**

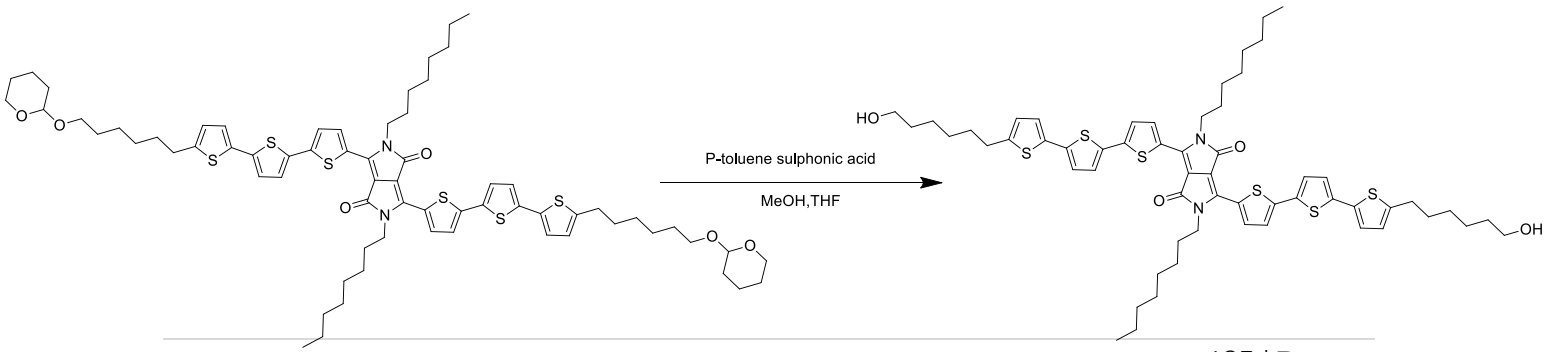

9

10

In a RBF with condenser add **9** (1.07g, 0.87mmol) to 40ml 1:1 MeOH :THF. Stir well and add 0.107g p-toluene sulphonic acid. Bring to reflux for 12 hours. Remove solvent and take up residue in H_2O. Filter and dry in vacuum oven at 50°C. Blue powder recovered quantitative yields.

^{1}H NMR ($CDCl_3$, 500Hz) : δ[ppm.] 8.94(d, J=4.2Hz, 2H) 7.223(d, J=3.9Hz, 2H) 7.05(d, J=4.02Hz, 2H) 7.03(d, J=3.71Hz, 2H) 6.71(d, J=3.71Hz, 2H) 4.09(t, J=7.8Hz, 4H) 3.65 (m, 7H) 2.81(t, J=7.5Hz, 5H) 1.79(m, 7H) 1.69(m, 13H) 1.416(m, 45H) 1.25(m, 68H) 0.87 (m, 16H)

Synthesis of (5",5""-(2,5-dioctyl-3,6-dioxo-2,3,5,6-tetrahydropyrrolo[3,4-c]pyrrole-1,4-diyl)bis([2,2':5',2"-terthiophene]-5",5-diyl))bis(hexane-6,1-diyl) diacrylate **(11)**

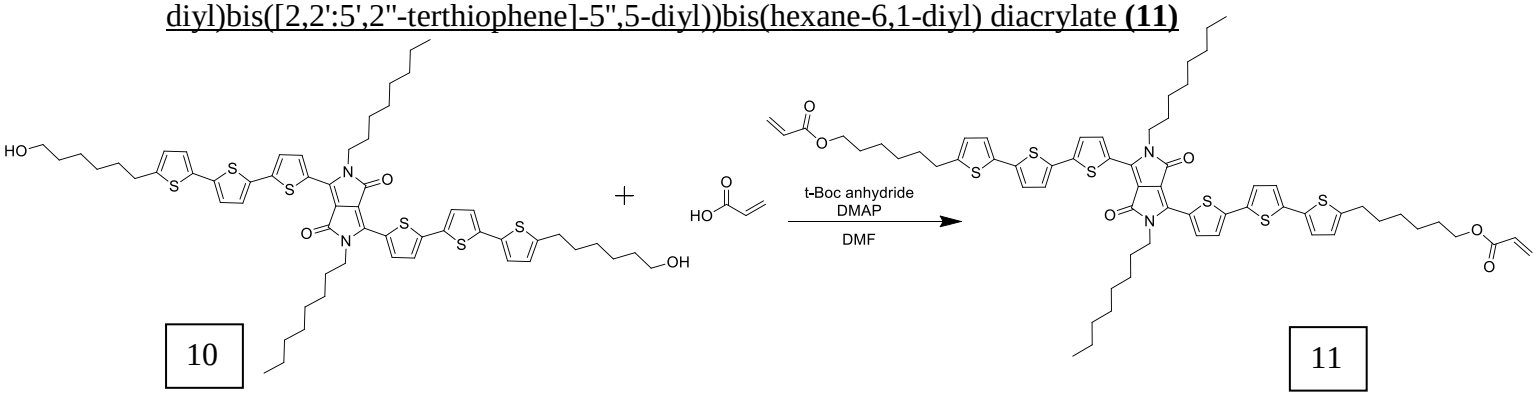

10

11

In a RBF add **10** (0.5g, 0.47mmol), Acrylic acid (0.17g, 2.3mmol), DMAP(0.011g, 0.1mmol) and Di-tert-butyl dicarbonate (0.52g, 2.4mmol) to 3ml of DMF. Stir at 40°C for 72 hours. The reaction is slow and comes to a point of equilibrium where no further reaction occurs. Dilute with CHCL3 and wash with water. Separate fractions dry with $MgSO_4$ and remove solvent under reduced pressure. Silica column with 4:1:1 $CHCl_3$: Ethyl Acetate: Heptane. Three fractions recovered, first fraction recovered is the desired product. 15% yield. Product has an affinity for silica making purification difficult. The reaction performs purely and could not be isolated by crystallisation only.

^{1}H NMR ($CDCl_3$, 500Hz) : δ[ppm.] 8.89(d, J=4.2Hz, 2H) 7.24(d, J=5.3Hz, 2H) 7.16(m, 4H) 7.109(d, J=4.9Hz, 2H) 6.95(d, J=3.48Hz, 4H) 6.65(d, J=3.27Hz, 2H) 6.401(dd, J=17.2Hz, 1.5Hz, 1H) 6.123(dd, J=17.4Hz, 10.2Hz, 1H) 5.8(d, J=10.35Hz, 1H) 4.05(t, J=7.19Hz, 6H)

2.7(t, J=7.84Hz, 4H) 2.33(s, 2H) 1.73(m, 5H) 1.65(m, 9H) 1.48(s, 6H) 1.41(m, 16H) 1.29(m, 17H) 0.88(t, J=7.14Mz, 6H)

13C NMR (CDCl3, 125.7 MHz): δ[ppm.] 167.19, 161.86, 146.77, 143.37, 139,61, 139.43, 137.53, 135.01, 134.93, 131.41. 129.90, 129.45, 129.02, 126.54, 125.92, 125.31, 124.76, 124.59, 108.92, 82.71, 67.90, 63.42, 43.16, 32.71, 32.22, 30.14, 30.11, 29.57, 29.40, 28.67, 27.83, 23.53, 15.00

Synthesis of 2-bromoethyl acrylate **(12)**

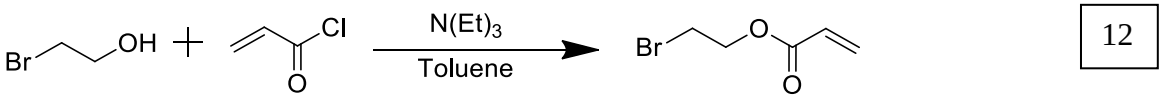

12

To a 3-neck RBF charge 2-bromoethanol (12.65g, 101.0mmol) and triethylamine (11.12g, 110mmol) to 100ml dry toluene. Bubble with Nitrogen to degas and continue to stir under inert atmosphere. Cool to -10°C before adding acryloyl Chloride (10g, 110mmol) dissolved in 20ml dry toluene dropwise with a dropping funnel. Allow to come to room temperature and stir overnight. A white precipitate forms. Monitor with GC-MS for completion. Wash the white solution with 100ml 5% Na_2CO_3 followed by 2x100ml 5% HCl and 2x100ml H_2O. Dry the organic phase and remove solvent under reduced pressure. (94% yield, 16.95g, 95mmol)

^{1}H NMR ($CDCl_3$, 500Hz): δ[ppm.] 6.42(d, J=17.2Hz, 1H) 6.12(dd, J=17.4Hz, 10.3Hz, 1H) 5.83(dd, J=11.2Hz, 1.1Hz, 1H) 4.42(t, J=6.12Hz, 2H) 3.514(t, J=5.37Hz, 2H)

Synthesis of ((3-hydroxyphenyl)azanediyl)bis(ethane-2,1-diyl) diacrylate **(13)**

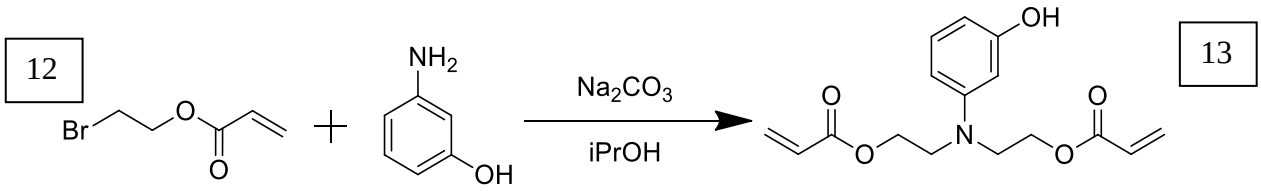

13

In a rbf suspend finely powdered Na_2CO_3(6.435g, 60mmol), 3-aminophenol (2.59g, 24mmol) and **12** (8.47g, 47mmol) in iPrOH 80ml. Reflux for 20hours. Cool, filter and remove solvent under reduced pressure. Thick oil recovered, was oil with heptane to remove residual acrylate and quickly dissolve in a small amount of ethyl acetate to reduce polymerisation. Purify with silica column with 3:1 ethyl acetate: heptane mobile phase. Do not let product go dry as it is extremely reactive and will self-polymerise spontaneously.

Synthesis of 1,3-bis(4-(bis(2-(acryloyloxy)ethyl)amino)-2-hydroxyphenyl)-4-oxocyclobut-2-en-1-yliumolate **(14)**

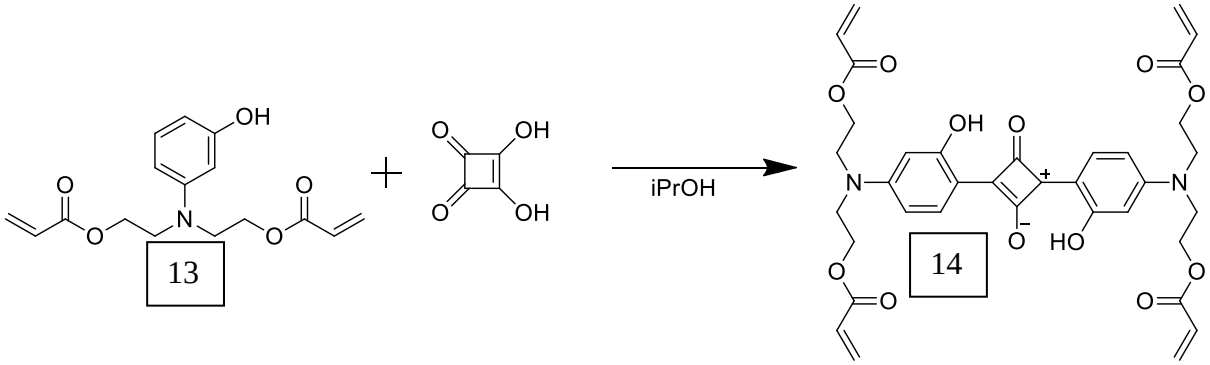

In a two-neck round bottom flask with condenser suspend **13** (1.58g, 5mmol) and squaric acid (0.29g,2.5mmol) in 6ml iPrOH. Bubble to degas with nitrogen. Reflux for 24 hours. Reaction turns dark green with red fluorescence. Multiple spots seen on TLC. Solvent was removed and sample was sonicated with 1) heptane 2) Et_2O and 3)H_2O/MeOH 1:1 with subsequent filtrations in between. This afforded a trace amount of shiny crystalline materials. By TLC 3 separate materials were seen from these crystals so product could not be recovered.

Synthesis of 2-([2,2'-bithiophen]-5-yl)-5,5-dimethyl-1,3-dioxane **(15)**

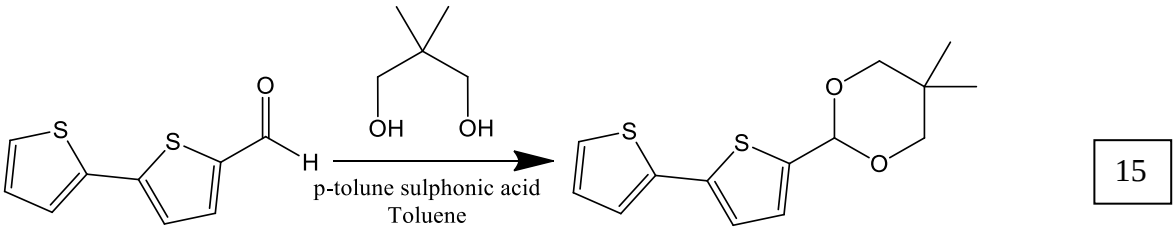

In a two-neck round bottom flask with dean stark, charge bithiophene-carboxaldehyde (0.3g, 1.5mmol), 2,2-dimethyl-1,3-propandiol (1.562g, 15mmol) and p-toluenesulfonic acid monohydrate (0.015g) under a nitrogen atmosphere. Add 80ml of dry toluene and heat to reflux. Remove water with dean stark trap and monitor reaction with GC-MS. Reaction is complete after 2 hours. Neutralise the solution with 200ml saturated sodium bicarbonate solution. Separate organic phase and was with 2x100mL water. Dry with sodium sulphate filter and remove solvent under reduced pressure. Resulting yellow oil will slowly crystallise. Quantitative yield.

^{1}H NMR ($CDCl_3$, 500Hz): δ[ppm.] 7.22(d, J=5.3Hz, 1H) 7.20(d, J=3.5Hz, 1H) 7.09(d, J=3.6Hz, 1H) 7.076(d, J=3.66Hz, 1H) 7.03(t, J=4.4Hz, 1H) 5.64(s, 1H) 3.79(d, J=10.6Hz, 2H) 3.66(d, J=11.1Hz, 2H) 1.34(s, 3H) 0.82(s, 3H)

Synthesis of tributyl(5'-(5,5-dimethyl-1,3-dioxan-2-yl)-[2,2'-bithiophen]-5-yl)stannane **(16)**

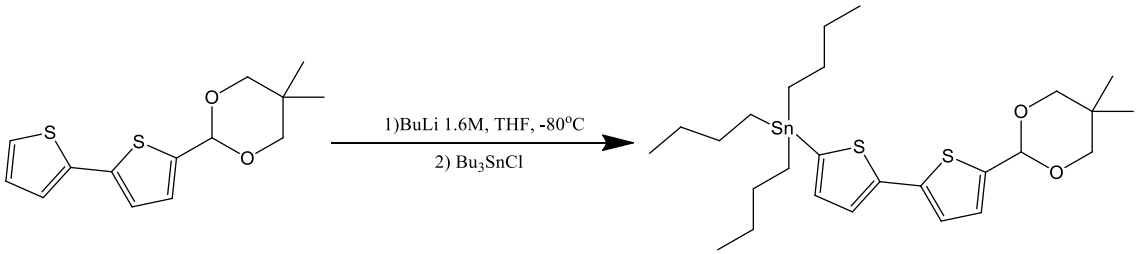

16

In a RBF charge **15** (0.46g, 1.64mmol) under nitrogen atmosphere. Add 10mL of dry THF and stir vigorously. Cool to -80°C and add BuLi 1.6M (1.94mL, 31.1mmol) stir for 15 mins before allowing to come to RT. Stir at RT for 20 mins. Cool to -80°C and add Bu_3SnCl. Stir for 3 hours allowing to come to RT. Remove solvent on manifold, yellow oil recovered with white precipitate. Keep under nitrogen atmosphere for immediate use.

H NMR (500MHz $CDCl_3$) δ [ppm]:

Synthesis of 3,6-bis(5"-(5,5-dimethyl-1,3-dioxan-2-yl)-[2,2':5',2"-terthiophen]-5-yl)-2,5-dioctylpyrrolo[3,4-c]pyrrole-1,4(2H,5H)-dione **(17)**

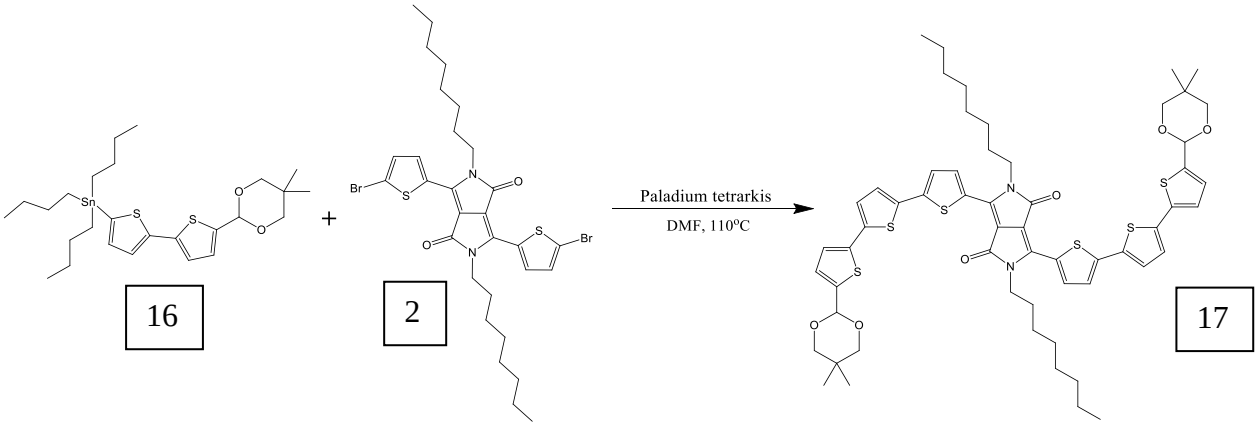

16 + 2 → 17

In a RBF with condenser and magnetic stirring bar, dissolve **2** (0.466g, 0.68mmol) and palladium tetrakis (50mg) in 15mL dry DMF. To this add material **16** dissolved in 10ml dry DMF. Bubble solution with nitrogen for 15 mins before heating to 110°C for 24 hours. Blue precipitate forms. Filter reaction mixture and wash with methanol. Recrystalise in acetonitrile. 80% yield (0.591g,0.546mmol)

^{1}H NMR ($CDCl_3$, 500Hz) : δ[ppm.] 8.94(d, 4.7, 2H) 7.28(d, J=4.2Hz, 2H) 7.21(d, J=4.7Hz, 2H) 7.101(d, J=3.66Hz, 2H) 7.08(d, J=3.8Hz, 2H) 7.04(d, J=3.41Hz, 2H) 5.61(s, 2H) 4.085(t, J=8.12Hz, 4H) 3.76(d, J=10.9Hz, 5H) 3.64(d, J=10.5Hz, 5H) 1.77(m, 7H) 1.56(m, 11H) 1.45(m, 7H) 1.28(m, 38H) 1.06(t, J=7.69Hz, 3H) 0.91(m, 5H) 0.87(m, 9H) 0.815(s, 8H)

Synthesis of 5",5""-(2,5-dioctyl-3,6-dioxo-2,3,5,6-tetrahydropyrrolo[3,4-c]pyrrole-1,4-diyl)bis([2,2':5',2"-terthiophene]-5-carbaldehyde) **(18)**

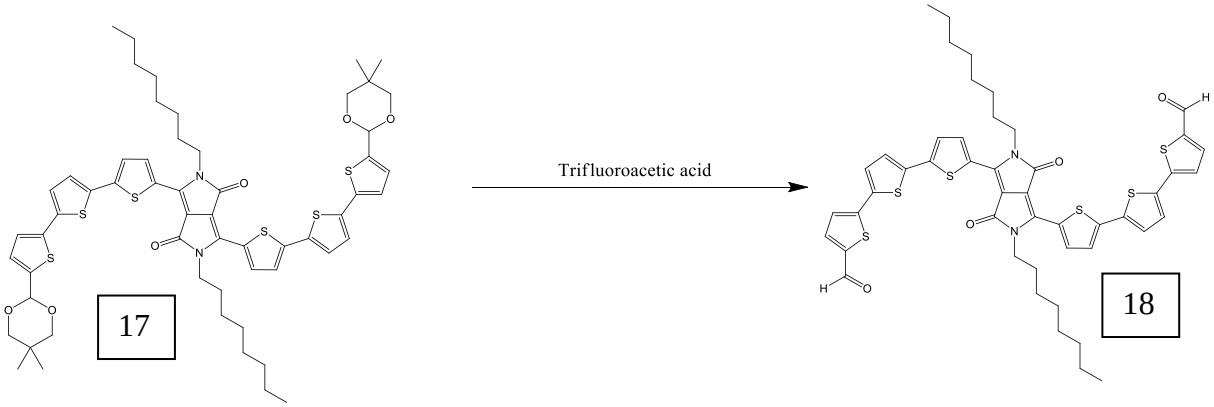

In a RBF add **17** (0.35g, 0.41mmol) to 20ml Trifluoroacetic acid reflux under nitrogen for one hour. Blue powder turns green. Pour into water and filter precipitate wash with excess water to remove acid residue.

^{1}H NMR ($CDCl_3$, 500Hz): δ[ppm.] 7.8(d, J=8.3Hz, 2H) 7.7(d, J=7.0Hz, 2H) 7.3(d, J=7.7Hz, 2H) 7.06(d, J=6.03Hz, 2H) 6.99(s, 4H) 3.7(s, 3H) 3.67(s, 3H) 2.48(s, 4H) 2.05(m, 4H) 1.82(d, J=4.3Hz, 8H) 0.96(t, J=7.7Hz, 6H) 0.89(t, J=6.3Hz, 6H)

Synthesis of 2,5-di(thiophen-2-yl)-1H-pyrrole **(19)**

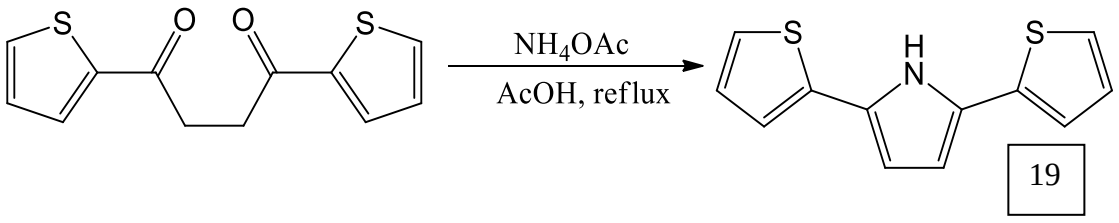

In a two neck RBF with condenser, stir 1,4-di(thiophen-2-yl) butane-1,4-dioxane (0.5g , 1.9mmol) and ammonium acetate (0.92g, 11.94mmol) in 13ml of Acetic acid. Reflux for 20

hours before pouring onto ice. Filter to collect solid. Wash rigorously with H_2O and dry under vacuum for light green product in quantitative yield.

^{1}H NMR ($CDCl_3$, 500Hz): δ[ppm.] 8.33(s, 1H) 7.177(s, 2H) 7.091(s, 2H) 7.036(dd, J=5Hz, 3.5Hz, 2H) 6.42(s, 2H)

Synthesis of tert-butyl 2,5-di(thiophen-2-yl)-1H-pyrrole-1-carboxylate **(20)**

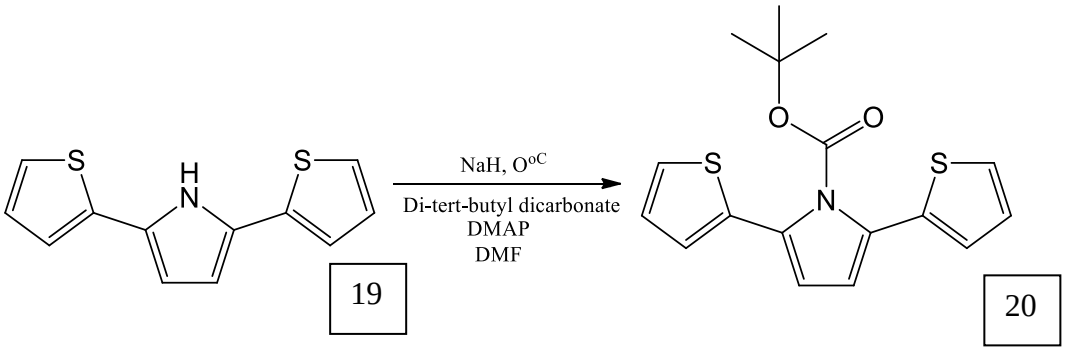

In a dry 100ml two neck round bottom flask charge **19** (1g, 4.3mmol) under nitrogen atmosphere. Dissolve with 20ml dry DMF and stir vigorously cooling to 0°C with an ice bath. With a large over flow of nitrogen slowly add (with preserving oils removed by a heptane wash) sodium hydride 60% in oils (0.188g, 4.7mmol) a portion at a time to the RBF. H_2 is seen bubbling off the reaction solution. Stir at 0°C for 1 hour before slowly adding Di-tert-butyl decarbonate (1.09g, 5mmol) and DMAP (1.12g, 10mmol) dissolved in 5ml of DMF. Stir for 12 hours before pouring into water. Product precipitates. Dissolve precipitate in diethyl ether and extract from the water wash with water and brine. Dry and remove solvent under reduced atmosphere. Purify on silica column 1:1 DCM: Heptane. Product is a light green crystalline material. 22% yield.

^{1}H NMR ($CDCl_3$, 500Hz): δ[ppm.] 7.31(d, J=5.2Hz, 2H) 7.08(d, J=3.27Hz, 2H) 7.04(dd, J=5.23Hz, 3.6Hz, 2H) 6.32(s, 2H) 1.266(s, 9H)

Synthesis of tert-butyl 2,5-bis(5-(tributylstannyl)thiophen-2-yl)-1H-pyrrole-1-carboxylate **(21)**

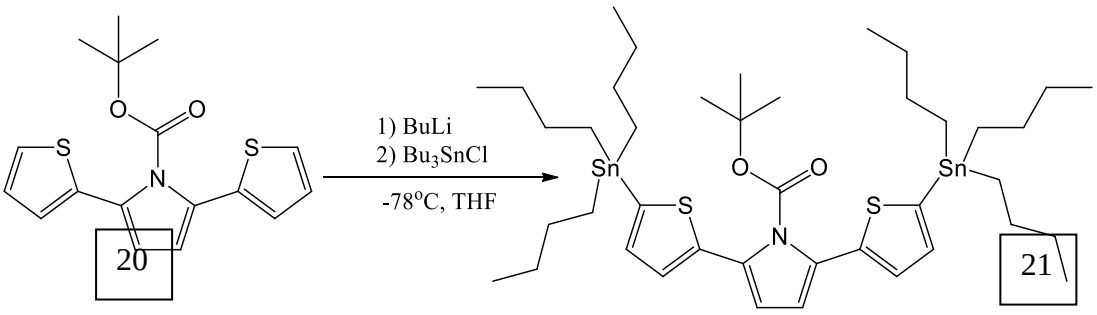

In a RBF under inert conditions, dissolve **20** (0.0725g, 0.21mmol) in 5ml of dry THF. Cool to -78°C. Slowly add BuLi 1.6M (0.328ml, 0.52mmol). Stir for 15mins at -78°C, bring to room temperature for 20 mins, reduce the temperature again to -78°C and add Bu_3SnCl (0.1545ml, 0.56mmol). Stir for 3 hours allowing to come to room temperature. Remove solvent directly on manifold and store under inert conditions.

Synthesis of tert-butyl 2,5-bis(5-(2,7-dihexyl-1,3,6,8-tetraoxo-1,2,3,6,7,8-hexahydrobenzo[lmn][3,8]phenanthrolin-4-yl)thiophen-2-yl)-1H-pyrrole-1-carboxylate **(22)**

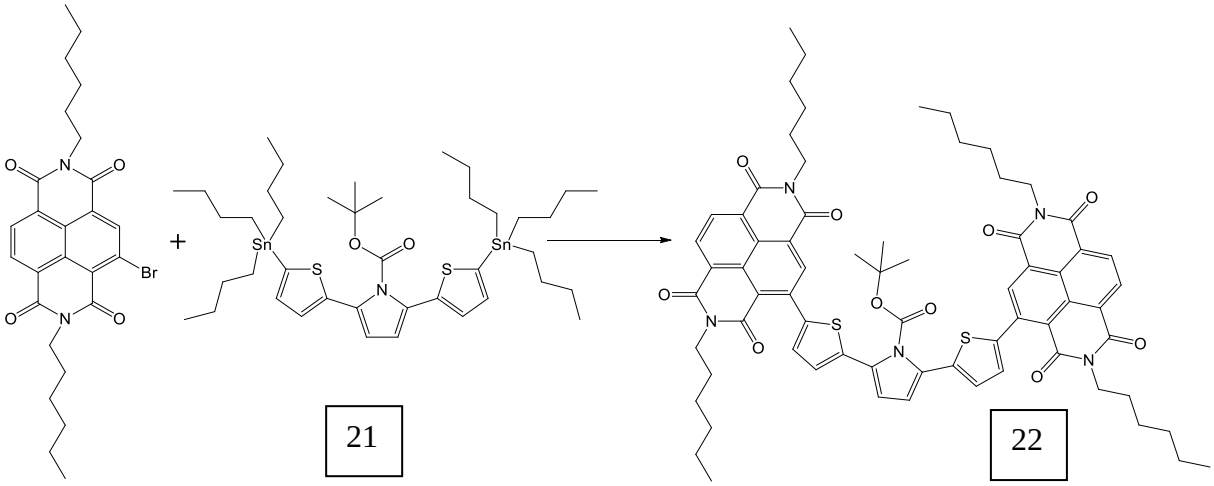

In a RBF with condenser under nitrogen, dissolve 4-bromo-2,7-dihexylbenzo[lmn][3,8]phenanthroline-1,3,6,8(2H,7H)-tetraone (0.225g, 0.438mmol) and Palladium tetrakis(0.05g, 0.04mmol) in 10 ml dry DMF. Take up stannyl solution **21** in 5ml Dry DMF and add it to the main reaction vessel. Heat to 110°C and stir vigorously overnight. Reaction mixture turns a dark green colour. Cool and dilute solution with 100ml ethanol. Precipitate forms. Filter and run through short plug column. Dark shiny green powder recovered. 57% yield

^{1}H NMR ($CDCl_3$, 500Hz): δ[ppm.] 8.78(d, J=7.6Hz, 2H) 8.70(m, 4H) 7.31(d, J=3.8Hz, 2H) 7.19(d, J=3.9Hz, 2H) 6.56(s, 2H) 4.16(m, 9H) 1.72(q, J=7.62Hz, 10H) 1.61(s, 10H) 1.42(m, 11H) 1.32(m, 221H) 1.25(s, 9H) 1.87(m, 20H)

Synthesis of 5"-hexyl-[2,2':5',2"-terthiophene]-5-carbonitrile **(23)**

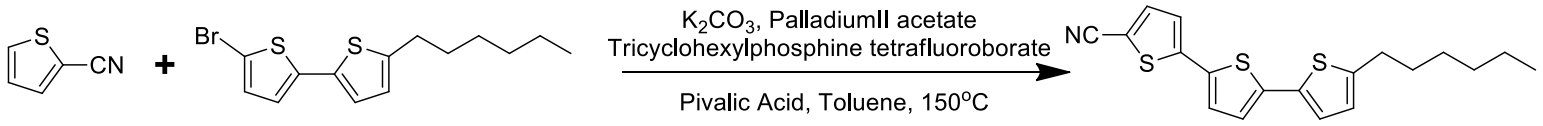

23

In a Nitrogen atmosphere load 5-bromo-5'hexly-2,2'bithiophene (3g, 9.18mmol), thiopehen-2-carbonitrile (2.61g, 23.96mmol), dried, ground K_2CO_3 (2.48g, 17.97mmol), Palladium II Acetate (53.79mg, 0.24mmol), Tricyclohexylphosphine tetrafluoroborate (195mg, 0.52mmol), Pivalic acid (367mg, 3.60mmol) and 40ml of Dry Toluene into a 100ml high pressure tube with magnetic stirring bar. The dispersion is alight yellow colour. Stir vigorously and heat to 150°C for 20hours with a blast shield in place. Allow to cool to room temperature before pouring the dark brown/yellow solution into 100mlof water. Dilute with a further 100ml and separate the organic phase. Wash with 2x100ml of Water and 100ml of Brine. Dry over $MgSO_4$ and remove solvent under reduced pressure. A dark oil is recovered. Purify with column chromatography gradient 3:7 Toluene: cyclohexane to 1:1 Toluene: cyclohexane. Product is a light yellow solid. Recrystalise in Pet. ether. 40% Yield.

^{1}H NMR ($CDCl_3$, 500Hz): δ[ppm.] 7.5(d, J=4.2Hz, 1H) 7.16(d, J=3.96Hz, 1H) 7.09(d, J=3.92Hz, 1H) 7.02(d, J=3.66Hz, 2H) 6.7(d, J=3.7Hz, 1H) 2.804(t, J=6.9Hz, 2H) 1.69(q, J=5.5Hz, 2H) 1.35(m, 6H) 0.86(t, J=6.27Hz, 3H)

Synthesis of 3,6-bis(5"-hexyl-[2,2':5',2"-terthiophen]-5-yl)pyrrolo[3,4-c]pyrrole-1,4(2H,5H)-dione **(24)**

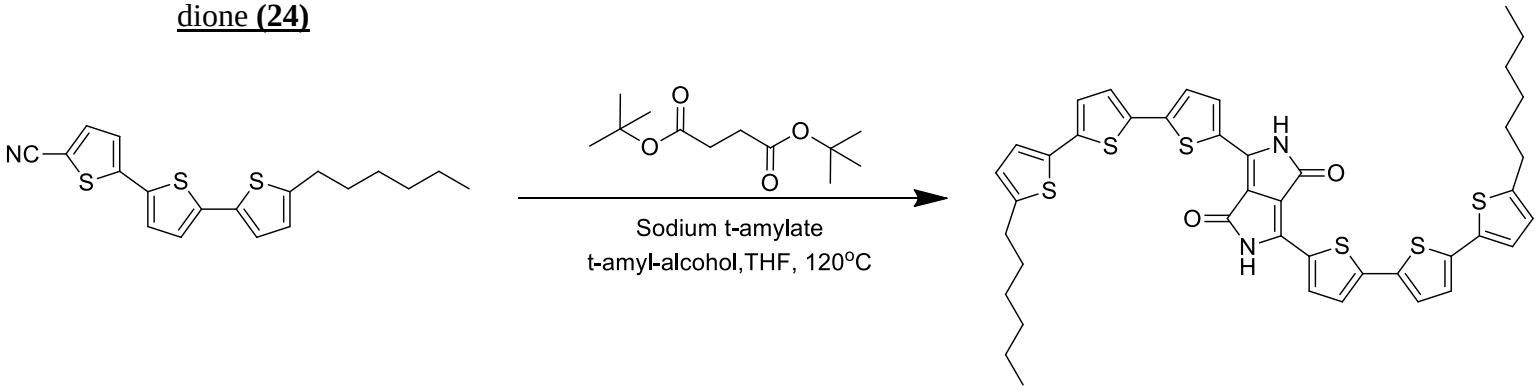

23 24

In a 50ml RBF with dean stark and dropping funnel under nitrogen, dissolve sodium t-amylate (0.52g, 4.7mmol) in t-amyl-alcohol 5ml. To this solution add **23** (1.3g, 3.6mmol) dissolved in THF 8ml. Heat to 120°C to distil off the THF. To the dropping funnel add a solution of di-tertbutyl succinate (0.364g, 1.5mmol) in THF 12ml. Add dropwise over 90 minutes. The solution darkens immediately upon addition. Stir for 3hours at 120°C before cooling to 50°C. Add 1.5ml iPrOH and stir for a further 10 minutes. Add 2ml Water and stir for a further 5 mins. Add 10ml of hot iPrOH before gravity filtering. Wash the resulting solid excessively with boiling 1:1 H_2O: iPrOH. Finally stir the resulting crude solid in boiling THF before hot filtering and drying under vacuum. Very Dark solid recovered 52% Yield

Synthesis of bis(5-methylhexyl) dicarbonate **(25)**

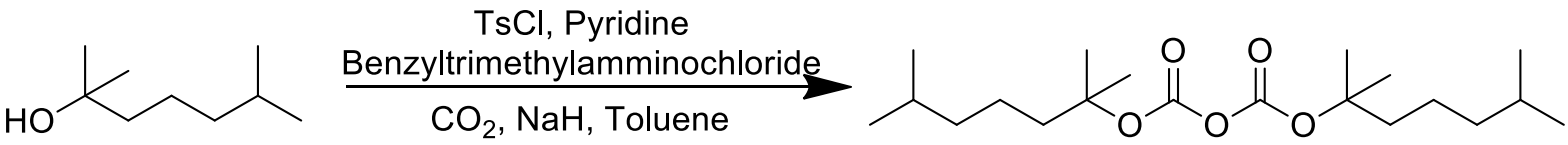

25

To a 5L, 4-neck reactor under nitrogen connect a thermometer, reflux condenser and a dropping funnel with a two-neck attachment connected to a valve operated gas bubbler. To this reactor

add NaH (protected with 40% parafum oil, 8.31g, 0.208mol) and wash with hexane to remove the parafum oil. Using a syringe remove the hexane and quench the solution in iPrOH. Remove the remaining solvent by vacuum on the manifold. Dissolve the NaH in 400ml Dry Toluene. Cool this solution to 5°C and add 2,6-dimethyl-2-heptanol (30g, 0.208mol) dropwise through the dropping funnel. A thick foam slowly forms. More solvent and heating to 40°C may be required to enable stirring as the solution thickens. Stir overnight at RT. Solution turns a white colour. Cool to 5°C and close the nitrogen line before slowly adding CO_2 pellets to the reaction while opening the gas bubbler (roughly 10g of dry ice pellets required). Reaction with CO_2 is exothermic. Keep reaction under 50°C. Reaction is complete when addition of CO_2 no longer results in temperature increase. Close the gas bubbler valve and restart the nitrogen line. The solution is now a cloudy yellow colour. Return to RT and add benzyltrimethlyammino chloride (0.538g, 3mmol), pyridine (0.493g, 6mmol) and TsCl (17.05g, 89mmol). Stir at RT for 100hours. Solution remains a creamy white colour. Reaction can be followed by GC-MS. Neutralise the solution with 5% H_2SO_4 before working up with a water separation. Dry organic phase over Na_2SO_4 remove solvent under reduced atmosphere and distil excess starting alcohol off at 30°C under vacuum. A light yellow viscous oil is recovered. Store in the fridge 42% Yield

^{1}H NMR ($CDCl_3$, 500Hz): δ[ppm.] 1.775(m, 2H) 1.57(m, 2H) 1.52(s, 6H) 1.46(m, 3H) 1.369(m, 4H) 1.22(s, 6H) 1.19(m, 4H) 0.904(dd, J=6.7Hz, 4.02Hz, 12H)

Synthesis of bis(2,6-dimethylheptan-2-yl) 3-(4-methoxyphenyl)-1,4-dioxo-6-(thiophen-2-yl)pyrrolo[3,4-c]pyrrole-2,5(1H,4H)-dicarboxylate **(26)**

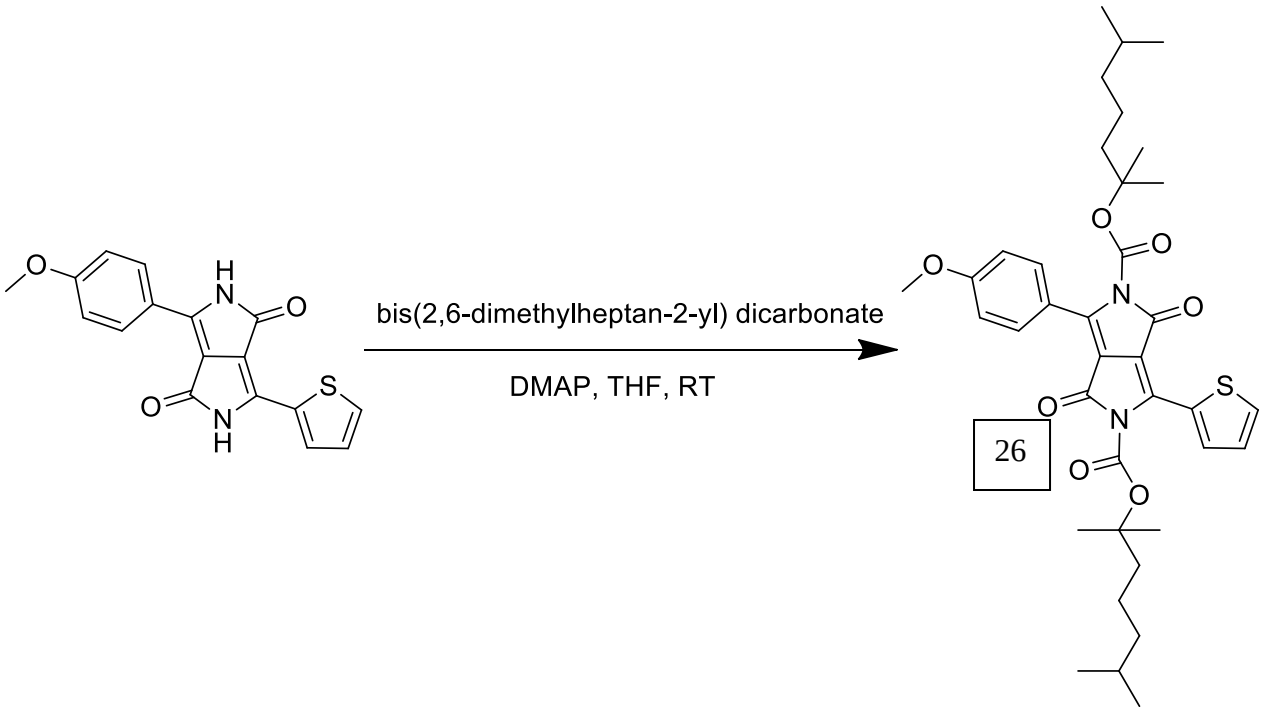

In a RBF add 3-(4-methoxyphenyl)-6-(thiophen-2-yl)pyrrolo[3,4-c]pyrrole-1,4(2H,5H)-dione (1.87g, 5.7mmol), **25** (5.09g 14.2mmol) and DMAP (1.53g, 12.5mmol) to 40 Dry THF. Stir Vigorously for 18 hours. Solution turns a light orange colour. Remove solvent under vacuum and take up solid in water. Filter and wash with water. Recrystalise resultant solid in cyclohexane. Material is very soluble recrystallization is slow. A bright red powder is recovered. 95% yield

^{1}H NMR ($CDCl_3$, 500Hz): δ[ppm.] 8.227(d, J=4.1Hz, 1H) 7.75(d, J=9Hz, 2H) 7.61(d, J=5.16Hz, 1H) 7.19(t, J=4.7Hz, 1H) 6.97(d, J=8.5Hz, 2H) 3.87(s, 3H) 1.77(m, 4H) 1.62(m, 4H) 1.57(s, 12H) 1.52(m, 4H) 1.48(s, 12H)

Synthesis of di-tert-butyl 3,6-bis(5"-hexyl-[2,2':5',2"-terthiophen]-5-yl)-1,4-dioxopyrrolo[3,4-c]pyrrole-2,5(1H,4H)-dicarboxylate **(27)**

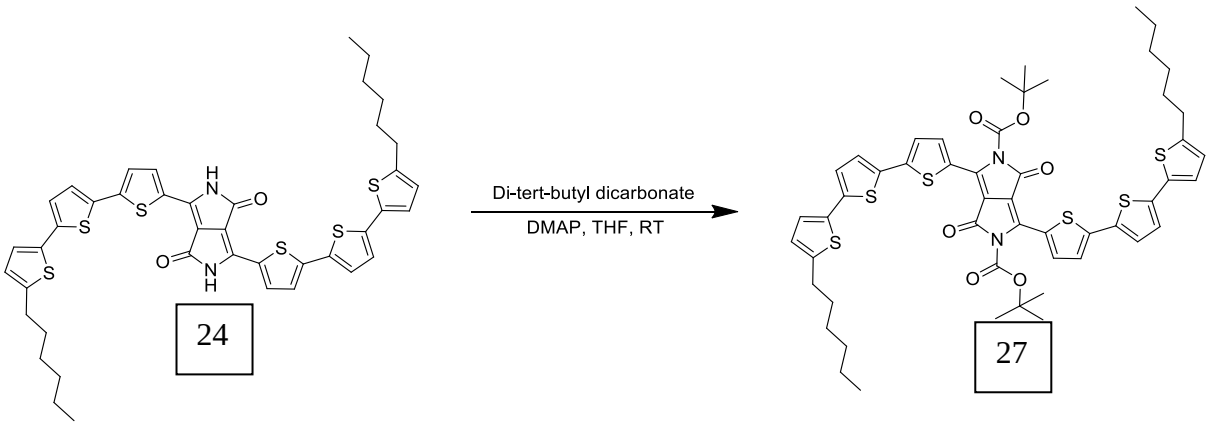

24 27

In a 50ml RBF dissolve **24** (0.758g, 0.9mmol), DMAP (0.29g, 2.3mmol) and di-tert-butyl dicarbonate (1.03g, 4.7mmol) in THF 12ml. stir vigorously for 12 hours. Green particles crash out of solution. Filter and wash with 20ml diethyl ether to afford the product 75% yield

1H NMR (CDCl3, 500 MHz): δ 8.27(d, J=4.17, 2H) 7.20(m, 4H) 6.70(d, J=3.5Hz, 2H) 2.79(t, J=7.5Hz, 4H) 1.65-1.71(m, 22H) 0.89(t, J=6.8Hz, 6H)

13C NMR (CDCl3, 125.7 MHz): δ 159.96, 149.87, 147.87, 147.42, 144.88, 140.16, 137.33, 136.33, 134.87, 134.84, 128.66, 127.16, 125.92, 125.09, 124.97, 124.77, 111.11, 86.87, 32.42, 32.41, 31.09, 29.61, 26.64, 23.44, 14.95

Synthesis of (E)-6,6'-dibromo-[3,3'-biindolinylidene]-2,2'-dione **(28)**

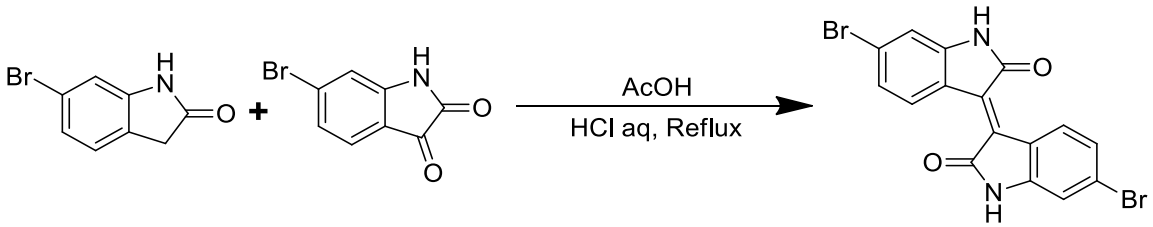

28

In a two neck RBF with condenser and septum, charge 6-bromooxindole (10g, 47.16mmol) and 6-bromoisatin (10.66g, 47.16mmol) under inert conditions. Cannula 200ml of acetic acid

and syringe in 2ml of conc. HCl. Reflux for 20 hours. Solution turns from a strong orange colour to a dark purple. Cool to RT and filter under vacuum. Wash excessively with water followed by ethanol and ethyl acetate. Dry in the oven at 65°C. Dark purple pigment recovered. 89% yield.

Synthesis of (E)-bis(2,6-dimethylheptan-2-yl) 6,6'-dibromo-2,2'-dioxo-[3,3'-biindolinylidene]-1,1'-dicarboxylate **(29)**

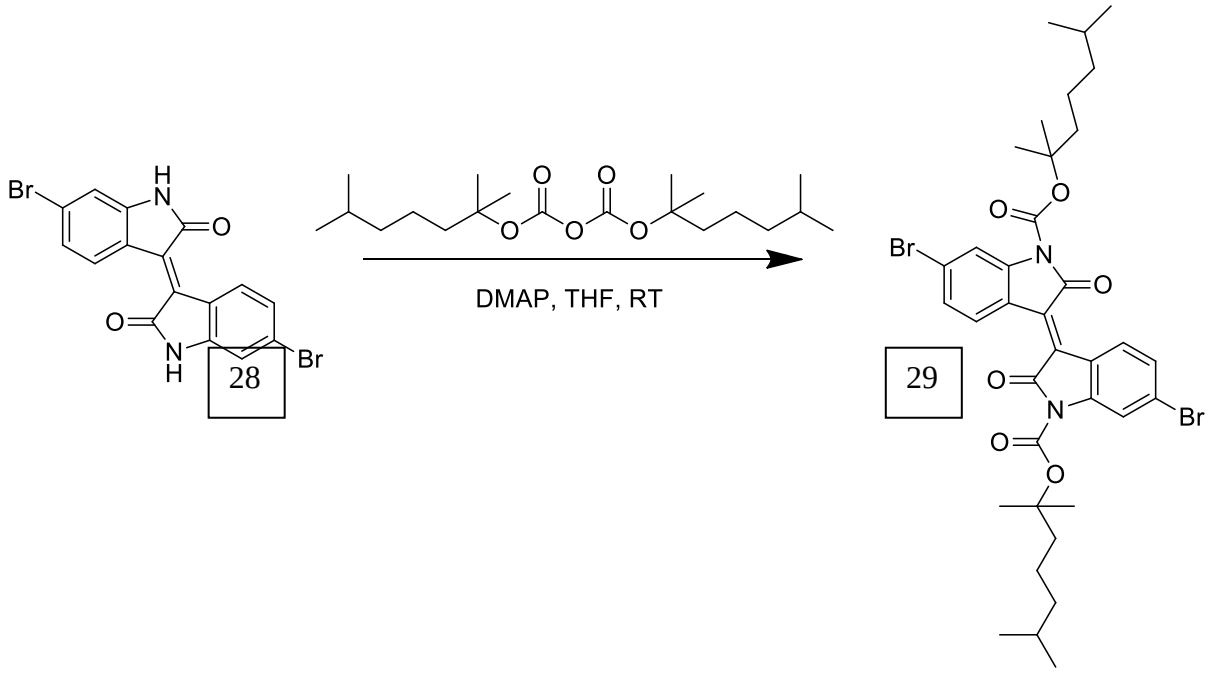

In a RBF under inert conditions, charge **28** (1g, 2.3mmol) DMAP (0.639g, 5.3mmol) and **25** (2.98g, 8.3mmol). Dissolve with 30ml of dry THF and stir vigorously at RT for 15 hours. Colour changes from red/brown colour to a dark orange. Remove solvent under reduced pressure and take up the resulting dark orange oil in heptane. A shiny light orange/red powder crashes out of the heptane. Filter and rinse with heptane. 96% Yield.

^{1}H NMR ($CDCl_3$, 500Hz) : δ[ppm.] 8.85(s, 1H) 8.83(s, 1H) 8.08(d, J=1.7Hz, 2H) 7.303(d, J=1.7Hz, 1H) 7.28(d, J=1.77Hz, 1H) 1.88(m, 4H) 1.65(s, 12H) 1.59(q, J=7.5Hz, 2H) 1.49(m, 6H) 1.27(t, J=8.34Hz, 4H) 0.913(d, J=8.3Hz, 12H)

Synthesis of (E)-di-tert-butyl 6,6'-dibromo-2,2'-dioxo-[3,3'-biindolinylidene]-1,1'-dicarboxylate **(30)**

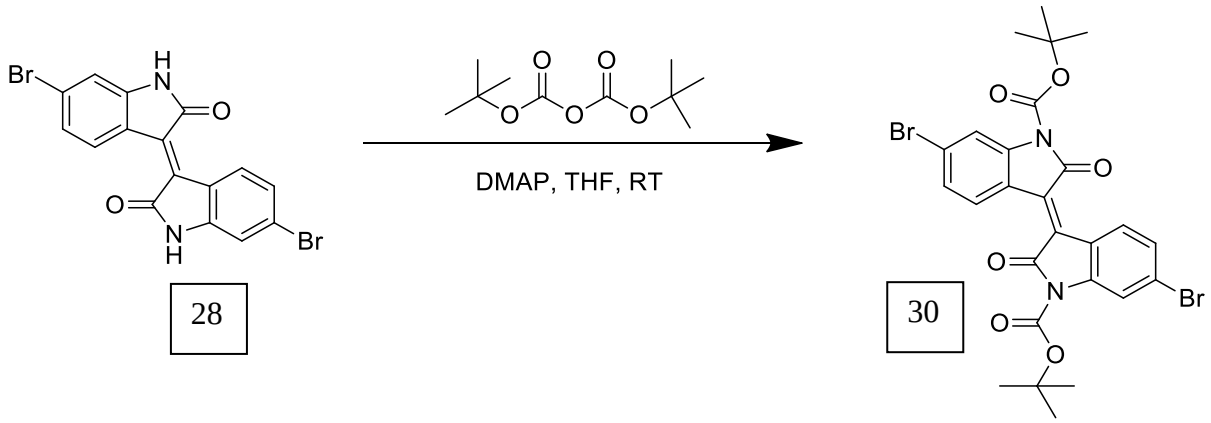

In a RBF under inert conditions, charge **28** (0.5g, 1.19mmol) DMAP (0.319g, 2.6mmol) and **25** (0.65g, 2.97mmol). Dissolve with 30ml of dry THF and stir vigorously at RT for 12 hours. Colour changes from red/brown colour to a dark orange. Remove solvent under reduced pressure and take up the resulting dark orange oil in water. A shiny light orange/red powder crashes out of the water. Filter and rinse with water, recrystalise in heptane. 91% Yield.

^{1}H NMR ($CDCl_3$, 500Hz) : δ[ppm.] 8.84(d, J=8.3Hz, 2H) 8.07(d, J=2.46Hz, 2H) 7.31(d, J=8.4Hz, 2H) 1.67(s, 18H)

Micellar Synthesis

General procedure

Reactions were carried out in 5ml glass bottles with magnetic stirring bars. These reactions are carried out in an open vessel laboratory atmosphere.

On equivalent of dibromide (0.5mmol), 2.5 equivalents of boronic acid or boronic pinacol ester (1.25mmol), and $Pd(dtbpf)Cl_2$ (0.01mmol) were all added directly to 1ml of a 2% by weight solution of Kolliphor EL in water with 10% Co-solvent. Followed directly by the addition of $N(Et)_3$ with vigorous stirring. Upon completion of reaction, the mixture was diluted with 10 mL of CH2Cl2 and filtered through a pad of silica. The filtrated solution was evaporated under reduced pressure and purified by chromatography.

Specific reactions.

Synthesis of (E)-6,6'-bis(5'-hexyl-[2,2'-bithiophen]-5-yl)-1,1'-bis(2-octyldodecyl)-[3,3'-biindolinylidene]-2,2'-dione **(31)**

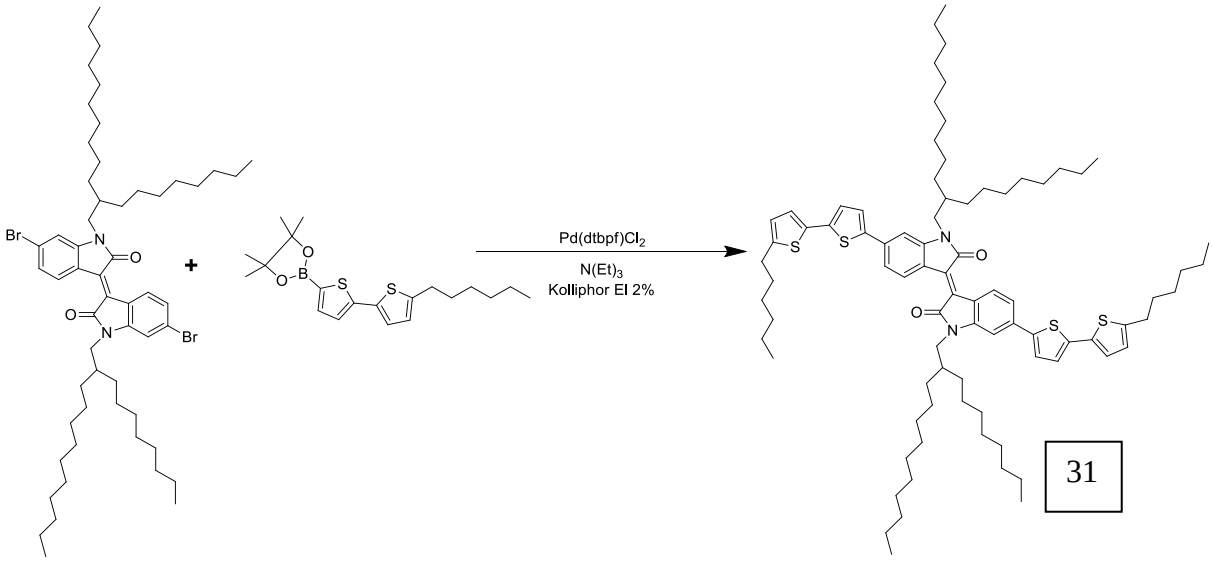

31

In a small beaker with magnetic stirrer add (E)-6,6'-dibromo-1,1'-bis(2-octyldodecyl)-[3,3'-biindolinylidene]-2,2'-dione (0.49g, 0.5mmol) 5'-hexyl-2,2'bithiophene-5-boronic pinacol ester (0.47g, 1.25mmol) and Pd(dtbpf)Cl_2 catalyst were added to a 1ml 2% by weight solution of Kolliphor EL in water followed by addition of $N(Et)_3$ (0.303g, 3mmol). The solution was stirred overnight. Solution turns a dark blue colour. Column on silica 4:6 $CHCl_3$: Heptane. Collect dark blue fraction and remove solvent under reduced pressure. Bronze coloured sheets of material recovered. 62% yield.

^{1}H NMR ($CDCl_3$, 500Hz) : δ[ppm.] 9.13(d, J=8.4Hz, 2H) 7.28(d, J=3.77Hz, 2H) 7.23(s, 2H) 7.08(d, J=3.3Hz, 2H) 7.03(d, J=3.4Hz, 2H) 6.88(s, 2H) 6.70(d, J=3.16Hz, 2H) 3.66(d, J=5.03Hz, 4H) 2.81(t, J=6.9Hz, 4H) 1.895(s, 2H) 1.70(q, J=7.3Hz, 4H) 1.28(m, 79H) 0.86(m, 18H)

C64 13C NMR (CDCl3, 125.7 MHz): δ[ppm.] 169.502, 146.95, 146.50, 142.84, 139.60, 138.21, 135.35, 132.49, 131.02, 125.79, 124.82, 124.60, 121.87, 119.55, 105.36, 45.27, 37.29, 32.80, 32.78, 32.66, 32.44, 32.42, 31.11, 30.92, 30.58, 30.54, 30.251, 30.22, 29.65, 27.59, 23.56, 23.55, 23.45, 14.98, 14.94

Synthesis of (E)-di-tert-butyl 6,6'-bis(5'-hexyl-[2,2'-bithiophen]-5-yl)-2,2'-dioxo-[3,3'-biindolinylidene]-1,1'-dicarboxylate **(32)**

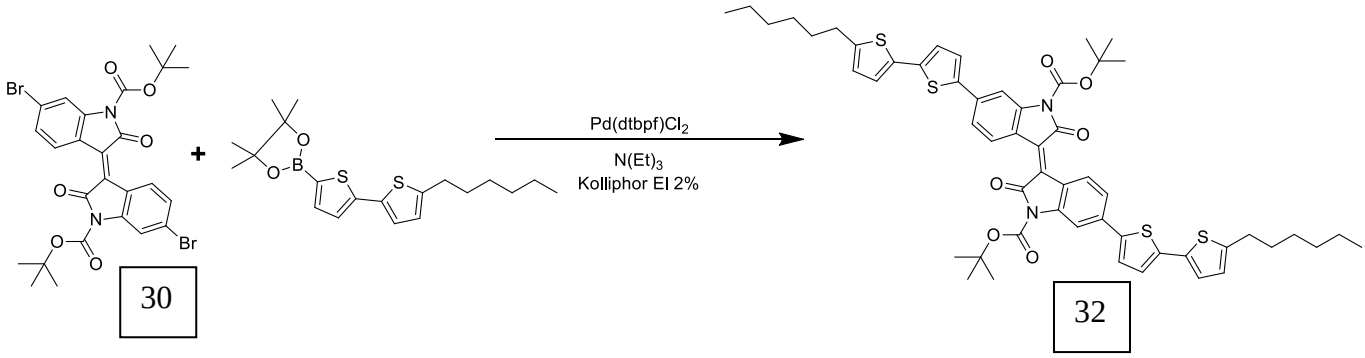

30 (0.31g, 0.05mmol), 5'-hexyl-2,2'bithiophene-5-boronic pinacol ester (0.47g, 1.25mmol) and Pd(dtbpf)Cl_2 catalyst were added to a 1ml 2% by weight solution of Kolliphor EL in water with 10% per volume of toluene in air, followed by addition of $N(Et)_3$ (3mmol) with vigorous stirring at 60°C. Reaction complete in 30 minutes. Solution diluted with 10 ml CH_2Cl_2 and passed through a silica plug column. 85% yield.

1H NMR (CDCl3, 500 MHz): δ 8.94(d, J=8.66Hz, 2H) 8.10(d, J=1.8Hz, 2H) 7.38(d, J=3.5Hz, 4H) 7.11(d, J=3.8Hz, 2H) 7.06(d, J=3.5Hz, 2H) 6.71(d, J=3.55Hz, 2H) 2.81(t, J=7.75Hz, 4H) 1.73(s, 18H) 1.68(q, J=7.45Hz, 4H) 1.39(m, 4H) 1.32(m, 8H) 0.90 (m, 6H)

Synthesis of (E)-bis(2,6-dimethylheptan-2-yl) 2,2'-dioxo-6,6'-diphenyl-[3,3'-biindolinylidene]-1,1'-dicarboxylate **(33)**

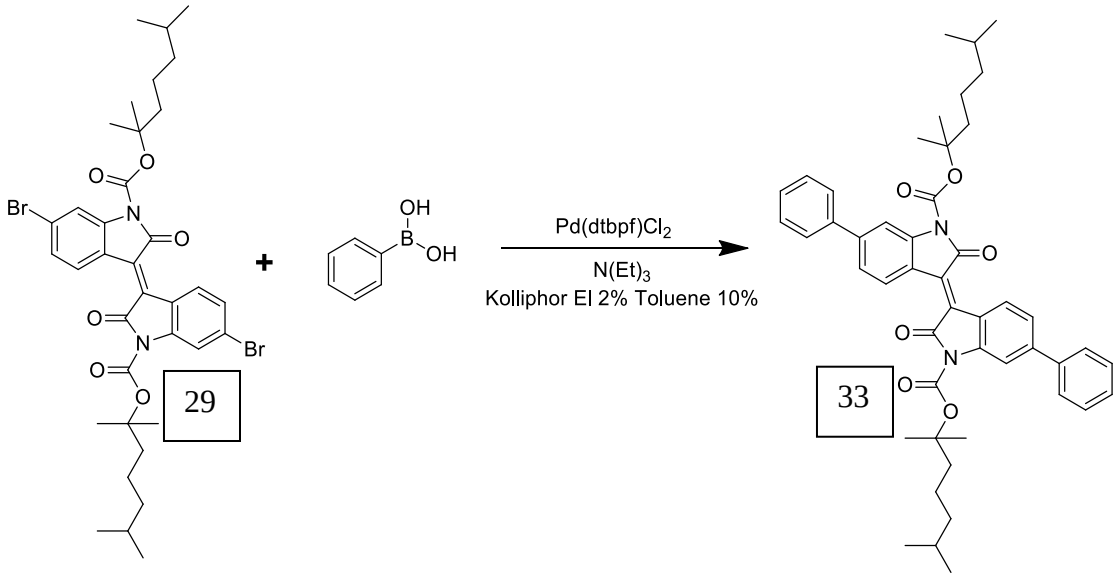

(E)-bis(2,6-dimethylheptan-2-yl) 6,6'-dibromo-2,2'-dioxo-[3,3'-biindolinylidene]-1,1'-dicarboxylate **29** (0.38g, 0.5mmol), phenylboronic acid (0.15g, 1.25mmol) and Pd(dtbpf)Cl_2 catalyst were added to a 1ml 2% by weight solution of Kolliphor EL in water with 10% per volume of toluene in air, followed by addition of $N(Et)_3$ (3mmol) with vigorous stirring at 60°C. Reaction complete in 30 minutes. Solution diluted with 10 ml CH_2Cl_2 and passed through a silica plug column. 94% yield.

1H NMR (CDCl3, 500 MHz): δ 9.02(d, J=8.4Hz, 2H) 8.15 (d, J=1.5 Hz, 2H) 7.68 (d, J=7.7 Hz, 4H) 7.48(t, J=15.35, 7.3Hz, 4H) 7.41(d, J=7.86Hz, 4H) 1.92(m, 4H) 1.68(s, 12H) 1.47-1.6(m, 6H) 1.23 (q, J=7.26Hz, 4H) 0.88(d, J=6.35Hz, 12H)

13C NMR (CDCl3, 125.7 MHz): δ 167.05, 149.71, 146.61, 142.72, 141.21, 132.45, 130.35, 129.80, 129.25, 128.05, 123.556, 121.98, 113.71, 88.16, 42.30, 39.91, 28.68, 26.93, 23.45, 22.508

Synthesis of di-tert-butyl 3,6-di([2,2'-bithiophen]-5-yl)-1,4-dioxopyrrolo[3,4-c]pyrrole-2,5(1H,4H)-dicarboxylate (**34)**

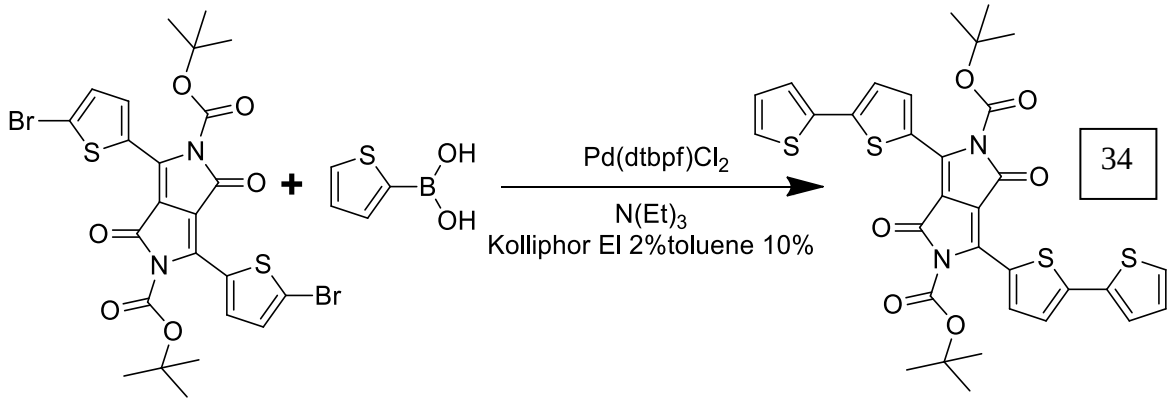

di-tert-butyl 3,6-bis(5-bromothiophen-2-yl)-1,4-dioxopyrrolo[3,4-c]pyrrole-2,5(1H,4H)-dicarboxylate (0.329g, 0.5mmol), 2-thienylboronic acid (0.16g, 1.25mmol) and Pd(dtbpf)Cl_2 catalyst were added to a 1ml 2% by weight solution of Kolliphor EL in water with 10% per volume of toluene in air, followed by addition of $N(Et)_3$ (3mmol) with vigorous stirring at 60°C. Solution diluted with 10 ml CH_2Cl_2 and passed through a silica plug column. 85% yield.

^{1}H NMR ($CDCl_3$, 500Hz) : δ[ppm.] 8.26(d, J=4.17Hz, 2H) 7.33(d, J=5Hz, 2H) 7.31(d, J=3.57Hz, 2H) 7.24(d, J=3.8Hz, 2H) 7.06(t, J=4.07Hz, 2H) 1.64(s, 18H)

13C NMR (CDCl3, 125.7 MHz): δ[ppm.] 159.95, 149.80, 144.97, 137.66, 137.02, 136.16, 129.16, 128.88, 127.41, 126.42, 125.41, 111.16, 86.88, 28.61

Synthesis of di-tert-butyl 3,6-bis(4-(5'-hexyl-[2,2'-bithiophen]-5-yl)phenyl)-1,4-dioxopyrrolo[3,4-c]pyrrole-2,5(1H,4H)-dicarboxylate **(35)**

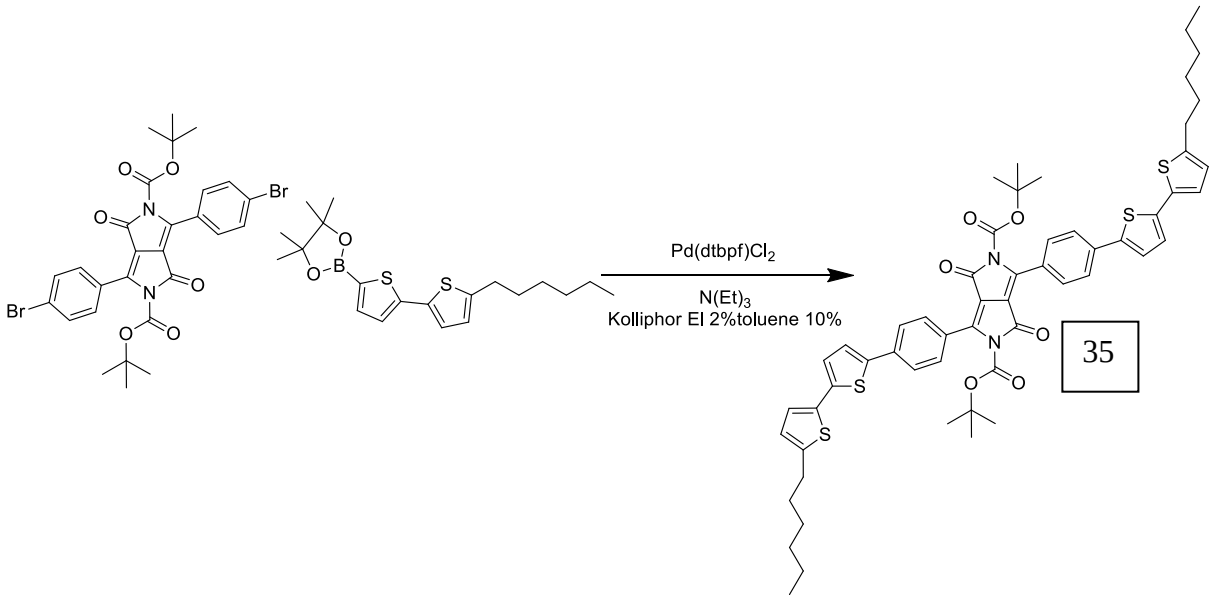

di-tert-butyl 3,6-bis(4-bromophenyl)-1,4-dioxopyrrolo[3,4-c]pyrrole-2,5(1H,4H)-dicarboxylate (0.32g, 0.5mmol), 5'-hexyl-2,2'bithiophene-5-boronic pinacol ester (0.47g, 1.25mmol) and $Pd(dtbpf)Cl_2$ catalyst were added to a 1mL 2% by weight solution of Kolliphor EL in water with 10% per volume of toluene in air, followed by addition of $N(Et)_3$ (3mmol) with vigorous stirring at 60°C Solution diluted with 10 ml CH_2Cl_2 and passed through a silica plug column. Product **(7)** 80% yield

1H NMR (CDCl3, 500 MHz): δ 7.82(d, J=8.31Hz, 4H) 7.71(d, J=8.4Hz, 4H) 7.35(d, J=3.8HZ, 2H)7.12(d, J=3.84Hz, 2H) 7.07(d, J=3.6Hz, 2H) 6.73(d, J=3.15, 2H) 2.83(t, J=15.42, 7.71Hz, 4H) 1.72(m, 4H) 1.5(s, 18H) 1.36(m, 12H) 0.93(t, J=12.9, 6.4Hz, 6H)

13C NMR (CDCl3, 125.7 MHz): δ 159.52, 148.38, 146.17, 145.29, 140.98, 139.05, 137.21, 134.41, 129.30, 126.72, 125.26, 124.97, 124.95, 124.08, 123.83, 112.35, 85.42, 31.57, 30.23, 28.76, 27.64, 22.58, 14.09.

Synthesis of (E)-di-tert-butyl 2,2'-dioxo-6,6'-di(thiophen-2-yl)-[3,3'-biindolinylidene]-1,1'-dicarboxylate (**36)**

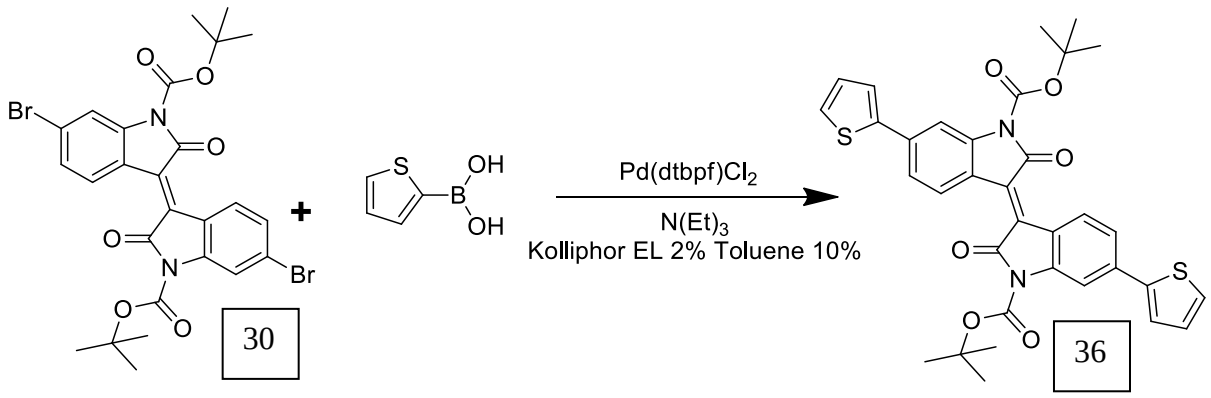

Boc-protected 6,6'-dibromoisoindigo **30** (0.31g, 0.05mmol), thiophene-2-boronic acid (0.15g, 1.25mmol) and Pd(dtbpf)Cl_2 catalyst were added to a 1ml 2% by weight solution of Kolliphor EL in water with 10% per volume of toluene in air, followed by addition of $N(Et)_3$ (3mmol) with vigorous stirring at 60°C. Solution diluted with 10 ml CH_2Cl_2 and passed through a silica plug column. Product **(36)** 80% yield.

1H NMR (CDCl3, 500 MHz): δ 8.98(d, J=8.7Hz, 2H) 8.13(d, J=1.85Hz, 2H) 7.49(dd, J=3.63, 0.8Hz, 2H) 4.44(dd, J=8.6, 1.8Hz, 2H) 7.39(dd, J=5, 0.9 Hz, 2H) 7.13(dd, J=5, 3.6 Hz, 2H) 1.72(s, 18H)

13C NMR (CDCl3, 125.7 MHz): 166.25, 148.59, 144.00, 141.67, 138.49, 130.80, 129.67, 128.47, 126.60, 124.84, 121.19, 121.10, 111.29, 84.93, 28.24.

Boc-protected 6,6'-dibromoisoindigo (**30**) (0.31g, 0.5mmol) thiophene-2-boronic acid (0.15g, 1.25mmol) and Pd(dtbpf)Cl_2 catalyst were added to a 1ml 2% by weight solution of Kolliphor EL in water with 10% per volume of tetrahydrofuran in air, followed by addition of $N(Et)_3$ (3mmol) with vigorous stirring at 60°C. Solution diluted with 10 ml CH_2Cl_2 and passed through a silica plug column. Product **(36)** 38% yield.

Boc-protected 6,6'-dibromoisoindigo (**30**) (0.31g, 0.05mmol), thiophene-2-boronic acid (0.15g, 1.25mmol) and Pd(dtbpf)Cl_2 catalyst were added to a 1ml 2% by weight solution of Kolliphor El in water with 10% per volume of acetone in air, followed by addition of $N(Et)_3$ (3mmol) with vigorous stirring at 60°C. Solution diluted with 10 ml CH_2Cl_2 and passed through a silica plug column. Product **(36)** 42% yield.

Synthesis of (E)-bis(2,6-dimethylheptan-2-yl) 2,2'-dioxo-6,6'-diphenyl-[3,3'-biindolinylidene]-1,1'-dicarboxylate **(37)**

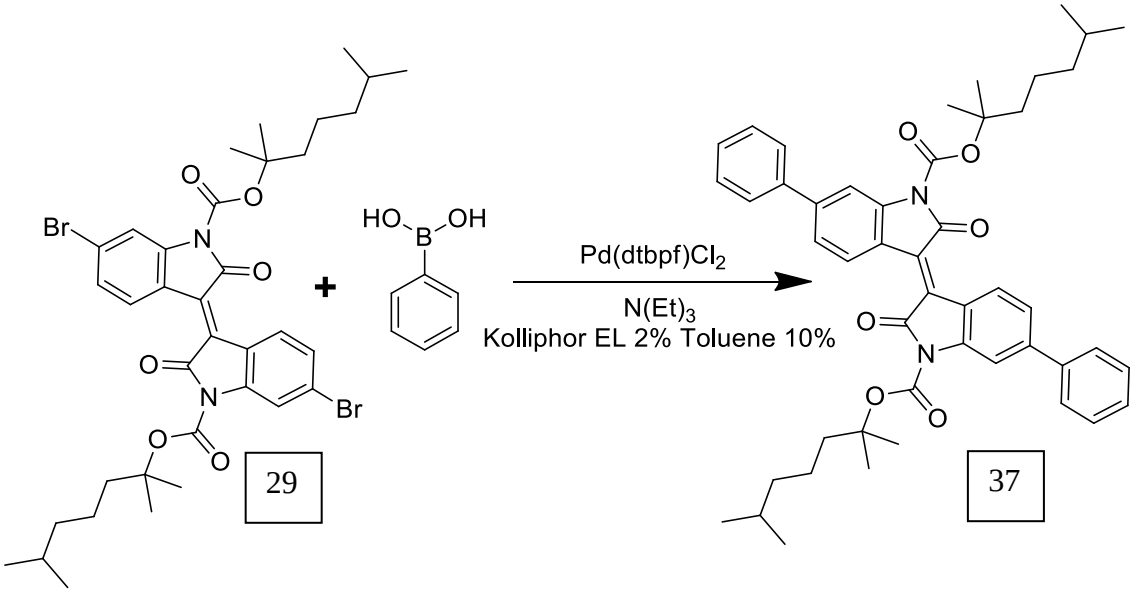

(E)-bis(2,6-dimethylheptan-2-yl) 6,6'-dibromo-2,2'-dioxo-[3,3'-biindolinylidene]-1,1'-dicarboxylate **29** (0.38g, 0.5mmol), phenylboronic acid (0.15g, 1.25mmol) and Pd(dtbpf)Cl_2 catalyst were added to a 1ml 2% by weight solution of Kolliphor EL in water with 10% per volume of toluene in air, followed by addition of $N(Et)_3$ (3mmol) with vigorous stirring at 60°C. Reaction complete in 30 minutes. Solution diluted with 10 ml CH_2Cl_2 and passed through a silica plug column. Product **(37)** 94% yield.

1H NMR (CDCl3, 500 MHz): δ 9.02(d, J=8.4Hz, 2H) 8.15 (d, J=1.5 Hz, 2H) 7.68 (d, J=7.7 Hz, 4H) 7.48(t, J=15.35, 7.3Hz, 4H) 7.41(d, J=7.86Hz, 4H) 1.92(m, 4H) 1.68(s, 12H) 1.47-1.6(m, 6H) 1.23 (q, J=7.26Hz, 4H) 0.88(d, J=6.35Hz, 12H)

13C NMR (CDCl3, 125.7 MHz): δ 167.05, 149.71, 146.61, 142.72, 141.21, 132.45, 130.35, 129.80, 129.25, 128.05, 123.556, 121.98, 113.71, 88.16, 42.30, 39.91, 28.68, 26.93, 23.45, 22.508

Synthesis of (E)-di-tert-butyl 6,6'-bis(1-methyl-1H-pyrrol-2-yl)-2,2'-dioxo-[3,3'-biindolinylidene]-1,1'-dicarboxylate **(38)**

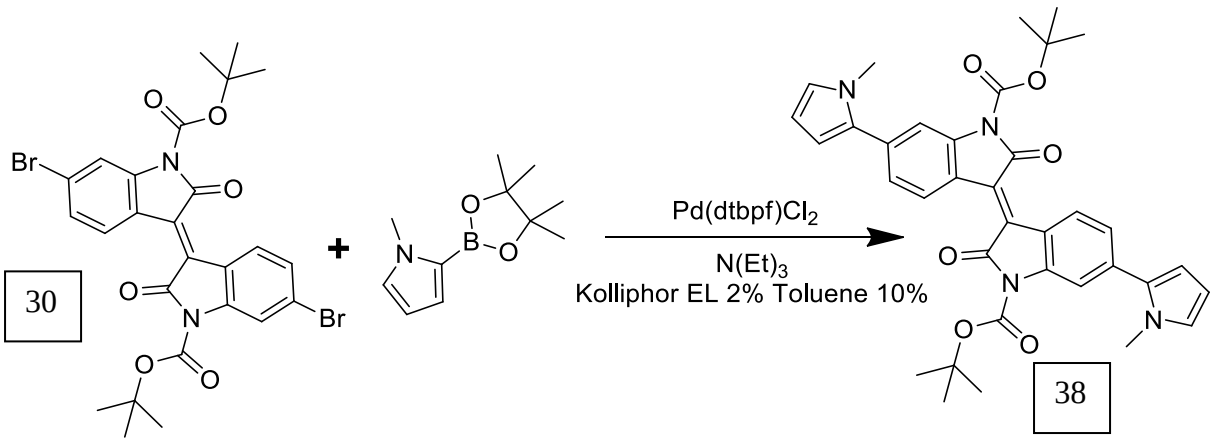

(1) (0.31g, 0.05mmol), 1-methyl-2-pyrroleboronic acid pinacol ester (0.25g, 1.25mmol) and $Pd(dtbpf)Cl_2$ catalyst were added to a 1ml 2% by weight solution of Kolliphor EL in water with 10% per volume of toluene in air, followed by addition of $N(Et)_3$ (3mmol) with vigorous stirring at 60°C. Reaction complete in 30 minutes. Solution diluted with 10 ml CH_2Cl_2 and passed through a silica plug column. TLC shows quantitative yield. Deprotection occurring on silica plug. Isolated Product **(5)** 50% yield

1H NMR (CDCl3, 500 MHz): δ 8.96(d, J=8.16Hz, 2H) 7.94(d, J=1.5Hz, 2H) 7.22(dd, J=8.4, 1.5Hz, 2H) 6.7(t, J=1.9Hz, 2H) 6.43(dd, J=3.49, 1.8Hz, 2H) 6.23(t, J=3.07Hz, 2H) 3.79(s,6H) 1.68(s,18H)

13C NMR (CDCl3, 125.7 MHz): δ 167.19, 149.69, 142.14, 138.30, 135.28, 131.62, 129.85, 126.81, 123.96, 121.11, 114.09, 111.67, 109.47, 85.60, 36.63, 29.06

Synthesis of di-tert-butyl 1,4-dioxo-3,6-di(thiophen-2-yl)pyrrolo[3,4-c]pyrrole-2,5(1H,4H)-dicarboxylate **(39)**

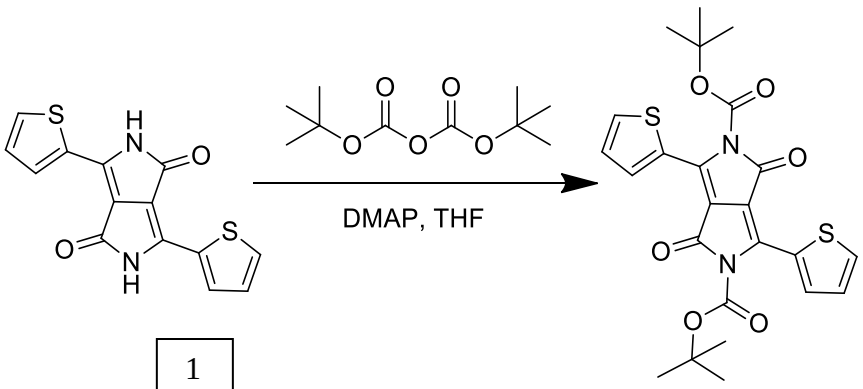

1 39

In a round bottom flask load **1** (0.15g, 0.5mmol) Di-tert-butyl dicarbonate (0.55g, 2.5mmol) and DMAP (0.183g, 1.5mmol) under a nitrogen atmosphere. Inject 10ml dry THF and stir vigorously for 6 hours. Solution turns a dark orange. Remove solvent and take up in MeOH. Shiny orange crystalline material is recovered by vacuum filtration. Wash with MeOH. Purify with silica Plug column in $CHCl_3$. Isolated product (**39**) 75% Yield

Synthesis of di-tert-butyl 3,6-bis(5-bromothiophen-2-yl)-1,4-dioxopyrrolo[3,4-c]pyrrole-2,5(1H,4H)-dicarboxylate (**40**)

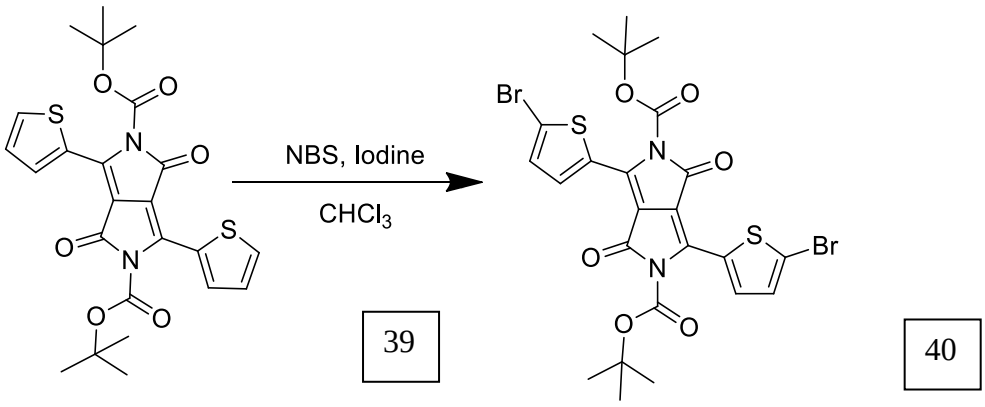

39 40

To a two-neck round bottom flask add **39** (0.16g, 0.3mmol) a single iodine crystal which acts as a catalyst and N-bromosuccinimide (0.124g, 0.7mmol) and place under inert conditions. Cool to 15ml of dry $CHCl_3$ -10°C and add to the reaction vessel. Stir vigorously and allow to slowly come to room temperature. Stir overnight. Workup with 50ml 10% NaOH and 2x50ml Brine wash. Separate layers, dry and remove solvent under reduced pressure. Take up residue in methanol and filter. Dark purple crystalline material recovered. Quantitative yields.

H NMR ($CDCl_3$, 500Hz) : δ[ppm.] 8.072 (d, J=3.94Hz, 2H) 7.15(d, J=4.3Hz, 2H) 1.61(s, 18H)

Synthesis of di-tert-butyl 3,6-bis(5"-hexyl-[2,2':5',2"-terthiophen]-5-yl)-1,4-dioxopyrrolo[3,4-c]pyrrole-2,5(1H,4H)-dicarboxylate **(41)**

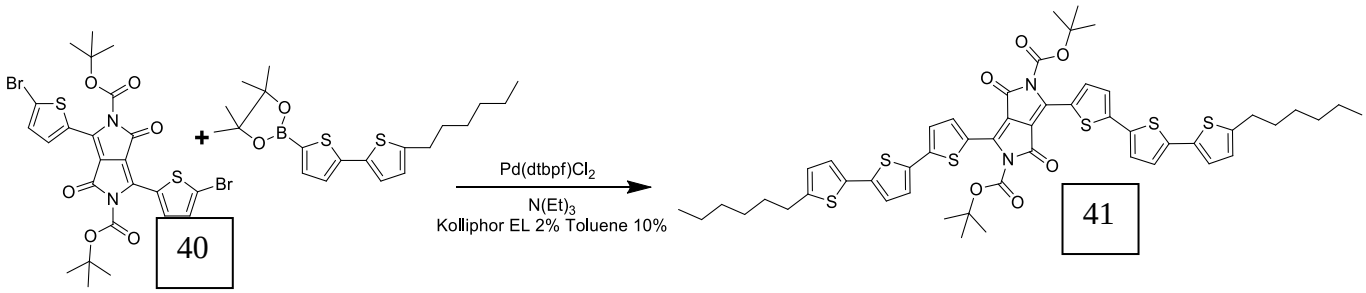

di-tert-butyl 3,6-bis(5-bromothiophen-2-yl)-1,4-dioxopyrrolo[3,4-c]pyrrole-2,5(1H,4H)-dicarboxylate(0.128g, 0.19mmol), 5'hexyl-2,2'-bithiophene-5-boronic piacol ester (0.157g, 0.418mmol) and Pd(dtbpf)Cl_2 catalyst were added to a 0.36ml 2% by weight solution of Kolliphor EL in water with 10% per volume of toluene in air, followed by addition of $N(Et)_3$ (1.14mmol) with vigorous stirring at 60°C. Reaction complete in 30 minutes. Solution diluted with 10 ml CH_2Cl_2 and passed through a silica plug column. Product **(6)** 77% yield

1H NMR (CDCl3, 500 MHz): δ 8.27(d, J=4.17, 2H) 7.20(m, 4H) 6.70(d, J=3.5Hz, 2H) 2.79(t, J=7.5Hz, 4H) 1.65-1.71(m, 22H) 0.89(t, J=6.8Hz, 6H)

13C NMR (CDCl3, 125.7 MHz): δ 159.96, 149.87, 147.87, 147.42, 144.88, 140.16, 137.33, 136.33, 134.87, 134.84, 128.66, 127.16, 125.92, 125.09, 124.97, 124.77, 111.11, 86.87, 32.42, 32.41, 31.09, 29.61, 26.64, 23.44, 14.95

Appendix-3 Cyclic Voltammetry

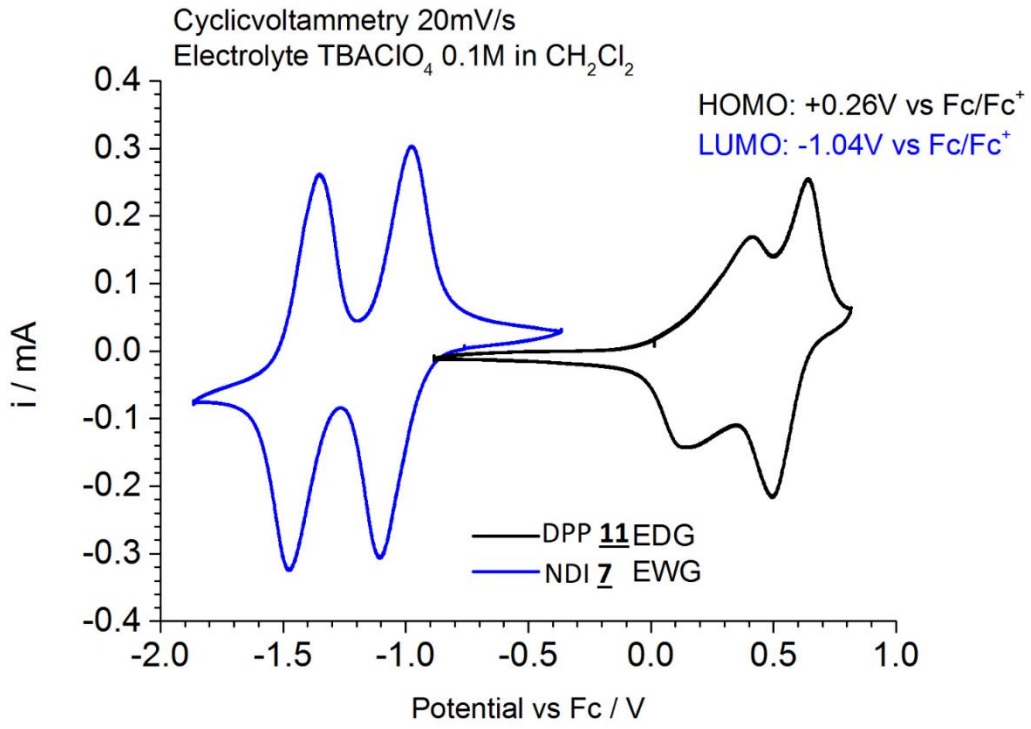

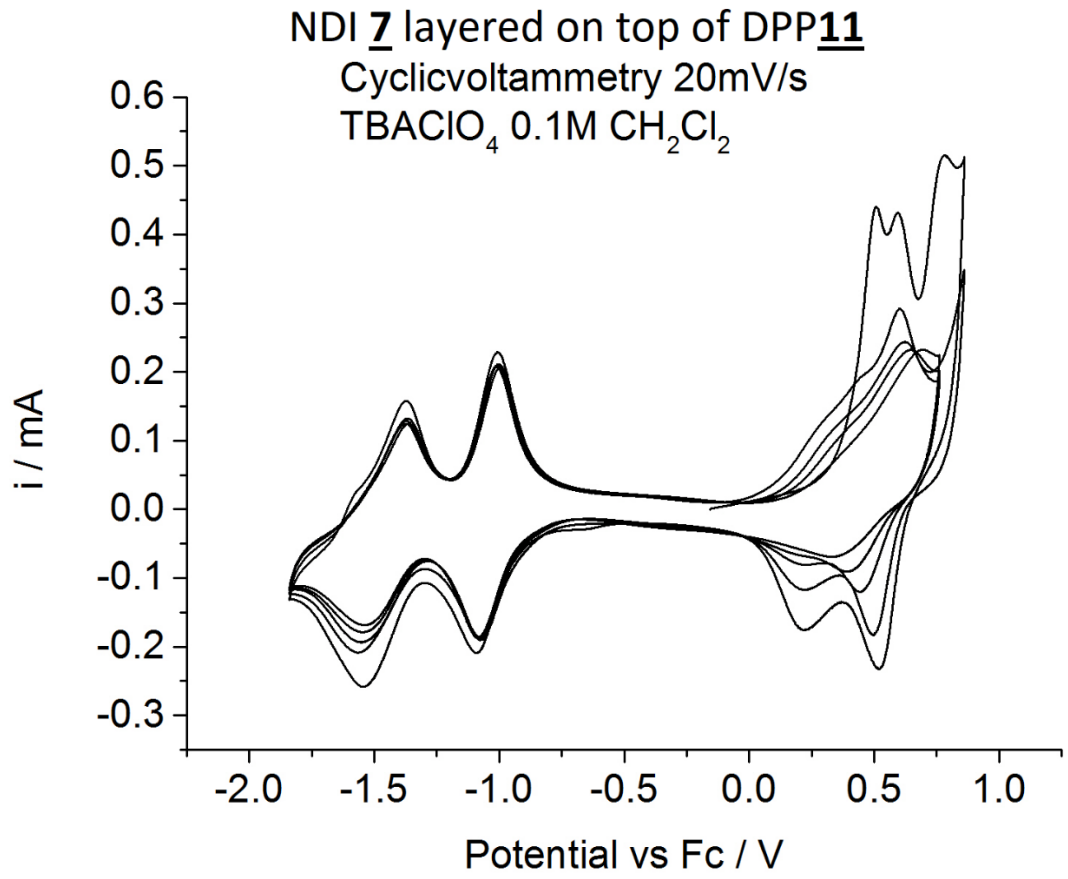
NDI 7 layered on top of DPP11
Cyclicvoltammetry 20mV/s
TBAClO4 0.1M CH2Cl2
i / mA
0.6
0.5
0.4
0.3
0.2
0.1
0.0
-0.1
-0.2
-0.3
-2.0
-1.5
-1.0
-0.5
0.0
0.5
1.0
Potential vs Fc / V

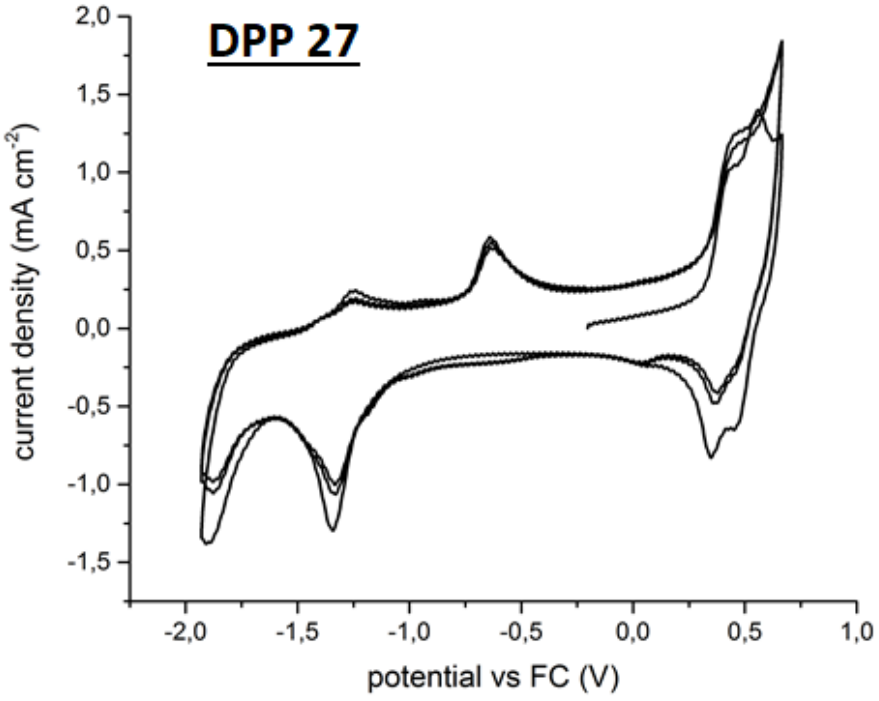
DPP 27
current density (mA cm-2)
potential vs FC (V)
2,0
1,5
1,0
0,5
0,0
-0,5
-1,0
-1,5
-2,0
-1,5
-1,0
-0,5
0,0
0,5
1,0

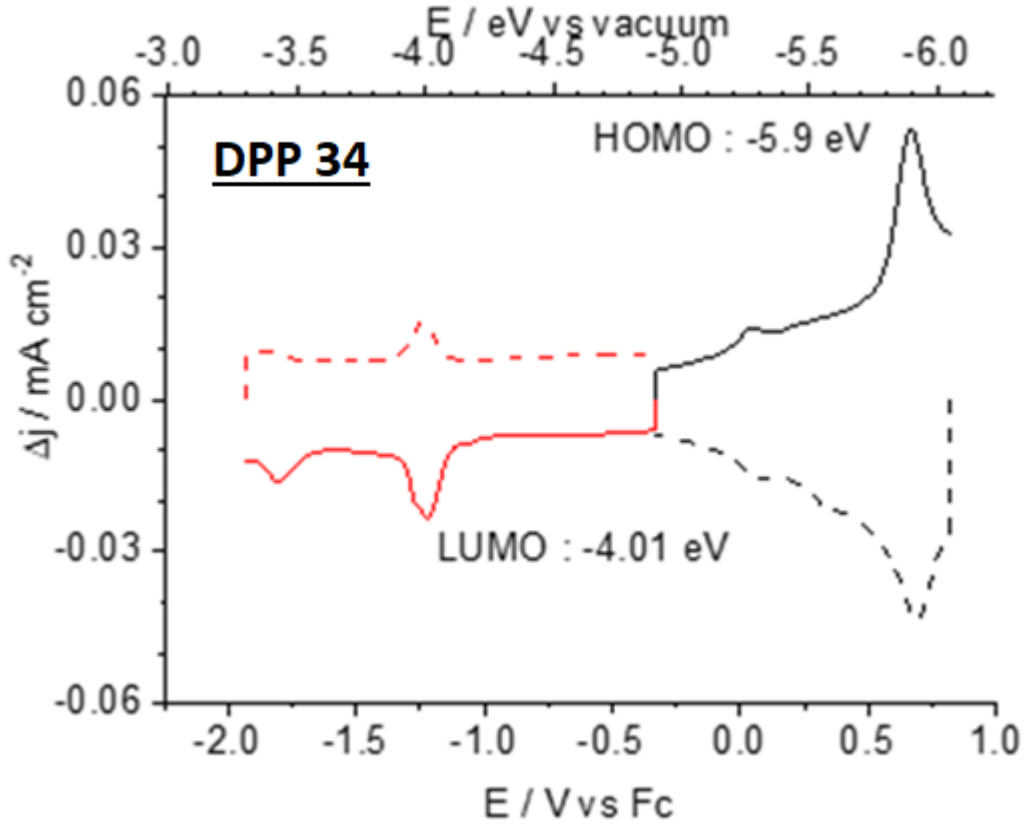
E / eV vs vacuum
-3.0
-3.5
-4.0
-4.5
-5.0
-5.5
-6.0
DPP 34
HOMO : -5.9 eV
LUMO : -4.01 eV
Δj / mA cm-2
0.06
0.03
0.00
-0.03
-0.06
-2.0
-1.5
-1.0
-0.5
0.0
0.5
1.0
E / V vs Fc

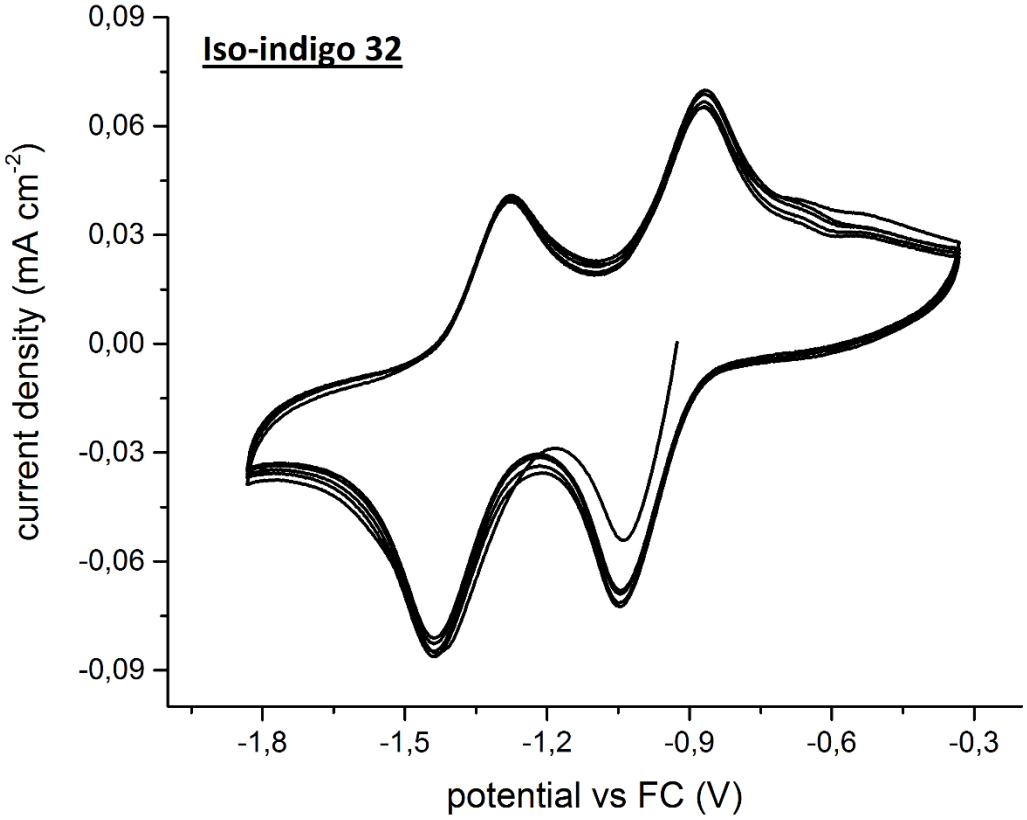
Iso-indigo 32
current density (mA cm-2)
potential vs FC (V)
0,09
0,06
0,03
0,00
-0,03
-0,06
-0,09
-1,8
-1,5
-1,2
-0,9
-0,6
-0,3

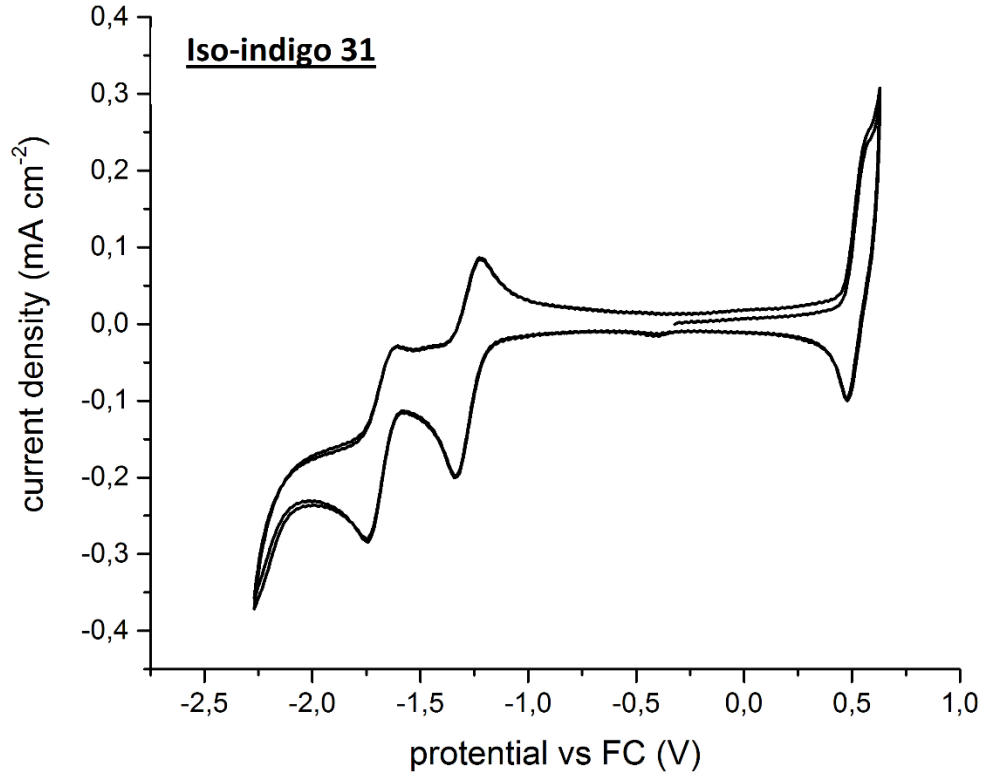
Iso-indigo 31
current density (mA cm-2)
protential vs FC (V)
0,4
0,3
0,2
0,1
0,0
-0,1
-0,2
-0,3
-0,4
-2,5
-2,0
-1,5
-1,0
-0,5
0,0
0,5
1,0

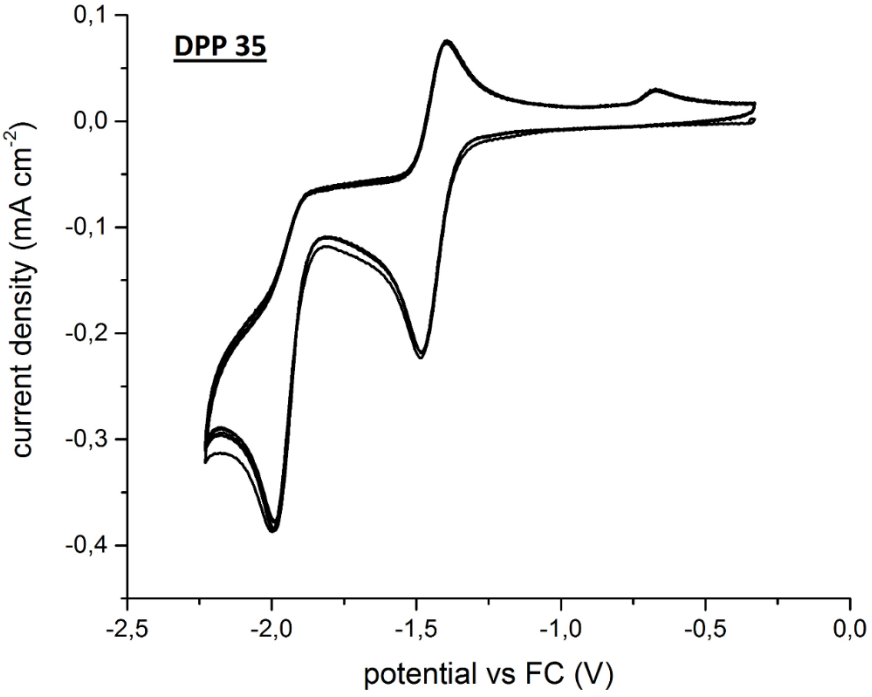

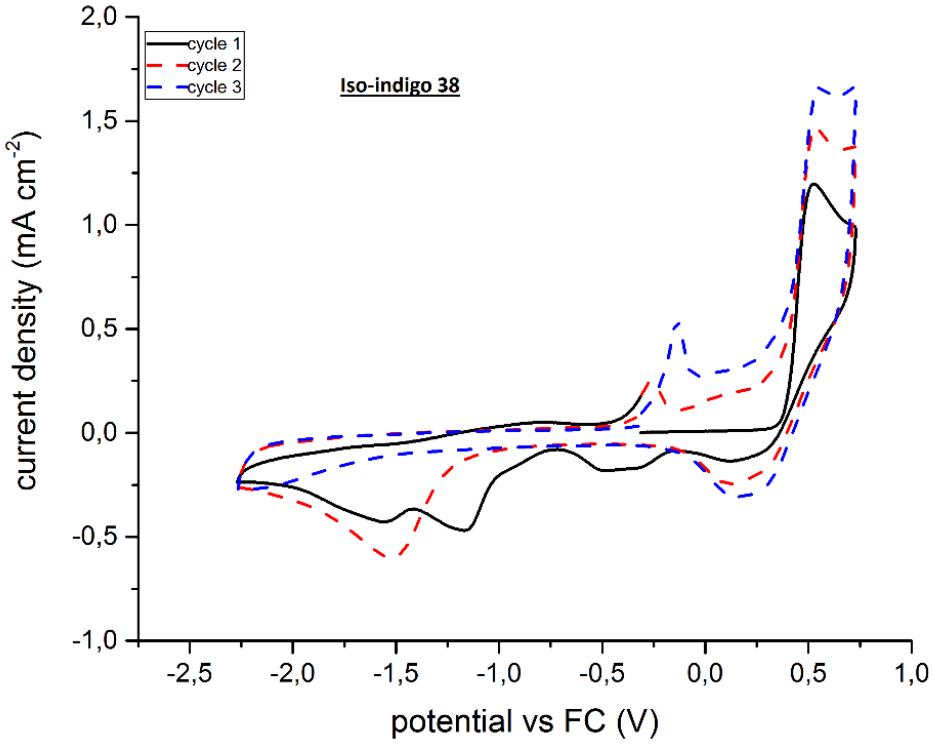

Iso-indigo 38 undergoes an electro polymerisation process


2,5-dioctyl-3,6-di(thiophen-2-yl)pyrrolo[3,4-c]pyrrole-1,4(2H,5H)-dione (2)
2.00
0.19
2.11
2.47
4.51
4.79
16.86
4.95
16.57
6.80
8.5
8.0
7.5
7.0
6.5
6.0
5.5
5.0
4.5
4.0
3.5
3.0
2.5
2.0
1.5
1.0
0.5
0.0
ppm
4466.56
4462.71
3823.84
3818.94
3648.65
3644.55
3639.75
2043.38
2035.58
2027.58
886.78
879.23
871.43
863.87
855.87
715.49
707.88
700.48
667.77
655.82
643.57
637.52
630.91
440.96
434.31
427.36

Appendix 4- NMR

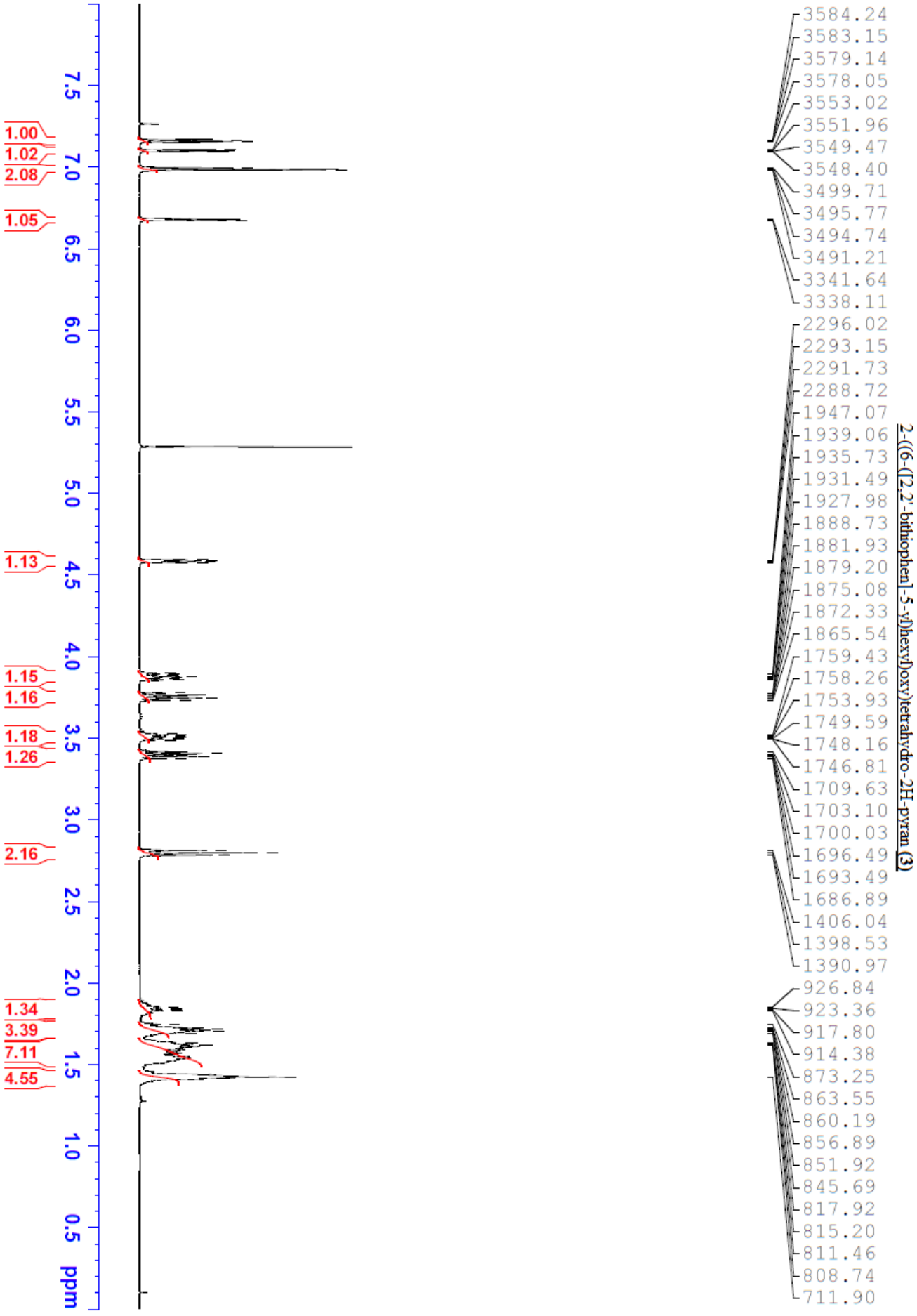

Appendix 4- NMR

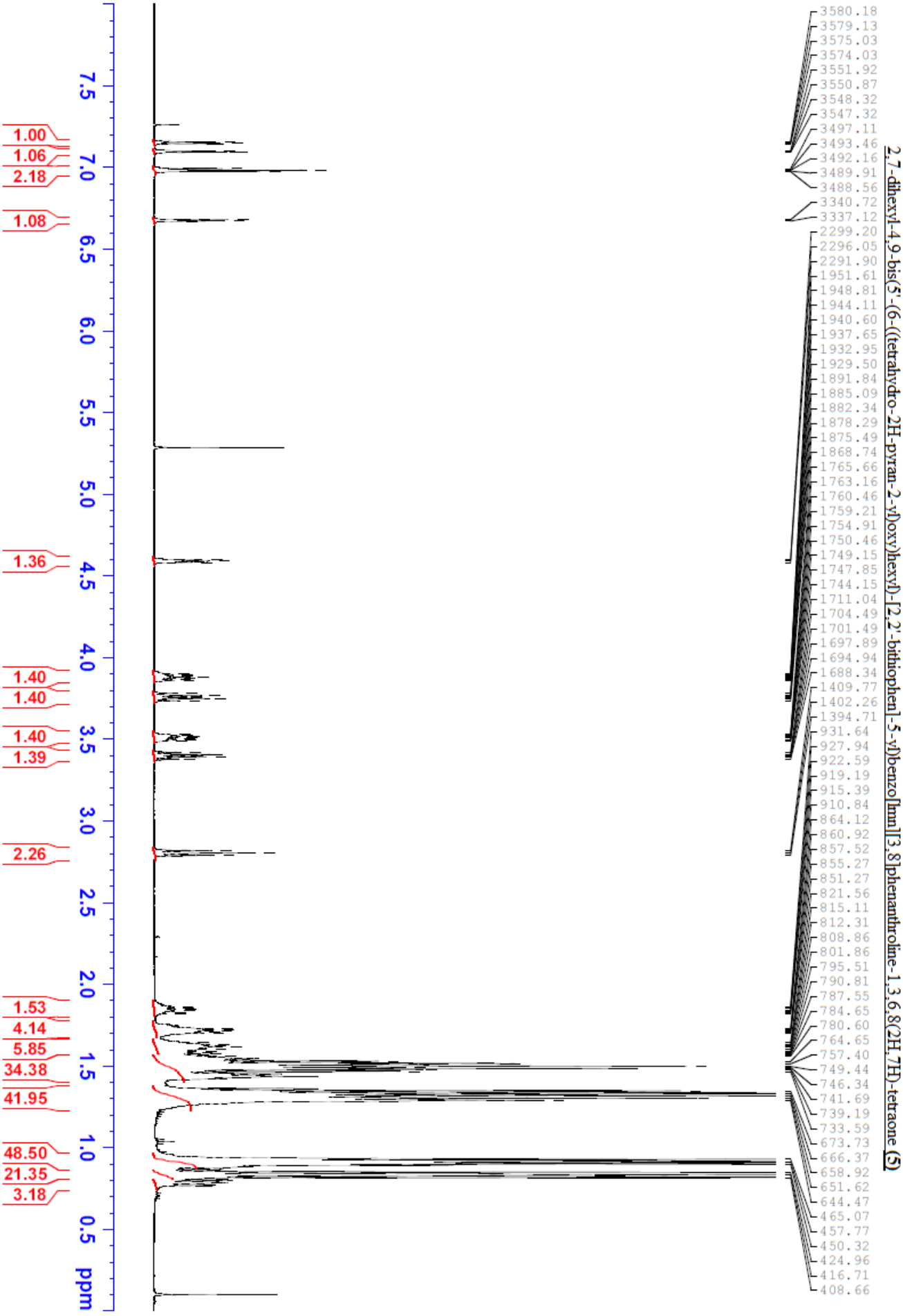

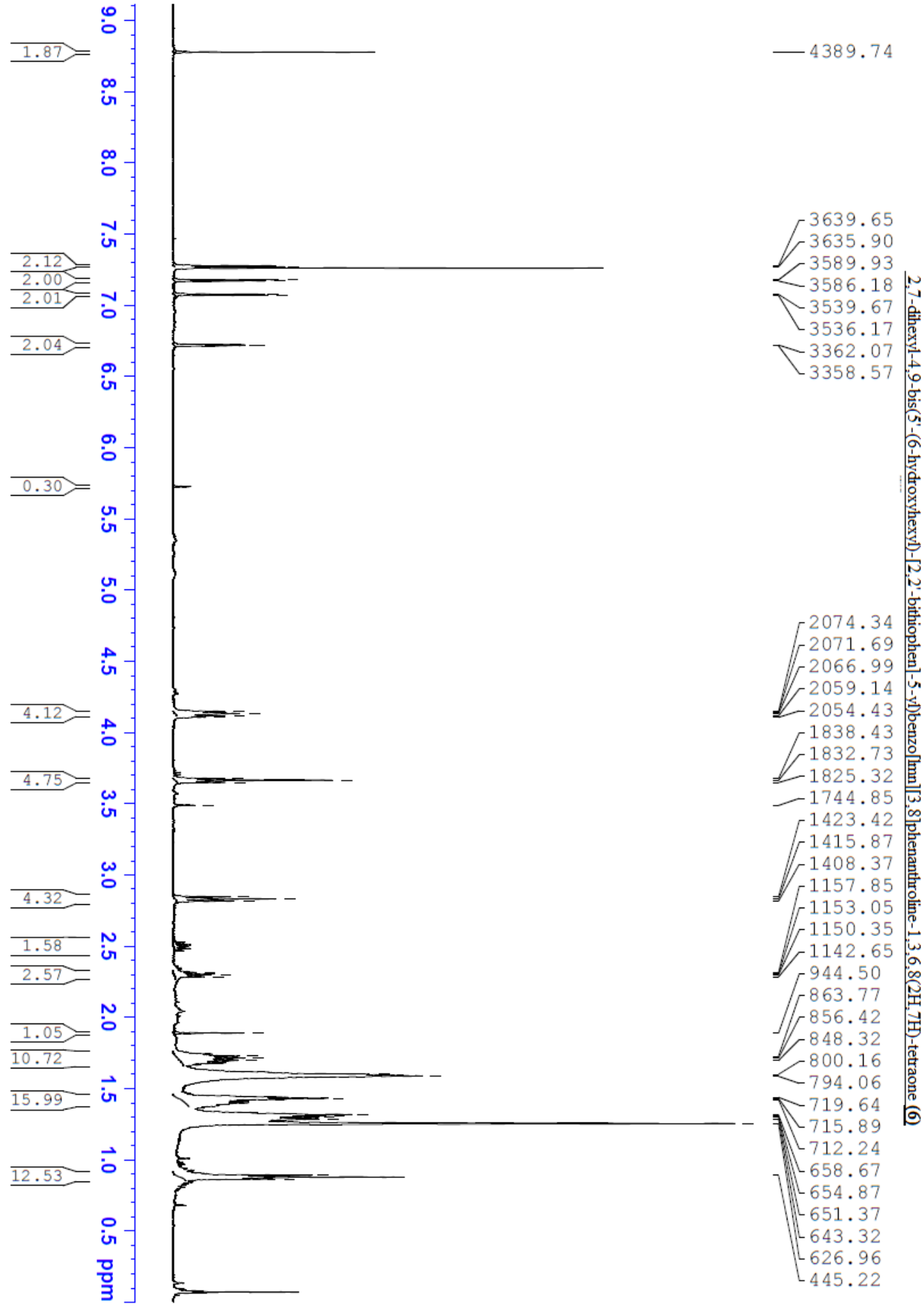
2,7-dihexyl-4,9-bis(5'-(6-hydroxyhexyl)-[2,2'-bithiophen]-5-yl)benzo[lmn][3,8]phenanthroline-1,3,6,8(2H,7H)-tetraone (6)
9.0
8.5
8.0
7.5
7.0
6.5
6.0
5.5
5.0
4.5
4.0
3.5
3.0
2.5
2.0
1.5
1.0
0.5
ppm
1.87
2.12
2.00
2.01
2.04
0.30
4.12
4.75
4.32
1.58
2.57
1.05
10.72
15.99
12.53
4389.74
3639.65
3635.90
3589.93
3586.18
3539.67
3536.17
3362.07
3358.57
2074.34
2071.69
2066.99
2059.14
2054.43
1838.43
1832.73
1825.32
1744.85
1423.42
1415.87
1408.37
1157.85
1153.05
1150.35
1142.65
944.50
863.77
856.42
848.32
800.16
794.06
719.64
715.89
712.24
658.67
654.87
651.37
643.32
626.96
445.22

Appendix 4- NMR

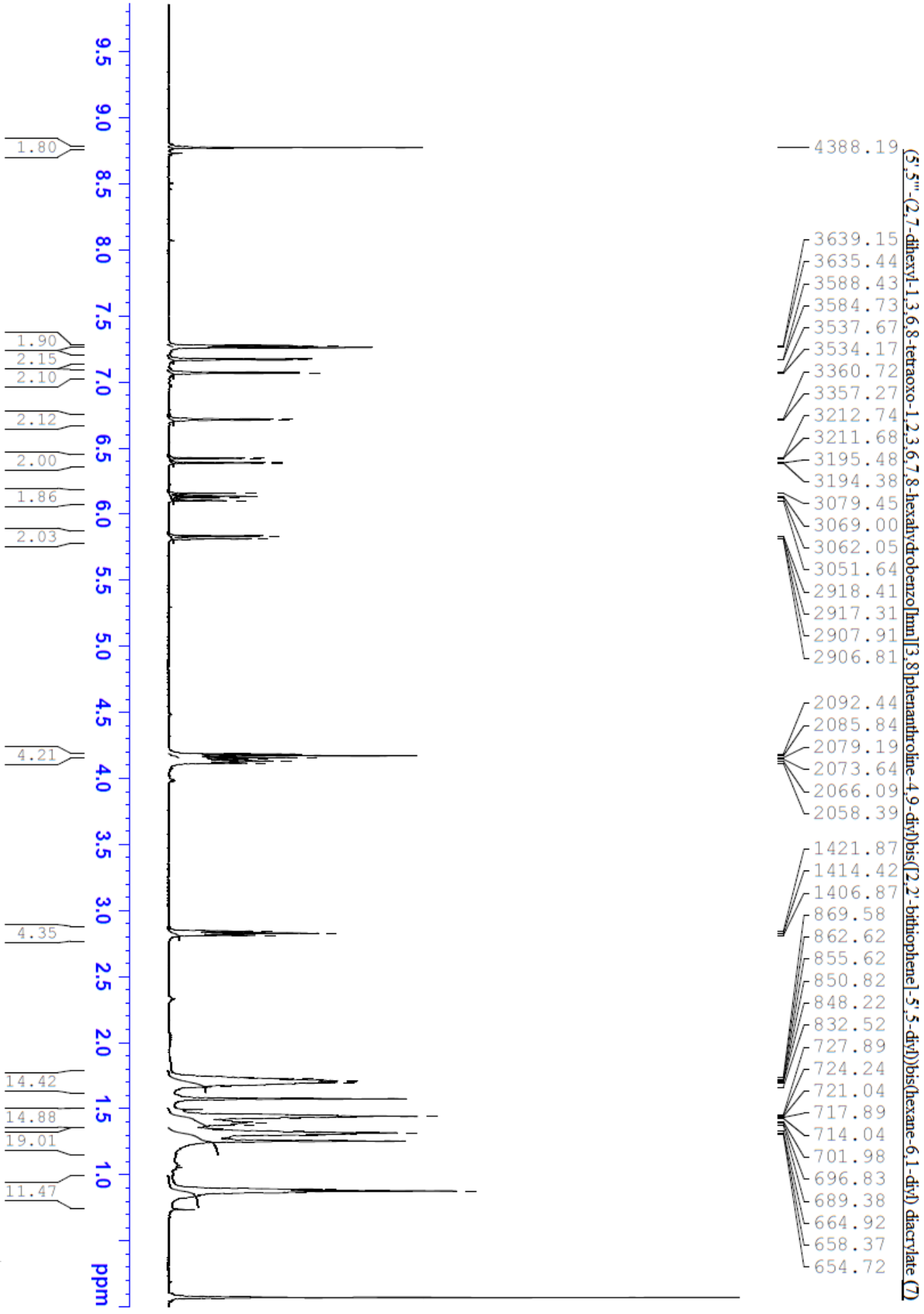

Appendix 4- NMR

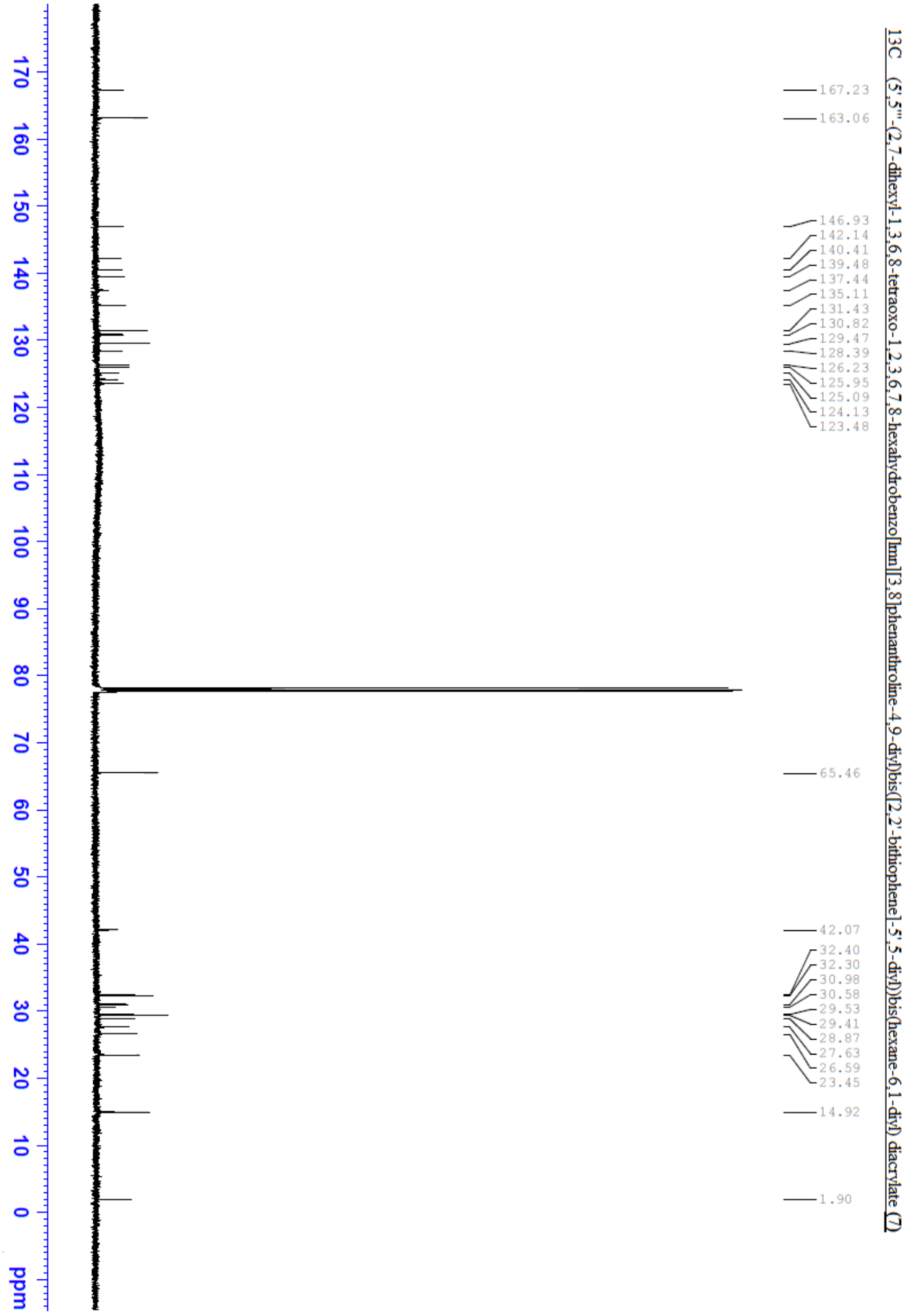

Appendix 4- NMR

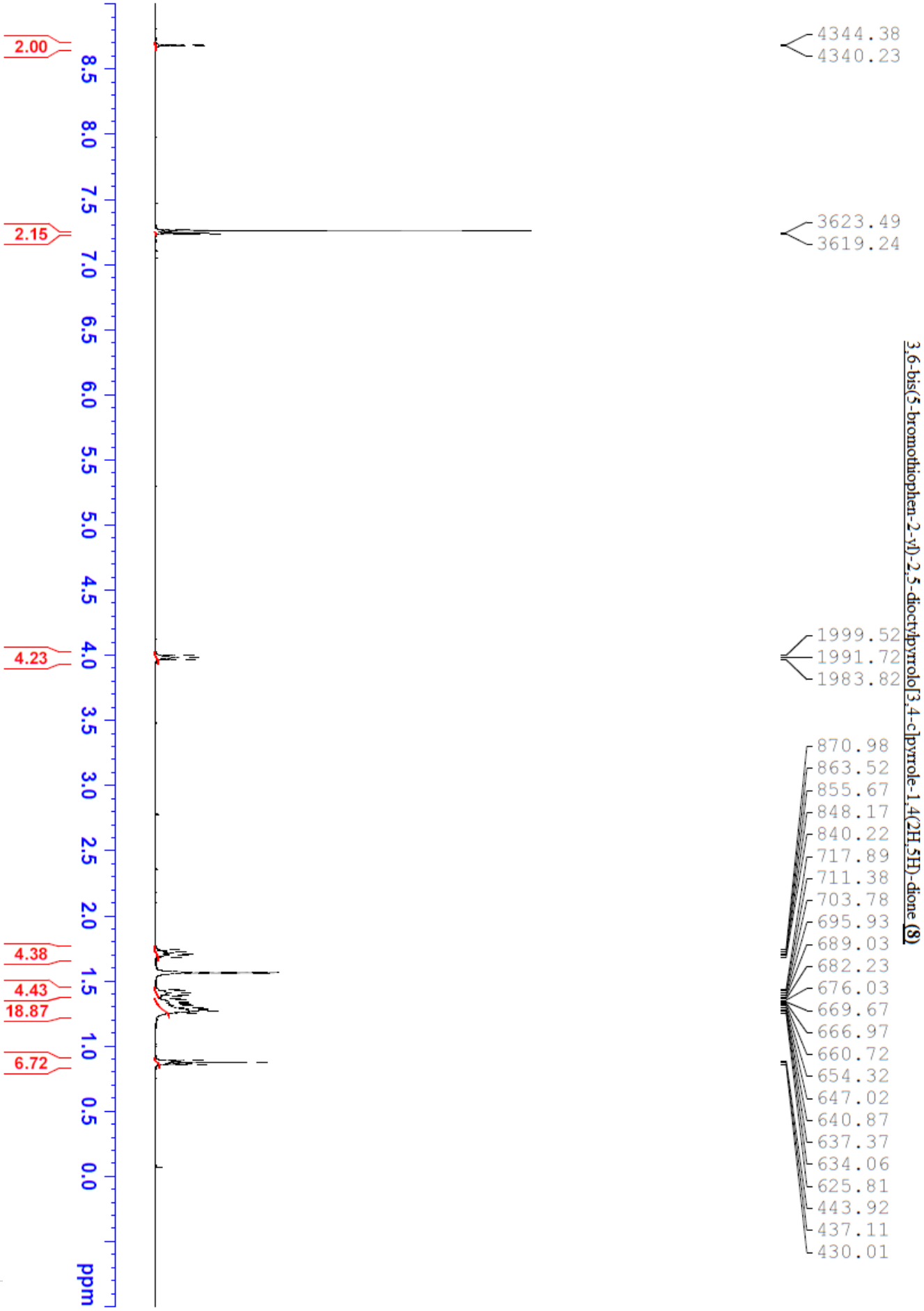

Appendix 4- NMR

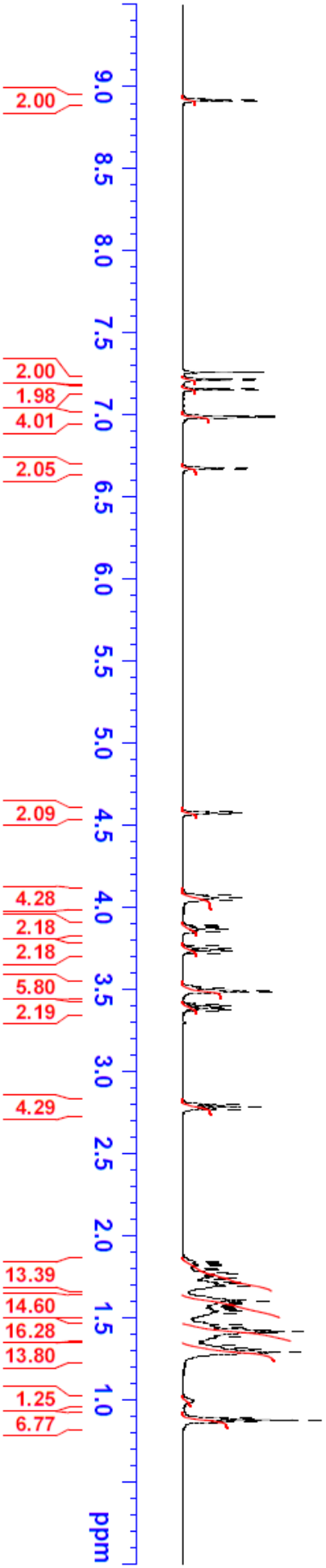

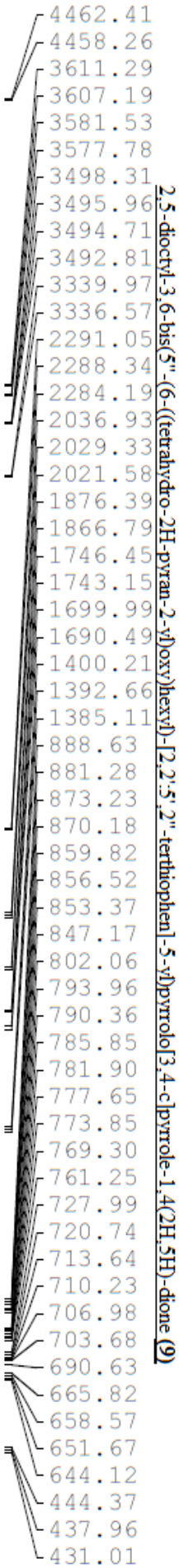

2,5-dioctyl-3,6-bis(5''-(6-((tetrahydro-2H-pyran-2-yl)oxy)hexyl)-[2,2':5',2''-terthiophen]-5-yl)pyrrolo[3,4-c]pyrrole-1,4(2H,5H)-dione (9)

Appendix 4- NMR

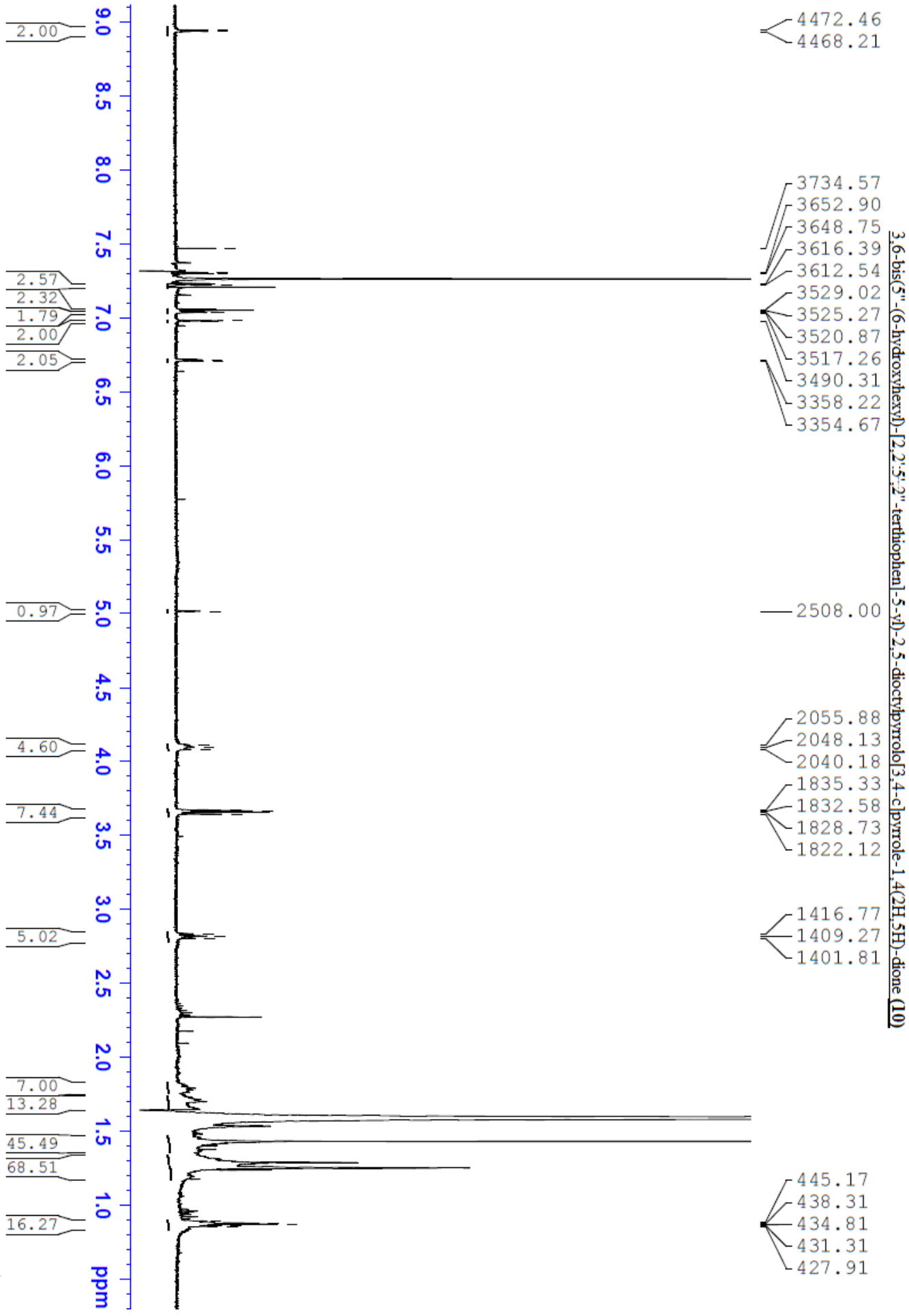

Appendix 4- NMR

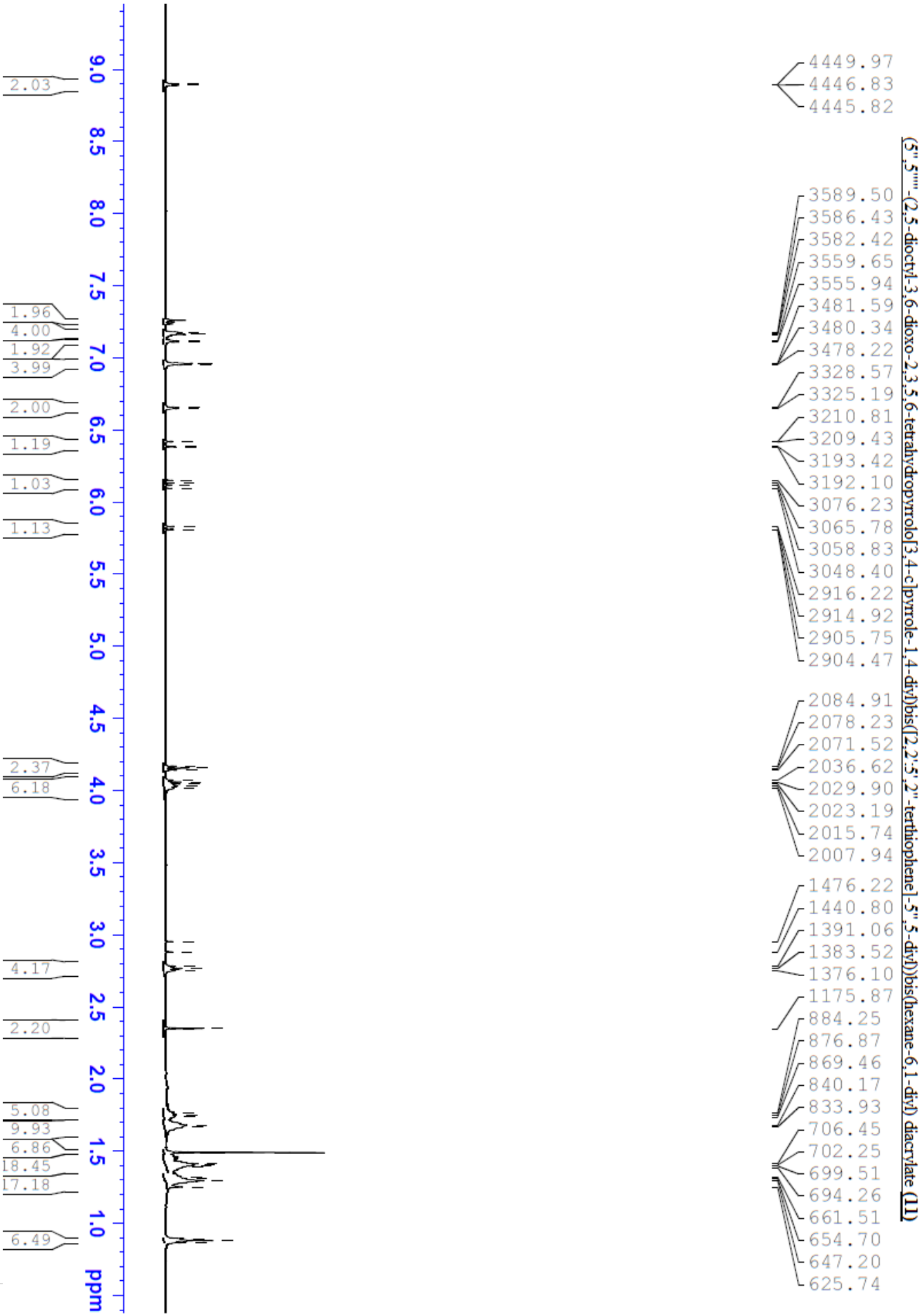

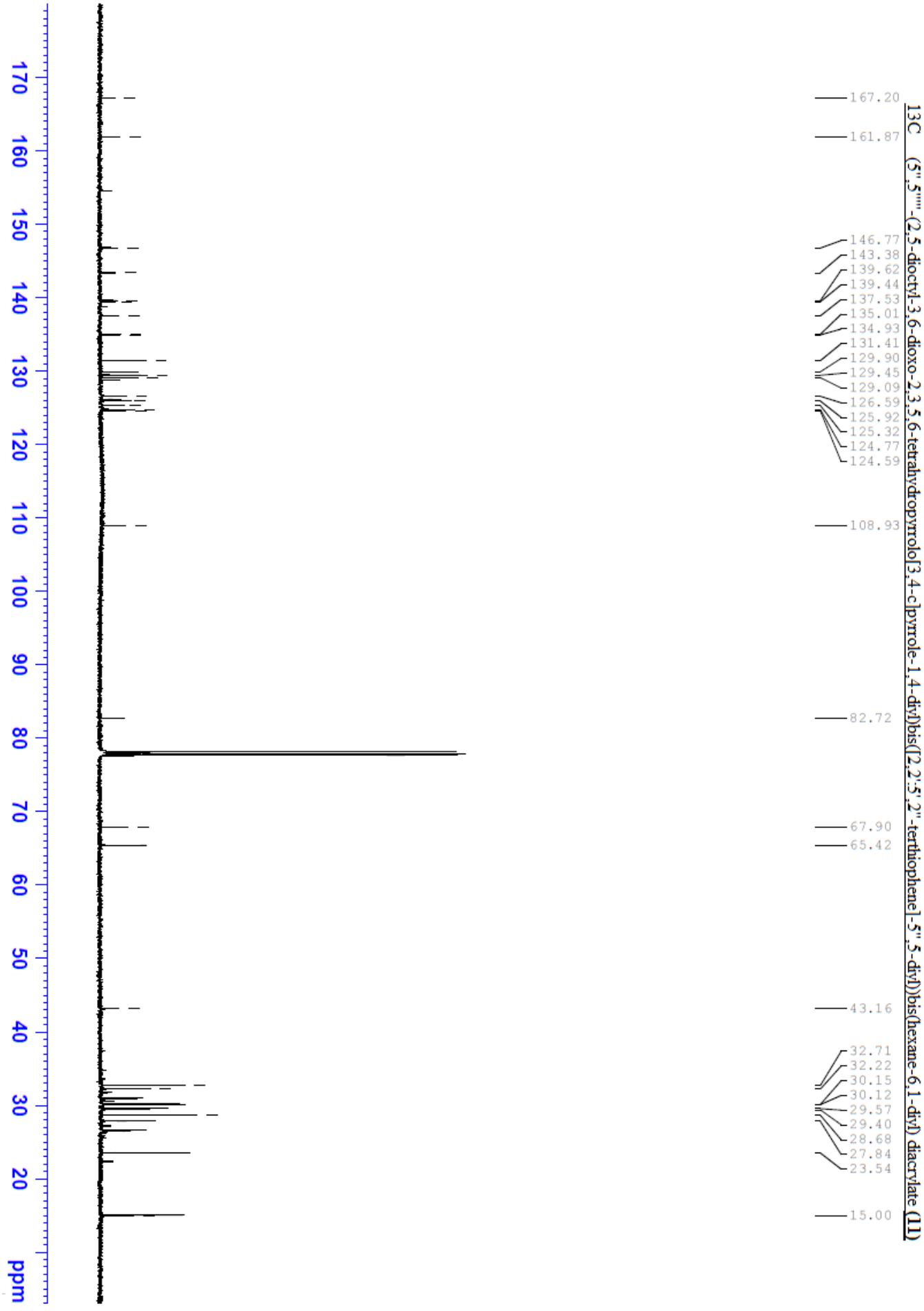
13C (5",5""-(2,5-dioctyl-3,6-dioxo-2,3,5,6-tetrahydropyrrolo[3,4-c]pyrrole-1,4-diyl)bis([2,2':5',2"-terthiophene]-5",5-diyl))bis(hexane-6,1-diyl) diacrylate (11)
167.20
161.87
146.77
143.38
139.62
139.44
137.53
135.01
134.93
131.41
129.90
129.45
129.09
126.59
125.92
125.32
124.77
124.59
108.93
82.72
67.90
65.42
43.16
32.71
32.22
30.15
30.12
29.57
29.40
28.68
27.84
23.54
15.00
170
160
150
140
130
120
110
100
90
80
70
60
50
40
30
20
ppm

Appendix 4- NMR

2-bromoethyl acrylate **(12)**

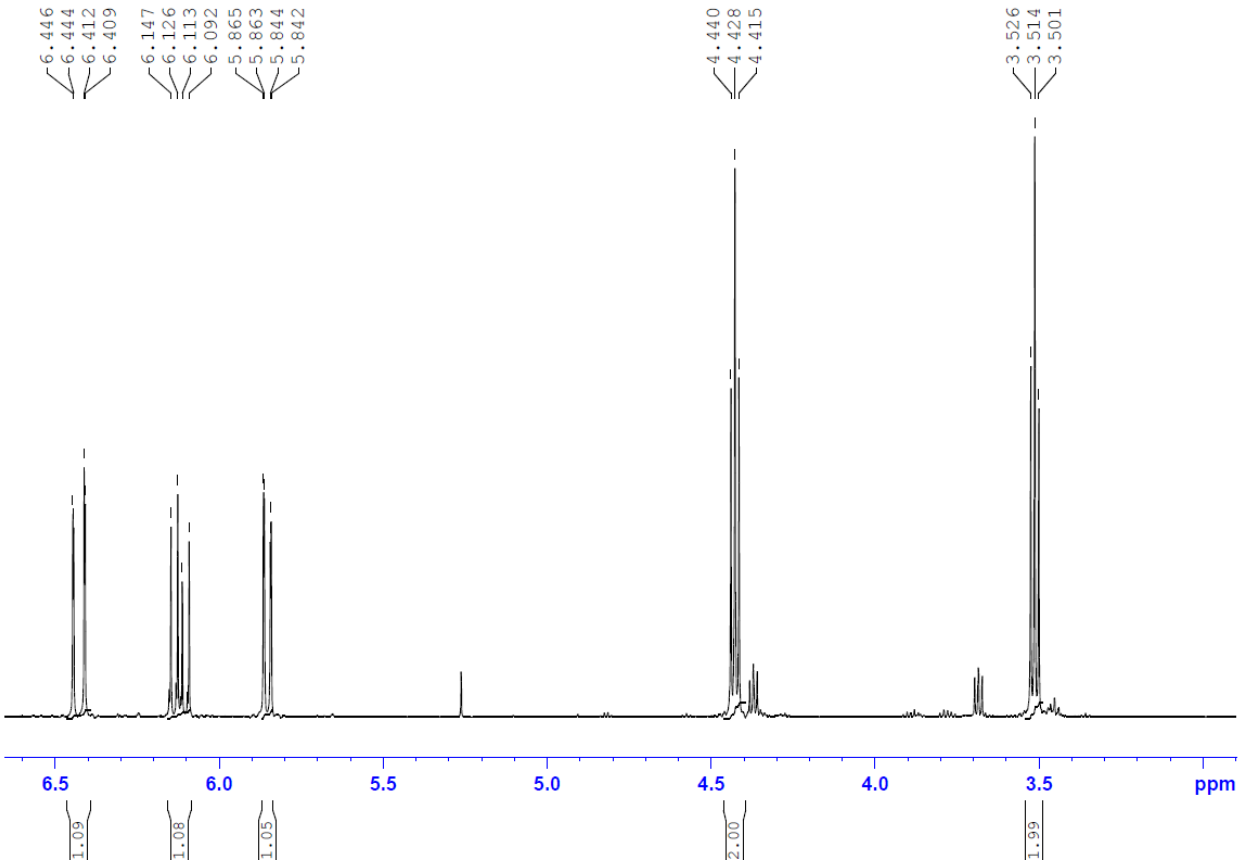

2-([2,2'-bithiophen]-5-yl)-5,5-dimethyl-1,3-dioxane **(15)**

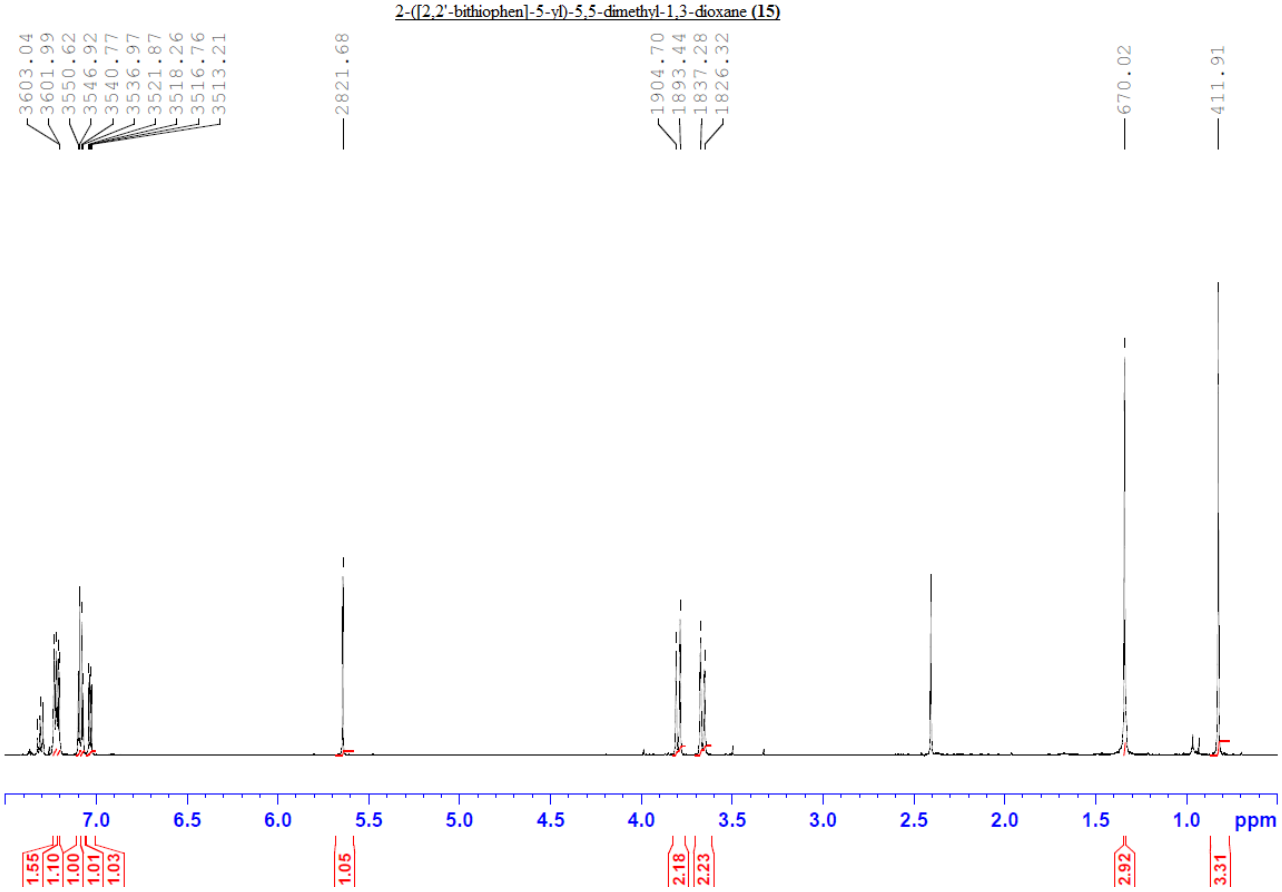

3,6-bis(5''-(5,5-dimethyl-1,3-dioxan-2-yl)-[2,2':5',2''-terthiophen]-5-yl)-2,5-dioctylpyrrolo[3,4-c]pyrrole-1,4(2H,5H)-dione **(17)**

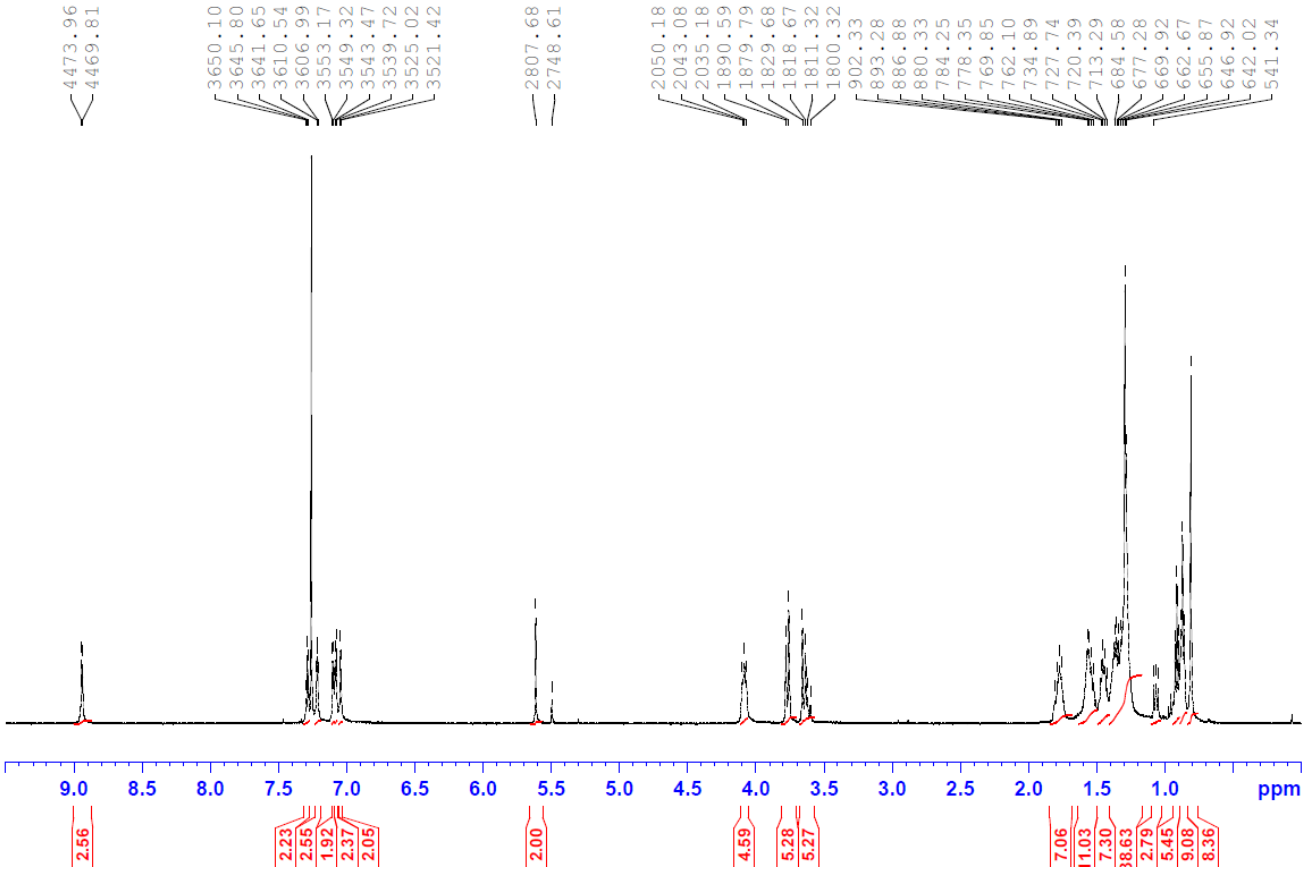

5'',5'''''-(2,5-dioctyl-3,6-dioxo-2,3,5,6-tetrahydropyrrolo[3,4-c]pyrrole-1,4-diyl)bis([2,2':5',2''-terthiophene]-5-carbaldehyde) **(18)**

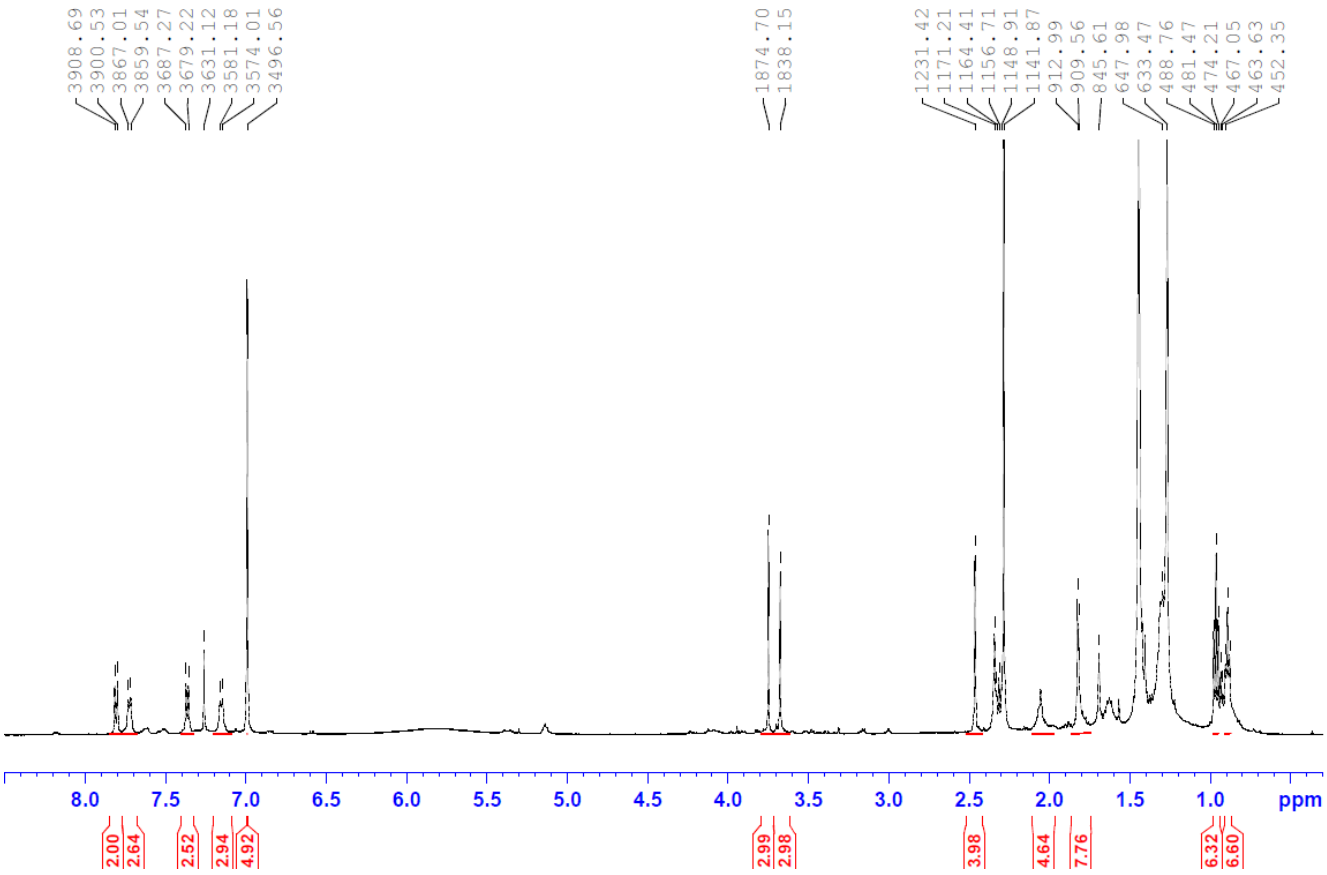

2,5-di(thiophen-2-yl)-1H-pyrrole **(19)**

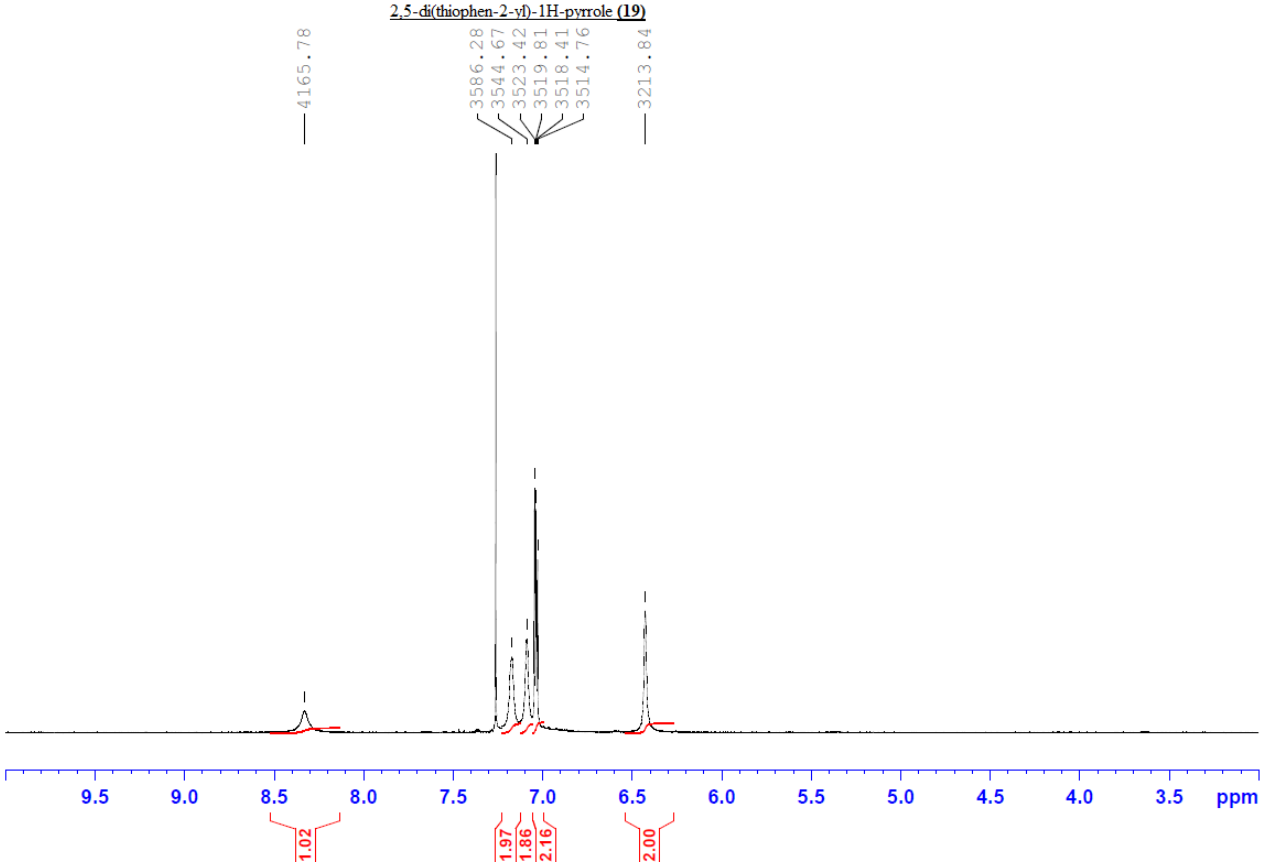

tert-butyl 2,5-di(thiophen-2-yl)-1H-pyrrole-1-carboxylate **(20)**

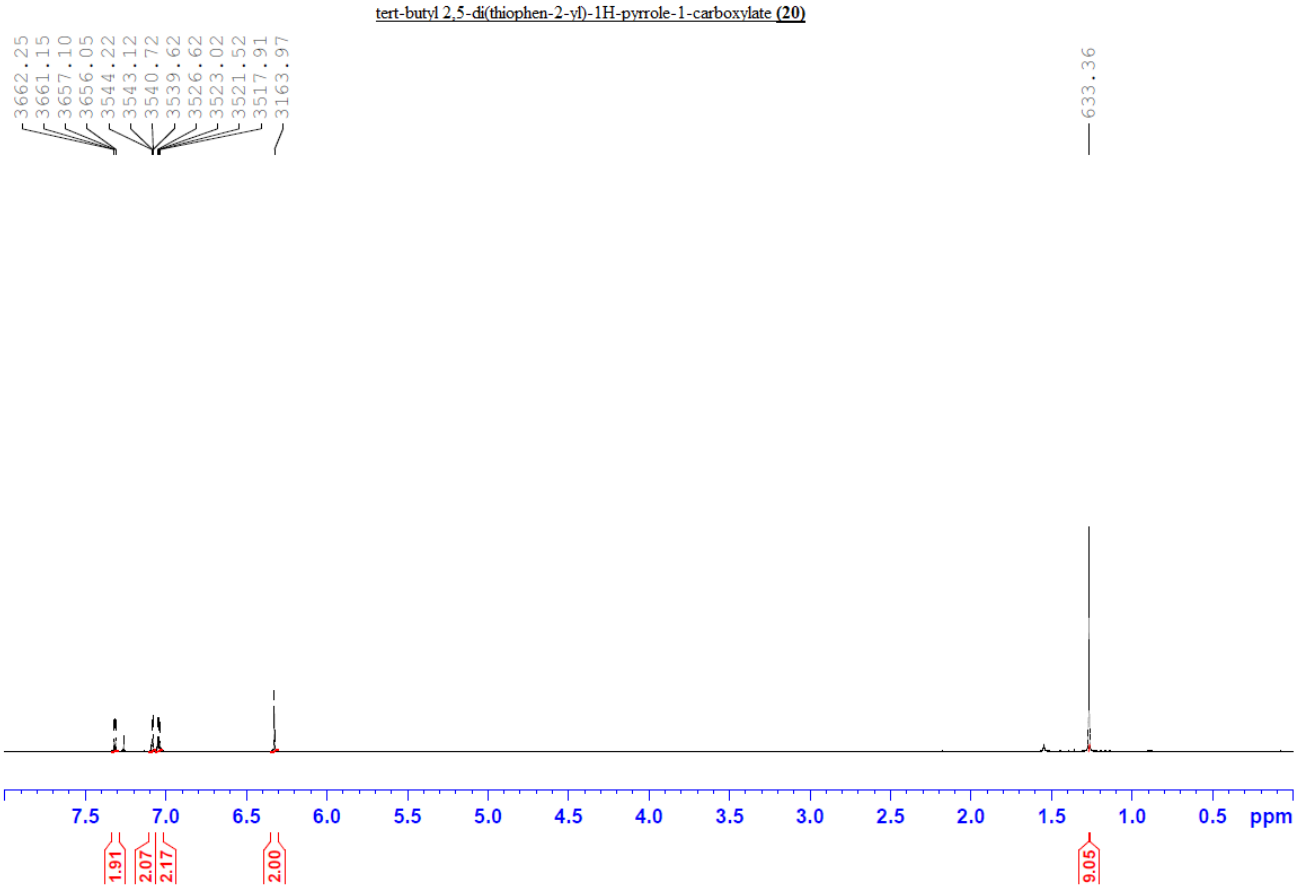

Appendix 4- NMR

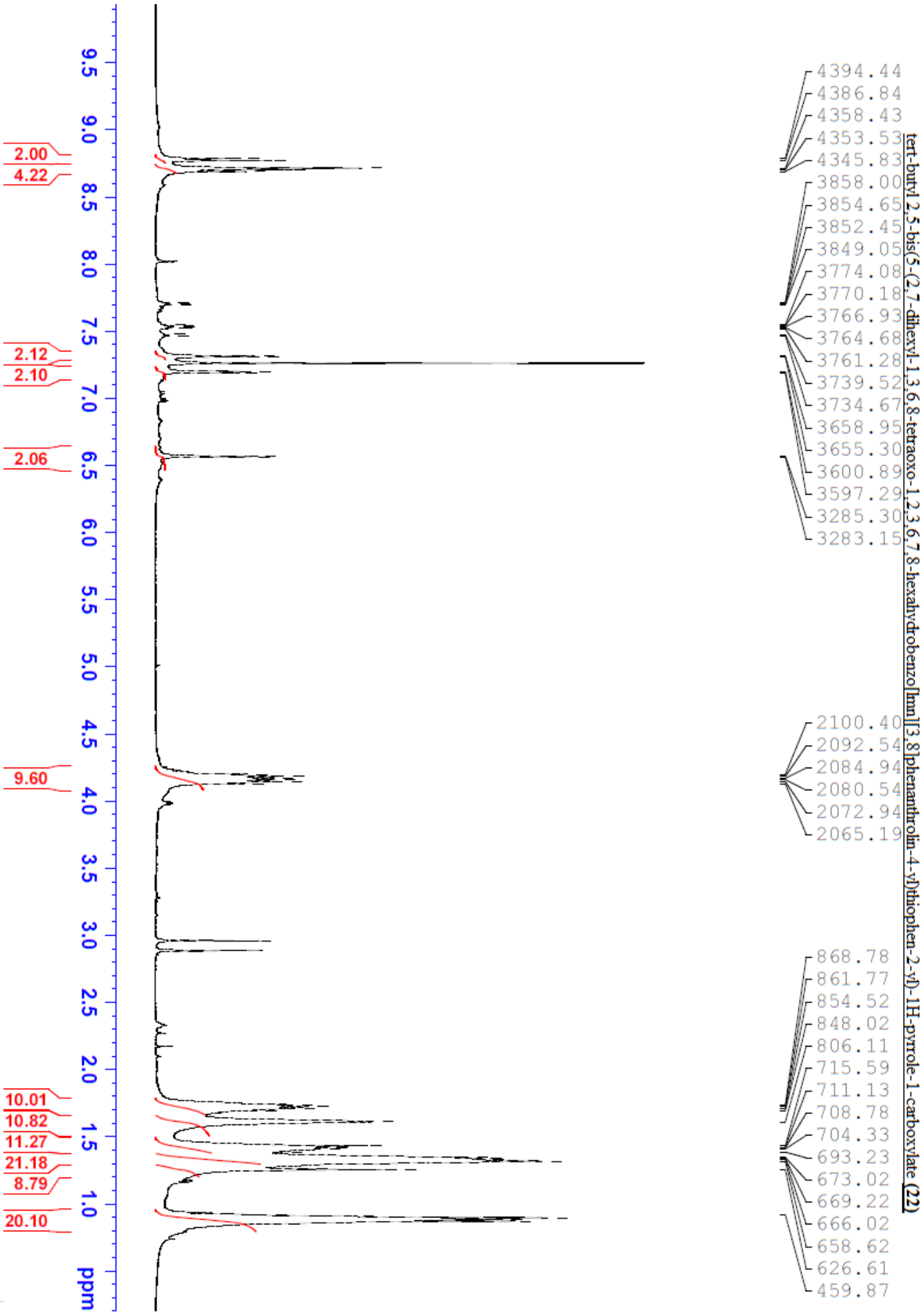

Appendix 4- NMR

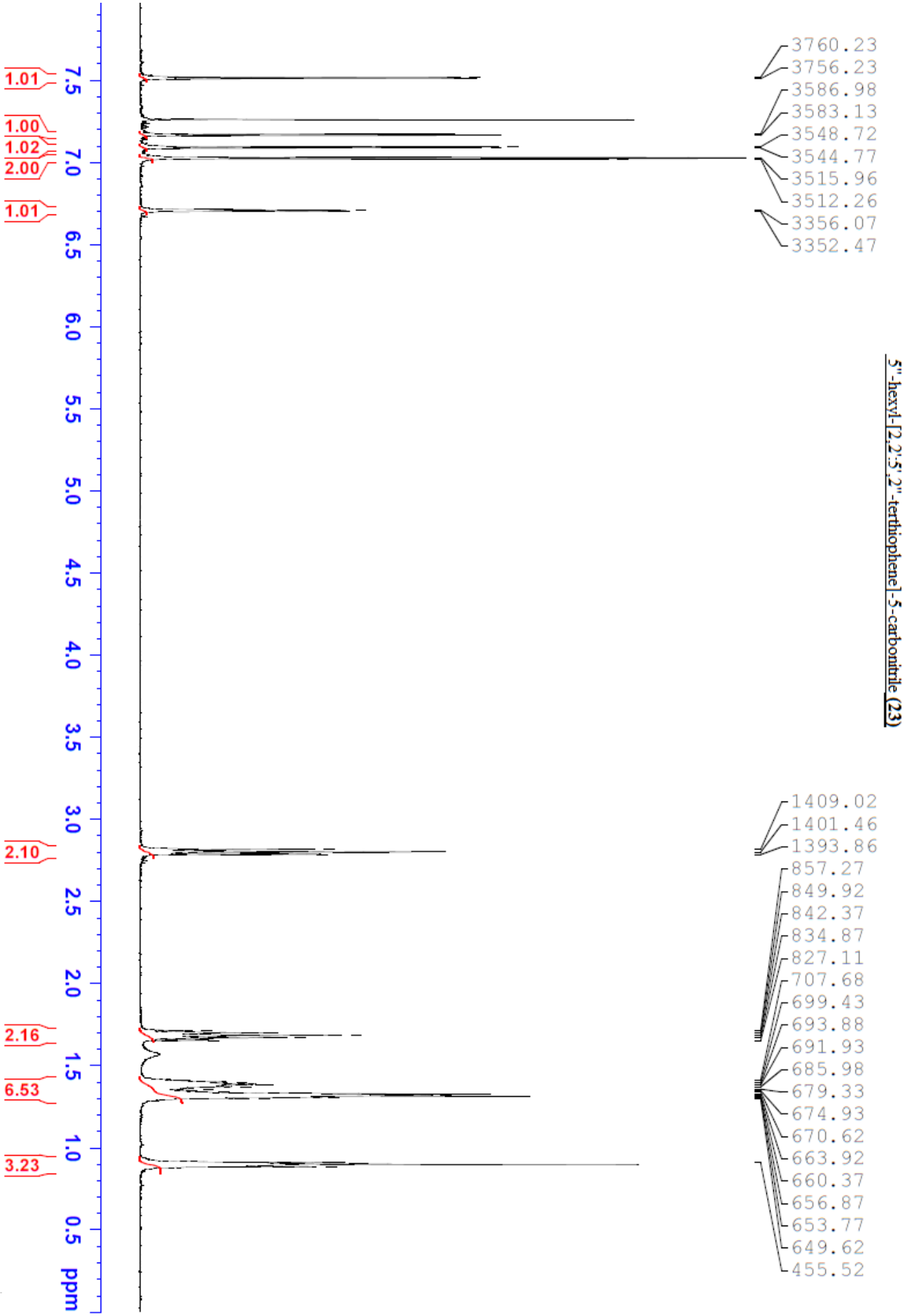

Appendix 4- NMR

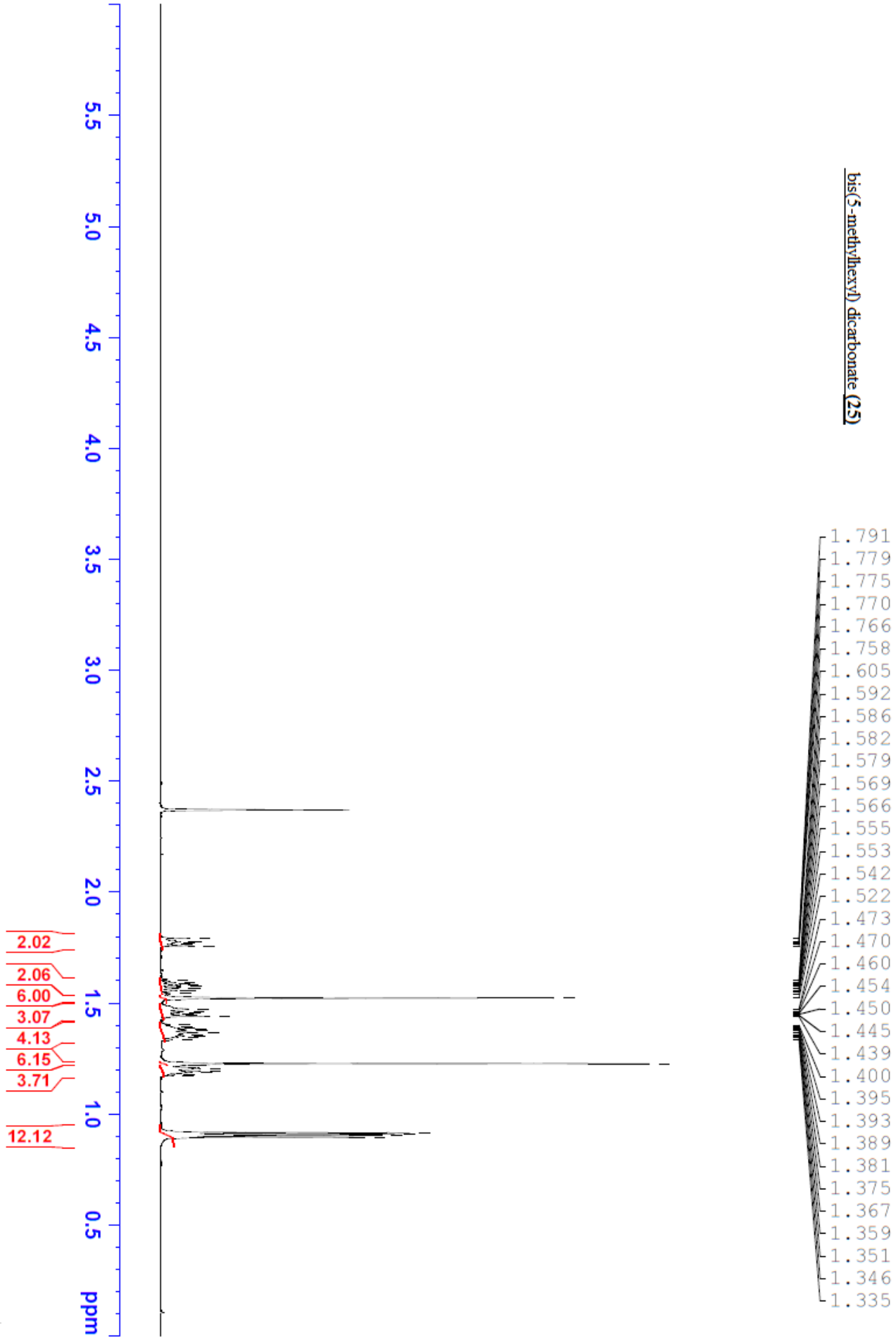

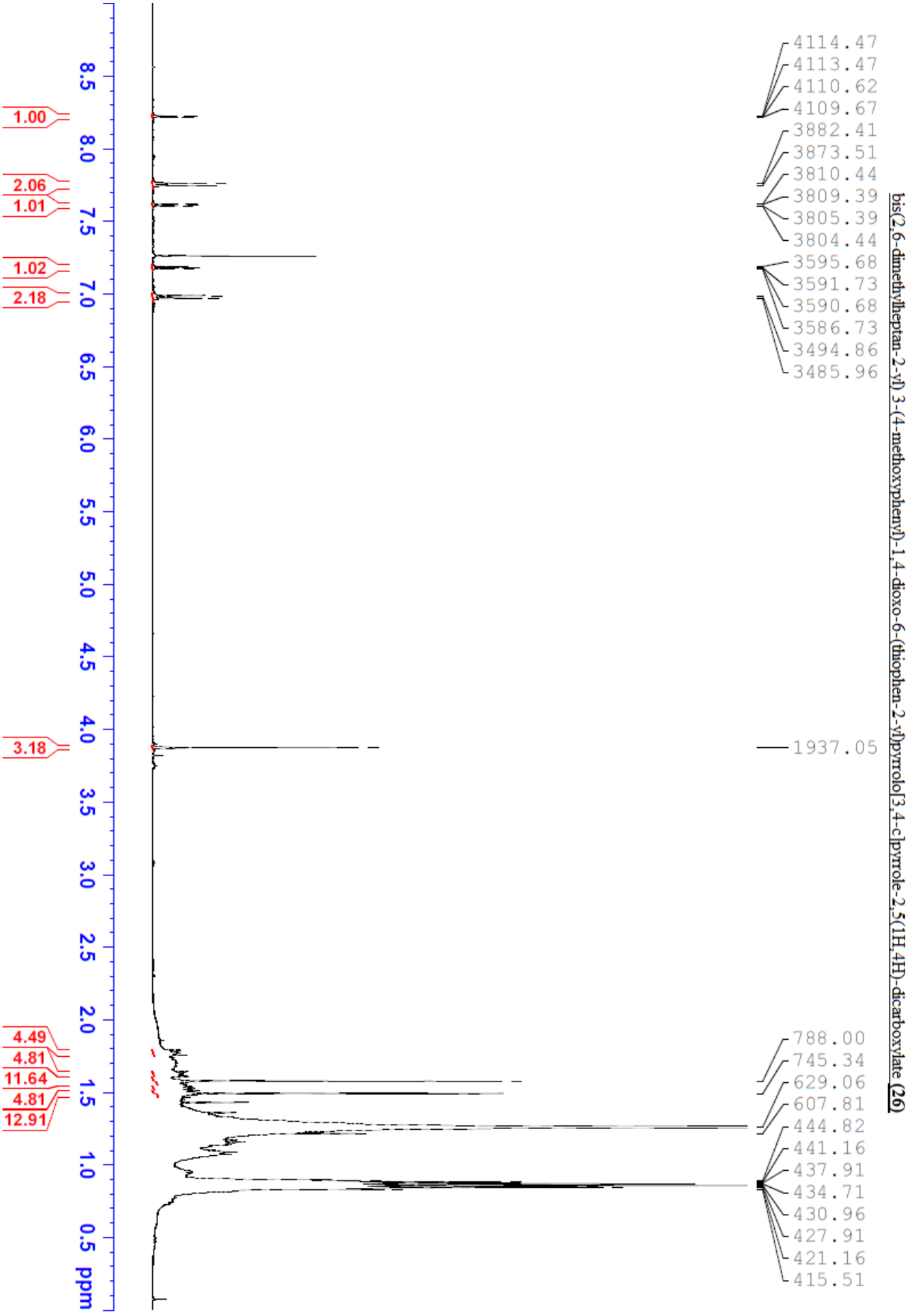
bis(2,6-dimethylheptan-2-yl) 3-(4-methoxyphenyl)-1,4-dioxo-6-(thiophen-2-yl)pyrrolo[3,4-c]pyrrole-2,5(1H,4H)-dicarboxylate (26)
4114.47
4113.47
4110.62
4109.67
3882.41
3873.51
3810.44
3809.39
3805.39
3804.44
3595.68
3591.73
3590.68
3586.73
3494.86
3485.96
1937.05
788.00
745.34
629.06
607.81
444.82
441.16
437.91
434.71
430.96
427.91
421.16
415.51
1.00
2.06
1.01
1.02
2.18
3.18
4.49
4.81
11.64
4.81
12.91
8.5
8.0
7.5
7.0
6.5
6.0
5.5
5.0
4.5
4.0
3.5
3.0
2.5
2.0
1.5
1.0
0.5
ppm

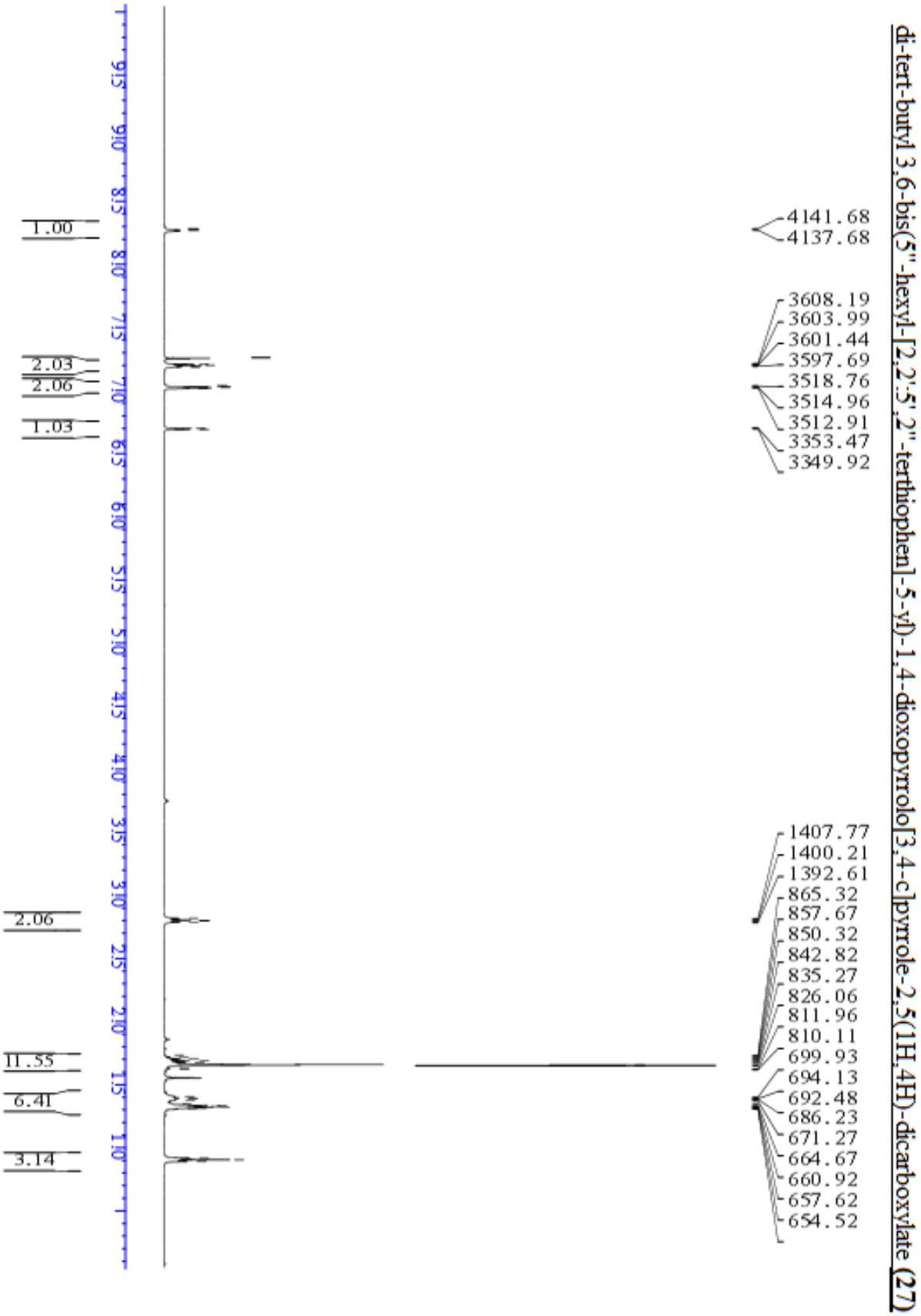
di-tert-butyl 3,6-bis(5''-hexyl-[2,2':5',2''-terthiophen]-5-yl)-1,4-dioxopyrrolo[3,4-c]pyrrole-2,5(1H,4H)-dicarboxylate (27)
1.00
2.03
2.06
1.03
2.06
11.55
6.41
3.14
4141.68
4137.68
3608.19
3603.99
3601.44
3597.69
3518.76
3514.96
3512.91
3353.47
3349.92
1407.77
1400.21
1392.61
865.32
857.67
850.32
842.82
835.27
826.06
811.96
810.11
699.93
694.13
692.48
686.23
671.27
664.67
660.92
657.62
654.52

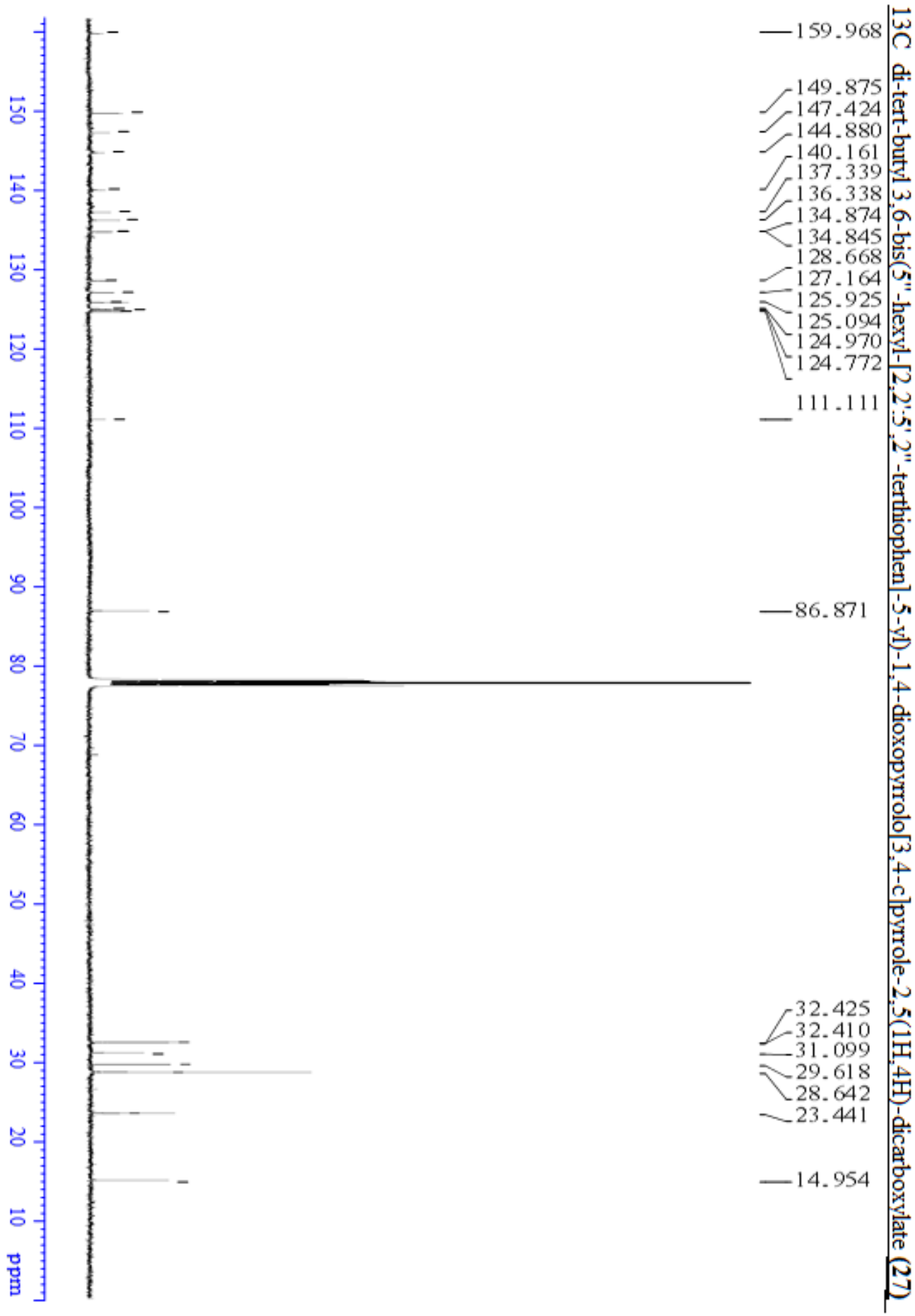
13C di-tert-butyl 3,6-bis(5''-hexyl-[2,2':5',2''-terthiophen]-5-yl)-1,4-dioxopyrrolo[3,4-c]pyrrole-2,5(1H,4H)-dicarboxylate (27)
159.968
149.875
147.424
144.880
140.161
137.339
136.338
134.874
134.845
128.668
127.164
125.925
125.094
124.970
124.772
111.111
86.871
32.425
32.410
31.099
29.618
28.642
23.441
14.954
150
140
130
120
110
100
90
80
70
60
50
40
30
20
10
ppm

Appendix 4- NMR

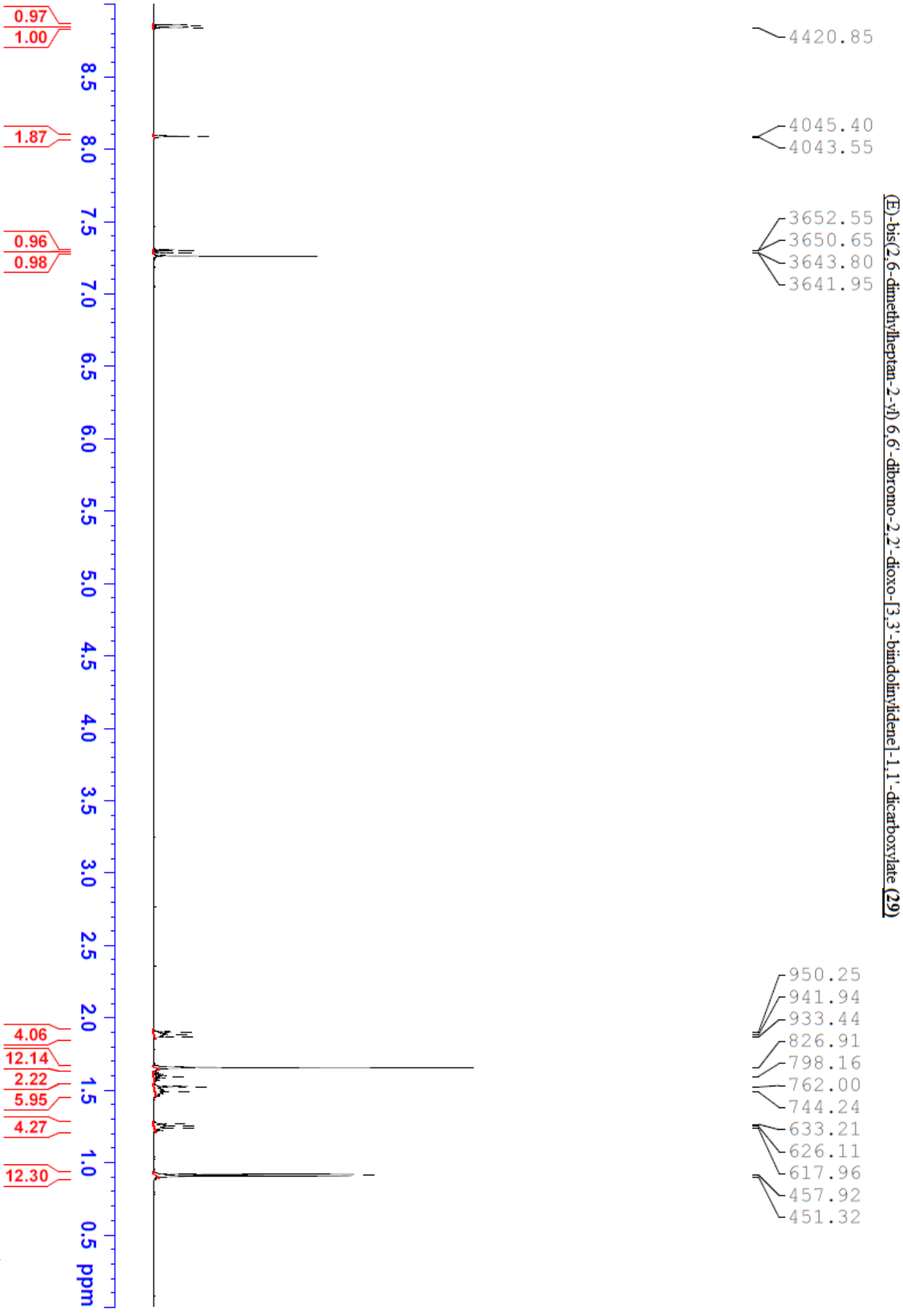

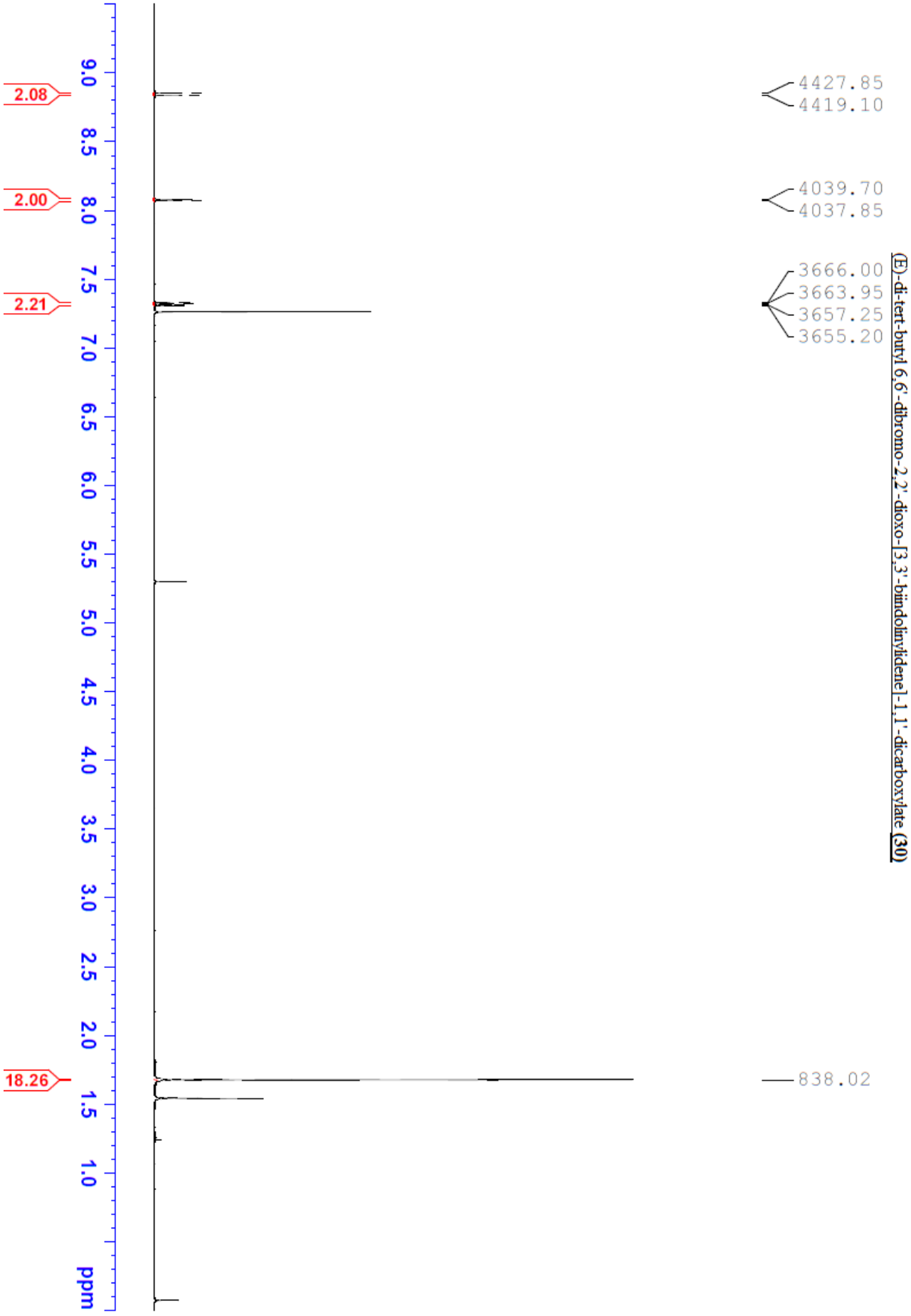
2.08
2.00
2.21
18.26
9.0
8.5
8.0
7.5
7.0
6.5
6.0
5.5
5.0
4.5
4.0
3.5
3.0
2.5
2.0
1.5
1.0
ppm
4427.85
4419.10
4039.70
4037.85
3666.00
3663.95
3657.25
3655.20
838.02
(E)-di-tert-butyl 6,6'-dibromo-2,2'-dioxo-[3,3'-biindolinylidene]-1,1'-dicarboxylate (30)

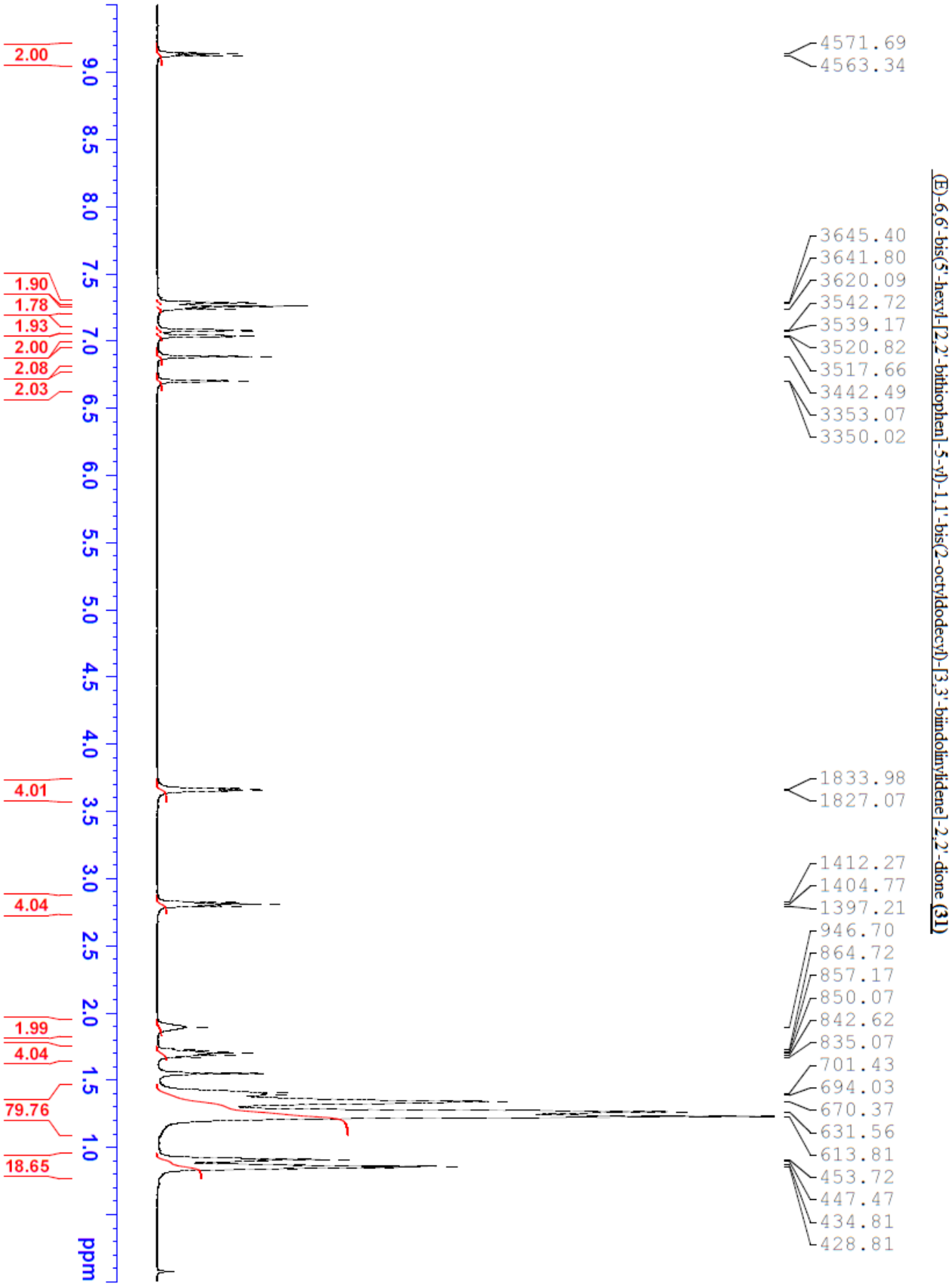
(E)-6,6'-bis(5'-hexyl-[2,2'-bithiophen]-5-yl)-1,1'-bis(2-octyldodecyl)-[3,3'-biindolinylidene]-2,2'-dione (31)
2.00
1.90
1.78
1.93
2.00
2.08
2.03
4.01
4.04
1.99
4.04
79.76
18.65
ppm
4571.69
4563.34
3645.40
3641.80
3620.09
3542.72
3539.17
3520.82
3517.66
3442.49
3353.07
3350.02
1833.98
1827.07
1412.27
1404.77
1397.21
946.70
864.72
857.17
850.07
842.62
835.07
701.43
694.03
670.37
631.56
613.81
453.72
447.47
434.81
428.81

Appendix 4- NMR

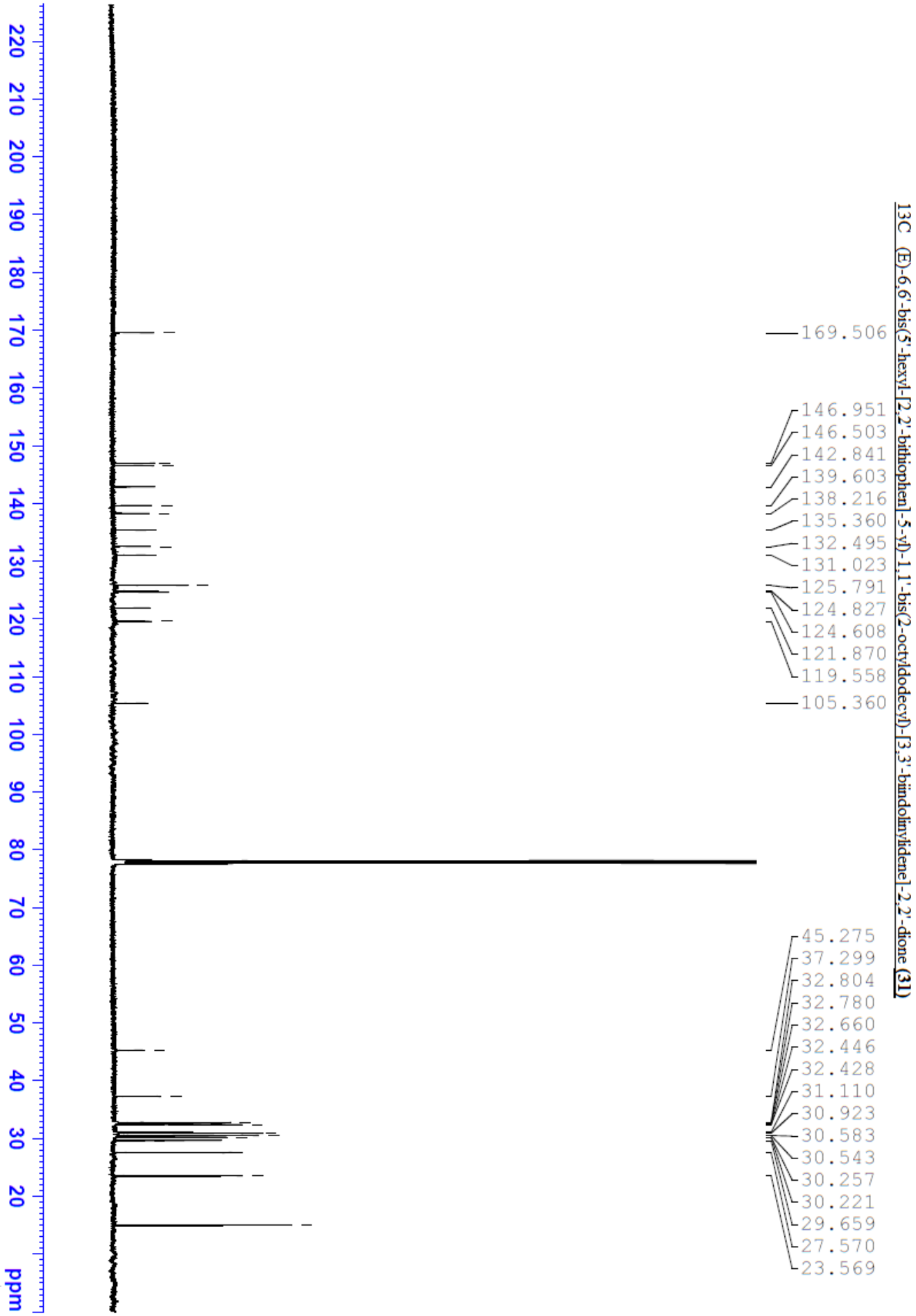

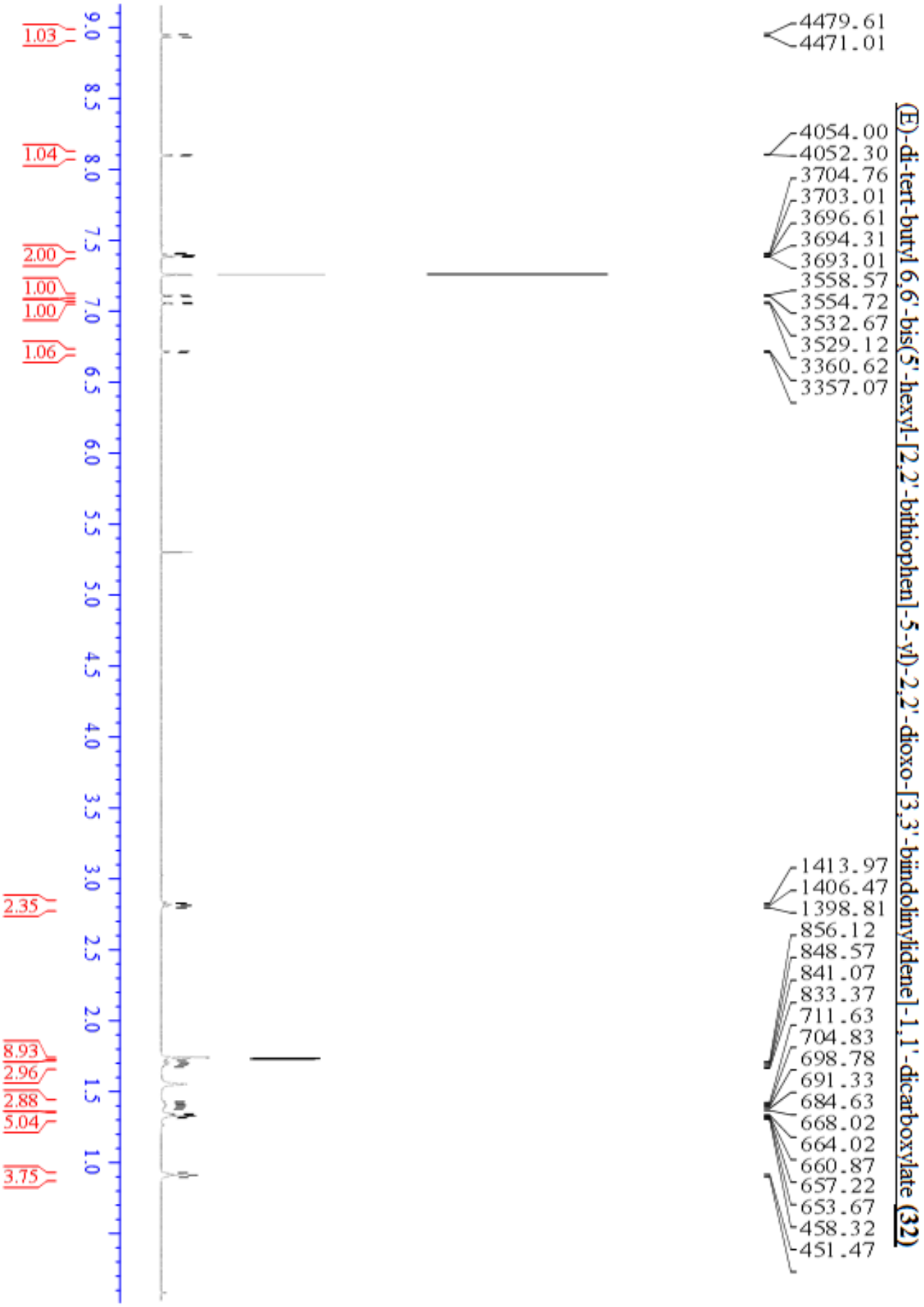
(E)-di-tert-butyl 6,6'-bis(5'-hexyl-[2,2'-bithiophen]-5-yl)-2,2'-dioxo-[3,3'-biindolinylidene]-1,1'-dicarboxylate (32)
4479.61
4471.01
4054.00
4052.30
3704.76
3703.01
3696.61
3694.31
3693.01
3558.57
3554.72
3532.67
3529.12
3360.62
3357.07
1413.97
1406.47
1398.81
856.12
848.57
841.07
833.37
711.63
704.83
698.78
691.33
684.63
668.02
664.02
660.87
657.22
653.67
458.32
451.47
1.03
1.04
2.00
1.00
1.00
1.06
2.35
8.93
2.96
2.88
5.04
3.75
9.0
8.5
8.0
7.5
7.0
6.5
6.0
5.5
5.0
4.5
4.0
3.5
3.0
2.5
2.0
1.5
1.0

Appendix 4- NMR

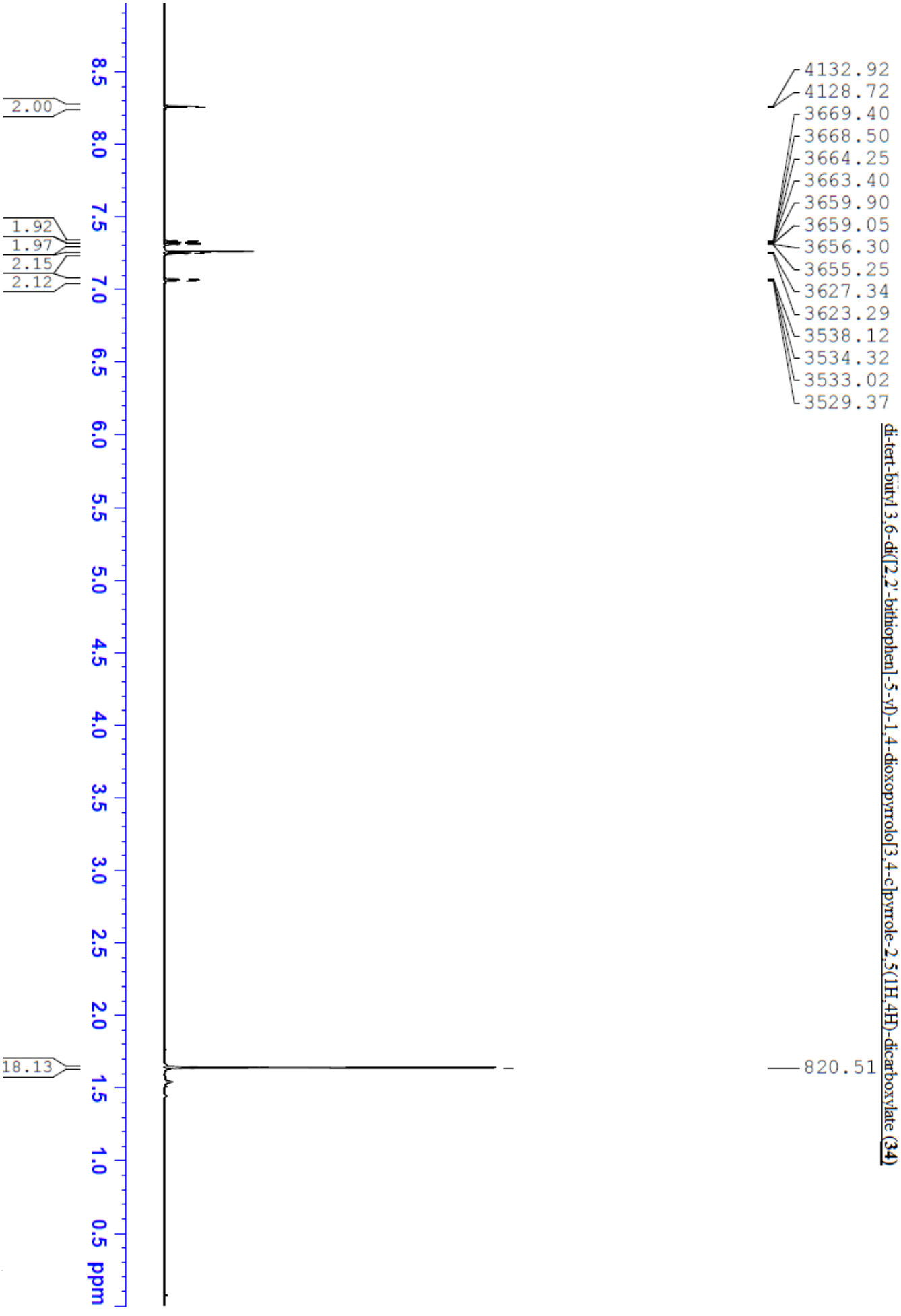

Appendix 4- NMR

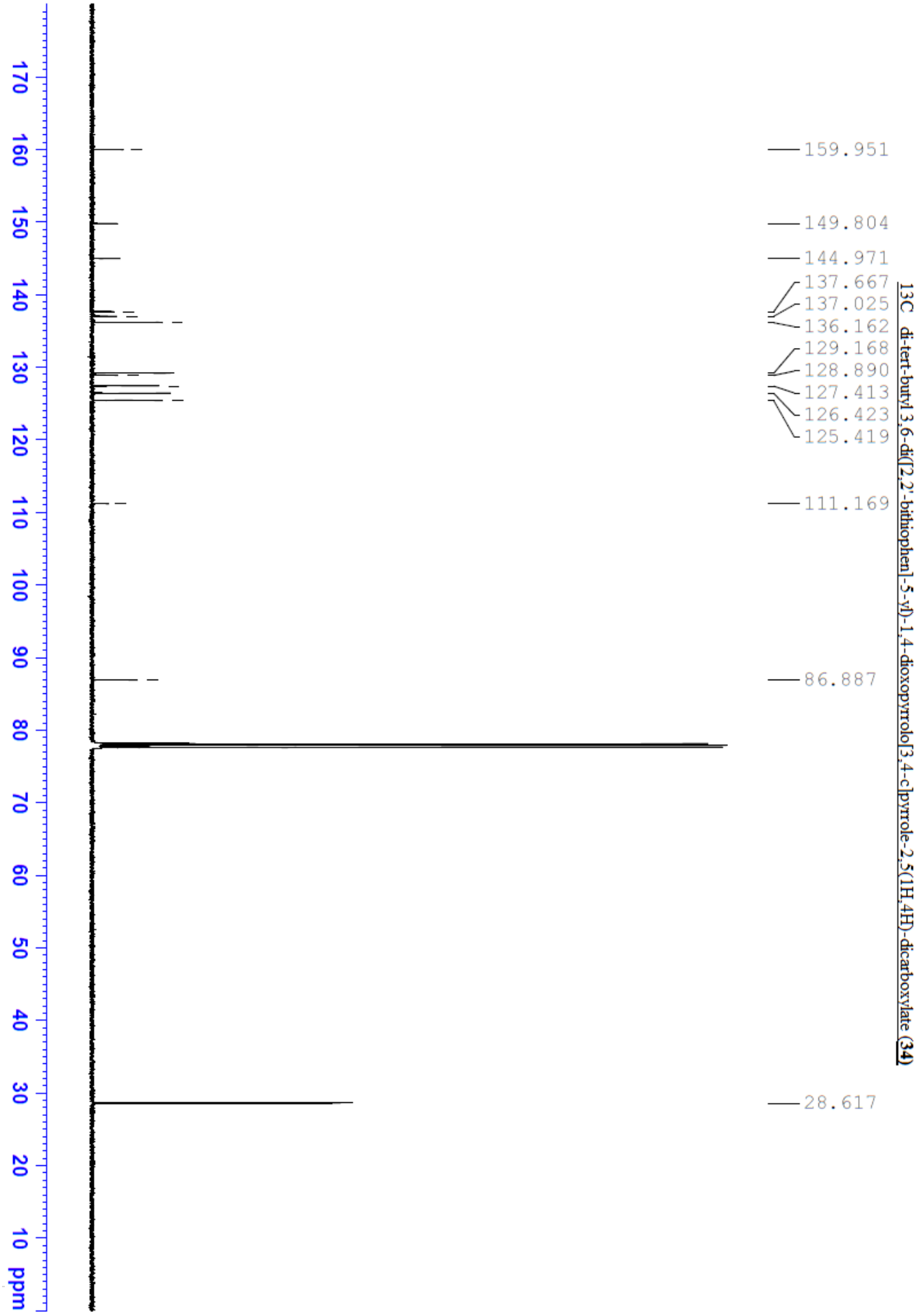

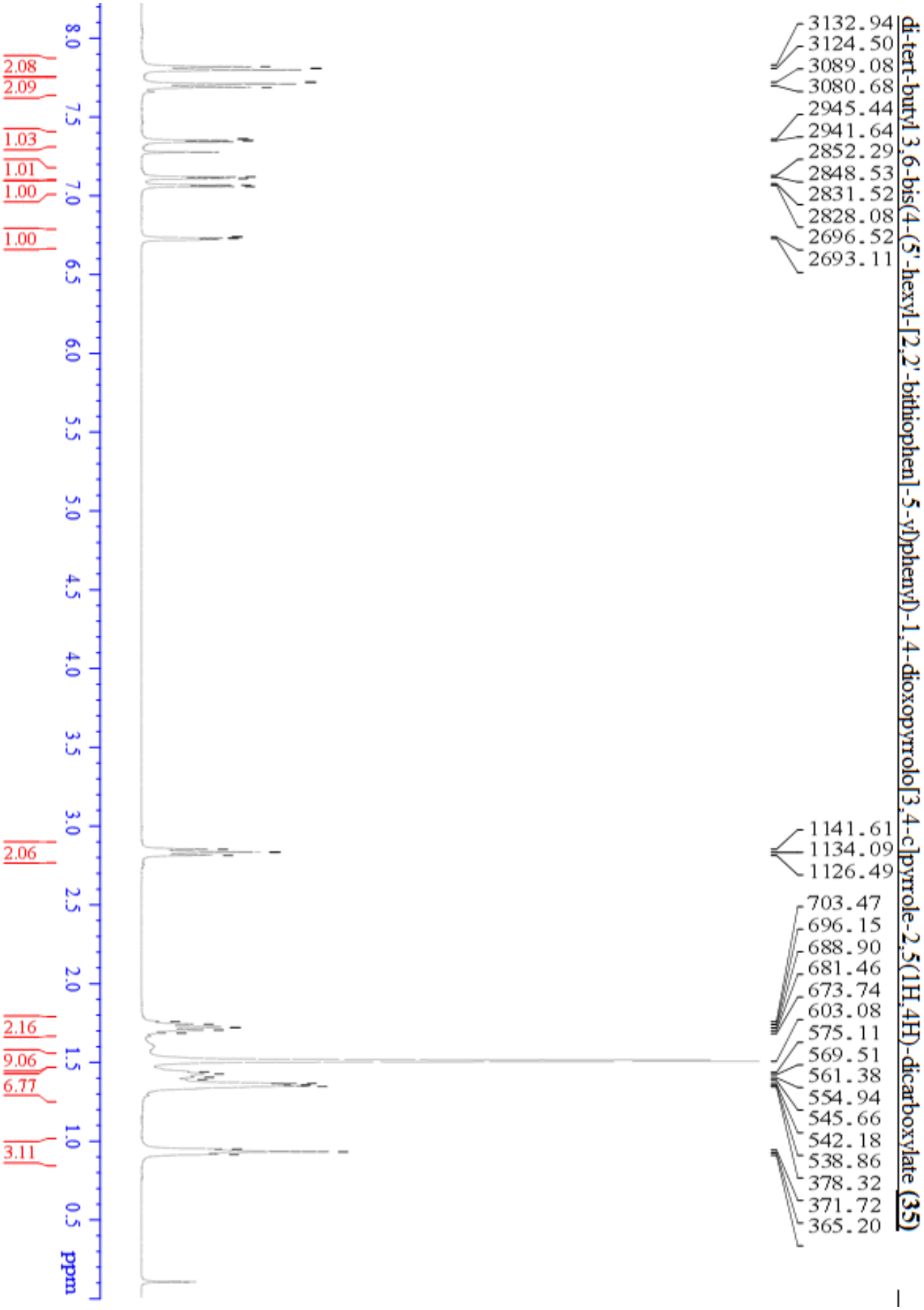
di-tert-butyl 3,6-bis(4-(5'-hexyl-[2,2'-bithiophen]-5-yl)phenyl)-1,4-dioxopyrrolo[3,4-c]pyrrole-2,5(1H,4H)-dicarboxylate (35)
3132.94
3124.50
3089.08
3080.68
2945.44
2941.64
2852.29
2848.53
2831.52
2828.08
2696.52
2693.11
1141.61
1134.09
1126.49
703.47
696.15
688.90
681.46
673.74
603.08
575.11
569.51
561.38
554.94
545.66
542.18
538.86
378.32
371.72
365.20
2.08
2.09
1.03
1.01
1.00
1.00
2.06
2.16
9.06
6.77
3.11
8.0
7.5
7.0
6.5
6.0
5.5
5.0
4.5
4.0
3.5
3.0
2.5
2.0
1.5
1.0
0.5
ppm

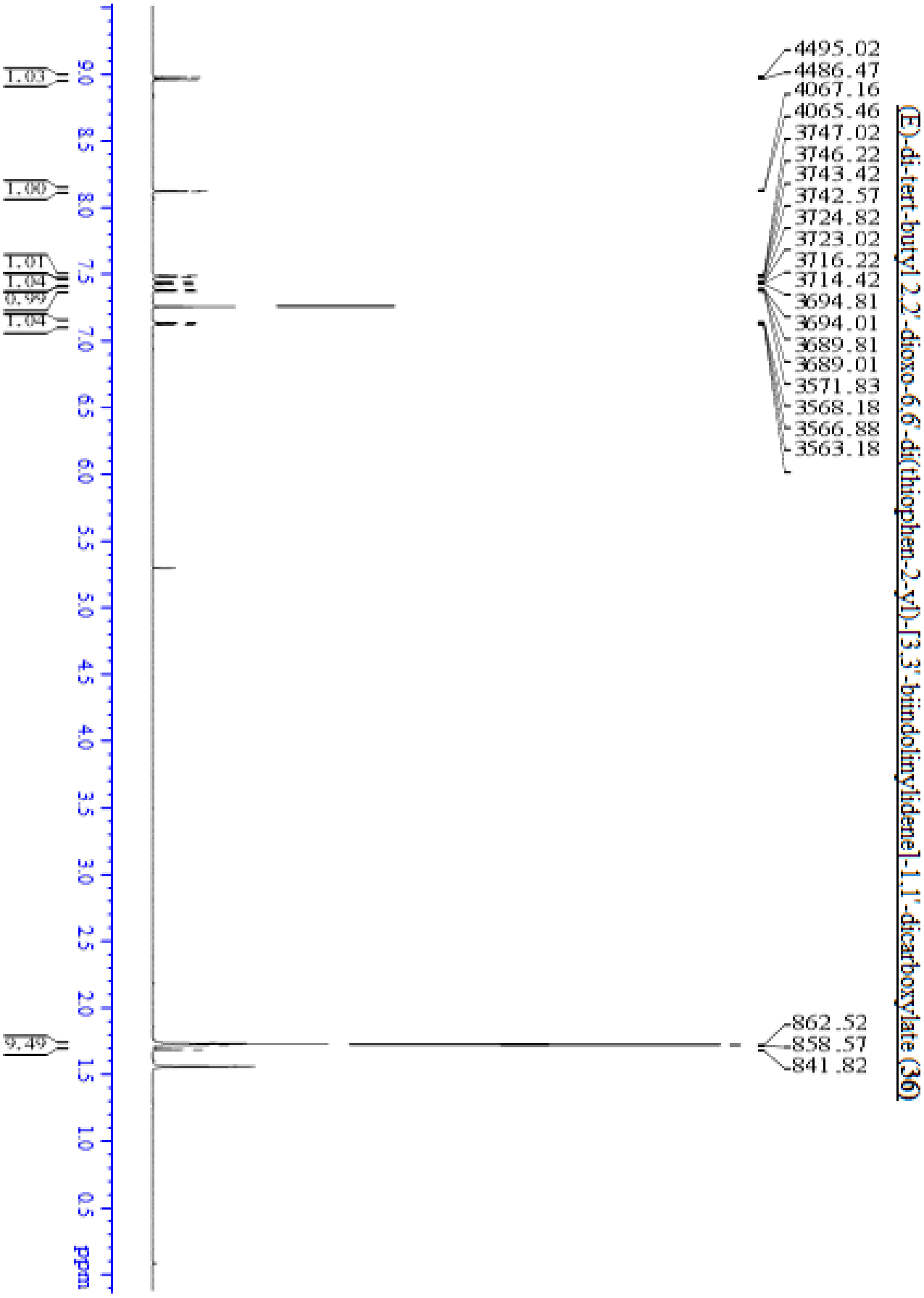
(E)-di-tert-butyl 2,2'-dioxo-6,6'-di(thiophen-2-yl)-[3,3'-biindolinylidene]-1,1'-dicarboxylate (36)
1.03
1.00
1.01
1.04
0.99
1.04
9.49
9.0
8.5
8.0
7.5
7.0
6.5
6.0
5.5
5.0
4.5
4.0
3.5
3.0
2.5
2.0
1.5
1.0
0.5
ppm
4495.02
4486.47
4067.16
4065.46
3747.02
3746.22
3743.42
3742.57
3724.82
3723.02
3716.22
3714.42
3694.81
3694.01
3689.81
3689.01
3571.83
3568.18
3566.88
3563.18
862.52
858.57
841.82

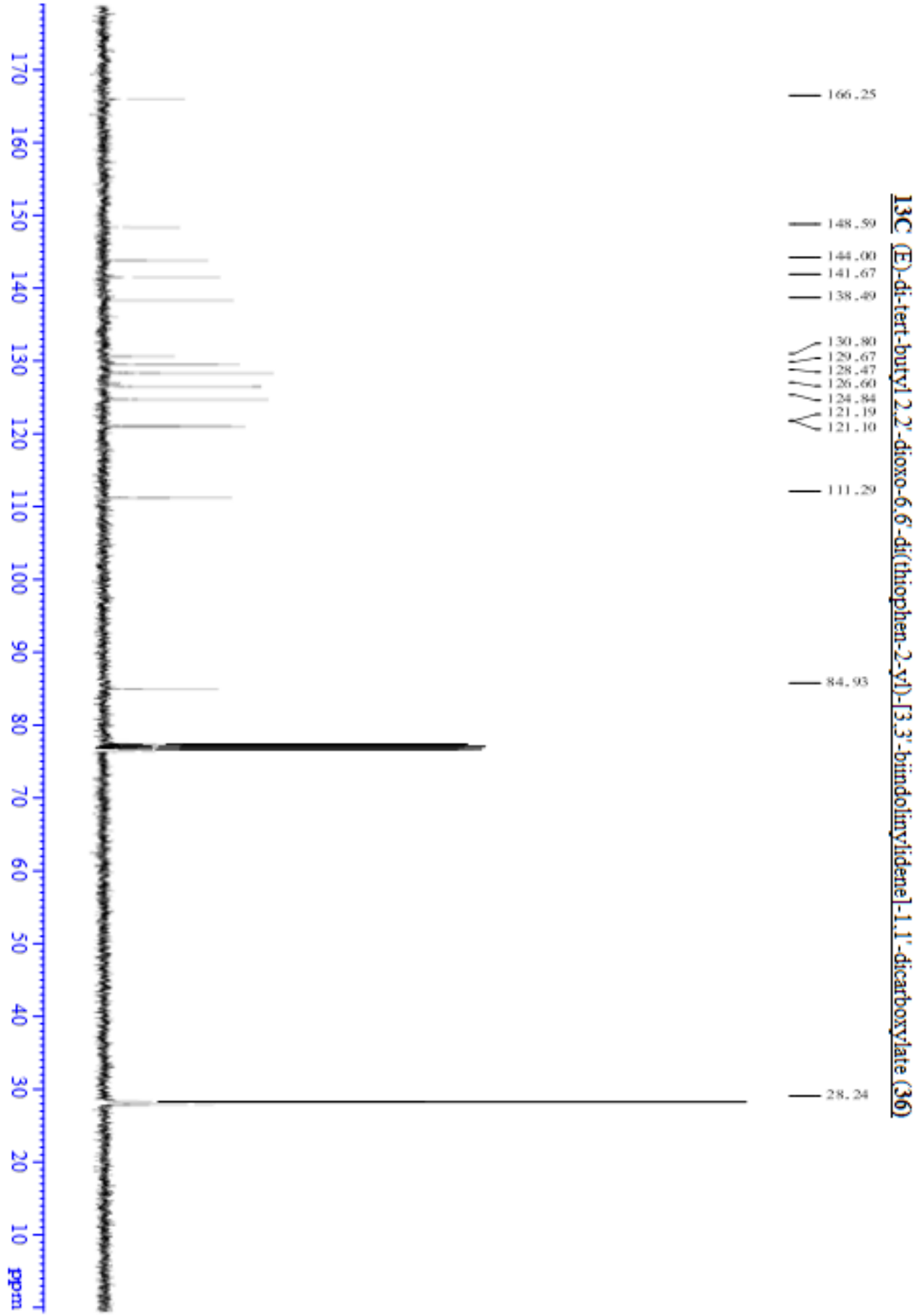
13C (E)-di-tert-butyl 2,2'-dioxo-6,6'-di(thiophen-2-yl)-[3,3'-biindolinylidene]-1,1'-dicarboxylate (36)
166.25
148.59
144.00
141.67
138.49
130.80
129.67
128.47
126.60
124.84
121.19
121.10
111.29
84.93
28.24
170
160
150
140
130
120
110
100
90
80
70
60
50
40
30
20
10
ppm

(E)-bis(2,6-dimethylheptan-2-yl) 2,2'-dioxo-6,6'-diphenyl-[3,3'-biindolinylidene]-1,1'-dicarboxylate **(37)**

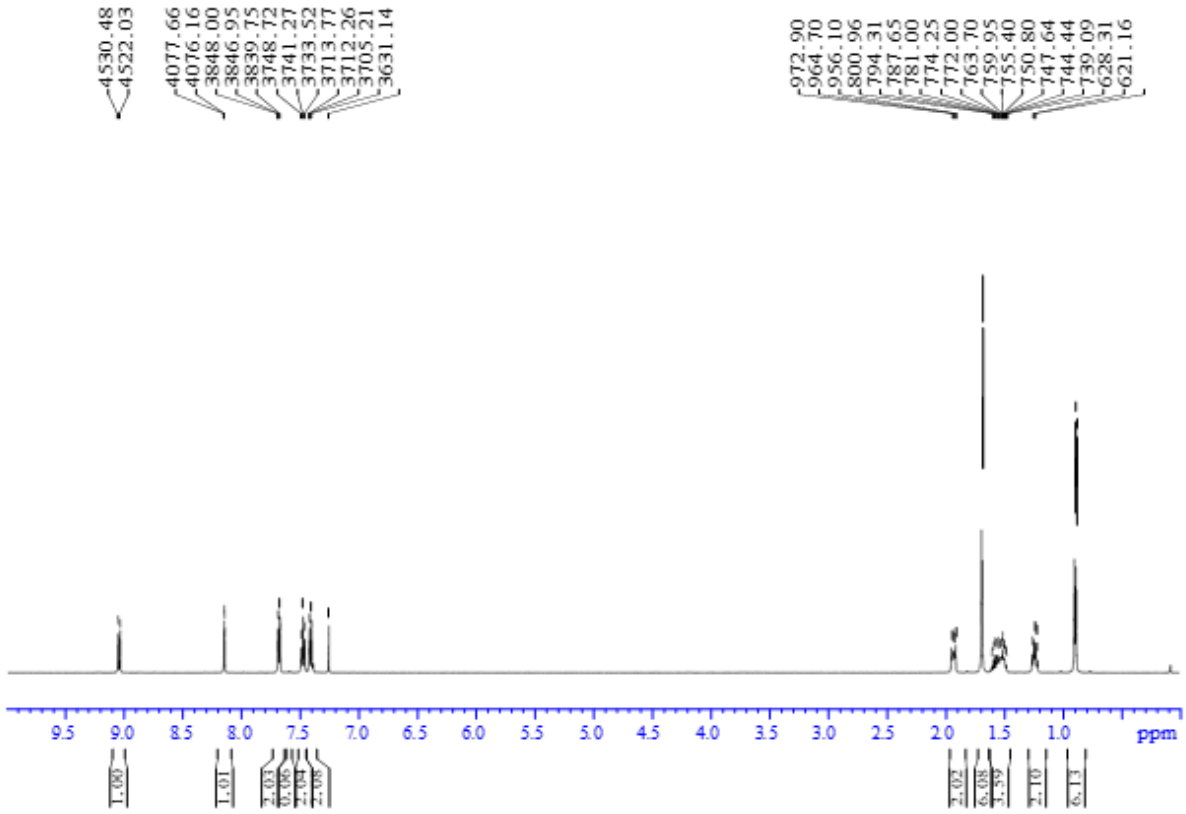

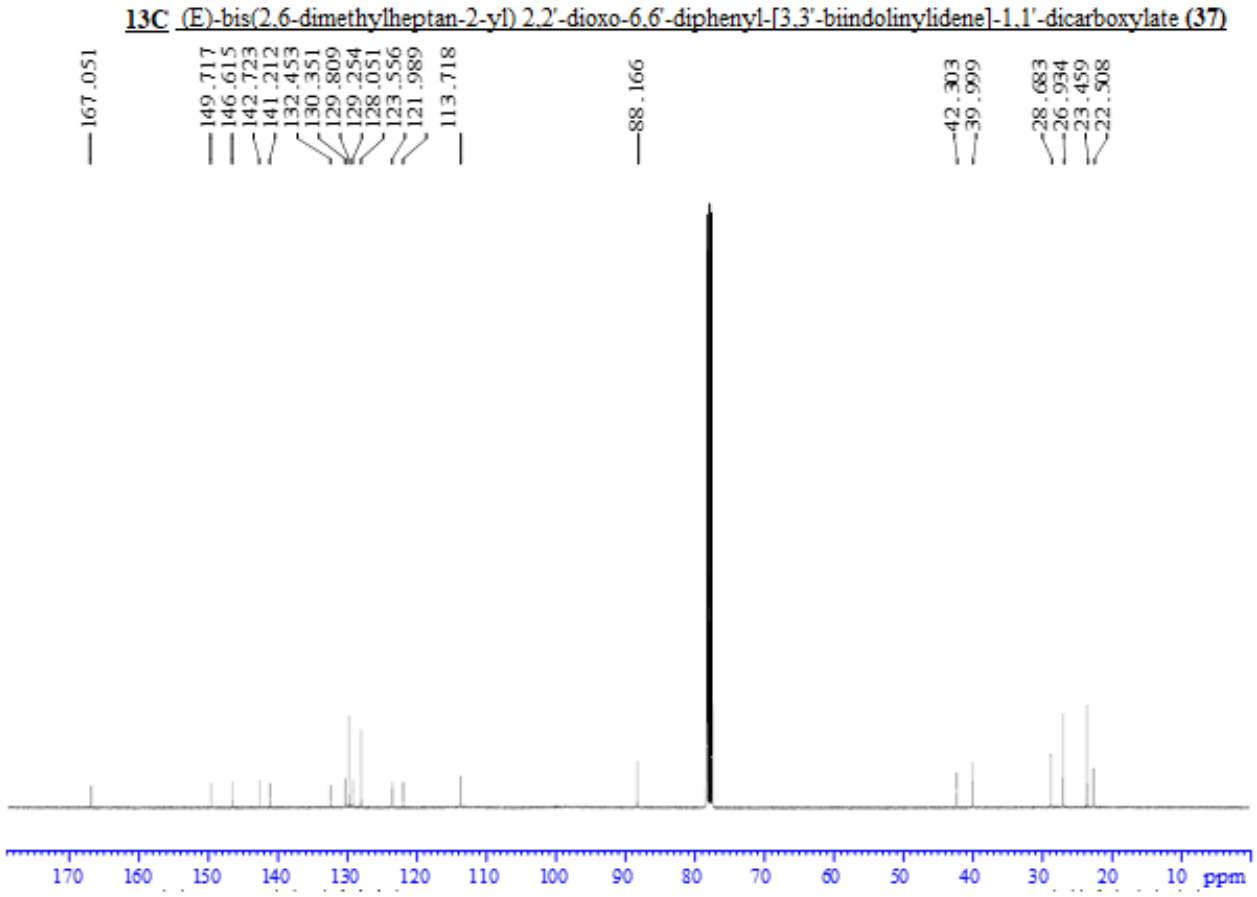
13C (E)-bis(2,6-dimethylheptan-2-yl) 2,2'-dioxo-6,6'-diphenyl-[3,3'-biindolinylidene]-1,1'-dicarboxylate (37)
167.051
149.717
146.615
142.723
141.212
132.453
130.351
129.809
129.254
128.051
123.556
121.989
113.718
88.166
42.303
39.999
28.683
26.934
23.459
22.908
170
160
150
140
130
120
110
100
90
80
70
60
50
40
30
20
10
ppm

Appendix 4- NMR

(E)-di-tert-butyl 6,6'-bis(1-methyl-1H-pyrrol-2-yl)-2,2'-dioxo-[3,3'-biindolinylidene]-1,1'-dicarboxylate **(38)**

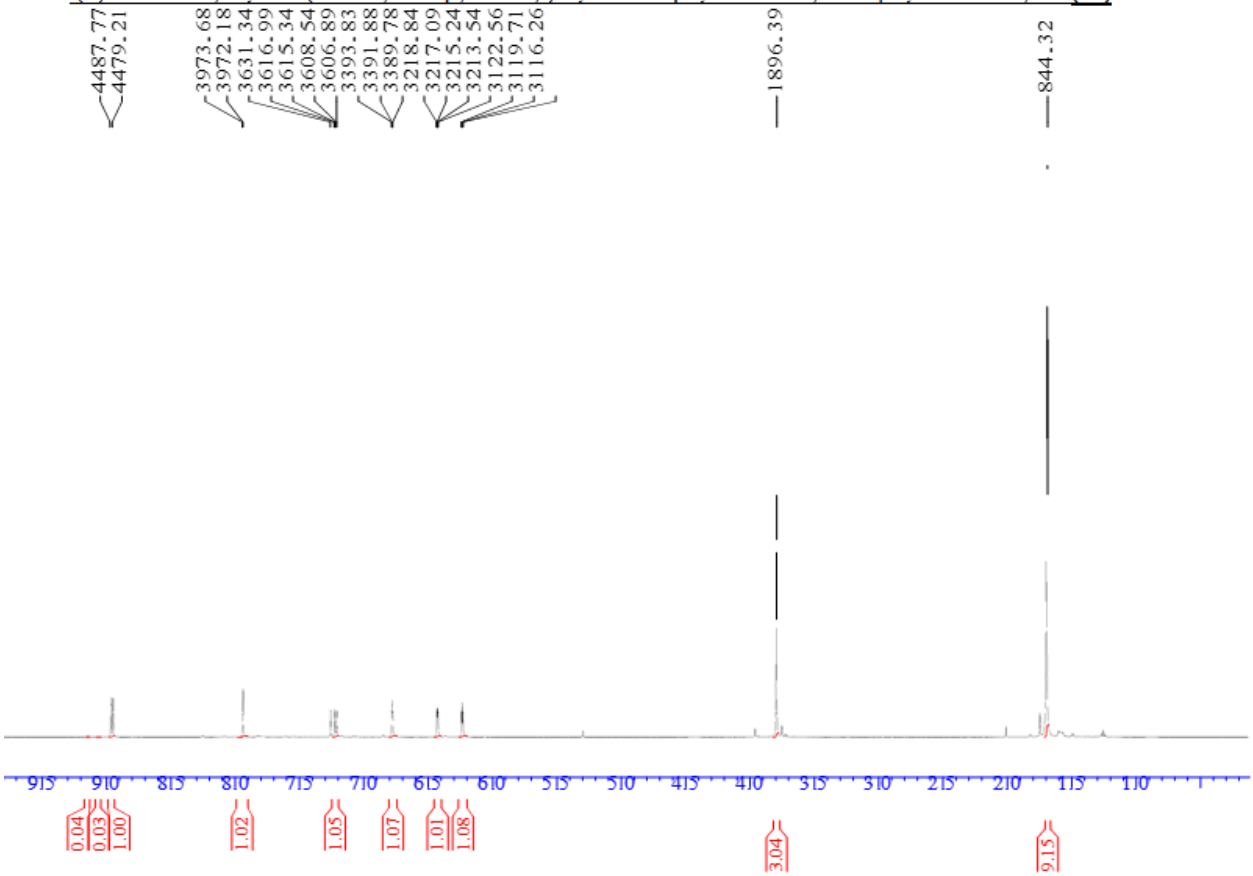

C13 (E)-di-tert-butyl 6,6'-bis(1-methyl-1H-pyrrol-2-yl)-2,2'-dioxo-[3,3'-biindolinylidene]-1,1'-dicarboxylate **(38)**

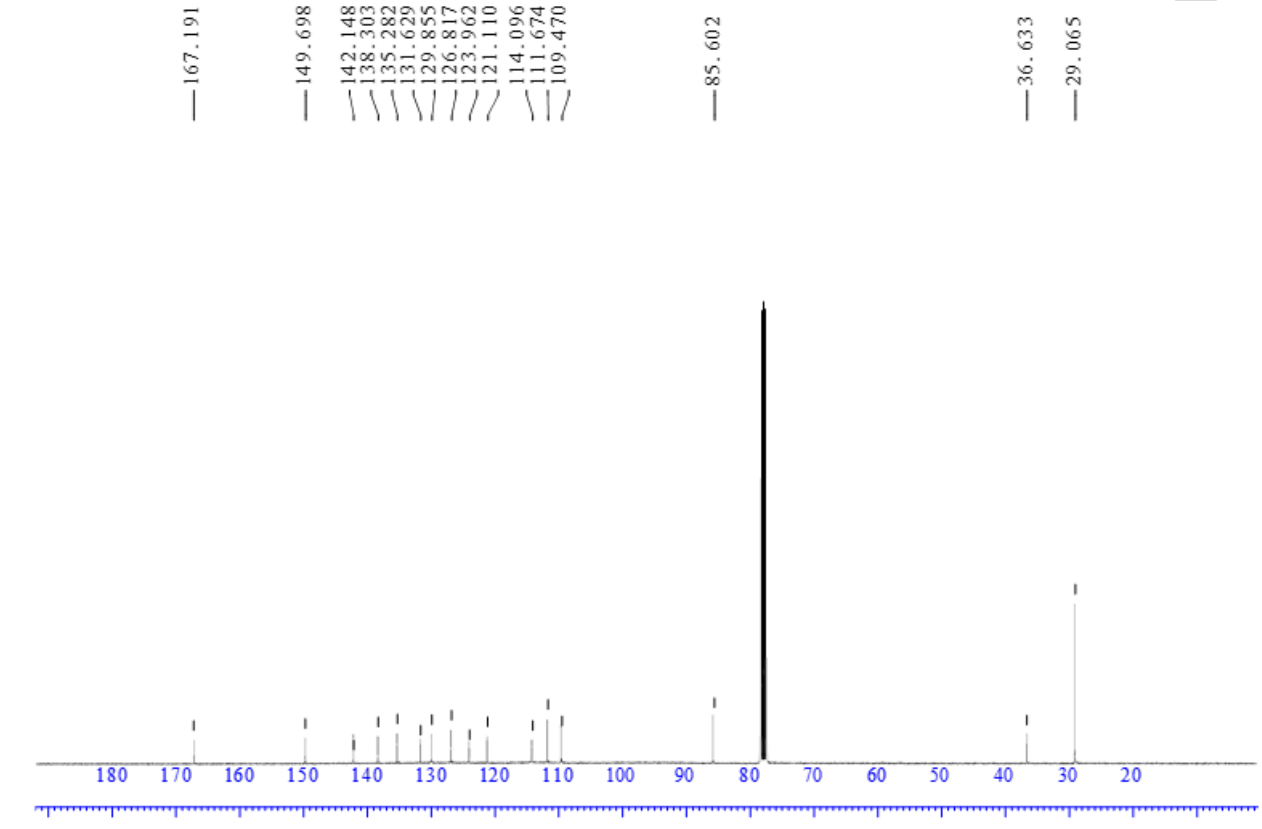

Appendix 4- NMR